ISSN 2071-4726
2071-0305

Инженерно-строительный журнал

НАУЧНОЕ ИЗДАНИЕ

№1(85) 2019

Федеральное государственное автономное образовательное учреждение
высшего образования
Санкт-Петербургский политехнический университет Петра Великого

ПОЛИТЕХ
Санкт-Петербургский политехнический университет Петра Великого

Инженерно-строительный институт
Центр дополнительных профессиональных программ
195251, г. Санкт-Петербург, Политехническая ул., 29,
тел/факс: 552-94-60, www.stroikursi.spbstu.ru,
stroikursi@mail.ru

Приглашает специалистов организаций, вступающих в СРО, на курсы повышения квалификации (72 часа)

Код	Наименование программы	Виды работ*
	Курсы по строительству	
БС-01-04	«Безопасность и качество выполнения общестроительных работ»	**п.1,2, 3, 5, 6, 7, 9, 10, 11, 12, 13, 14**
БС-01	«Безопасность и качество выполнения геодезических, подготовительных и земляных работ, устройства оснований и фундаментов»	**1,2,3,5**
БС-02	«Безопасность и качество возведения бетонных и железобетонных конструкций»	**6,7**
БС-03	«Безопасность и качество возведения металлических, каменных и деревянных конструкций»	**9,10,11**
БС-04	«Безопасность и качество выполнения фасадных работ, устройства кровель, защиты строительных конструкций, трубопроводов и оборудования»	**12,13,14**
БС-05	«Безопасность и качество устройства инженерных сетей и систем»	**15,16,17,18,19**
БС-06	«Безопасность и качество устройства электрических сетей и линий связи»	**20,21**
БС-08	«Безопасность и качество выполнения монтажных и пусконаладочных работ»	**23,24**
БС-12	«Безопасность и качество устройства мостов, эстакад и путепроводов»	**29**
БС-13	«Безопасность и качество выполнения гидротехнических, водолазных работ»	**30**
БС-14	«Безопасность и качество устройства промышленных печей и дымовых труб»	**31**
БС-15	«Осуществление строительного контроля»	**32**
БС-16	«Организация строительства, реконструкции и капитального ремонта. Выполнение функций технического заказчика и генерального подрядчика»	**33**
	Курсы по проектированию	
БП-01	«Разработка схемы планировочной организации земельного участка, архитектурных решений, мероприятий по обеспечению доступа маломобильных групп населения»	**1,2,11**
БП-02	«Разработка конструктивных и объемно-планировочных решений зданий и сооружений»	**3**
БП-03	«Проектирование внутренних сетей инженерно-технического обеспечения»	**4**
БП-04	«Проектирование наружных сетей инженерно-технического обеспечения»	**5**
БП-05	«Разработка технологических решений при проектировании зданий и сооружений»	**6**
БП-06	«Разработка специальных разделов проектной документации»	**7**
БП-07	«Разработка проектов организации строительства»	**8**
БП-08	«Проектные решения по охране окружающей среды»	**9**
БП-09	«Проектные решения по обеспечению пожарной безопасности»	**10**
БП-10	«Обследование строительных конструкций и грунтов основания зданий и сооружений»	**12**
БП-11	«Организация проектных работ. Выполнение функций генерального проектировщика»	**13**
Э-01	«Проведение энергетических обследований с целью повышения энергетической эффективности и энергосбережения»	
	Курсы по инженерным изысканиям	
И-01	«Инженерно-геодезические изыскания в строительстве»	**1**
И-02	«Инженерно-геологические изыскания в строительстве»	**2,5**
И-03	«Инженерно-гидрометеорологические изыскания в строительстве»	**3**
И-04	«Инженерно-экологические изыскания в строительстве»	**4**
И-05	«Организация работ по инженерным изысканиям»	**7**

***(согласно приказам Минрегионразвития РФ N 624 от 30 декабря 2009 г.)**

По окончании курса слушателю выдается удостоверение о краткосрочном повышении квалификации установленного образца (72 ак. часа)

Для регистрации на курс необходимо выслать заявку на участие, и копию диплома об образовании по телефону/факсу: 8(812) 552-94-60, 535-79-92, , e-mail: stroikursi@mail.ru.

Инженерно-строительный журнал
НАУЧНОЕ ИЗДАНИЕ

ISSN 2071-4726, 2071-0305

Свидетельство о государственной регистрации: ПИ №ФС77-38070, выдано Роскомнадзором

Специализированный научный журнал. Выходит с 09.2008.

Включен в Перечень ведущих периодических изданий ВАК РФ

Периодичность: 8 раз в год

Учредитель и издатель:

Санкт-Петербургский политехнический университет Петра Великого

Адрес редакции:

195251, СПб, ул. Политехническая, д. 29, Гидрокорпус-2, ауд. 245

Дата выхода: 15.05.2019

Содержание

Контакты:
E-mail: mce@spbstu.ru
Web: http://www.engstroy.spbstu.ru

Magazine of Civil Engineering
SCHOLAR JOURNAL

ISSN 2071-4726, 2071-0305
Peer-reviewed scientific journal
Start date: 2008/09
8 issues per year

Publisher:

Peter the Great St. Petersburg Polytechnic University

Indexing:

Scopus, Russian Science Citation Index (WoS), Compendex, DOAJ, EBSCO, Google Academia, Index Copernicus, ProQuest, Ulrich's Serials Analysis System

Corresponding address:

245 Hydro Building, 29 Polytechnicheskaya st., Saint-Petersburg, 195251, Russia

Date of issue: 15.05.2019

Contents

E-mail: mce@spbstu.ru
Web: http://www.engstroy.spbstu.ru/eng/index.html

Magazine of Civil Engineering. 2019. 85(1). Pp. 3–14
Инженерно-строительный журнал. 2019. № 1(85). С. 3–14

Magazine of Civil Engineering

ISSN 2071-0305

journal homepage: http://engstroy.spbstu.ru/

DOI: 10.18720/MCE.85.1

Heat loss through the window frames of buildings

***A.Kh. Baiburin*[a*], *M.M. Rybakov*[a], *N.I. Vatin*[b]**
[a] South Ural State University, Chelyabinsk, Russia
[b] Peter the Great St. Petersburg Polytechnic University, St. Petersburg, Russia
** E-mail: abayburin@mail.ru*

Keywords: buildings; windows; window frame; energy efficiency; thermal insulation; heat loss; heat transfer factors; mathematic simulation

Abstract. The object of investigation is window frames of buildings since they are critical zones in terms of thermal insulation. It was studied how the properties of window frame affect the change in heat flow and temperature fields. It was analyzed the heat loss that depends on a range of structural features of a window frame, such as geometrical, thermal and physical properties of walls, windows, lintels, and joints. An experiment was designed, computer simulation and laboratory tests were conducted. Eight different types of frame units were analyzed. Their finite-element models in the ELCUD software was developed. The laboratory tests proved the adequacy of finite-element models. The comparative results obtained from tests and numerical models were in consistency. We conducted a full factorial experiment and excluded insignificant factors using statistical analysis. Mathematical models of the joint effect of these factors were developed. A detailed analysis of the join effect of factors on the heat loss through the window frame was performed. The results can be used for the energy classification of buildings in use.

1. Introduction

Attention to ecologically safe and energy-efficient technologies, particularly in the field of construction and design, has increased under the conditions of escalating tensions in the economy of certain regions, which is now a global tendency, and urgent environmental problems related to the emission of oxide compounds, caused by heat and energy production [1–7]. This paper describes a new aspect that makes it possible to reduce energy consumption by reducing heat release into the environment. The research focuses on window frames, which are significant boundary zones related to heat losses.

Window frames are one of the most important elements of a building envelope that are thermally and technically non-uniform. Unlike outer corners, and joints between walls, floors, and ceiling, inner walls can have the lowest temperatures [8–12].

Many researchers [8–14] have proved that it is important to take into account these zones when determining the reduced total thermal resistance. Some researchers [8, 10, 14] point out the most significant factors that affect the heat flow through a window frame unit.

It was established in [14, 15] that the thicker the wall, the greater the extra losses through a window frame. It allows us to conclude that the thickness of thermal insulator and the heat transfer coefficients of wall and insulation materials also affect the heat flow through a window frame unit. If the window frame is moved to the inner wall, heat losses through window frames decrease, but the wall temperature on the inner wall near the window falls [8, 9, 14, 15]. The paper [10] suggests shifting the window frame to the wall center in order to solve the problem of great heat losses through the window frame.

According to the calculations in [14], the location of the window has the following effect on heat losses through window frames: compared to a blind brick wall, there is an increase in heat losses of 18, 14, and 16 %, when the distance between the window frame and the outer wall side is 120, 250, and 380 mm, respectively.

Baiburin, A.Kh., Rybakov, M.M., Vatin, N.I. Heat loss through the window frames of buildings. Magazine of Civil Engineering. 2019. 85(1). Pp. 3–14. DOI: 10.18720/MCE.85.1.

Байбурин А.Х., Рыбаков М.М., Ватин Н.И. Тепловые потери через оконные рамы зданий // Инженерно-строительный журнал. 2019. № 1(85). С. 3–14. DOI: 10.18720/MCE.85.1.

It was established in [13] that insulation of the inner frame negatively affects thermal and physical properties of the envelope. The window frame remains in the cold zone, and the insulator prevents the window frame from warming. As a result, there is condensation and accumulation of moisture in the insulator. The research confirmed the result described in [13], therefore this factor will not be considered in further studies.

It was established in [12] that if a joint is filled with a more thermally conductive material, the density of the heat flow increases, leading to increased heat losses.

According to [14], the thicker the window frame, the lower extra heat losses through the window frame. It is logical to assume that the coefficient of thermal conductivity of the window profile will also affect the heat flow.

However, the reviewed studies did not consider the joint effect of factors.

This research aims to model the joint effect of structural features of envelope constructions in a window frame zone on thermal insulation. To achieve the goal, we solved the following tasks:

1. determined the factors that affect heat transfer through a window frame;
2. chose a method for studying the joint effect;
3. conducted a screening experiment to exclude insignificant factors;
4. conducted a full factorial experiment;
5. processed the results and verified the adequacy of the developed models;
6. developed software to facilitate the use of these models.

First, we chose the factors that affect heat transfer through a window frame unit. These factors include:

– thickness of the wall and the coefficient of thermal conductivity of wall material;

– thickness of the inner and outer insulator and the coefficient of thermal conductivity of insulator material;

– position of the window frame across the width of the window aperture;

– thickness of the window profile, its material and coefficient of thermal conductivity;

– width of the joint and the coefficient of thermal conductivity of the joint filling;

– size of the heat-insulating insert and the coefficient of thermal conductivity of heat-insulating insert material;

– height of the lintel and the coefficient of thermal conductivity of lintel material (top jamb).

Figure 1 shows the effect of each factor on the value of heat flow through a window frame unit, obtained from the experiment described in the studies [14, 15].

The values of heat flow under varying values ranged from 3.092 W/m to 25.16 W/m. The factor "coefficient of thermal conductivity of lintel material" has the greatest effect (296.6 %), and the factor "height of the lintel" has the least effect (0.528 %).

2. Methods

Having analyzed the effect of different factors on the degree of heat insulation (Figure 1), we found out that quantitative estimates of the effect that each factor has vary significantly. To determine the joint effect of the factors, a full factorial experiment (FFE) is required. Due to a significant number of factors and complexity of their joint action, it was decided to carry out 8 independent experiments for the following boundary zones:

1. side jamb of the window structure with a PVC profile and the wall without a rabbet;
2. top jamb of the window structure with a PVC profile and the wall without a rabbet;
3. side jamb of the window structure with a PVC profile and the wall with a rabbet;
4. top jamb of the window structure with a PVC profile and the wall with a rabbet;
5. side jamb of the window structure with an aluminum profile and the wall without a rabbet;
6. top jamb of the window structure with an aluminum profile and the wall without a rabbet;
7. side jamb of the window structure with an aluminum profile and the wall with a rabbet;
8. top jamb of the window structure with an aluminum profile and the wall with a rabbet.

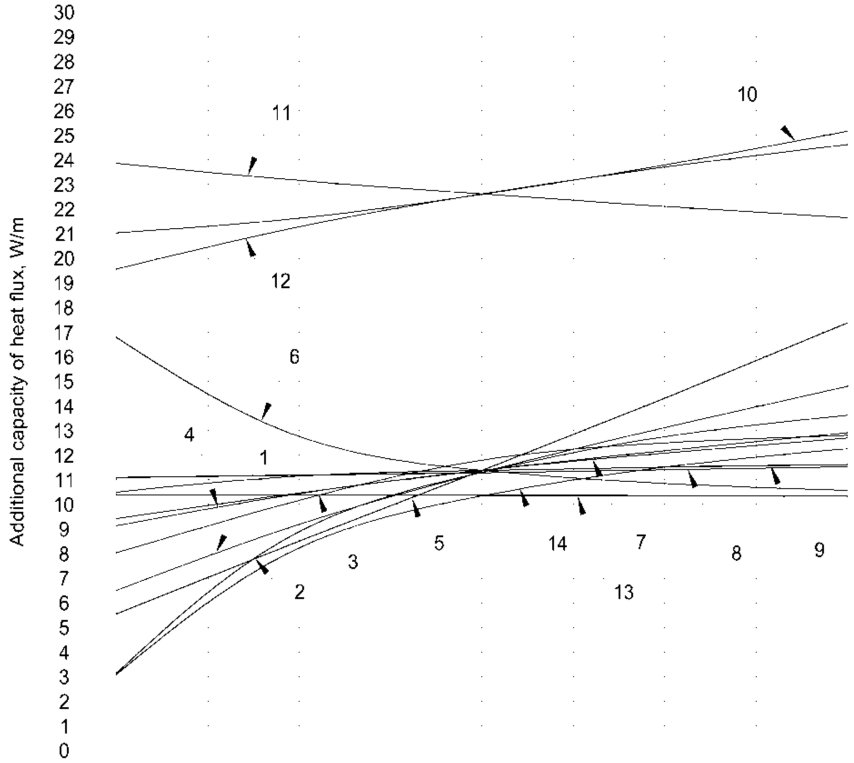

1-Thickness of the wall, m	0.12	0.185	0.25	0.315	0.38	0.445	0.51	0.575	0.64
2-Thermal conductivity of the wall material, W/(m*C)	0.12	0.361	0.603	0.844	1.085	1.326	1.568	1.809	2.05
3-Thickness of the insulation of outer wall, m	0.04	0.0663	0.0925	0.119	0.145	0.171	0.198	0.224	0.25
4-Thermal conductivity of the insulation material, W/(m*C)	0.03	0.0375	0.045	0.0525	0.06	0.0675	0.075	0.0825	0.09
5-Position of the window in an aperture, % of the thickness of the wall from outer edge	0	12.5	25.0	37.5	50.0	62.5	75.0	87.5	100.0
6-Width of the assembly seam, m	0.01	0.0188	0.0275	0.0363	0.045	0.0538	0.0625	0.0713	0.08
7-Thermal conductivity of the assembly seam, W/(m*C)	0.02	0.0363	0.0525	0.0689	0.085	0.101	0.118	0.134	0.15
8-Thickness of the window profile, m	0.06	0.065	0.07	0.075	0.08	0.085	0.09	0.095	0.01
9-Thermal conductivity of the window profile, W/(m*C)	0.1	0.25	0.4	0.55	0.7	0.85	1.0	1.15	1.3
10-Width of the thermal filler, m	0.01	0.0275	0.045	0.0625	0.08	0.0975	0.115	0.1325	0.15
11-Depth of the thermal filler, m	0.065	0.0721	0.0793	0.0864	0.0935	0.101	0.108	0.115	0.122
12-Thermal conductivity of the thermal filler material, W/(m*C)	0.03	0.0775	0.125	0.1725	0.22	0.2675	0.315	0.3625	0.41
13-Height of lintel, m	0.065	0.13	0.195	0.26	0.325	0.39	0.455	0.52	0.585
14-Thermal conductivity of the lintel, W/(m*C)	0.06	0.309	0.558	0.806	1.055	1.304	1.553	1.801	2.05

Figure 1. Dependence of heat flow through a window frame unit on the values of the factors.

This choice is based on the fact that a top jamb differs from a side jamb and a bottom jamb (drip cap, apron) as it is influenced by additional factors (the height of the lintel and the coefficient of thermal conductivity of lintel material), as well as a wall with a rabbet compared to a wall without a rabbet. It was decided to use a heat-insulating insert for a wall with a window rabbet and apply it as the reference point for the window frame position, while the window frame position in a wall without a window rabbet is an independent factor, and heat insulation of the outer jamb is used as a heat-insulating insert. The studied PVC profiles were considered as uniform, since the values of the coefficients of thermal conductivity of main materials, i.e. PVC and air, are close to each other (0.19 W/(m·°C) and 0.15 W/(m·°C) respectively). It allowed us to vary the value of the coefficient of thermal conductivity of the profile from 0.1 to 1.3 W/(m·°C). Since the value of the coefficient of thermal conductivity of aluminum is high (221 W/(m·°C)) as compared to those of PVC and air, it is impossible to consider the aluminum profile as uniform, as it will lead to inaccurate calculations. Therefore, when studying the aluminum profile, we chose the most common construction design according to the results of analyzing design solutions and observations at construction sites. Table 1 shows the selection of factors for the eight experiments.

Table 1. Studied factors and levels of their variation.

Factor	Factor value corresponding to the level of its variation		Number of experiment							
	min (–1)	max (+1)	1	2	3	4	5	6	7	8
Wall thickness, m	0.12	0.64	X_1	X_1	X_1	X_1	X_1	X_1	X_1	X_1
Coefficient of thermal conductivity of wall material, W/(m·°C)	0.12	2.05	X_2	X_2	X_2	X_2	X_2	X_2	X_2	X_2
Outer wall insulation, m	0.04	0.25	X_3	X_3	X_3	X_3	X_3	X_3	X_3	X_3
Coefficient of thermal conductivity of the insulator, W/(m·°C)	0.03	0.09	X_4	X_4	X_4	X_4	X_4	X_4	X_4	X_4
Position of the window frame in the window aperture, % of the wall width from the outer side	0	100	X_5	X_5	–	–	X_5	X_5	–	–
Window profile thickness, m	0.060	0.100	X_6	X_6	X_5	X_5	–	–	–	–
Coefficient of thermal conductivity of the window profile, W/(m· °C)	0.1	1.3	X_7	X_7	X_6	X_6	–	–	–	–
Joint width, m	0.01	0.08	X_8	X_8	X_7	X_7	X_6	X_6	X_5	X_5
Coefficient of thermal conductivity of the joint, W/(m·°C)	0.02	0.15	X_9	X_9	X_8	X_8	X_7	X_7	X_6	X_6
Width of the heat-insulating insert, m	0.01	0.15	–	–	X_9	X_9	–	–	X_7	X_7
Depth of the heat-insulating insert, m	0.065	0.122	–	–	X_{10}	X_{10}	–	–	X_8	X_8
Coefficient of thermal conductivity of heat-insulating insert, W/(m·°C)	0.03	0.41	–	–	X_{11}	X_{11}	–	–	X_9	X_9
Height of the lintel, m	0.065	0.585	–	X_{10}	–	X_{12}	–	X_8	–	X_{10}
Coefficient of thermal conductivity of the lintel, W/(m·°C)	0.06	2.05	–	X_{11}	–	X_{13}	–	X_9	–	X_{10}

Notes:

1. X_1-X_{13} indicate the number of a specific factor in a specific experiment;
2. In experiments with a rabbeted wall (experiments 3, 4, 7, 8), the wall thickness is taken in the range from 0.38 to 0.64 m;
3. In experiments with top jambs (experiments 2, 4, 6, 8), the coefficient of thermal conductivity of the wall is taken from 0.12 to 0.99 W/(m·°C), whereas in a rabbeted wall (experiments 3, 4, 7, 8) it is taken in the range from 0.47 to 0.87 W/(m·°C);
4. In experiments with an aluminum profile window (experiments 5, 6, 7, 8), the joint width is taken in the range from 0.01 to 0.05 m.

In order to determine the joint effect of the studied factors on the thermal insulation level of an envelope fragment, we conducted an experiment using computer simulation. This experiment was carried out according to a special plan, where the value of heat loss rates through a window frame unit was used as a response function.

All possible combinations for the studied factors were studied using a complete factorial experiment. Each studied factor has two levels, therefore the number of tests within the complete factorial experiment was determined by the formula $N = 2^m$, where m is the number of factors.

Since the number of tests would be $N = 2048$, in case the number of factors $m = 11$, it was decided to conduct a screening experiment, which allowed us to reduce the number of factors and tests, and to identify the significant factors. After insignificant factors had been excluded, a complete factorial experiment was carried out with the remaining factors, which allowed us to describe the response function.

To carry out the screening experiment, we used Plackett-Burman experimental designs, because they are optimal if there are no parallel experiments. The number of experiments in these matrices is a multiple of four ($N = 4k$), and they can be used to study the effect of $(4k - 1)$ factors. As these designs are orthogonal, linear effects of the factors are determined independently from each other.

After the screening experiment, the results were statistically processed, that is, the effect of each factor was calculated and the significance of factors was verified using Student's t-test with a significance value $\alpha = 0.05$. To determine dispersion of the estimated coefficients, fake factors were used in each test.

After the screening experiment and identification of the significant factors, we performed a two-level complete factorial experiment using a linear polynomial.

$$y(k) = b_0 + \sum b_i \cdot x_i + \sum b_{ij} \cdot x_{ij} + \sum b_{ijk} \cdot x_{ijk}, \tag{1}$$

where $y(k)$ is the response function;

b_i is the linear coefficient; b_{ij} is the coefficient of double interaction;

b_{ijk} is the coefficient of triple interaction;

x_i is the coded value of the factor.

The coefficient of the joint effect of the significant factors forecast according to the model, as well as the linear coefficient and the coefficients of double and triple interaction were determined by the least square procedure.

After that, the results were statistically evaluated, that is, the significance of all coefficients was verified using Student's *t*-test with the significance value $\alpha = 0.05$, and the adequacy of the model was verified according to the Fisher criterion. To simplify the calculation, coefficients that resulted insignificant were excluded from the model. An abbreviated model was created according to all the tests.

The coefficient of the joint effect of significant factors on thermal insulation of a window frame was studied experimentally using computer simulation in the software product ELCUT, which was developed by the "Tor" company. The software has a certificate of conformance for the use in construction No. ROSS RU.SP15.N00904.

Figure 2 shows an example of the finite element model developed in the ELCUT software and the temperature field of the studied fragment.

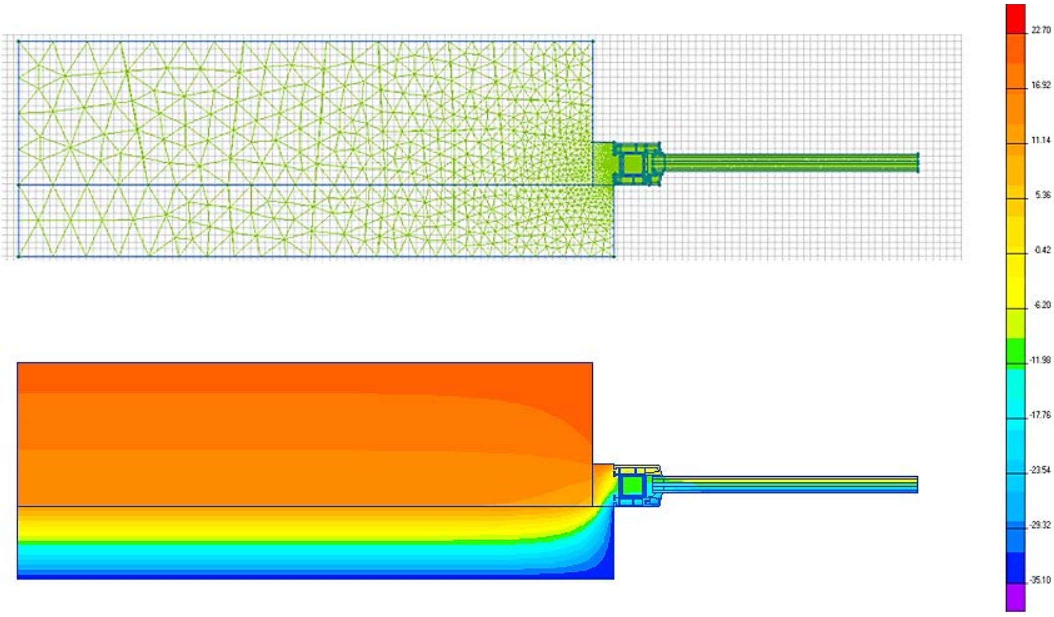

Figure 2. Example of the finite element model and the temperature field.

To confirm the adequacy of the computer calculation, the most typical defects were simulated under laboratory conditions. The tests were carried out in a certified research laboratory of the department "Construction Operations and Theory of Structures", SUSU (NRU). The research method complied with GOST 30971-2012 "Joints of connections between window blocks and wall openings".

The conditions of stationary heat flow were created with the climate chamber KKhTV-24.0 (climate chamber of cold, heat, and moisture) produced by OOO "NPO Spetsklimat" with available storage capacity of 24 m^3. A set of instrumentation included: a FLIR E60 thermographic camera; a 10-channel ITP-MG4.03.10 Flow device; a TGTs-MG4 thermohygrometer; a TEMP-3.2 thermohygrometer; an ISP-MG4 Probe thermal conductivity meter.

The study focused on a fragment of a multilayer envelope with a window (Figure 3). The fragment dimensions were the following: height – 1400 mm, width – 1600 mm, thickness – 300 (250) mm. The usable space of the fragment was 1.69 m^2. The multilayer envelope structure was made of 400×200×200 mm slag block and Isover Facade mineral wool heat insulator. The thickness of the insulator ranged from 50 to 100 mm. The slag block was laid with 15-millimeter-thick M150 cement-sand mortar. The insulation was fastened with Koelner disk-shaped dowels with steel nails of 10 mm in diameter.

The experiment was carried out in temperature conditions corresponding to the Chelyabinsk region. The laboratory temperature was 21 °C, in the climate chamber – minus 34 °C.

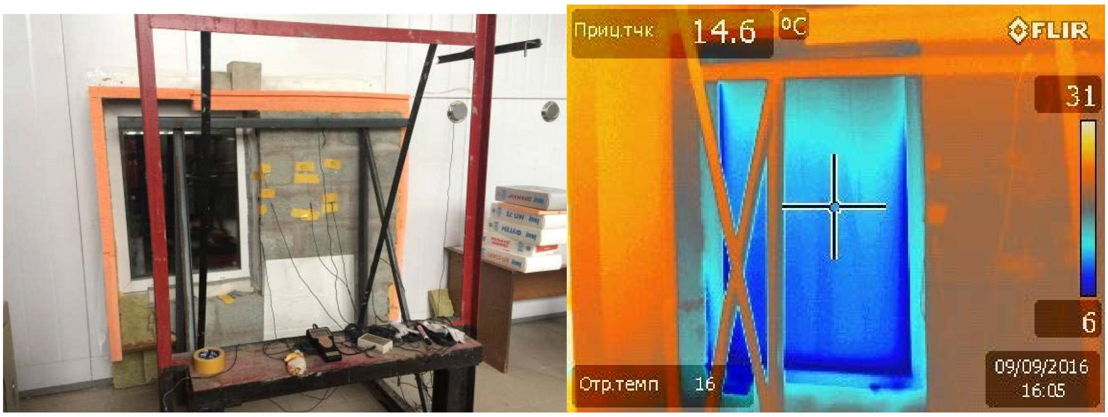

a *b*

Figure 3. Studied sample:
***a* is a test bench for the laboratory experiment; *b* is the thermogram of the test structure.**

Having obtained the results of the laboratory experiment, we used the ELCUT software to develop a computer model, and evaluated the consistency of the results. The discrepancies between the results of the laboratory experiment and the computer modeling ranged from 1.01 to 9.13 % as compared to the values of the heat flow, which is less than the permissible error. Thus, the use of computer simulation in this study has been proved adequate.

3. Results and Discussion

To facilitate further analysis, all the data obtained during the study was summarized as a matrix of design and experimental results. Table 2 shows a fragment of the matrix for a side jamb of the window structure with a PVC profile and a rabbeted wall (experiment 3).

Table 2. Fragment of the matrix of the design and the results of determining the joint effect of the significant factors on the value of the heat loss rates through the side jamb unit.

No.	X_2	X_3	X_4	X_6	X_7	X_9	X_{11}	Heat loss		
								Experiment	Complete model	Abbreviated model
1	+	+	+	+	+	+	+	0.426	0.414	0.414
2	+	+	+	+	+	+	–	0.294	0.301	0.301
3	+	+	+	+	+	–	+	0.327	0.329	0.329
…	…	…	…	…	…	…	…	…	…	…
126	–	–	–	–	–	+	–	0.121	0.124	0.124
127	–	–	–	–	–	–	+	0.156	0.154	0.154
128	–	–	–	–	–	–	–	0.142	0.151	0.151

As a result of the experiment, a model of the joint effect of the significant factors on the thermal properties of the window frame was developed for each type of the frame unit, using formula (1) (Table 3).

Table 3. Models of the joint effect of the significant factors on the thermal properties of the window frame.

Experiment number	Mathematical model	Determination coefficient
1	$y(k)=0.178+0.0575\cdot x_1+0.0832\cdot x_2+0.0248\cdot x_3+ +0.0172\cdot x_4+0.0522\cdot x_5-0.0485\cdot x_8+0.0363\cdot x_1\cdot x_2+ +0.0158\cdot x_1\cdot x_4+0.0433\cdot x_1\cdot x_5+0.0152\cdot x_2\cdot x_3+ +0.0161\cdot x_2\cdot x_4+0.0366\cdot x_2\cdot x_5-0.0162\cdot x_2\cdot x_8+ +0.0171\cdot x_3\cdot x_5+0.00881\cdot x_4\cdot x_5+0.0122\cdot x_1\cdot x_2\cdot x_4+ +0.0355\cdot x_1\cdot x_2\cdot x_5+0.0153\cdot x_1\cdot x_3\cdot x_5+0.0108\cdot x_2\cdot x_3\cdot x_5+ +0.01\cdot x_2\cdot x_4\cdot x_5$	0.949
2	$y(k)=0.132+0.0531\cdot x_1+0.015\cdot x_4+0.0442\cdot x_5+ +0.0123\cdot x_1\cdot x_4+0.0344\cdot x_1\cdot x_5+0.0349\cdot x_1\cdot x_{11}+ +0.0173\cdot x_3\cdot x_5+0.0185\cdot x_4\cdot x_{11}+0.0309\cdot x_5\cdot x_{11}+ +0.0255\cdot x_1\cdot x_5\cdot x_{11}$	0.861

Experiment number	Mathematical model	Determination coefficient
3	$y(k)=0.258+0.0616\cdot x_2+0.054\cdot x_3-0.0264\cdot x_4+$ $+0.0204\cdot x_6-0.0216\cdot x_7+0.0145\cdot x_9+0.0289\cdot x_{11}+$ $+0.0119\cdot x_2\cdot x_3-0.00609\cdot x_2\cdot x_4+0.00184\cdot x_2\cdot x_9+$ $+0.00454\cdot x_2\cdot x_{11}+0.00328\cdot x_3\cdot x_4+0.00171\cdot x_3\cdot x_6-$ $-0.00181\cdot x_3\cdot x_7+0.01\cdot x_3\cdot x_9+0.00336\cdot x_3\cdot x_{11}-$ $-0.00644\cdot x_4\cdot x_9-0.00199\cdot x_4\cdot x_{11}-0.0182\cdot x_6\cdot x_7+$ $+0.00274\cdot x_6\cdot x_9-0.00307\cdot x_6\cdot x_{11}-0.00239\cdot x_7\cdot x_9+$ $+0.00264\cdot x_7\cdot x_{11}+0.022\cdot x_9\cdot x_{11}$	0.992
4	$y(k)=0.305+0.046\cdot x_3-0,0227\cdot x_4+0.00656\cdot x_6+$ $+0.00659\cdot x_9+0.0229\cdot x_{11}+0.24\cdot x_{13}+0.00873\cdot x_3\cdot x_4+$ $+0.00777\cdot x_3\cdot x_9+0.00232\cdot x_3\cdot x_{11}+0.0407\cdot x_3\cdot x_{13}-$ $-0.00493\cdot x_4\cdot x_9-0.0014\cdot x_4\cdot x_{11}-0.0225\cdot x_4\cdot x_{13}-$ $-0.00153\cdot x_6\cdot x_{11}+0.00145\cdot x_6\cdot x_{13}+0.0169\cdot x_9\cdot x_{11}+$ $+0.0168\cdot x_{11}\cdot x_{13}+0.00184\cdot x_3\cdot x_4\cdot x_9+0.00654\cdot x_3\cdot x_4\cdot x_{13}+$ $+0.00186\cdot x_3\cdot x_9\cdot x_{11}+0.00468\cdot x_3\cdot x_9\cdot x_{13}+0.00135\cdot x_3\cdot x_{11}\cdot x_{13}$ $-0.00116\cdot x_4\cdot x_9\cdot x_{11}-0.00322\cdot x_4\cdot x_9\cdot x_{13}+0.0125\cdot x_9\cdot x_{11}\cdot x_{13}$	0.999
5	$y(k)=0.175+0.0586\cdot x_1+0.0792\cdot x_2+0.0239\cdot x_3+$ $+0.0209\cdot x_4+0.0571\cdot x_5-0.0421\cdot x_6+0.0356\cdot x_1\cdot x_2+$ $+0.016\cdot x_1\cdot x_4+0.0422\cdot x_1\cdot x_5+0.0152\cdot x_2\cdot x_3+$ $+0.0182\cdot x_2\cdot x_4+0.039\cdot x_2\cdot x_5-0.0129\cdot x_2\cdot x_6+$ $+0.0186\cdot x_3\cdot x_5+0.01\cdot x_4\cdot x_5+0.0121\cdot x_1\cdot x_2\cdot x_4+$ $+0.034\cdot x_1\cdot x_2\cdot x_5+0.0155\cdot x_1\cdot x_3\cdot x_5+0.0113\cdot x_2\cdot x_3\cdot x_5+$ $+0.0116\cdot x_2\cdot x_4\cdot x_5+0.0085\cdot x_3\cdot x_4\cdot x_5$	0.925
6	$y(k)=0.18+0.0584\cdot x_1+0.0209\cdot x_3+$ $+0.0196\cdot x_4+0.0571\cdot x_5-0.038\cdot x_6+0.0916\cdot x_9+$ $+0.0121\cdot x_1\cdot x_4+0.0413\cdot x_1\cdot x_5+0.0396\cdot x_1\cdot x_9+$ $+0.0182\cdot x_3\cdot x_5+0.0141\cdot x_3\cdot x_9+0.00727\cdot x_4\cdot x_5+$ $+0.0176\cdot x_4\cdot x_9+0.0397\cdot x_5\cdot x_9-0.0104\cdot x_6\cdot x_9+$ $+0.015\cdot x_1\cdot x_3\cdot x_5+0.0118\cdot x_1\cdot x_4\cdot x_9+$ $+0.0313\cdot x_1\cdot x_5\cdot x_9+0.00706\cdot x_3\cdot x_4\cdot x_5+$ $+0.0124\cdot x_3\cdot x_5\cdot x_9+0.00924\cdot x_4\cdot x_5\cdot x_9$	0.954

Experiment number	Mathematical model	Determination coefficient
7	$y(k) = 0.265 + 0.062 \cdot x_2 + 0.0546 \cdot x_3 - 0.0265 \cdot x_4 - 0.023 \cdot x_5 + 0.016 \cdot x_7 + 0.0277 \cdot x_9 + 0.012 \cdot x_2 \cdot x_3 - 0.00639 \cdot x_2 \cdot x_4 + 0.0024 \cdot x_2 \cdot x_7 + 0.00478 \cdot x_2 \cdot x_9 + 0.00309 \cdot x_3 \cdot x_4 - 0.00283 \cdot x_3 \cdot x_5 + 0.0103 \cdot x_3 \cdot x_7 + 0.00339 \cdot x_3 \cdot x_9 + 0.00168 \cdot x_4 \cdot x_5 - 0.00653 \cdot x_4 \cdot x_7 - 0.00197 \cdot x_4 \cdot x_9 - 0.00463 \cdot x_5 \cdot x_7 + 0.00434 \cdot x_5 \cdot x_9 + 0.0208 \cdot x_7 \cdot x_9 + 0.00383 \cdot x_2 \cdot x_3 \cdot x_4 + 0.00124 \cdot x_2 \cdot x_3 \cdot x_7 - 0.00079 \cdot x_2 \cdot x_4 \cdot x_7 - 0.00107 \cdot x_2 \cdot x_5 \cdot x_7 + 0.0032 \cdot x_2 \cdot x_7 \cdot x_9 + 0.00233 \cdot x_3 \cdot x_4 \cdot x_7 + 0.00265 \cdot x_3 \cdot x_7 \cdot x_9 - 0.00169 \cdot x_4 \cdot x_7 \cdot x_9 + 0.00246 \cdot x_5 \cdot x_7 \cdot x_9$	0.999
8	$y(k) = 0.291 + 0.0476 \cdot x_3 - 0.0231 \cdot x_4 + 0.0117 \cdot x_6 + 0.0139 \cdot x_7 + 0.0428 \cdot x_{10} + 0.195 \cdot x_{11} + 0.00758 \cdot x_3 \cdot x_4 + 0.009 \cdot x_3 \cdot x_7 + 0.0317 \cdot x_3 \cdot x_{11} - 0.00573 \cdot x_4 \cdot x_7 - 0.018 \cdot x_4 \cdot x_{11} - 0.00257 \cdot x_7 \cdot x_{10} - 0.00212 \cdot x_7 \cdot x_{11} + 0.0735 \cdot x_{10} \cdot x_{11} + 0.00316 \cdot x_3 \cdot x_4 \cdot x_{10} + 0.00513 \cdot x_3 \cdot x_4 \cdot x_{11} + 0.00342 \cdot x_3 \cdot x_7 \cdot x_{11} + 0.0148 \cdot x_3 \cdot x_{10} \cdot x_{11} - 0.00223 \cdot x_4 \cdot x_7 \cdot x_{11} - 0.00734 \cdot x_4 \cdot x_{10} \cdot x_{11} + 0.00808 \cdot x_7 \cdot x_{10} \cdot x_{11}$	0.998

The obtained models suggest that when determining the heat loss through a window frame unit, there is a complex joint effect of factors leading to a significant change in heat loss. This allows us to conclude that separate study of each factor can be used mainly to illustrate the significance of factors and to test design solutions [16–19].

The literature review failed to find any studies of the joint effect of factors on a window frame. Earlier studies [16, 19, 20–24] considered the separate and joint effect of thermotechnical nonuniformities and defects in wall structures. In [8–14, 25–32], the temperature regimes of modern windows were studied, but the joint effect of factors on heat loss through a window frame was not studied. The study [16, 30] was based on similar methods, but focused on a different structure: a suspended facade system.

The coded values of the factors that are substituted in the formulas of the models (see Table 3) are determined by the formula:

$$X_i = \frac{\hat{X}_i - (\hat{X}_{i\max} + \hat{X}_{i\min})/2}{(\hat{X}_{i\max} - \hat{X}_{i\min})/2}, \quad (2)$$

where X_i is the coded value of the *i*-factor;

$\hat{X}_i$ is the current natural value of the i-factor;

$\hat{X}_{i\max}$, $\hat{X}_{i\min}$ are maximum and minimum natural values of the *i*-factor.

These models will help to determine the significant rates of heat loss through a window frame unit at construction sites without computer modeling of the unit. For calculating, Table 1 should be used to determine the number of the experiment and the factors, which should be measured. After that, the coded values of the factors in the range between –1 and 1 are defined by formula (2) and substituted in the appropriate models.

Due to possible difficulties in practical application of these models because of their awkwardness, software was developed in C# for greater convenience. The software makes it possible to calculate the rates of heat loss through a window frame, selecting the required structure parameters (type of jamb, wall and window structure) and setting the required natural values of factors determined for a specific building. The software calculates the coded values of the required factors, determines the model that is required for calculations, and displays the value of heat loss rates. This value can be used when performing thermotechnical calculations to more accurately determine the reduced total thermal resistance of the envelope structure, taking into account some thermal nonuniformities.

The developed models can be used to make specifications for installing translucent structures from the point of view of regulating the allowance for their structure according to the criterion of energy efficiency.

4. Conclusions

The experimental results are the following:

1.Eight most common types of window jambs were identified, and for each of them it is necessary to calculate the value of heat loss rates according the appropriate factors. These types include:

– Side jamb of the window structure with a PVC profile and the wall without a rabbet;

– Top jamb of the window structure with a PVC profile and the wall without a rabbet;

– Side jamb of the window structure with a PVC profile and the wall with a rabbet;

– Top jamb of the window structure with a PVC profile and the wall with a rabbet;

– Side jamb of the window structure with an aluminum profile and the wall without a rabbet;

– Top jamb of the window structure with an aluminum profile and the wall without a rabbet;

– Side jamb of the window structure with an aluminum profile and the wall with a rabbet;

– Top jamb of the window structure with an aluminum profile and the wall with a rabbet.

2. To determine the joint effect of structural features of a window frame on the value of heat loss rates for each of the eight types of jambs, we conducted an experiment. The experiment resulted in modeling joint effects, which make it possible to determine the value of heat loss rates with high accuracy and without computer simulation. The maximum discrepancy between the experimentally obtained value and the calculation according to the model was 15.2 %. The discrepancies between the results of the laboratory experiment and the computer modeling ranged from 1.01 to 9.13 %.

3. To simplify the calculation according to the models, we developed C# software that makes it possible to determine the reduced total thermal resistance of the envelope structure taking into account thermal nonuniformities.

4. The developed models can be used to make specifications for installing translucent structures from the point of view of regulating the allowance for their structure according to the criterion of energy efficiency.

5. The results can be used for the buildings in use energy classification. For EU countries, it is necessary to use the national classification of buildings for energy efficiency. The calculation results will be the same when using different Russian and European software products [33] based on the finite element method and the theory of heat transfer.

The work was supported by Act 211 Government of the Russian Federation, contract № 02.A03.21.0011.

References

1. Ananin, M., Perfilyeva, N., Vedishcheva, I., Vatin, N. Investigation of different materials usage expediency for a low-rise public building from the energy efficiency standpoint. IOP Conf. Series: Materials Science and Engineering 365 (2018).
2. Vasilyev, G.P., Lichman, V.A., Yurchenko, I.A., Kolesova, M.V. Method of evaluation of thermotechnical uniformity coefficient by analyzing thermograms. Magazine of Civil Engineering. 2016. 66(6). Pp. 60–67. DOI: 10.5862/MCE.66.6.
3. Blengini, G.A., Di Carlo, T. Energy-saving policies and low-energy residential buildings: An LCA case study to support decision makers in piedmont (Italy). International Journal of Life Cycle Assessment, 2010. No. 15 (7). Pp. 652-665.
4. Danilevskiy, L.N., Danilevskiy, S.L. The algorithm and accuracy of definition of heattechnical indicators of buildings. Magazine of Civil Engineering. 2017. 73(5). Pp. 49–61. DOI: 10.18720/MCE.73.5.
5. Taylor, T., Counsell, J., Gill, S. Energy efficiency is more than skin deep: Improving construction quality control in new-build housing using thermography. Energy and Buildings. 2013. No. 66. Pp. 222-231
6. Vatin, N.I., Nemova, D.V., Rymkevich, P.P., Gorshkov, A.S. Vliyaniye urovnya teplovoy zashchity ograzhdayushchikh konst-ruktsiy na velichinu poter teplovoy energii v zdanii [The impact of the thermal protection level of cladding by the value of a heat loss in a building]. Magazine of Civil Engineering. 2012. No. 8(34). Pp. 4–14. (rus)

7. Korniyenko, S.V., Vatin, N.I., Gorshkov, A.S. Thermophysical field testing of residential buildings made of autoclaved aerated concrete blocks. Magazine of Civil Engineering. 2016. No. 4(64). Pp. 10–25. DOI: 10.5862/MCE.64.2
8. Samarin, O.D. O temperature na vnutrenney poverkhnosti okonnykh otkosov i ikh teplotekhnicheskoy bezopasnosti [About a temperature on inner surface of windows jambs and their thermotechnical safety]. Translucent construction. 2007. No. 3. Pp. 14–17. (rus).
9. Kasper, F.-J., Mueller, R., Rudolphi, R., Wagner, A. Computer Simulation of Tests Demonstrated by the Example of Thermal Protection of Window Constructions. Materials Testing. 1986. No. 28(4). Pp. 107–108.
10. Krivoshein, A.D., Kharlamov, D.A. K voprosu ob uluchshenii temperaturnogo rezhima sovremennykh okon v krayevykh zonakh [To question about improvement of thermal mode of modern windows in edge zones]. Translucent construction. 2005. No. 1. Pp. 10–14. (rus)
11. Golovnev, S.G., Rusanov, Ye.A., Mozgalev, K.M. Otsenka teplozashchitnykh svoystv svetoprozrachnykh konstruktsiy pri stroitelstve i ekspluatatsii zdaniy [Evaluation of the heat-protective properties of translucent structures in the construction and operation of buildings]. Academic Bulletin UralNIIproekt RAASN. 2013. No. 4. Pp. 76–79. (rus)
12. Yakovlev, P.V. Vozmozhnosti energosberezheniya pri proyektirovanii i rekonstruktsii okonnykh proyemov [Possibility of energy efficiency in design and reconstruction of windows aperture]. Translucent construction. 2009. No. 5–6. Pp. 33–35. (rus)
13. Korniyenko, S.V. Sovershenstvovaniye konstruktivnogo resheniya svetoprozrachnykh ograzhdeniy pri otsenke teplopoter [Improving the constructive solution of translucent fences in the evaluation of heat loss]. Construction Materials. 2010. No. 6. Pp. 72–73. (rus)
14. Petrov, Ye.V. Vliyaniye razlichnykh faktorov na teplovyye kharakteristiki okonnykh zapolneniy [The influence of various factors on the thermal characteristics of window fillings]: avtoref. dis. … kand. tehn. nauk: 05.23.03. Tomsk, 2000. 23 p. (rus)
15. Rybakov, M.M. Faktory, vliyayushchiye na teploperedachu cherez uzel okonnogo otkosa [Factors affecting the heat transfer through the window jamb unit]. Internet-magazine «Naukovedenie». 2016. Vol. 8. No. 2. [Online]. URL: http://naukovedenie.ru/PDF/55 TVN216.pdf (open access). (rus)
16. Rusanov, A.Ye., Golovnev, S.G. Issledovaniye vliyaniya defektov ustroystva navesnykh fasadnykh sistem na teplo-zashchitnyye svoystva stenovykh ograzhdayushchikh konstruktsiy [The study of defects influence in the device hinged facade systems on the heat-shielding properties of wall enclosing structures]. Academic Bulletin UralNIIproekt RAASN. 2014. No. 2. Pp. 92–95. (rus)
17. Kuzema, G.P. O teploperedache cherez okna (analiz i nemnogo istorii) [About heat transfer through windows (analysis and a bit of history)]. Translucent construction. 2009. No. 5–6. Pp. 25–28. (rus)
18. Korniyenko, S.V. The experimental analysis and calculative assessment of building energy efficiency. Applied Mechanics and Materials. 2014. Vol. 618. Pp. 509–513.
19. Korniyenko, S.V. Povysheniye energoeffektivnosti zdaniy za schet snizheniya teplopoter cherez krayevyye zony ograzhdayushchikh konstruktsiy [Increasing the energy efficiency of buildings by reducing heat losses through the edge zones of enclosing structures]. Academia. Architecture and building. 2010. No. 3. Pp. 348–351. (rus)
20. Kraynov, D.V., Safin, I.Sh., Lyubimtsev, A.S. Raschet dopolnitelnykh teplopoter cherez teploprovodnyye vklyuche-niya ograzhdayushchikh konstruktsiy (na primere uzla okonnogo otkosa) [Calculation of additional capacity of heat flux through conductive inclusion of cladding (for example of window jamb unit)]. Magazine of Civil Engineering. 2010. No. 6 (16). Pp. 17–22. (rus)
21. Song, Y., Park, J., Park, J., Lim, H., Song, Y. Influence of Thermal Bridges on the Insulation Performance of Curtain Wall Panel Systems. Journal of Asian Architecture and Building Engineering. 2015. No. 748. Pp. 741–748.
22. Song, Y., Park, J., Chung, M., Choi, B., Park, J. Thermal performance evaluation of curtain wall frame type. Journal of Asian Architecture and Building Engineering. 2013. No. 12 (1). Pp. 157–163.
23. Carbary, L., Yee, S., Bagatelos, N. Thermal and Structural Performance for Use in Curtainwall Constructions. Architecture Insulation Modules. 2014. Pp. 1–18.
24. Filonenko, O., Yurin, O., Kodak, O. Thermal modernization of the panel buildings external walls. International Journal of Engineering and Technology (UAE), 2018. No. 7(3). Pp. 116–122.
25. Griffith, B.T., Türler, D., Arasteh, D. Surface temperature of insulated glazing units: infrared thermography laboratory measurements. ASHRAE Transactions. 1996. No. 102 (2). Pp. 479–488.
26. Ingeli, R., Vavrovič, B., Čekon, M., Paulovičová, L. Thermal bridges minimizing through window jamb in low energy buildings. Advanced Materials Research. 2014. No. 899. Pp. 66–69.
27. Fedorczak-Cisak, M., Radoń, M. New generation window glazing and other solution in low energy buildings. CESB 2013 Prague - Central Europe Towards Sustainable Building 2013: Sustainable Building and Refurbishment for Next Generations. Pp. 333–336.
28. Fissore, A., Fonseca, N. Measurement results and experimental analysis study of the thermal balance of a window. Building and Environment, 2007. No. 42(10). Pp. 3570–3581.
29. Korniyenko, S.V. O primenimosti metodiki SP 50.13330.2012 k raschetu vlazhnostnogo rezhima ograzhdayushchikh konstruktsiy s multizonalnoy kondensatsiyey vlagi [On the applicability of the methodology SP 50.13330.2012 to the calculation of the moisture regime of enclosing structures with multi-zone moisture condensation]. Construction and reconstruction. 2014. No. 5 (55). Pp. 29–37. (rus)
30. Petritchenko, M.R., Kotov, E.V., Nemova, D.V., Tarasova, D.S., Sergeev, V.V. Numerical simulation of ventilated facades under extreme climate conditions. Magazine of Civil Engineering. 2018. No. 77 (1). Pp. 130–140.
31. Gamayunova, O., Gumerova, E., Miloradova, N. Smart glass as the method of improving the energy efficiency of high-rise buildings. E3S Web of Conferences 33. 2018. Art. no. 02046.
32. Vatin, N., Gamayunova, O. Choosing the right type of windows to improve energy efficiency of buildings. Applied Mechanics and Materials, 633–634. 2014. Pp. 972–976.
33. Tarasova, D., Staritcyna, A., Nemova, D., Andreev, K. The using feasibility Russian and European software products at thermal calculations. MATEC Web of Conferences, 53. 2016. Art. no. 01007.

Contacts:

Albert Baiburin, +79222313827; abayburin@mail.ru
Mikhail Rybakov, +79634638973; rybakov.mixail@mail.ru
Nikolai Vatin, +79219643762; vatin@mail.ru

Инженерно-строительный журнал

ISSN 2071-0305

сайт журнала: http://engstroy.spbstu.ru/

DOI: 10.18720/MCE.85.1

Тепловые потери через оконные рамы зданий

А.Х. Байбурин[a], М.М. Рыбаков[a], Н.И. Ватин[b]

[a] ФГБОУ ВПО Южно-Уральский государственный университет, г. Челябинск, Россия

[b] Санкт-Петербургский политехнический университет Петра Великого, Санкт-Петербург, Россия

** E-mail: abayburin@mail.ru*

Ключевые слова: здания; окна; оконная рама; энергоэффективность; теплозащита; потери теплоты; математическое моделирование

Аннотация. Объект исследования - оконные рамы зданий, так как они являются критическими зонами с точки зрения теплоизоляции. Было изучено, как свойства оконной рамы влияют на изменение теплового потока и температурных полей. Был проведен анализ потерь тепла, которые зависят от ряда конструктивных особенностей оконной рамы, таких как геометрические, тепловые и физические свойства стен, окон, перемычек и стыков. Был разработан эксперимент, проведено компьютерное моделирование и лабораторные испытания. Было проанализировано восемь различных типов рамы. Были разработаны их конечно-элементные модели в программном обеспечении ELCUD. Лабораторные испытания подтвердили адекватность конечно-элементных моделей. Сравнительные результаты, полученные в результате испытаний и численных моделей, были согласованы. Мы провели полный факторный эксперимент и исключили незначительные факторы с помощью статистического анализа. Разработаны математические модели совместного влияния этих факторов. Был проведен подробный анализ влияния факторов влияния на потери тепла через оконную раму. Результаты могут быть использованы для энергетической классификации эксплуатируемых зданий.

Литература

1. Ananin M., Perfilyeva N., Vedishcheva I., Vatin N. Investigation of different materials usage expediency for a low-rise public building from the energy efficiency standpoint // IOP Conf. Series: Materials Science and Engineering 365 (2018).
2. Васильев Г.П., Личман В.А., Юрченко И.А., Колесова М.В. и др. Метод оценки коэффициента теплотехнической однородности из анализа термограмм // Инженерно-строительный журнал. 2016. № 6(66). С. 60–67. DOI: 10.5862/MCE.66.6.
3. Blengini G.A., Di Carlo T. Energy-saving policies and low-energy residential buildings: An LCA case study to support decision makers in piedmont (Italy) // International Journal of Life Cycle Assessment, 2010. No. 15 (7). Pp. 652-665.
4. Данилевский Л.Н., Данилевский С.Л. Алгоритм и точность определения теплотехнических показателей зданий // Инженерно-строительный журнал. 2017. № 5(73). С. 49–61. DOI: 10.18720/MCE.73.5.
5. Taylor T., Counsell J., Gill S. Energy efficiency is more than skin deep: Improving construction quality control in new-build housing using thermography // Energy and Buildings. 2013. No. 66. Pp. 222-231
6. Ватин Н.И., Немова Д.В., Рымкевич П.П., Горшков А.С. Влияние уровня тепловой защиты ограждающих конст-рукций на величину потерь тепловой энергии в здании // Инженерно-строительный журнал. 2012. № 8(34). С. 4–14.
7. Корниенко С.В., Ватин Н.И., Горшков А.С. Натурные теплофизические испытания жилых зданий из газобетонных блоков // Инженерно-строительный журнал 2016. №4 (64). С.10–25.
8. Самарин О.Д. О температуре на внутренней поверхности оконных откосов и их теплотехнической безопасности // Светопрозрачные конструкции. 2007. № 3. С. 14–17.
9. Kasper F.-J., Mueller R., Rudolphi R., Wagner A. Computer Simulation of Tests Demonstrated by the Example of Thermal Protection of Window Constructions // Materials Testing. 1986. No. 28(4). Pp. 107–108.
10. Кривошеин А.Д., Харламов Д.А. К вопросу об улучшении температурного режима современных окон в краевых зонах // Светопрозрачные конструкции. 2005. № 1. С. 10–14.
11. Головнев С.Г., Русанов Е.А., Мозгалев К.М. Оценка теплозащитных свойств светопрозрачных конструкций при строительстве и эксплуатации зданий // Академический вестник УралНИИпроект РААСН. 2013. № 4. С. 76–79.
12. Яковлев П.В. Возможности энергосбережения при проектировании и реконструкции оконных проемов // Светопрозрачные конструкции. 2009. № 5–6. С. 33–35.
13. Корниенко С.В. Совершенствование конструктивного решения светопрозрачных ограждений при оценке теплопотерь // Строительные материалы. 2010. № 6. С. 72–73.
14. Петров Е.В. Влияние различных факторов на тепловые характеристики оконных заполнений: автореф. дис. … канд. техн. наук: 05.23.03. Томск, 2000. 23 с.
15. Рыбаков М.М. Факторы, влияющие на теплопередачу через узел оконного откоса // Интернет-журнал «Науковедение». 2016. Т. 8. № 2 [Электронный ресурс]. URL: http://naukovedenie.ru/pdf/55tvn216.pdf (доступ свободный).

16. Русанов А.Е., Головнев С.Г. Исследование влияния дефектов устройства навесных фасадных систем на тепло-защитные свойства стеновых ограждающих конструкций // Академический вестник УралНИИпроект РААСН. 2014. Вып. 2. С. 92–95.
17. Кузема Г.П. О теплопередаче через окна (анализ и немного истории) // Светопрозрачные конструкции. 2009. № 5–6. С. 25–28.
18. Korniyenko S.V. The experimental analysis and calculative assessment of building energy efficiency // Applied Mechanics and Materials. 2014. Vol. 618. Pp. 509–513.
19. Корниенко С.В. Повышение энергоэффективности зданий за счет снижения теплопотерь через краевые зоны ограждающих конструкций // Academia. Архитектура и строительство. 2010. № 3. С. 348–351.
20. Крайнов Д.В., Сафин И.Ш., Любимцев А.С. Расчет дополнительных теплопотерь через теплопроводные включения ограждающих конструкций (на примере узла оконного откоса) // Инженерно-строительный журнал. 2010. № 6 (16). С. 17–22.
21. Song Y., Park J., Park J., Lim H., Song Y. Influence of Thermal Bridges on the Insulation Performance of Curtain Wall Panel Systems // Journal of Asian Architecture and Building Engineering. 2015. No. 748. Pp. 741–748.
22. Song Y., Park J., Chung M., Choi B., Park J. Thermal performance evaluation of curtain wall frame type // Journal of Asian Architecture and Building Engineering. 2013. No. 12 (1). Pp. 157–163.
23. Carbary L., Yee S., Bagatelos N. Thermal and Structural Performance for Use in Curtainwall Constructions // Architecture Insulation Modules. 2014. Pp. 1–18.
24. Filonenko O., Yurin O., Kodak O. Thermal modernization of the panel buildings external walls // International Journal of Engineering and Technology (UAE). 2018. No. 7(3). Pp. 116–122.
25. Griffith B.T., Türler D., Arasteh D. Surface temperature of insulated glazing units: infrared thermography laboratory measurements // ASHRAE Transactions. 1996. No. 102 (2). Pp. 479–488.
26. Ingeli R., Vavrovič B., Čekon M., Paulovičová L. Thermal bridges minimizing through window jamb in low energy buildings // Advanced Materials Research, 2014. No. 899. Pp. 66–69.
27. Fedorczak-Cisak M., Radoń M. New generation window glazing and other solution in low energy buildings // CESB 2013 Prague - Central Europe Towards Sustainable Building 2013: Sustainable Building and Refurbishment for Next Generations. Pp. 333–336.
28. Fissore A., Fonseca N. Measurement results and experimental analysis study of the thermal balance of a window // Building and Environment, 2007. No. 42(10). Pp. 3570–3581.
29. Корниенко С.В. О применимости методики СП 50.13330.2012 к расчету влажностного режима ограждающих конструкций с мультизональной конденсацией влаги // Строительство и реконструкция. 2014. № 5 (55). С. 29-37.
30. Petritchenko M.R., Kotov E.V., Nemova D.V., Tarasova D.S., Sergeev V.V. Numerical simulation of ventilated facades under extreme climate conditions // Magazine of Civil Engineering. 2018. No. 77 (1). Pp. 130-140.
31. Gamayunova O., Gumerova E., Miloradova N. Smart glass as the method of improving the energy efficiency of high-rise buildings // E3S Web of Conferences 33. 2018. Art. no. 02046.
32. Vatin N., Gamayunova O. Choosing the right type of windows to improve energy efficiency of buildings // Applied Mechanics and Materials, 633–634. 2014. Pp. 972-976.
33. Tarasova D., Staritcyna A., Nemova D., Andreev K. The using feasibility Russian and European software products at thermal calculations // MATEC Web of Conferences, 53. 2016. Art. no. 01007.

Контактные данные:

Альберт Халитович Байбурин, +79222313827; эл. почта: abayburin@mail.ru
Михаил Михайлович Рыбаков, +79634638973; эл. почта: rybakov.mixail@mail.ru
Николай Иванович Ватин, +79219643762; эл. почта: vatin@mail.ru

Magazine of Civil Engineering. 2019. 85(1). Pp. 15–27
Инженерно-строительный журнал. 2019. № 1(85). С. 15–27

Magazine of Civil Engineering

ISSN 2071-0305

journal homepage: http://engstroy.spbstu.ru/

DOI: 10.18720/MCE.85.2

Numerical simulation of the turbulent flow over submerged bridge decks

T.K.C. Thai,
University of Transport and Communications, Hanoi, Vietnam
E-mail: chittk@utc.edu.vn

Keywords: bridge deck; drag coefficient; flow; turbulence; numerical simulation

Abstract. Today climate change is one of the most significant threats and global issues that should be concerned. It causes the increased number of natural disasters such as hurricanes, storms, typhoons and floods. Under these critical hydrological conditions, transportation infrastructure includes bridges easily got submerged, damaged and lead to its failures. Evaluation of bridge stability, hydrodynamic forces acted to bridges and understanding the complex flow behavior in particular during and after flooding plays an important role to estimate the probability of failure risks for existing bridges and optimal design of future bridges. In the present paper, the turbulent flow with high Reynolds number over a fully submerged bridge deck with various length-to-thickness ratios is numerically investigated by using ANSYS FLUENT. The blockage and submergence ratios are defined as 0.23 and 2, respectively. The realizable k–ε model and volume of fraction (VOF) is applied to predict the complex water surface profiles over the bridge deck and turbulence characteristics including backwater effect upstream of the bridge. Effects of the aspect ratio to the drag coefficient are studied.

1. *Introduction*

Bridge is an essential important infrastructure, a vital joint of the transportation network. Nowadays because of climate change and global warming, number and frequency of natural disasters such as hurricanes, storms, typhoons and floods has increased and caused devastating impacts on transportation infrastructures include bridges. It can cause the inundation, damages and lead to failures of bridge structures which were not designed for critical hydrological conditions.

Vietnam is one of the five countries worst affected by climate change. In Vietnam, there are over 3450 rivers and streams with a 3260 km long coastline. Hence, Vietnam is always at highest risk from natural disaster as recently ranks eighth in the most affected countries by extreme weather events between 1996 and 2015 and fourth among countries with the highest proportion of the population exposed to river flood risk worldwide [1].

According to Ministry of Transportation and Communication, Vietnam's transportation infrastructure was often damaged by the flooding. For example, during October–December 2016 five floods caused heavy damage to the transportation infrastructure, mostly roads and bridges, in the eighteen provinces. Flood flows from upstream rivers inundated the surrounding areas and damaged many bridges. Figure 1(a) shows the picture of A-Sap Bridge partially inundated by the flood. The middle section of this bridge was completely washed away and severed a village with more than 1400 people on November 2, 2016. Figure 2 demonstrates the photo of a collapsed bridge in Binh Dinh Province due to flooding. Four villages of An Nghia and Hoai An communes have been isolated.

Thai, T.K.C. Numerical simulation of the turbulent flow over submerged bridge decks. Magazine of Civil Engineering. 2019. 85(1). Pp. 15–27. DOI: 10.18720/MCE.85.2.

Тхай Т.К.Т. Численное моделирование турбулентных потоков над подтопленными плитами мостов // Инженерно-строительный журнал. 2019. № 1(85). С. 15–27. DOI: 10.18720/MCE.85.2

Table 1 shows the number of damaged and collapsed bridges caused by the floods of 2016 in the four most suffered provinces Binh Dinh, Ninh Thuan, Phu Yen, Quang Ngai, according to the data provided by the provincial governments [2, 3].

Figure 1. A-Sap bridge collapsed in Thua Thien Hue province, Vietnam, November 2016.

Figure 2. A bridge collapsed in Hoai An, Binh Dinh province, Vietnam, 2016.

Table 1. Number of damaged and collapsed bridges.

Province	Binh Dinh	Ninh Thuan	Phu Yen	Quang Ngai	Total
Number of damaged and collapsed bridges	57	43	113	40	253

During flood and other natural disasters, the water level in river rapidly increases and consequently the bridges are got fully or partially submerged. Hydrodynamic forces caused by flood flows strongly affect the bridges structures. It can cause the shearing or overturning of the bridge deck and failure of the bridge superstructures. The bridges subjected to inundated conditions are more liable to failure. Therefore, understanding the complex turbulent flow and determination the hydrodynamic forces acted on the bridge under extreme hydrological conditions are crucial to evaluate the bridge safety, the probability of failure risks for existing bridges and optimal design of future bridges.

In order to estimate the stability of bridges, the drag force plays very important role. The drag force is a combination of viscous (friction) drag and pressure drag (or form drag), which is dependent mainly on the geometry of the body, the location of separation and reattachment points. Generally, the viscous drag on a bridge deck is negligible when compared with the form drag. Some relationships between the drag coefficient and parameters of bridges and flows were examined. Most studies in the literature have studied hydrodynamic forces acting on unsubmerged bridge decks but there are only a few studies about water flow over inundated bridges and the accompanying water surface profiles.

Naudascher and Medlarz (1983) determined theoretically and experimentally the hydrodynamic forces acting on the partially submerged bridge deck. They introduced a relationship between the drag coefficient, the elevation of the bridge and the angle between the flow and the bridge axis. The force coefficients were proposed to estimate the peak hydrodynamic loading acting on the bridge deck induced by flow instability and vortex formation [4].

In 1995, The Federal Highway Administration (FHWA) researched on the hydrodynamic loads on piers and the bridge deck. They suggested a constant value of drag coefficient within the range 2.0 to 2.2 [5]. The drag coefficient for fully or partially submerged bridge superstructure can be calculated using the following equation:

$$F_D = \frac{C_D \rho U_0^2 H}{2}, \qquad (1)$$

where F_D is drag force per unit length of bridge, N/m;

ρ is the water density, assumed equal to 1000 kg/m^3;

H is depth of submergence, m;

U_0 is flow velocity, m/s;

C_D is drag coefficient per unit length.

Okajima A. et. al (1997) analyzed the blockage effect on the drag coefficient for a rectangular bridge deck in a uniform flow at Reynolds number $R_e = 4 \cdot 10^3$. The results showed that drag coefficient depends greatly on blockage ratios D/H_0, where D is the thickness of the cylinder and H_0 is the depth of the upstream flow [6].

Malavasi & Guadagnini (2003, 2004, 2007) carried out experiments applying a time resolved PIV technique to investigate the flow field and examine the hydrodynamic loading on bridge decks with the aspect ratio of the cylinder was $L/D = 3$ and $L/D = 1$ (where L is the streamwise length of the cylinder) for different submergence levels, Reynolds numbers and deck Froude numbers. Their results showed that due to the presence of a free surface, force coefficients can either be larger (by more than a factor of 2) or lower than the corresponding values of an unbounded domain. The flow fields around the deck had strong asymmetry and a complex vortex-shedding regime. The blockage ratio affects the forces acted on the bridge deck [7–10].

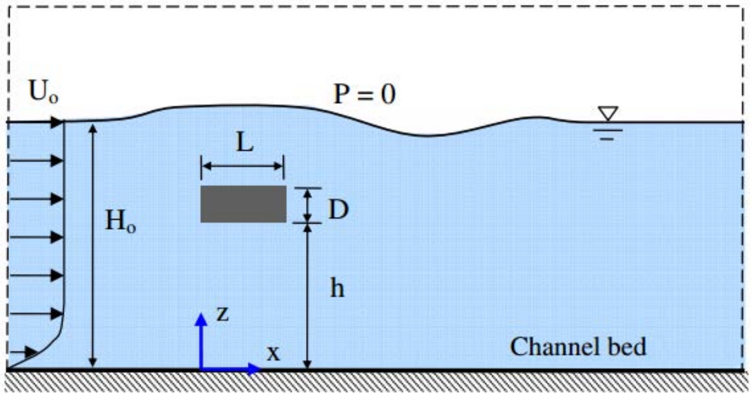

Figure 3. A Schematic diagram of a fully submerged cylinder (Malavasi & Guadagnini, 2003).

T. Picek, Havlik, Mattas, & Mares (2007) conducted experiments to calculate of flow through partially and fully submerged rectangular bridge decks of a rectangular shape. They proposed equations for a calculation of the backwater using empirical equations treating the relative height of an obstacle as a major parameter and the discharge of the pressure flow through decks using the scheme dividing the total flow into the pressure flow and the weir flow [11].

In 2008, Malavasi with Trabucchi used a three-dimensional k-ε turbulence model to simulate the hydrodynamic loading and investigate the bounding effects of a solid wall on the flow around a rectangular cylinder with aspect ratio $L/D = 3$ placed in a steady flow, above a solid wall with different gap ratios h/D. They found that the pressure distribution in the gap zone highly changes when the cylinder is closed to the wall [12].

Arslan T. et al. (2013) used a large eddy simulation (LES) model and flume experiments to study the flow field around a partially submerged sharp-edged rectangular cylinder. The drag and lift forces were estimated and compared with the measurements. Their results indicated that the drag forces increase with the submergence ratio. The flow separation and reattachment underneath the cylinder and the vortex formation in the wake region were highly affected by the submergence ratio and the turbulence intensity in the approaching flow [13].

Chu C. et al. (2012, 2016) used a Large Eddy Simulation (LES) model to investigate the interactions between a free surface flow and fully submerged bridge decks for different Reynolds number, Froude number, submergence ratio and blockage ratio. He also conducted an experiment in a water flume on a rectangular cylinder with the aspect ratio $L/D = 3$. They concluded that the drag coefficient of the cylinder was dependent on the deck Froude number and blockage ratio, rather than the Reynolds number [14, 15].

In reality most of the bridge decks are quite elongated but all the above mentioned studies only examined the flow over the bridge deck with the aspect ratio $L/D \leq 3$. The flow mostly was steady or sub-critical. Results obtained through experiments and numerical simulations mainly by using OpenFOAM. There are no available studies about the water flow over bridge decks with aspect ratios larger than 3. The effect of the free surface mostly was not considered. Besides it, the definition of the drag, lift and moment are clear, but the specific formula is almost impossible based on the theoretical derivation due to the dependence of force coefficients on the shape of objects.

Therefore, the aim of the present paper is to numerically study the behavior of the turbulent flow over the fully submerged bridge deck but with different aspect ratio of the deck $L/D = 1...7$. Based on the obtained data, the relationship between the drag coefficient and the bridge deck's ratio was determined. In order to reduce the cost and time solving problem, the $2D$ computational domain and boundaries are chosen as economical and reliable approach to provide a valuable view of the flow over submerged bridge decks.

2. Methods

In fluid mechanics, the governing equations of fluid flow are the conservation laws of the mass, momentum and energy. According to that, the rate of increase of mass in a fluid element equals the net rate of flow of mass into that fluid element:

$$\frac{\partial\rho}{\partial t}+\frac{\partial(\rho u)}{\partial x}+\frac{\partial(\rho v)}{\partial y}+\frac{\partial(\rho w)}{\partial z}=0, \qquad (2)$$

The time rate of change of momentum in a fluid element equals the net rate of momentum flow out of the fluid element plus the sum of forces acting on the fluid element. The momentum equations for incompressible flow called the Navies – Stokes equations have bellowed forms [16, 17]:

$$\rho\frac{Du}{Dt}=\rho g_x-\frac{\partial\rho}{\partial x}+\mu\left(\frac{\partial^2 u}{\partial x^2}+\frac{\partial^2 u}{\partial y^2}+\frac{\partial^2 u}{\partial z^2}\right), \qquad (3)$$

$$\rho\frac{Dv}{Dt}=\rho g_y-\frac{\partial\rho}{\partial y}+\mu\left(\frac{\partial^2 v}{\partial x^2}+\frac{\partial^2 v}{\partial y^2}+\frac{\partial^2 v}{\partial z^2}\right), \qquad (4)$$

$$\rho\frac{Dw}{Dt}=\rho g_z-\frac{\partial\rho}{\partial z}+\mu\left(\frac{\partial^2 w}{\partial x^2}+\frac{\partial^2 w}{\partial y^2}+\frac{\partial^2 w}{\partial z^2}\right). \qquad (5)$$

The increase rate of energy of a fluid particle equals net rate of heat added to the fluid particle plus net rate of work done on the fluid particle. The energy of a fluid is defined as the sum of internal (thermal) energy $\hat{u}$, kinetic energy *k* and gravitational potential energy. In total there are 5 equations (mass, x-, y-, z momentum and energy) with 7 unknowns (density, pressure, velocity, internal energy, temperature).

In this study, numerical simulations were carried out using FLUENT package. This is a strong analysis tool for modeling based on the finite volume method. The finite element method is developed for numerical solution of complex problems in different fields with varying geometries, material types and loadings. In this method, the complex models are first divided into smaller, simpler and solvable elements called finite elements. Then, by assembling the results of solving each element into larger system, the total solution of model is obtained.

Under critical hydrological conditions, the turbulent flow is irregular, random and chaotic flow, characterized by fluctuating velocity. Hence, the most difficulty in numerically modeling the turbulent flow over the bridge deck is the adequate reproduction of the wake region in the downstream and vortex shedding phenomenon. There are different turbulence models available in FLUENT such as Reynolds – Averaged Navier-Stokes (RANS) models, Large Eddy Simulation (LES), Direct Numerical Simulation (DNS) [18, 22–25].

DNS (Direct Numerical Simulation) model requires very small time steps and high cost that is not suitable for practical industrial applications available today. As for the Large Eddy Simulation (LES), the excessively high resolution is required for wall boundary layers that can only be achieved for flows at very low Reynolds number and on very small geometric scales. For this reason in this paper, the realizable k-ε model, one of the RANS models, is chosen to model the turbulent flow over the submerged bridge deck with different aspect ratios.

RANS models are the most economic approach for computing complex turbulent flows. These models simplify the problem to the solution of two additional transport equations and introduce an Eddy-Viscosity (turbulent viscosity) to compute the Reynolds Stresses [19–21, 26–28]. The Reynolds-averaged momentum equations are as follows:

$$\rho\left(\frac{\partial\overline{u_i}}{\partial t}+\overline{u_k}\frac{\partial\overline{u_i}}{\partial x_k}\right)=-\frac{\partial\overline{p}}{\partial x_i}+\frac{\partial}{\partial x_j}\left(\mu\frac{\partial\overline{u_i}}{\partial x_j}\right)+\frac{\partial R_{ij}}{\partial x_j}, \qquad (6)$$

Realizable k–ε model was developed by Shih et al. (1994) and contains a different transport equation for the turbulent dissipation rate ε, than the traditional k-ε approach. This turbulence model differs from the other model in two ways: it contains a new alternative formulation for the turbulent viscosity and a new modified transport equation for the ε derived from an exact equation for the transport of the mean-square vorticity fluctuations. The term realizable means that the model satisfies some certain mathematical constraints on the Reynolds stresses consistent with the physics of turbulent flows [29–32]

Comparing with standard model, the realizable k-ε model has many advantages such as: more accurately predicts the spreading rate of both planar and round jets; provide superior performance for flows involving rotation, boundary layers under strong adverse pressure gradients, separation, recirculation and strong streamline curvature.

The modeled transport equations for k and ε in the realizable k-ε model are:

$$\frac{\partial}{\partial t}(\rho k)+\frac{\partial}{\partial x_j}\left(\rho k u_j\right)=\frac{\partial}{\partial x_j}\left[\left(\mu+\frac{\mu_t}{\mu_k}\right)\frac{\partial k}{\partial x_j}\right]+G_k+G_b+\rho\varepsilon-Y_M+S_k, \tag{7}$$

$$\frac{\partial}{\partial t}(\rho\varepsilon)+\frac{\partial}{\partial x_j}\left(\rho\varepsilon u_j\right)=\frac{\partial}{\partial x_j}\left[\left(\mu+\frac{\mu_t}{\sigma_\varepsilon}\right)\frac{\partial\varepsilon}{\partial x_j}\right]+\rho C_1 S\varepsilon-\rho C_2\frac{\varepsilon^2}{k+\sqrt{\nu\varepsilon}}+C_{1\varepsilon}\frac{\varepsilon}{k}C_{3\varepsilon}G_b+S_\varepsilon, \tag{8}$$

$$C_1=\max\left[0.43,\frac{\eta}{\eta+5}\right], \tag{9}$$

$$\eta=S\frac{k}{\varepsilon}, \tag{10}$$

$$S=\sqrt{2S_{ij}S_{ij}}, \tag{11}$$

where G_k – the generation of turbulence kinetic energy due to the mean velocity gradients;

G_b – the generation of turbulence kinetic energy due to buoyancy;

Y_M – the contribution of the fluctuating dilatation in compressible turbulence to the overall dissipation rate;

C_2, $C_{1\varepsilon}$ – constants;

σ_k, σ_ε – the turbulent Prandtl numbers for k and ε, respectively;

S_k, S_ε – user-defined source terms.

According to Launder et al., the values of the constants in the realizable k-ε model are given in Table 2 [20].

Table 2. The values of the constants in the realizable k-ε model

C_μ	C_μ	C_μ	σ_k	σ_ε
0.09	1.44	1.9	1.0	1.2

Beside the realizable k-ε model, the Volume of Fraction method was considered to determine more accurately the water surface profiles. Based on the obtained data, the drag coefficient can be determined.

The VOF method is proposed by Hirt and Nichols in 1981 [21]. VOF model belongs to the Euler-Euler approach, which is based on the concept of a fractional volume of fluid to calculate the shape and location of a constant-pressure free surface boundary. In this scheme, two or more fluids can be modeled by solving one set of momentum equations for all fluids and for turbulent flows; a single set of turbulence transport equation is solved. The Interface tracking scheme is used to locate free surface flow. It is assumed that two or more fluids in the flow domain are not interpenetrating. The Navier Stoke equations are solved in either Cartesian or cylindrical coordinates.

In this method, the volume fraction α in the two-phase flow varies from 0 to 1 and is obtained from a transport equation:

$$\frac{\partial\alpha}{\partial t}+\frac{\partial}{\partial x_j}\left(\alpha\bar{u}_j\right)=0. \tag{12}$$

The value of $\alpha=1$ corresponds to a cell full of water; and $\alpha=0$ to the cell is full of air.

Data from works carried out by Chu (2016) were adopted as benchmark to clarify the accuracy of the FLUENT numerical model in simulating flows over submerged bridge decks. The conditions set for the numerical simulations were the same as those used in the experiment.

Design Modeler and Meshing tool of Workbench were used to create the geometry model and generate the mesh model relatively. The bridge deck is modeled in a rectangular shape. Initial data were: thickness $D = 0.06$ m, distance from the underside of the deck to the channel floor was $h = 0.14$ m, upstream velocity $U = 1$ m/s, water depth of the undisturbed flow $H = 0.26$ m. In this case, the flow is turbulent and supercritical as the Reynolds number equals:

$$\mathrm{Re} = \frac{UD}{\nu} = 60000. \tag{13}$$

The Froude number of the flow and the deck respectively are:

$$Fr = \frac{U}{\sqrt{gH}} = 0.63; \tag{14}$$

$$Fr_D = \frac{U}{\sqrt{gD}} = 1.3. \tag{15}$$

The blockage ratio was defined as:

$$Br = D / H = 0.23. \tag{16}$$

The submergence ratio is the ratio of the depth of water above the bridge deck to its thickness:

$$h^* = \left(H - h\right) / D = 2. \tag{17}$$

The size of the computational domain plays a great important role. The upstream and downstream lengths of the computational model are chosen in such way that the inlet and outlet boundary conditions do not significantly influence free surface development, flow around the bridge deck, and forces on the bridge. Because of the turbulent flow, the inlet is placed $30D$ upstream of the deck and the outlet $30D$ downstream to capture the whole velocity field and give accurate results. The same domain is used for all aspect ratios.

The grid near the bridge deck was denser because the flow pattern in the region is more complex and gradually increases away from the bridge deck. The height of first layer near the surface of bridge deck is $0.005D$. The minimum orthogonal quality is larger than 0.6, which is considered as good quality.

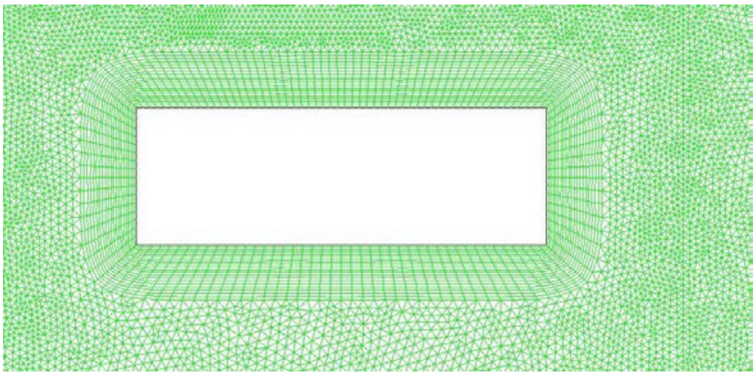

Figure 4. Mesh in region around bridge deck.

The boundary conditions for modeling consist of the inlet, the outlet and the walls. Considering the VOF method, the flow domain was divided into two phases, air and water. Air was considered as the secondary phase. The operating pressure is 101325 Pascal. The operating density was set as the density of the lightest phase (air) that is 1.225 kg/m^3. Respectively, the inlet has two parts: the lower part where water is coming in and upper part is for air. At the water inlet part, a uniform velocity is applied. The interaction coefficient between water and air is set as 0.072.

The outlet boundary was defined as the pressure outlet used to specify a static gauge pressure at the boundary. Top boundary is given as pressure outlet with a zero atmospheric pressure. Bottom and deck are considered as no-slip wall. The geometry of the $2D$ solution domain and the boundary conditions used for the numerical simulations are shown in Figure 2.

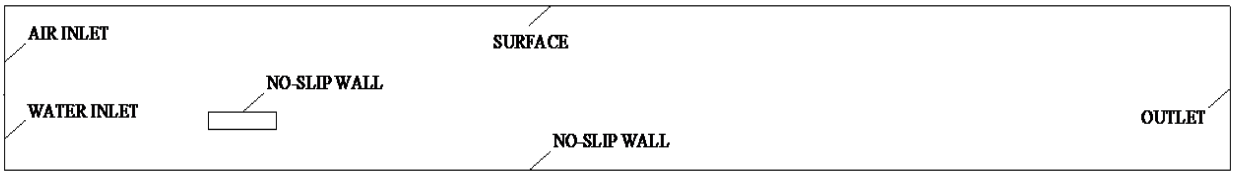

Figure 5. Computational domain and boundary conditions.

The numerical solution was considered converged when the residuals of the discretized transport equation reached a value of 1×10^{-6} for all variables including pressure, velocity, turbulent kinetic energy and turbulence dissipation rate. To obtain results more accurately, in the present study, the PISO algorithm (Pressure Implicit with Splitting of Operators) is used for pressure-velocity coupling. The Pressure-Implicit with Splitting of Operators (PISO) pressure-velocity coupling scheme is based on the higher degree of the approximate relation between the corrections for pressure and velocity. The PISO algorithm performs two additional corrections: neighbor correction and skewness correction. It can carry on a stable calculation with larger time step and under-relaxation factors for both momentum and pressure compared to other schemes [18].

Pressure was discretized with a PRESTO Scheme. QUICK Schemes which based on a weighted average of second-order-upwind and central interpolations of the variable is used for pressure discretization and for momentum, kinetic energy and dissipation equations. The inlet flow domain is patched with inlet velocity along with initialization of turbulence kinetic energy and turbulence dissipation rate.

3. Results and Discussion

As mentioned in section 2, before employing the numerical model to study the flow over the bridge deck, the numerical simulation for the deck with the aspect ratio $L/D=3$ have been performed and compared with the data from Chu's works in order to validate models using by author. As the results, the drag coefficient, obtained by the present model equals 2.45. Comparing to the drag coefficient obtained by Chu (2016), a good agreement between them has been observed. The error was $(2.64-2.45)\cdot100/2.64=7.2$ %.

The simulated water surfaces are compared in Figure 6. Overall, the free surface water profile obtained from the present numerical model shows reasonable agreement with the profile from Chu's model. Based on these mentioned above results, the capability of the present numerical model can be proved.

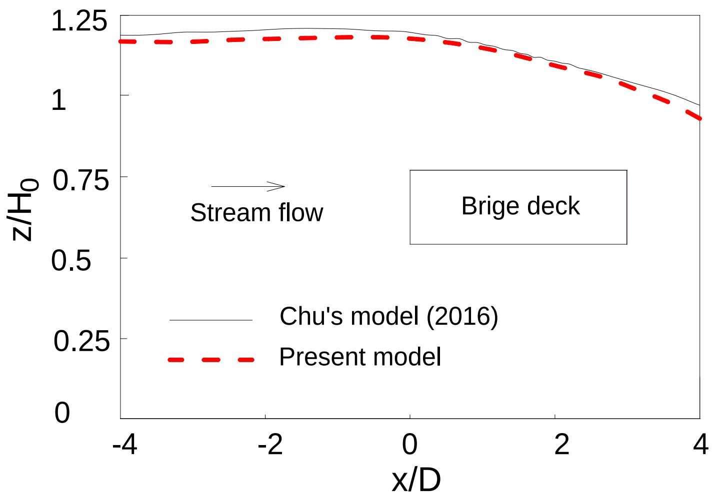

Figure 6. Free surface water profile of the flow over the decks

Figure 7 shows the free surface water profiles of the flow over the decks with different aspect ratios $L/D=1;3;5;6$. As the cross-sectional shape of the bridge deck varies, the behavior of the flow changes.

As we can see from these pictures, the shape of water surface profiles over submerged bridge deck is quite complex. First, a backwater effect appeared at the upstream of the deck, the water surface was elevated and then the water surface suddenly dropped and gradually recovered. The deck's aspect ratio decreases, the water level decreased more dramatically at the downstream.

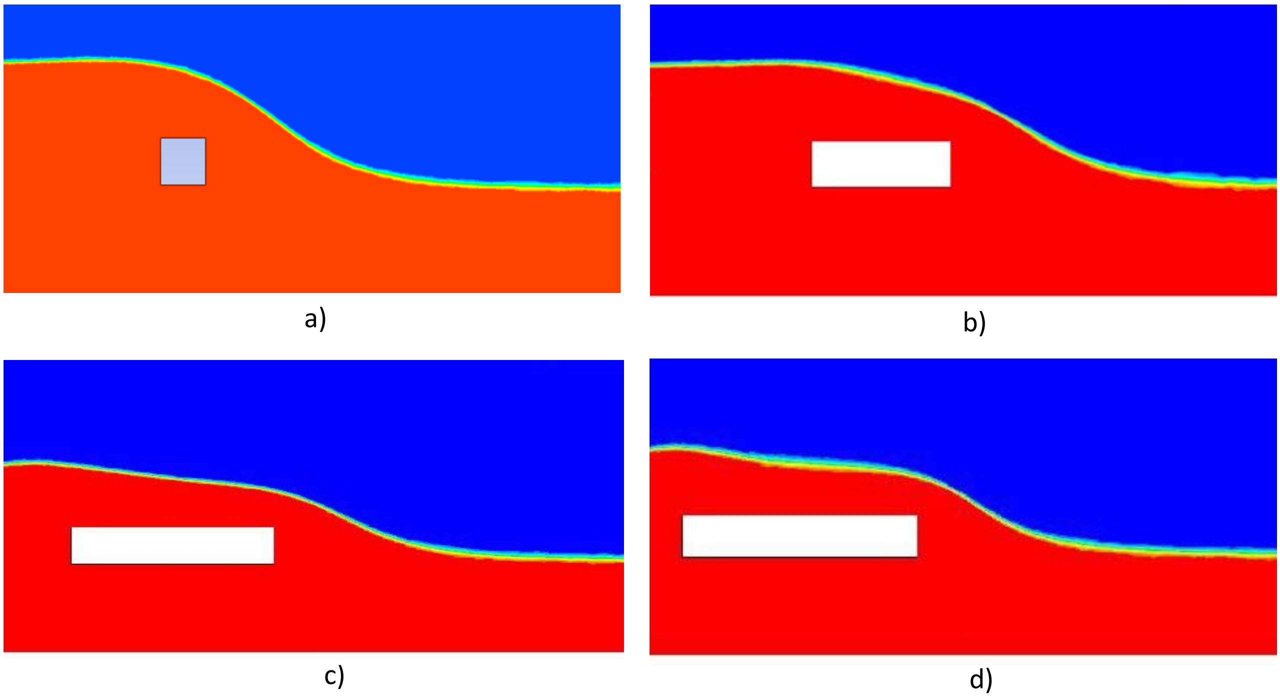

Figure 7. Free surface water profiles
a) $L/D = 1$; **b)** $L/D = 3$; **c)** $L/D = 5$; **d)** $L/D = 6$.

The velocity streamlines over the bridge decks are shown in Figure 8. This figure shows that the flow around the decks is significantly affected by the aspect ratios (L/D) of the deck. For bridge deck with small aspect ratio $L/D < 5$, no reattachment is presented at the lower side due to the short length of the deck. In the case of greater L/D ratio such as $L/D \geq 5$, flow changes from separated to reattachment type of flow. The length of the deck is long enough to allow reattachment of the separated flow. Reattachment of flow along the side surface causes the wake to expand considerably less than the flow without reattachment.

As the shear layer separates at the leading corner, the main vortex is formed along the cylinder side. Under the effect of the free surfaces, vortices around the bridge deck are asymmetry. A small vortex is generated at the upper side of the deck. The reattachment occurs at the end of this vortex.

In case of bridge deck with small aspect ratio $L/D = 1$, no vortex is formed right at the bottom of bridge deck. For greater ratios $L/D > 1$, a vortex is formed at the lower side with the length about $2D$ in the case $L/D = 2$ and then increased to about $3D$. The main vortex acting on the lower side of bridge deck (if existing) always has a longer length than on the upper side.

In the wake region, a reversed flow is generated. Two vortices are formed in the reversed flow region along the rear sides of the deck. The vortices in this reversed flow region fluctuate along the rear sides of the deck. In the case of $L/D = 1$, the below vortex placed lower than the bottom side of the deck. As the aspect ratio increases, the place of this vortex is going up and its size also decreases. In the case of $L/D = 6$, the two vortices in the wake region are most asymmetry through horizontal middle line of bridge deck. In addition, as the aspect ratio increases, the distance where the shear layers from upper and lower side of the deck meets decreases. For the case of $L/D = 1$, this distance is about $2D$ but then decreases to about $1D$ when $L/D = 6$.

The drag coefficient of the bridge deck is dependent on the deck aspect ratio. Results of the numerical modeling are presented in Table 3.

The Figure 9 shows the variations of the mean drag coefficient according to the aspect ratio. The largest values of the mean drag coefficient are found for aspect ratio $L/D = 2$. As shown in this graph, the drag coefficient is increased quite rapidly as the aspect ratio L/D increased from 1 to 2. But in the case of the aspect ratio $L/D > 2$, as the aspect ratio increases, the drag coefficient decreases. In the case of $2 < L/D \leq 6$ the difference in drag force between two aspect ratios decreases dramatically but declines slowly when $L/D > 6$.

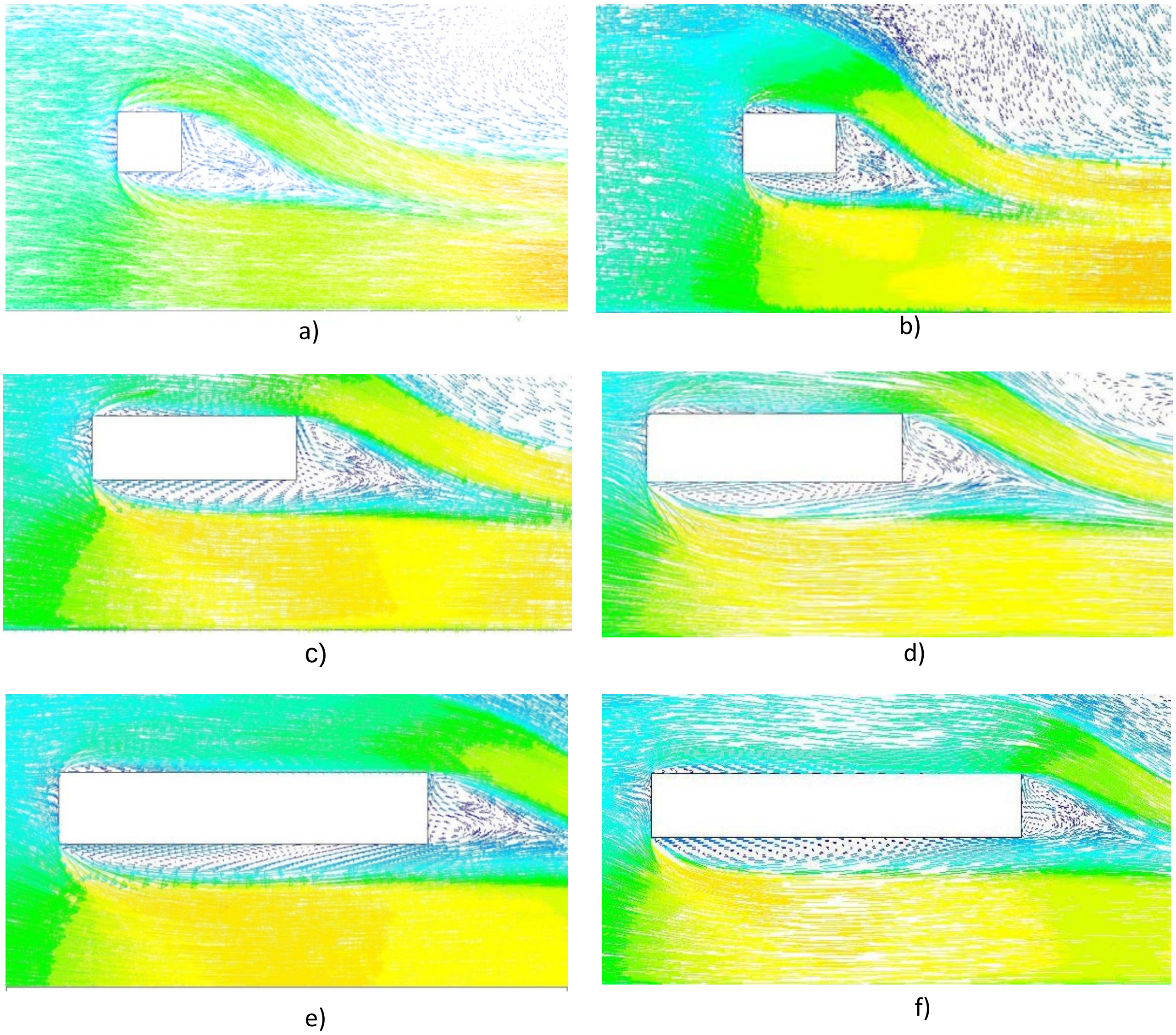

Figure 8. Structure of flow over bridge deck.

a) $L/D=1$; **b)** $L/D=2$; **c)** $L/D=3$; **d)** $L/D=4$ **e)** $L/D=5$; **f)** $L/D=6$.

Table 3. Drag coefficient at different aspect ratio of bridge deck.

L/D	1	2	3	4	5	6	7
C_D	2.36	2.5	2.45	2.38	2.31	2.2	2.18

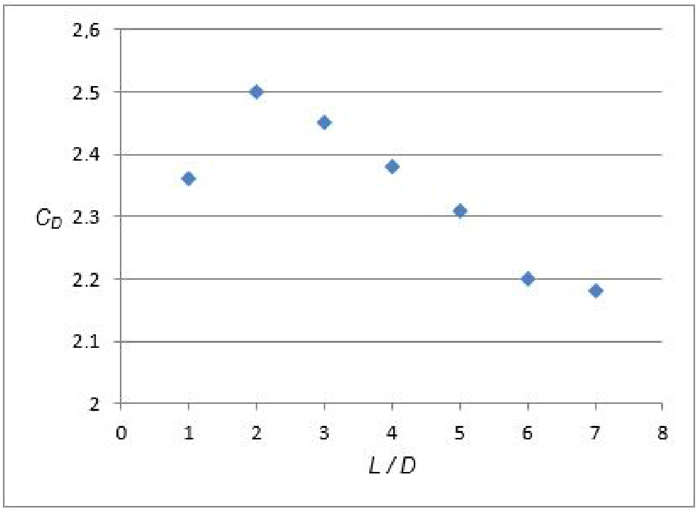

Figure 9. Variation of the mean drag coefficient according to aspect ratio.

This tendency can be explained by the fact that the drag force is dependent on the geometry of the bridge deck and the location of separation and reattachment points. From $L/D=1$ to $L/D=2$, the vortex formation region moves closer to the deck and creates the higher base suction. Thus, in this case, the drag force increases. As the aspect ratio increases, the pressure distribution along the side surface of the deck changes, a region of higher pressure called the pressure recovery region occurs after flow reattachment. This pressure recovery region pushes the vortices further downstream. The further downstream the vortices form from the trailing edge of the cylinder, the base suction pressure decreases and also the drag. In another word, as the aspect ratio increases, the effect of the base suction decreases. Besides it, the friction between flows and bridge decks also affects the drag force. As the aspect ratio increases, the frictional effect leads to the increase of the drag force. According to The Federal Highway Administration (FHWA), the submerged bridge deck in these cases is not in safe zone but at high risk of damages as the drag coefficient always larger than 2.1.

4. Conclusions

In this study, the numerical modeling was performed for the fully submerged bridge decks with various aspect ratios using ANSYS FLUENT package. The realizable k–ε model and Volume of Fraction method were used to investigate the turbulent flow over the bridge deck.

The present study showed that ANSYS FLUENT software is useful tool to study the turbulent flow without going for expensive and time consuming experiments. The water surface profiles and drag coefficient on submerged bridge decks can be accurately predicted. Effects of the aspect ratio to the flow behavior and drag coefficient are studied. As the aspect ratio of bridge decks decreases, the water level decreased more dramatically at the downstream. The flow changes from separated to reattachment type in the case of $L/D \geq 5$. Two vortices are formed in the reversed flow of the wake region along the rear sides of the deck. As the aspect ratio increases, the distance where the shear layers from upper and lower side of the deck meets also decreases. The largest values of the mean drag coefficient are found for aspect ratio $L/D=2$. In the case of the aspect ratio $L/D>2$, as the aspect ratio increases, the drag coefficient decreases.

The goal of this work is to obtain a better knowledge of the hydrodynamic characteristics of the flow over a bridge deck section with different aspect ratio and determine the drag coefficient in the case of the blockage and submergence ratios were 0.23 and 2, respectively. In future, this work can extend to other cases of different blockage and submergence ratios. Author hopes that it can help researchers to evaluate the bridge safety under critical hydrological conditions.

References

1. National disaster risk in Vietnam in the period 2006-2016 and forecasting and warning system. National Center for Hydro-Meteological Forecasting. Ministry of Natural Resources and Environment, Vietnam, 2017. 21 p.
2. The World Bank. Vietnam 2016: Rapid Flood Damage and Needs Assessment (RFDNA). 2016. 42 p.
3. NHMS: Statistics of annual major storms (Levels from 6 to 12) struck Vietnam between 1961 and 2014, National Hydro – Meteorological Service (NHMS), Ministry of Natural Resources and Environment, Vietnam, 2015.
4. Naudascher, E., Medlarz, H.J. Hydrodynamic loading and backwater effect of partially submerged bridges. J. Hydraul. Res. 1983. No. 21(3). Pp. 213–232.
5. Federal Highway Administration (FHWA). Stream stability at highway structures. Rep. No. FHWA-HI-96-032, FHWA, Washington D.C.1995. Pp. 56-59.
6. Okajima, A., Yi, D., Kimura, S., Kiwat, T. The blockage effects for an oscillating rectangular cylinder at moderate Reynolds number. Journal of Wind Engineering and Industrial Aerodynamics. 1997. Vol. 69–71. Pp. 997–1011.
7. Cigada, A., Malavasi, S., Vanali, M. Direct forces measurement on a submerged bridge model. Proceedings of the First International Conference on Fluid Structure Interaction. 26–28 September, Halkidiki, Greece. 2001. Pp. 305–314.
8. Malavasi, S., Guadagnini, A. Hydrodynamic loading on river bridges. J. Hydraul. Eng.. 2003. Vol. 129(11). Pp. 854–861.
9. Malavasi, S., Franzetti, S., Blois, G. PIV investigation of flow around submerged river bridge deck. River Flow 2004: Proc., 2ndInt. Conf. on Fluvial Hydraulics, Taylor and Francis, London, 2004. Pp. 601–608.
10. Malavasi, S., Guadagnini, A. Interactions between a rectangular cylinder and a free-surface flow. J. Fluids Struct. 2007. Vol. 23(8). Pp. 1137–1148.
11. Picek, T., Havlik, A., Mattas, D., Mares, K. Hydraulic calculation of bridges at high water stages. J. Hydraul. Res. 2007. No. 45(3). Pp. 400–406.
12. Malavasi, S., Trabucchi, N. Numerical investigation of the flow around a rectangular cylinder near a solid wall. Proc., Bluff Bodies Aerodynamics and Applications, Milano, Italy, 2008. Pp. 20–24.
13. Arslan, T., Malavasi, S., Pettersen, B., Andersson, H. Turbulent flow around a semi-submerged rectangular cylinder. J. Offshore Mech. Arct. Eng. 2013. Vol. 135(4). Pp. 0418011–04180111.
14. Chu Chia, Chih Jung Huang, Tso Ren Wu, Chung Yue Wang. Numerical simulation of hydrodynamic loading on submerged rectangular bridge decks. The Seventh International Colloquium on Bluff Body Aerodynamics and Applications (BBAA7), Shanghai, China, September 2–6, 2012. Pp. 1508–1517.
15. Chu Chia & Chung, Chun-Hsuan & Wu, Tso-Ren & Wang, Chung-Yue. Numerical Analysis of Free Surface Flow over a Submerged Rectangular Bridge Deck. Journal of Hydraulic Engineering. 2016. Vol. 143. Pp. 040160601–0401606011.
16. Hamill, L. Bridge hydraulics. E&FN Spon, London, 1999. 384 p.

17. Fox, R.W., McDonald, A.T., Pritchard, P.J. An introduction to fluid mechanics, 9th Ed., Wiley, New York, 2016. 672 p.
18. ANSYS Fluent Theory Guide. Release 15.0. ANSYS, Inc. November 2013. 814 p.
19. Shih, T.H., Liou, W.W., Shabbir, A., Yang, Z., Zhu, A New Eddy-Viscosity Model for High Reynolds Number Turbulent Flows – Model Development and Validation. Computers Fluids. 1995. Vol. 24(3). Pp. 227–238.
20. Launder, B.E.; Spalding, D.B. The numerical computation of turbulent flows. Computer Methods in Applied Mechanics and Engineering. 1974. Vol. 3(2). Pp. 269–289.
21. Hirt, C.W., Nichols, B.D. Volume of fluid (VOF) method for the dynamics of free boundaries. J. Comp. Phys. 1981. Vol. 39(1). Pp. 201–225.
22. Cigada, A., Malavasi, S., Vanali, M. Direct forces measurement on a submerged bridge model. Fluid structure interaction, WIT Press, Boston, 2001. Pp. 305–314.
23. Shimada, K., Ishihara, T. Application of a modified k−ε model to the prediction of aerodynamic characteristics of rectangular cross-section cylinders. J. Fluids Struct. 2002. Vol. 16(4). Pp. 465-485.
24. Lee, D., Nakagawa, H., Kawaike, K., Baba, Y., Zhang, H. Inundation flow considering overflow due to water level rise by river structures. Annuals of Disaster Prevention Research Institute, Kyoto University. 2010. No. 53 B. Pp. 607–616.
25. Ramamurthy, A.S., Junying, Qu, Oiep, Vo. Volume of fluid model for open channel flow problem. ‖ Canadian Journal of Civil Engineering. 2005. Vol. 32.5. Pp. 996–1001.
26. Zhaoding, X., Bushra, A., Anju, S.T, Kornel, K., Guo, J. CFD Modeling of drag and lift of inundated bridge decks. 33rd IAHR Congress held from August 10–14, 2009. Water Engineering for Sustainable Environment, Vancouver, Canada, 2009. Pp. 2575–2585.
27. Khrabry, A.I., Smirnov, E.M., Zaytsev, D.K. Numerical Study of wall friction effects on dambreak flows in the presence of an obstacle. 6th European Conference on Computational Fluid Dynamics (ECFD VI), 20–25 July 2014, Barcelona, Spain. Pp. 1–2.
28. Platonov, D.V., Minakov, A.V., Dekterev, A.A., Sentyabov, A.V. Chislennoye modelirovaniye prostranstvennykh techeniy s zakrutkoy potoka [Numerical modeling of spatial flows with spin flow]. Kompyuternyye issledovaniya i modelirovaniye. 2012. No. 2(1). Pp. 161–172. (rus)
29. Valger, S.A, Fedorov, A.V., Fedorova, N.N. Modelirovaniye neszhimayemykh turbulentnykh techeniy v okrestnosti plokhoobtekayemykh tel s ispolzovaniyem PK ANSYS [Fluent Simulation of incompressible turbulent flows in the vicinity of poorly streamlined bodies using the ANSIS Fluent PC]. Vychislitelnyye tekhnologii. 2013. No. 5(18). Pp. 27–40. (rus)
30. Khrabryy, A.I., Zaytsev, D.K., Smirnov, Ye.M. Chislennoye modelirovaniye techeniy so svobodnoy poverkhnostyu na osnove metoda VOF [Numerical simulation of free-surface flows based on the VOF method]. Trudy TsNII im. akad. A. N. Krylova (Trudy Krylovskogo gosudarstvennogo nauchnogo tsentra). 2013. Vyp. 78 (362). Pp. 53–64. (rus)
31. Khrabryy, A.I., Smirnov, Ye.M., Zaytsev, D.K. Vliyaniye modeli turbulentnosti na rezultaty rascheta obtekaniya prepyatstviya potokom vody posle obrusheniya damby [The influence of the turbulence model on the results of the calculation of the flow around an obstacle by the flow of water after the dam collapses]. Nauchno-tekhnicheskiye vedomosti SPbGPU. 2013. No. 1(165). Pp. 182–187. (rus)
32. Korkodinov, Ya.A. Obzor semeystva k-ε modeley dlya modelirovaniya turbulentnosti [An overview of the family of k-ε models for modeling turbulence]. Vestnik PNIPU. Mashinostroyeniye, materialovedeniye. 2013. No. 2(15). Pp. 5–16. (rus)

Contacts:

Thi Kim Chi Thai, +840988115110; chittk@utc.edu.vn

Инженерно-строительный журнал

ISSN 2071-0305

сайт журнала: http://engstroy.spbstu.ru/

DOI: 10.18720/MCE.85.2

Численное моделирование турбулентных потоков над подтопленными настилами мостов

Т.К.Т. Тхай,
Университет транспорта и коммуникации, г. Ханой, Вьетнам
E-mail: chittk@utc.edu.vn

Ключевые слова: настил моста; коэффициент сплошности конструкций; турбулентность; численное моделирование

Аннотация. В настоящее время изменение климата является одной из самых серьезных угроз и глобальных проблем. Оно вызывает увеличение числа стихийных бедствий, таких как ураганы, штормы, тайфуны и наводнения. В этих критических гидрологических условиях, транспортная инфраструктура, включающая в себя мосты, легко подтапливается, повреждается и разрушается. Оценка устойчивости моста, определение гидродинамических сил, действующих на мосты, и понимание сложного режима потока во время и после затопления, играют важную роль в определении вероятности возникновения рисков аварии для существующих мостов и оптимальной конструкции будущих мостов. В настоящей работе турбулентный поток с большим числом Рейнольдса над подтопленным настилом моста с различным соотношением длины к толщине был численно исследован с использованием программы ANSYS FLUENT. Соответственно, коэффициенты поджатия потока и затопления равны 0,23 и 2. Используемая k–ε модель и объем фракции (VOF) были применены для прогнозирования совокупности профилей свободной поверхности воды над настилом моста и характеристики турбулентности, включая влияние подпора в верхнем бьефе моста. Была изучена зависимость соотношения длины к толщине настилов мостов от коэффициента сплошности конструкций.

Литература

1. National disaster risk in Vietnam in the period 2006-2016 and forecasting and warning system. National Center for Hydro-Meteological Forecasting. Ministry of Natural Resources and Environment, Vietnam, 2017. 21 p.
2. The World Bank. Vietnam 2016: Rapid Flood Damage and Needs Assessment (RFDNA). 2016. 42 p.
3. NHMS: Statistics of annual major storms (Levels from 6 to 12) struck Vietnam between 1961 and 2014, National Hydro -Meteorological Service (NHMS), Ministry of Natural Resources and Environment, Vietnam, 2015.
4. Naudascher E., Medlarz H. J. Hydrodynamic loading and backwater effect of partially submerged bridges // J. Hydraul. Res. 1983. No. 21(3). Pp. 213–232.
5. Federal Highway Administration (FHWA). Stream stability at highway structures. Rep. No. FHWA-HI-96-032, FHWA, Washington D.C. 1995. Pp. 56–59.
6. Okajima A., Yi D., Kimura S., Kiwat T. The blockage effects for an oscillating rectangular cylinder at moderate Reynolds number // Journal of Wind Engineering and Industrial Aerodynamics. 1997. Vol. 69–71. Pp. 997–1011.
7. Cigada A., Malavasi S., Vanali M. Direct forces measurement on a submerged bridge model. Proceedings of the First International Conference on Fluid Structure Interaction. 26–28 September, Halkidiki, Greece. 2001. Pp. 305–314.
8. Malavasi S., Guadagnini A. Hydrodynamic loading on river bridges // J. Hydraul. Eng. 2003. Vol. 129 (11). Pp. 854–861
9. Malavasi S., Franzetti S., Blois G. PIV investigation of flow around submerged river bridge deck. River Flow 2004: Proc., 2ndInt. Conf. on Fluvial Hydraulics, Taylor and Francis, London, 2004. Pp. 601–608.
10. Malavasi S., Guadagnini A. Interactions between a rectangular cylinder and a free-surface flow // J. Fluids Struct. 2007. Vol. 23(8). Pp. 1137–1148.
11. Picek T., Havlik A., Mattas D., Mares K. Hydraulic calculation of bridges at high water stages // J. Hydraul. Res. 2007. No. 45(3). Pp. 400–406.
12. Malavasi S., Trabucchi N. Numerical investigation of the flow around a rectangular cylinder near a solid wall // Proc., Bluff Bodies Aerodynamics and Applications, Milano, Italy, 2008. Pp. 20–24.
13. Arslan T., Malavasi S., Pettersen B., Andersson H. Turbulent flow around a semi-submerged rectangular cylinder // J. Offshore Mech. Arct. Eng. 2013. Vol. 135(4). Pp. 0418011–04180111.
14. Chu Chia, Chih Jung Huang, Tso Ren Wu, Chung Yue Wang. Numerical simulation of hydrodynamic loading on submerged rectangular bridge decks. The Seventh International Colloquium on Bluff Body Aerodynamics and Applications (BBAA7), Shanghai, China, September 2–6, 2012. Pp. 1508–1517.

15. Chu Chia & Chung, Chun-Hsuan & Wu, Tso-Ren & Wang, Chung-Yue. Numerical Analysis of Free Surface Flow over a Submerged Rectangular Bridge Deck // Journal of Hydraulic Engineering. 2016. Vol. 143. Pp. 040160601–0401606011.
16. Hamill L. Bridge hydraulics. E&FN Spon, London, 1999. 384 p.
17. Fox R.W., McDonald A.T., Pritchard P.J. An introduction to fluid mechanics, 9th Ed., Wiley, New York, 2016. 672 p.
18. ANSYS Fluent Theory Guide. Release 15.0. ANSYS, Inc. November 2013. 814 p.
19. Shih T.H., Liou W.W., Shabbir A., Yang Z., Zhu. A New Eddy-Viscosity Model for High Reynolds Number Turbulent Flows – Model Development and Validation. Computers Fluids. 1995. Vol. 24(3). Pp. 227–238.
20. Launder B.E.; Spalding D.B. The numerical computation of turbulent flows // Computer Methods in Applied Mechanics and Engineering. 1974. Vol. 3(2). Pp. 269–289.
21. Hirt C.W., Nichols B.D. Volume of fluid (VOF) method for the dynamics of free boundaries // J. Comp. Phys. 1981. Vol. 39(1). Pp. 201–225.
22. Cigada A., Malavasi S., Vanali M. Direct forces measurement on a submerged bridge model. Fluid structure interaction, WIT Press, Boston, 2001. Pp. 305–314.
23. Shimada K., Ishihara T. Application of a modified k−ε model to the prediction of aerodynamic characteristics of rectangular cross-section cylinders // J. Fluids Struct. 2002. Vol. 16(4), Pp. 465–485.
24. Lee D., Nakagawa H., Kawaike K., Baba Y., Zhang H. Inundation flow considering overflow due to water level rise by river structures // Annuals of Disaster Prevention Research Institute, Kyoto University. 2010. No. 53 B. Pp. 607–616.
25. Ramamurthy A.S., Junying Qu, Oiep Vo. Volume of fluid model for open channel flow problem // ‖ Canadian Journal of Civil Engineering. 2005. Vol. 32.5. Pp. 996–1001.
26. Zhaoding X., Bushra A., Anju S.T, Kornel K., Guo J. CFD Modeling of drag and lift of inundated bridge decks // 33rd IAHR Congress held from August 10–14, 2009. Water Engineering for Sustainable Environment, Vancouver, Canada, 2009. Pp. 2575–2585.
27. Khrabry A.I., Smirnov E.M., Zaytsev D.K. Numerical Study of wall friction effects on dambreak flows in the presence of an obstacle // 6th European Conference on Computational Fluid Dynamics (ECFD VI), 20–25 July 2014, Barcelona, Spain. Pp. 1–2.
28. Платонов Д.В. , Минаков А.В., Дектерев А.А., Сентябов А.В. Численное моделирование пространственных течений с закруткой потока // Компьютерные исследования и моделирование. 2012. № 2(1). С. 161–172.
29. Вальгер С.А, Федоров А.В., Федорова Н.Н. Моделирование несжимаемых турбулентных течений в окрестности плохообтекаемых тел с использованием ПК ANSYS Fluent // Вычислительные технологии. 2013. № 5(18). С. 27–40.
30. Храбрый А.И., Зайцев Д.К., Смирнов Е.М. Численное моделирование течений со свободной поверхностью на основе метода VOF // Труды ЦНИИ им. акад. А.Н. Крылова (Труды Крыловского государственного научного центра). 2013. Вып. 78 (362). С. 53–64.
31. Храбрый А.И., Смирнов Е.М., Зайцев Д.К. Влияние модели турбулентности на результаты расчета обтекания препятствия потоком воды после обрушения дамбы // Научно-технические ведомости СПбГПУ. 2013. № 1 (165). С. 182–187.
32. Коркодинов Я.А. Обзор семейства k-ε моделей для моделирования турбулентности // Вестник ПНИПУ. Машиностроение, материаловедение. 2013. № 2(15). С. 5–16.

Контактные данные:

Тхи Ким Тьи Тхай, +840988115110; эл. почта: chittk@utc.edu.vn

Magazine of Civil Engineering. 2019. 85(1). Pp. 28–38
Инженерно-строительный журнал. 2019. № 1(85). С. 28–38

Magazine of Civil Engineering

ISSN 2071-0305

journal homepage: http://engstroy.spbstu.ru/

DOI: 10.18720/MCE.85.3

Composite binders for concretes with improved shock resistance

R.S. Fediuk[a]*, V.S. Lesovik[b], Yu.L. Liseitsev[a], R.A. Timokhin[a], A.V. Bituyev[c], M.Ye. Zaiakhanov[c], A.V. Mochalov[a]

[a] Far Eastern Federal University, Vladivostok, Russia
[b] V.G. Shukhov Belgorod State Technological University, Belgorod, Russia
[c] East Siberia State University of Technology and Management, Ulan-Ude, Russia
** E-mail: roman44@yandex.ru*

Keywords: self-compacting concrete; rice husk ash; pozzolanic materials; shock resistance; fresh properties; mechanical properties

Abstract. The qualitative and quantitative composition and properties of the initial materials, composite binders and concrete samples were studied. Optimal compositions of concrete for protective structures that provide the maximum static and dynamic strength characteristics are selected. In this case, the effect of increasing the shock endurance increases to 6 times. It has been found that concretes with a small number of defects, high packing density and uniformity, good adhesion between the aggregate and cement stone, an increased ratio of static tensile strength to static compressive strength Rtens / Rcompr and ductility have the best resistance to dynamic impact. It is proved that this ratio can be increased, in the case of the use of dispersed reinforcement of concrete (so-called fibrous concrete). In experimental studies on penetration of both unreinforced and fiber-reinforced concrete slabs, it was noted that samples of unreinforced concrete were completely destroyed in large and small pieces, while samples of fiber-reinforced concrete were not completely destroyed, and only through penetration at the impact site was observed; that is, fibrous concrete has the best impact resistance. These results can be applied to the design of various special structures, such as protective structures of civil defense and emergency situations, concrete structures of nuclear power plants, etc.

1. Introduction

In the modern world, which saturated with natural and man-made hazards, the protection of human life must be ensured by the optimization of the "man-material-habitat" system through the continuous improvement of structural materials for protective structures. In view of the fact that the large-tonnage production of cement also significantly worsens the ecological habitat of humans, its use should be minimized. Thus, the increase in the efficiency of concrete must be achieved through the use of a composite binder (CB).

There are several technological ways to solve the problem of increasing the shock endurance of concrete. One of them is an increase in the static strength of concrete, and this way is practiced in a number of foreign countries. It is based on the use of high-quality cements, fractionated aggregates, superplasticizers. Another direction is the technology of modifying the structure of concrete by introducing into the concrete mixture the porous dispersed components (damping additives). This method of increasing the shock endurance of concretes was researched by R. Oyguc [1], M. Kristoffersen [2], A. Maazoun [3], Z.I. Syed [4], K. Makita [5], etc. However, these concretes provide a relatively moderate increase in shock endurance – up to 2–4 times, which is not sufficient for protective structures in conditions of the action of the means of destruction, which create high dynamic loads on the enclosing structures.

Fediuk, R.S., Lesovik, V.S., Liseitsev, Yu.L., Timokhin, R.A., Bituyev, A.V., Zaiakhanov, M.Ye., Mochalov, A.V. Composite binders for concretes with improved shock resistance. Magazine of Civil Engineering. 2019. 85(1). Pp. 28–38. DOI: 10.18720/MCE.85.3.

Федюк Р.С., Лесовик В.С., Лисейцев Ю.Л., Тимохин Р.А., Битуев А.В., Заяханов М.Е., Мочалов А.В. Композиционные вяжущие для бетонов повышенной ударной стойкости // Инженерно-строительный журнал. 2019. № 1(85). С. 28–38. DOI: 10.18720/MCE.85.3

The use of fiber-reinforced concrete for the production of enclosing structures of protective structures is promising (the studies of V.S. Lesovik [6–7], R.S. Fediuk [8–9], A. Abrishambaf [10], D.-Y. Yoo [11–13], N. Ranjbar [14–15]), because it has high impact resistance. Dispersed reinforcement allows to substantially increase the whole set of mechanical characteristics of concrete, such as static strength, crack toughness, impact resistance [5].

However, the application of new types of nanodispersed mineral additives, as well as the principles of their compatibility to ensure the required performance characteristics of CBs, have not been studied sufficiently. In particular, the study of shock endurance of composites of various compositions has not been practically investigated.

To expand the use of composite binders in construction, it is necessary to study the compositions of Portland cement and multicomponent finely dispersed mineral and organic additives to obtain the required properties of binders and composites based on them for protective structures.

Thus, the goal of the paper is the development of composite binder for concrete enhanced impact resistance.

To achieve the paper goal, composite binders were prepared, obtained by joint grinding of the following components: 52–59 % of Portland cement, 30–32 % of rice husk ash (RHA), 5–7 % of quartz sand, 6–8 % of limestone crushing waste, 2–4 % hyperplasticizer (HP). Water was added in the amount necessary to ensure the same mobility, but from the calculation of the water-binding ratio not higher than 0.25. Cement stones were studied at the age of 1, 3, 7, 28 days.

2. Methods

The study of qualitative and quantitative compositions and properties of raw materials, composite binders and concrete samples was carried out using standard methods. The study of the morphological features of the microstructure was carried out using the Carl Zeiss CrossBeam 1540XB scanning electron microscope. The study of the mineral composition and structure was carried out using X-ray diffraction analysis by the D8 Advance powder diffractometer (Bruker AXS). Derivatograms of the samples were obtained by the Shimadzu DTG-60H thermogravimetric analyzer.

Specific surface of binders as well as mineral additives was measured by the device PSH-11, which operates on the principle of air permeability through a layer of pre-compacted material.

The compressive strength at the static load action (cubic strength), prismatic strength and modulus of elasticity were determined on the cubes with an edge of 150 mm and prisms with a base of 100×100 mm and a height of 400 mm.

The modulus of elasticity was calculated for each sample at a loading level of 30 % of the destructive one, according to formula

$$\mathrm{E}_{\sigma} = \frac{\sigma_1}{\varepsilon_{1y}},$$

here σ_1 is the increment of the voltage from the conditional zero to the level of the external load equal to 30 % of the destructive one;

ε_1 is the increment of the elastic relative longitudinal deformation of the sample, corresponding to the load level $P_1 = 0.3P_d$ and measured at the beginning of each stage of its application;

P_d is the destructing load measured on the scale of the press (machine).

To study the shock endurance, two series of tests were carried out: on panels and on cylinders.

Panels measuring 600×600×50 mm were removed from the mold 24 hours after casting and left in the laboratory until the testing age. The impact capacity of the panels was tested on day 28.

The shock endurance test was carried out with the aid of a falling hammer based on the international regulatory document ACI Committee 544, in which the impact-resistant specimen was subjected to repeated shocks at the same location. In this test, a hammer weighing 10 kg falls from a height of 600 mm on the panel. The number of impacts that caused the first visible crack and destruction was observed and used to calculate the first crack and the impact energy for destruction of concrete, respectively. The impact energy is given in the following equation:

$$\mathrm{E}_{sh} = m \cdot g \cdot h \cdot N,$$

here E_{sh} is the shock energy,

J; m – mass of the hammer = 10 kg;

g = 9.81 m/s^2;

N is the number of impacts.

The ratio of the number of shocks causing the failure, N_f to the number of shocks causing the first crack, N_c is defined as the impact coefficient $\mu_i = N_f/N_c$. The width of the crack of the entire fiber-reinforced concrete panel was measured using the Dino-Lite AM3713TB microscope immediately after the appearance of the first crack, and the crack growth was studied.

3. Results and Discussions

At the first stage, an almost linear dependence of the required time of grinding of the CB was revealed to achieve a different specific surface in the range from 280 to 900 m^2/kg (Figure 1, a, b). Obviously, with these data, the required grinding time can be predicted to reach a certain specific surface area. After grinding the CB components and measuring the surface area, water was added and the compressive strength was measured after 28 days. The results are shown in Figure 1, a. It can be seen that the maximum compressive strength was obtained at a surface area of 550 to 600 m^2/kg. The increase in the surface area does not lead to a further increase in strength, and even to a decrease. This is due to the excess of fine particles, because the superplasticizer limit was reached, which we investigated earlier [16]. This behavior was also observed in the change in the viscosity of the mixture when the surface area of the particles was above 600 m^2/kg. It is expected that an increase in the amount of superplasticizer will lead to the creation of concrete with an even greater compressive strength.

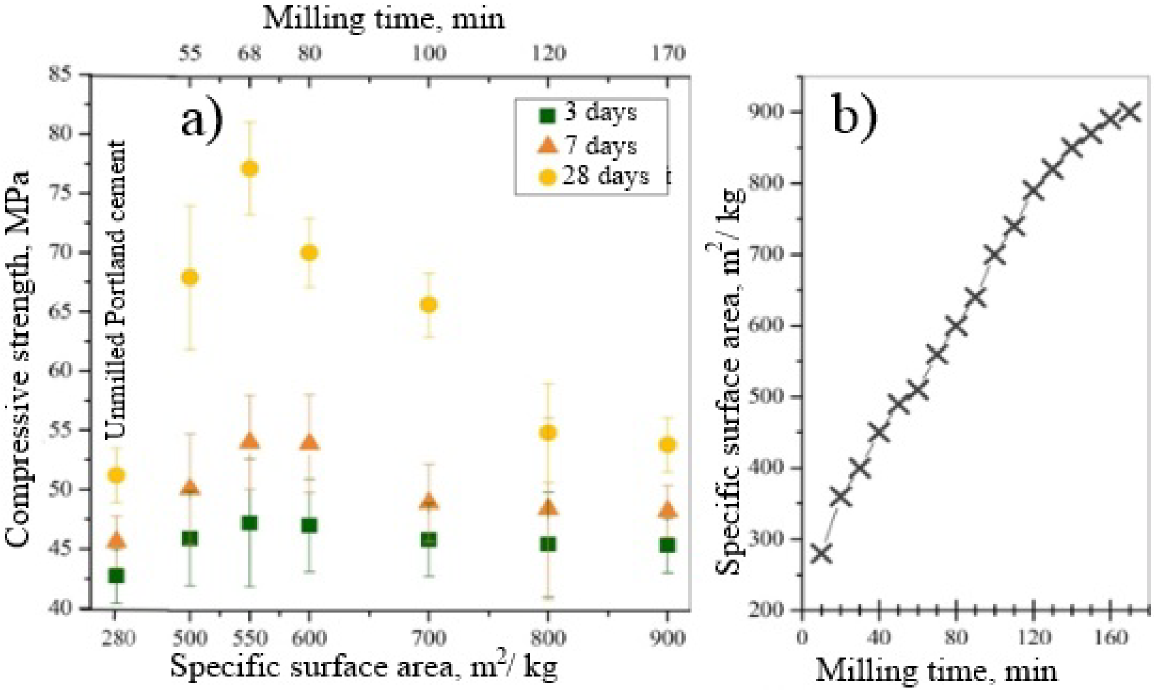

Figure 1. Microphotographs of cement stone without additives (*a*) and cement stone with replacing 25 % of cement by rice husk ash (*b*).

The microstructural analysis showed that cement matrix from a no-additive cement is characterized by a matrix with a large number of voids and microcracks, the overwhelming majority of which is represented by poorly crystallized and amorphous neoplasms, against which hexagonal plates of portlandite are visible (Figure 2, a, c).

The use of the developed composite binder allows to compact the microstructure, to obtain clearly distinguishable systems of needle and lamellar neoplasms filling anisometric and isometric voids (Figure 2, b, d). This leads to the formation of a rigid matrix with reduced porosity, which, in turn, leads to hardening of the cement stone [17–19].

Based on the results of XRD for the diffractogram of cement stone of the developed CB (Figure 3), the intensity of the peaks corresponding to clinker minerals is characteristic: an alite with d/n = 3.04; 2.97; 2.78; 2.74; 2.75; 2.61; 2.18; 1.77 Å and belite with d/n = 2.89; 2.67; 2.72; 2.76; 2.75; 2.78; 1.77 Å, which indicates the acceleration of hydration processes when using the CB. In addition, the CB contributes to a decrease in the intensity of the portlandite peaks with d/n = 4.93; 2.63; 1.93 Å.

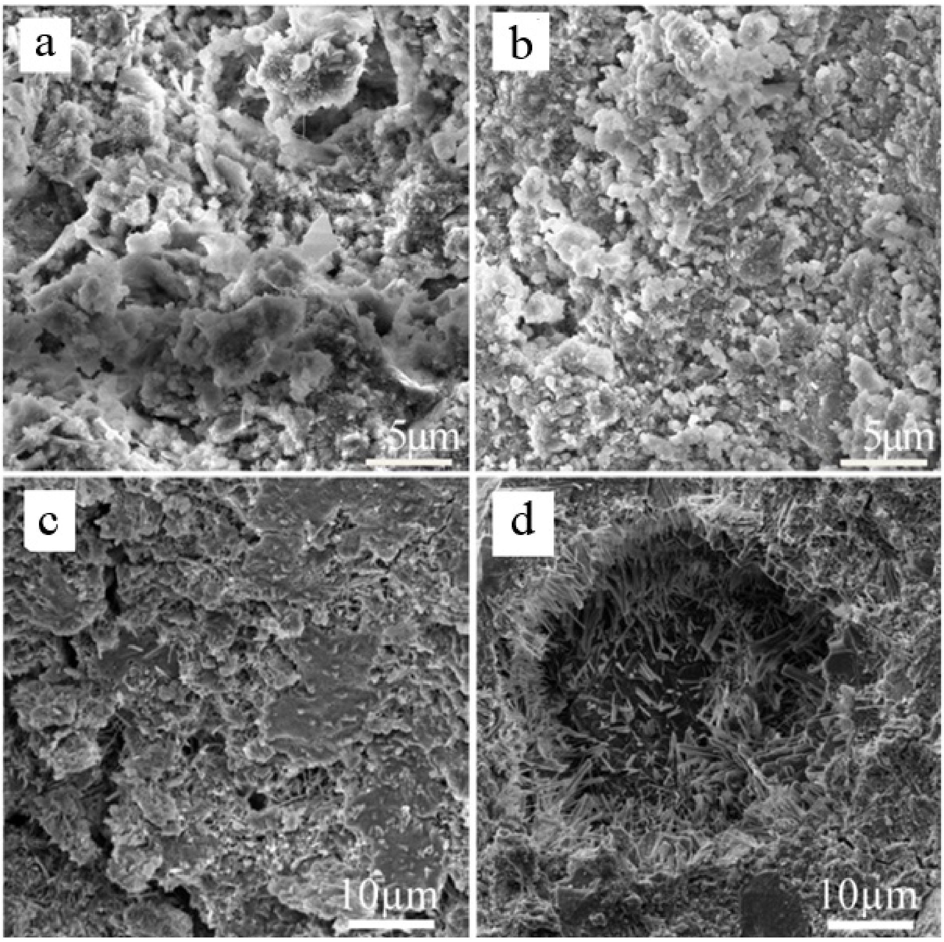

Figure 2. Microstructure of neoplasms (age 28 days): pure cement stone (a, c) and cement stone of the developed CB (b, d).

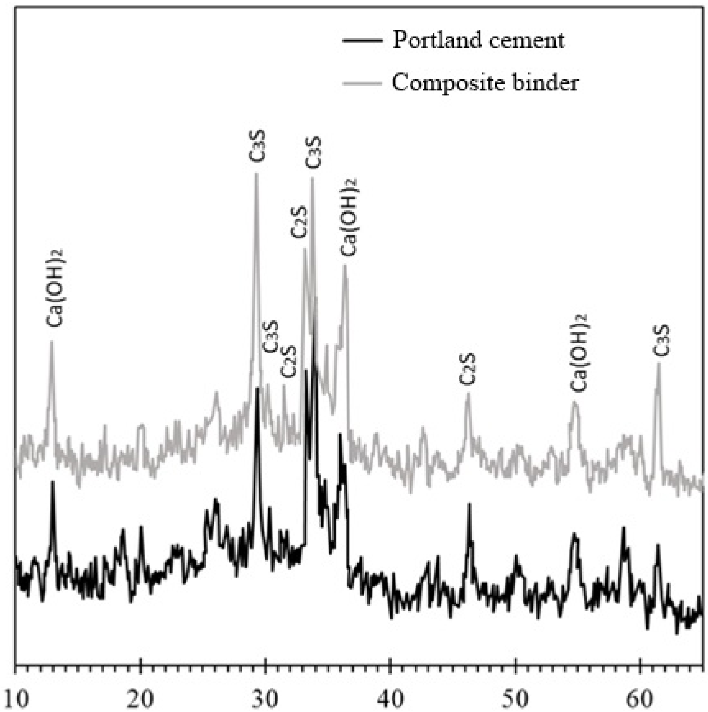

Figure 3. XRD of neoplasms.

Differential-thermal analysis (DTA) of the Portland cement stone and cement stone ot the CB showed the presence of three main endothermic effects (Figure 4). The first (at a temperature of about 160 °C) is caused by the loss of adsorption water from the gel-like hydration products. Reduction of the area of this effect on the results of DTA cement stone of the CB, shows a decrease in the content of gel-like neoplasms as a result of their transition to a crystalline state.

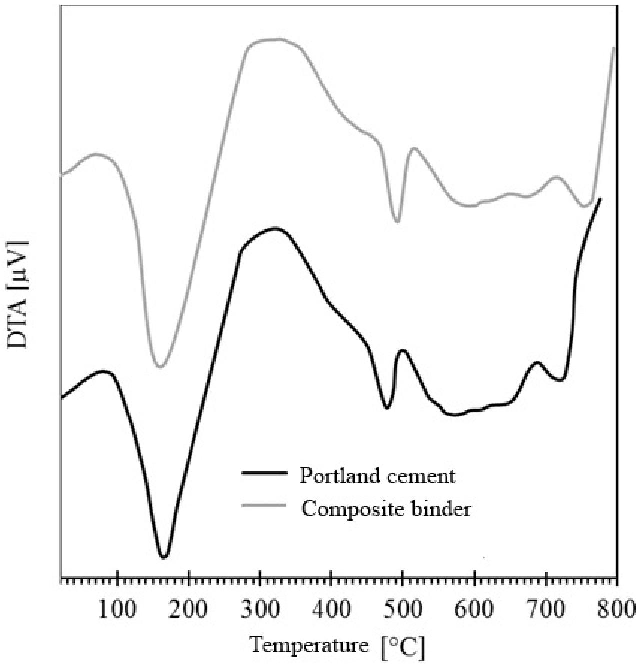

Figure 4. DTA results for pure cement stone and cement stone of the CB.

The next endothermic effect (at a temperature about 475 °C) corresponds to the dehydration of calcium hydroxide. The increase in the area of this peak on the thermogram of the no-additive cement stone shows a greater content of portlandite in its composition.

The last endothermic effect (at a temperature of 525–650 °C) can be associated with the decomposition of calcium carbonate.

In the initial period of curing, due to the fact that the crystal hydrates occupy an insignificant volume, the chemical and mineralogical characteristics of the additives and their pozzolanic activity practically do not affect the basic properties of the binder system.

In the second stage of hydration of the composite binder, the role of chemical processes that contribute to a significant modification of the phase composition of the system increases: the balance shifts from primary crystalline hydrates (calcium hydroxide and highly basic calcium hydrosilicates) toward more stable secondary fine crystalline hydrates represented by low-basic CSH. Mainly, the balance shift depends on the chemical composition and activity of the fine-milled additives. An obligatory condition of compaction, and, accordingly, hardening of cement stone is the shift of balance towards increasing the amount of low-basic calcium hydrosilicates CSH (I). Obviously, this condition will be sufficient until an excessive amount of filler will not envelop the surface of new phases, thereby preventing the formation of contacts and the fusion of crystalline hydrates. Proceeding from this, we conclude that in the mixed system is the optimum volume concentration of the ultradispersed additive taking into account its pozzolanic activity. When an inert filler is used, its optimum dosage will be determined by the amount of capillary pores necessary to seal the structure of the material.

Thus, it is possible to single out a number of positive factors leading to optimization of the physical and mechanical properties of cement stones as a result of the use of the developed CB:

– the speed of strength growth of the composite is increased in the early period as a result of the fact that the silica-containing components play the role of nucleation centers of neoplasms;

– Increasing the fineness of the particles and the concentration of the filler in the volume leads to a decrease in the total porosity of the composite;

– hydrosilicates of the second generation appear as a result of the reaction of amorphized RHA with portlandite;

– due to the large surface energy of the particles of the binder, clusters “binder – filler” are formed.

Investigation of the mechanical properties of fine-grained concrete (Table 1) showed that the use of composite binder allows to increase the technical characteristics of concrete, in comparison with similar compositions made with the use of traditional binder materials. This fact is explained by the denser structure of the cement stone of the developed composite binder, with a lower porosity, due to less water in the concrete. The best mechanical characteristics showed composition 2-2. It should be noted that with an increase in the amount of ash and a decrease in the amount of cement to ensure the uniformity of the formulations, it is necessary to increase the amount of water introduced into the concrete mix.

Table 1. Mechanical characteristics of fine-grained concrete depending on the composition of the binder.

Composition	Consumption of materials per 1 m^3				Cubic strength, MPa	Prism strength, MPa	Elastic modulus, GPa
	Cement, kg	Fillers of CB, kg	Aggregates, kg	Water, l			
1-2	646	508	1020	223	73.6	54.0	41.0
2-2	606	548	1020	231	82.6	65.2	55.3
3-2	565	589	1020	236	75.3	50.3	41.3
CEM I 42.5 N	545	-	1634	218	62.9	41.8	35.2
CEM I 42.5 N +31% RHA*	376	169	1634	241	71.2	52.3	44.0
CEM I 42.5 N +3% HP	512	33	1634	182	65.3	49.2	41.2

* – rice husk ash was crushed to 550 m^2 / kg

In order to obtain high density fibrous concrete, the effect of introducing reinforcing fibers into the concrete matrix was studied. As a basis for the concrete matrix was adopted the composition of 2-2 according to Table. 1.

To determine the optimal percentage of reinforcement of fine-grained fibrous concrete, samples of concrete of the same composition (2-2) with different contents of steel- and basalt fiber were molded. The results of the study of the dependence of the strength properties on the percentage of reinforcement by different types of disperse reinforcement are shown in Figure 5.

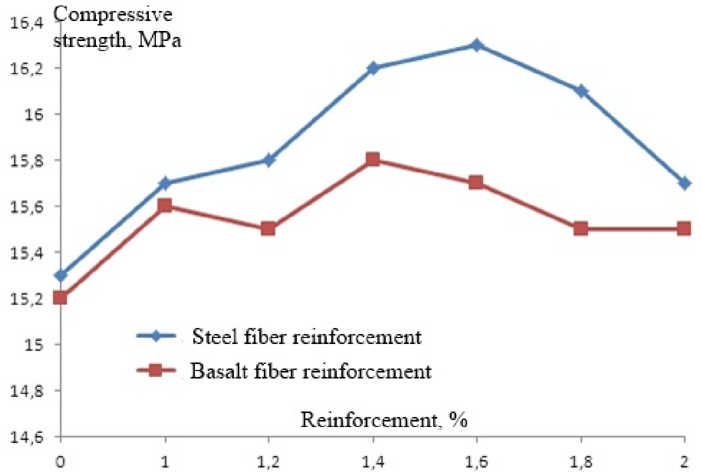

Figure 5. Dependence of tensile strength of fiber-reinforced concrete on the percentage of reinforcement by different types of fiber.

In the study of shock endurance of fiber-reinforced concrete with different types of fiber, the following results were obtained (Figure 6, 7).

Figure 6, 7 present that after the addition of steel or basalt fiber, the concrete strength (before the formation of the first crack) is increased to 9 times in comparison with the corresponding mixtures without fiber. Both steel and basalt fibers were effective in preventing the growth of microcracks and reducing the spread of these cracks before the cracks were combined with the formation of macrocracks.

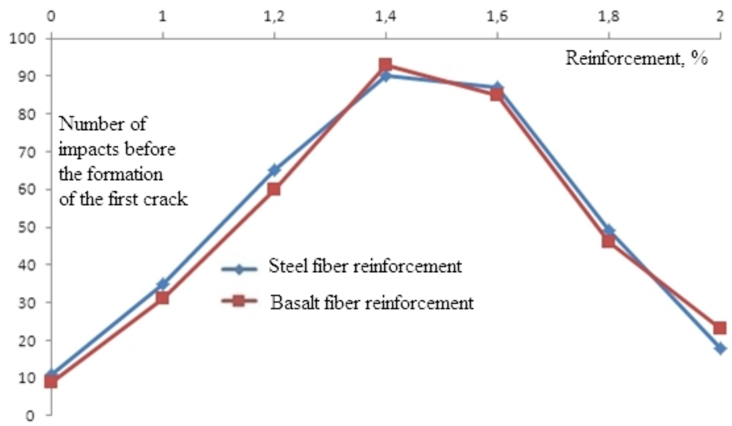

Figure 6. Dependence of the number of strokes before the formation of the first crack on the volume concentration of fiber.

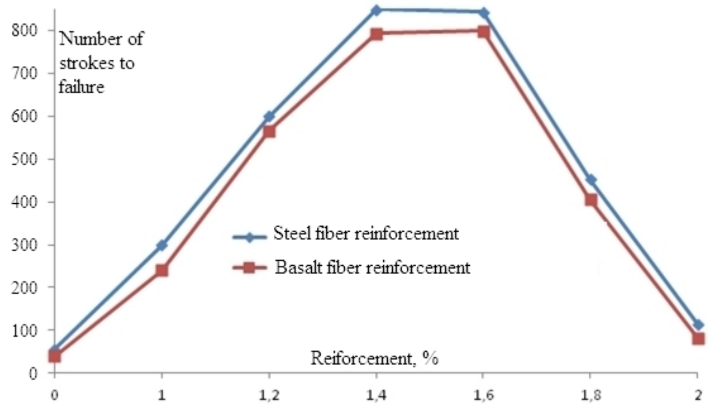

Figure 7. Dependence of the number of impacts to the destruction of fiber-reinforced concrete on the volume concentration of fiber.

The destruction scheme in samples with fibers and without is shown in Figure 8. The unreinforced concrete panel was broken into four parts after the destruction (Figure 8, a). The sample lost its structural integrity and geometry, reaching the energy capacity of the impact. The destruction of the fiber-reinforced concrete slab (Figure 8, b) was due to the perforation of the panels by the falling hummer, and the sample was not broken up into pieces, unlike simple concrete panels. This behavior showed that the fiber-reinforced concrete panels remained structurally integral, as well as viscous. Figure 8, b shows a significant number of secondary cracks.

Dynamic impacts are characterized by a continuous change in parameters, high intensity and short duration. Shock-, or dynamic strength, to a greater extent than static, depends on the initial defects in the structure of the concrete due to the reduction in the possibilities of redistribution of stresses due to the delay in the development of microplastic deformations. Fibers, influencing the processes of structure formation, help to reduce internal stresses and reduce the number of foci of occurrence of internal defects of concrete and their dimensions, thus preventing their further development.

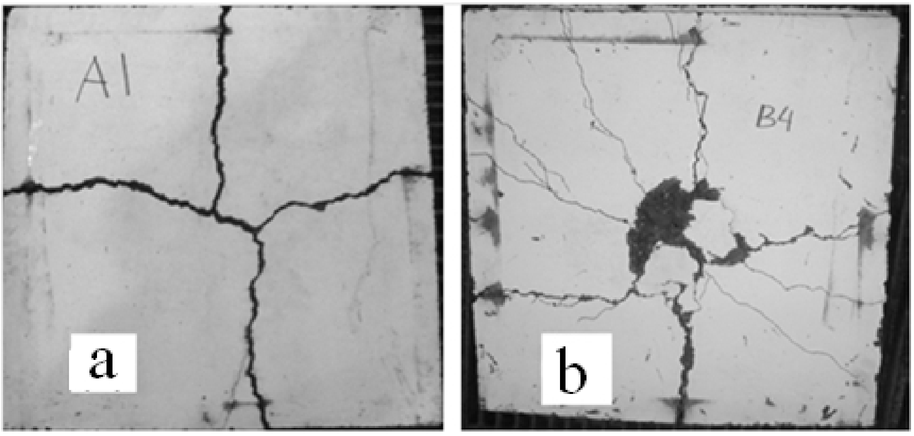

Figure 8. Destruction of samples without fiber and with fiber.

Further, studies were carried out of various compositions of fiber-reinforced concrete for impact endurance. It was revealed that the maximum number of blows withstands composition 2-2. Despite the fact that the largest coefficient of impact strength showed sample 1–2, this parameter can not be decisive in the design of protective structures, and its number of strokes to the first crack and the number of strokes before the destruction of the sample showed low results (Table 2).

Table 2. Shock resistance of fiber-reinforced concrete depending on the composition of the binder (1.4 % steel fiber reinforcement).

Composition (labeling according to Table 1)	Number of strokes for the first crack	Shock energy (first crack), J	The number of shocks for destruction the sample	Shock energy (destruction of the sample), J	Coefficient of impact strength, μ
1-2	6	354	198	11682	33
2-2	9	531	242	14278	27
3-2	8	472	191	11269	24
CEM I 42.5 N	1	59	6	354	5
CEM I 42.5 N +31% RHA	1	59	15	885	15
CEM I 42.5 N +3% HP	3	177	51	3009	17

Table 3 shows the width of the crack and the number of secondary cracks before the panel is destroyed. The initial width of the crack was used as a comparative study to determine the efficiency of steel fiber in bridged microcracks in fiber-reinforced concrete.

Table 3. Investigation of crack formation during fracture of samples.

Composition (labeling according to Table 1)	Opening of the first crack, mm	Crack opening before sample breaking, mm	Number of secondary cracks
1-2	0.132	1.789	13
2-2	0.095	1.876	18
3-2	0.187	1.843	14
CEM I 42.5 N	0.234	1.112	7
CEM I 42.5 N +31% RHA	0.187	1.160	10
CEM I 42.5 N +3% HP	0.197	1.324	12

The fiber bridge determines the absorption of the impact energy after the beginning of the cracking and, consequently, the shock plasticity of the concrete. The coefficient of impact strength μi, expressed as the ratio between the final and initial impact energies and shown in Table. 2, is a good indicator of the plasticity of concrete subjected to shock loading. Obviously, the final shock energy (before destruction) is much higher than the energy expended for the appearance of the first crack. Even after the formation of the first cracks, the sample was able to withstand a large amount of shock load before it destructed. The ultimate shock energy (before destruction) exceeded the published results for high-strength concrete [20–24]. This means that the developed fiber-reinforced concrete has a high impact strength and an excellent potential for use as a structural material for protective structures.

4. Conclusion

1. Principles of increasing the efficiency of fiber-reinforced concrete are proposed, which consist in the complex influence of the composite binder on the processes of structure formation of cement stone. In this case, the effect of increasing strength in static compression of fiber-reinforced concrete increases by 31%, and shock endurance – up to 6 times.

2. The best resistance to dynamic impact is possessed by concretes with a small number of defects, high density and uniformity, good adhesion between the aggregate and cement stone, an increased ratio of static tensile strength to static compressive strength R_{flex}/R_{compr} and ductility. This ratio can be increased if dispersed reinforcement of concrete is used.

3. The complex analysis of the system "composition (raw materials) – structure (raw materials, material) – properties (material)" is the methodological basis of the scientific research carried out. The results of the work were obtained using modern scientific methods of research, using standardized methods for determining the composition and properties of raw materials, binder and concrete using certified and certified equipment of the Far Eastern Federal University, as well as the Institute of Chemistry, Far Eastern Branch of the Russian Academy of Sciences.

4. It has been established that the use of CB consisting of 55.5 % cement, 31 % RHA, 10.5 % inert filler complex and 3 % hyperplasticizer, which is comminuted to a specific surface area of 550 m^2/kg, helps optimize the structure of the cement stone and increase its limit compressive strength of more than 60 %.

5. Compositions were designed on the basis of certain natural technogenic resources of the Primorye Territory, which have high adhesion to the cement matrix and close coefficients of deformation characteristics.

6. Comparison of the results of the tests carried out on fiber-reinforced concrete showed that with an increase in the deformation rate, an increase in strength was observed both during compression and in tension. In addition, a careful analysis of the experimental data has proved the fulfillment of the main provisions of the methods used, and the obtained dependences of the dynamic hardening coefficient on the strain rate qualitatively and quantitatively agree well with the results of domestic and foreign studies of various concretes.

7. In the penetration experiments it was noted that samples of unreinforced concrete were completely destroyed in large and small pieces, while the samples of fibrous concrete were not completely destroyed, and only through penetration at the impact site was observed; that is, fiber-reinforced concrete has better impact resistance.

References

1. Oyguc, R., Oyguc, E., Tonuk, G. Case study on seismic behavior of aseismically designed reinforced concrete frame structures. Bulletin of Earthquake Engineering. 2018. No. 16(7). Pp. 3057–3080.
2. Kristoffersen, M., Pettersen, J.E., Aune, V., Børvik, T. Experimental and numerical studies on the structural response of normal strength concrete slabs subjected to blast loading. Engineering Structures. 2018. Vol. 174. Pp. 242–255.
3. Maazoun, A., Belkassem, B., Reymen, B., Matthys, S., Vantomme, J., Lecompte, D. Blast response of RC slabs with externally bonded reinforcement: Experimental and analytical verification. Composite Structures. 2018. Vol. 200. Pp. 246–257.

4. Syed, Z.I., Raman, S.N., Ngo, T., Mendis, P., Pham, T. The Failure Behaviour of Reinforced Concrete Panels Under Far-field and Near-field Blast Effects. Structures. 2018. Vol. 14. Pp. 220–229.
5. Makita, K., Uda, Y., Yoshikado, H., Mori, K., Sato, Y., Kaneko, Y. Drop-Weight Test for RC Frame Made of Polypropylene Fiber-Reinforced Concrete. Journal of Advanced Concrete Technology. 2018. Vol. 16(1). Pp. 36–45.
6. Lesovik, V.S. Stroitel'nye materialy. nastoyashchee i budushchee [Conctruction Materials. the Present and the Future]. Vestnik MGSU [Proceedings of Moscow State University of Civil Engineering]. 2017. Vol. 12, issue 1 (100). Pp. 9–16.
7. Lesovik, V.S., Strokova, V.V., Krivenkova, A.N., Hodykin, E.I. Kompozicionnoe vjazhushhee s ispol'zovaniem kremnistyh porod [Composite binder using siliceous rocks]. Vestnik BGTU im. V.G. Shuhova – Bulletin of BSTU n.a. V.G. Shukhov. 2009. No. 1. Pp. 25–27. (rus)
8. Fediuk, R., Smoliakov, A., Stoyushko, N. Increase in composite binder activity. IOP Conference Series: Materials Science and Engineering. 2016. No. 156(1). Pp. 012042.
9. Fediuk, R.S. Mechanical Activation of Construction Binder Materials by Various Mills. IOP Conference Series: Materials Science and Engineering. 2016. No. 125(1). Pp. 012019.
10. Abrishambaf, A., Pimentel, M., Nunes, S. Influence of fibre orientation on the tensile behaviour of ultra-high performance fibre reinforced cementitious composites. Cement and Concrete Research. 2017. No. 97. Pp. 28–40.
11. Yoo, D.-Y., Banthia, N. Mechanical properties of ultra-high-performance fiber-reinforced concrete: A review. Cement and Concrete Composites. 2016. No. 73. Pp. 267–280.
12. Yoo, D.-Y., Banthia, N., Yoon, Y.-S. Predicting service deflection of ultra-high-performance fiber-reinforced concrete beams reinforced with GFRP bars. Composites Part B: Engineering. 2016. No. 99. Pp. 381–397.
13. Yang, J.-M., Shin, H.-O., Yoo, D.-Y. Benefits of using amorphous metallic fibers in concrete pavement for long-term performance. Archives of Civil and Mechanical Engineering. 2017. No. 17(4). Pp. 750–760.
14. Ranjbar, N., Behnia, A., Alsubari, B., Birgani, P.M., Jumaat, M.Z. Durability and mechanical properties of self-compacting concrete incorporating palm oil fuel ash. Journal of Cleaner Production. 2016. Vol. 112. Pp. 723–730.
15. Ranjba,r N., Kuenzel, C. Influence of preheating of fly ash precursors to produce geopolymers. Journal of American Ceramic Society. 2017. Vol. 00. Pp. 1–10.
16. Fediuk, R.S., Yevdokimova, Y.G., Smoliakov, A.K., Stoyushko, N.Y., Lesovik, V.S. Use of geonics scientific positions for designing of building composites for protective (fortification) structures (Conference paper). IOP Conference Series: Materials Science and Engineering. 2017. Vol. 221(1). Pp. 012011.
17. Lesovik, V.S., Urkhanova, L.A., Gridchin, A.M., Lkhasaranov, S.A. Composite binders on the basis of pearlite raw material of Transbaikalia. Research Journal of Applied Sciences. 2014. Vol. 9(12), Pp. 1016–1020.
18. Ibragimov, R.A., Bogdanov, R.R. The influence of a complex modifying agent on the hydration and structure formation of self-compacting concrete. ZKG International. 2017. Vol. 70(4). Pp. 44–49.
19. Klyuev, S.V., Klyuev, A.V., Abakarov, A.D., Shorstova, E.S., Gafarova, N.G. The effect of particulate reinforcement on strength and deformation characteristics of fine-grained concrete. Magazine of Civil Engineering. 2017. No. 7. Pp. 66–75. DOI: 10.18720/MCE.75.6
20. Loganina, V.I., Pyshkina, I.S., Martyashin, G.V. Effect of the supplement based on calcium hydrosilicates on the resistance of lime coatings. Magazine of Civil Engineering. 2017. No. 4. Pp. 20–27. DOI: 10.18720/MCE.72.3
21. Pelin, G., Pelin, C.-E., Ştefan, A., Dincă, I., Andronescu, E., Ficai, A. Mechanical and tribological properties of nanofilled phenolic-matrix laminated composites. Materiali in Tehnologije. 2017. Vol. 51 (4). Pp. 569–575.
22. Shi, C., Wu, Z., Cao, Z., Ling, T.C., Zheng, J. Performance of mortar prepared with recycled concrete aggregate enhanced by CO2 and pozzolan slurry. Cement and Concrete Composites. 2018. Vol. 86. Pp. 130–138.
23. Sata, V., Jaturapitakkul, C., Kiattikomol, K. Influence of pozzolan from various by-product materials on mechanical properties of high-strength concrete. Construction and Building Materials. 2007. Vol. 21. Pp. 1589–1598.
24. Volodchenko, A.A., Lesovik, V.S., Volodchenko, A.N., Glagolev, E.S., Zagorodnjuk, L.H., Pukharenko, Y.V. Composite performance improvement based on non-conventional natural and technogenic raw materials. International Journal of Pharmacy and Technology. 2016 Vol. 8(3). Pp. 18856–18867.

Contacts:

Roman Fediuk, +79502817945; roman44@yandex.ru
Valeriy Lesovik, +79103613263; naukavs@mail.ru
Yuriy Liseitsev, +79502817945; gera210307@ya.ru
Roman Timokhin, +79502817945; gera210307@yandex.ru
Aleksandr Bituyev, +79502817945; office@esstu.ru
Mikhail Zaiakhanov, +79502817945; roman44@ya.ru
Aleksandr Mochalov, +79502817945; captainvmf@yandex.ru

Инженерно-строительный журнал

ISSN 2071-0305

сайт журнала: http://engstroy.spbstu.ru/

DOI: 10.18720/MCE.85.3

Композиционные вяжущие для бетонов повышенной ударной стойкости

Р.С. Федюк[a]*, В.С. Лесовик[b], Ю.Л. Лисейцев[a], Р.А. Тимохин[a], А.В. Битуев[c], М.Е. Заяханов[c], А.В. Мочалов[a]

[a] Дальневосточный Федеральный Университет, г. Владивосток, Россия,

[b] Белгородский государственный технологический университет им. В.Г. Шухова, г. Белгород, Россия

[c] Восточно-Сибирский государственный университет технологий и управления, г. Улан-Удэ, Республика Бурятия, Россия

** E-mail: roman44@yandex.ru*

Ключевые слова: самоуплотняющийся бетон, зола рисовой шелухи, пуццолановые материалы, ударная выносливость, свойства бетонной смеси, механические свойства.

Аннотация. Исследованы и предложены химико-технологические принципы оптимизации физико-механических свойств и эксплуатационных характеристик дисперсно-армированных композиционных материалов, заключающиеся в комплексном влиянии композиционного вяжущего на процессы структурообразования цементного камня. Изучен качественный и количественный состав и свойства исходных материалов, композиционного вяжущего и бетонных образцов. Подобраны оптимальные составы бетонов для защитных сооружений, обеспечивающих максимальные статические и динамические прочностные характеристики. При этом эффект увеличения ударной выносливости возрастает до 6 раз. Выявлено, что наилучшим сопротивлением динамическому воздействию обладают бетоны с небольшим количеством дефектов, высокой плотностью упаковки и однородностью, хорошим сцеплением между заполнителем и цементным камнем, повышенным отношением статической прочности на растяжение к статической прочности на сжатие Rp/Rсж и пластичностью. Доказано, что это отношение можно повысить, в случае применения дисперсного армирования бетонов (так называемые, фибробетоны). В экспериментальных исследованиях по пробитию, как неармированных, так и фибробетонных плит отмечено, что образцы неармированного бетона полностью разрушались на крупные и мелкие куски, в то время как образцы фибробетона разрушались не полностью, а наблюдалось только сквозное их пробитие в месте воздействия ударника; то есть фибробетон обладает лучшей ударной стойкостью. Данные результаты могут быть применимы при проектировании различных специальных сооружений, таких как защитные сооружения гражданской обороны, бетонные конструкции атомных электростанций и т.д.

Литература

1. Oyguc R., Oyguc E., Tonuk G. Case study on seismic behavior of aseismically designed reinforced concrete frame structures // Bulletin of Earthquake Engineering. 2018. № 16(7). Pp. 3057–3080.
2. Kristoffersen M., Pettersen J.E., Aune V., Børvik T. Experimental and numerical studies on the structural response of normal strength concrete slabs subjected to blast loading // Engineering Structures. 2018. Vol. 174. Pp. 242–255.
3. Maazoun A., Belkassem B., Reymen B., Matthys S., Vantomme J., Lecompte D. Blast response of RC slabs with externally bonded reinforcement: Experimental and analytical verification // Composite Structures. Vol. 200. Pp. 246–257.
4. Syed Z.I., Raman S.N., Ngo T., Mendis P., Pham T. The Failure Behaviour of Reinforced Concrete Panels Under Far-field and Near-field Blast Effects // Structures. 2018. Vol. 14. Pp. 220–229.
5. Makita K., Uda Y., Yoshikado H., Mori K., Sato Y., Kaneko Y. Drop-Weight Test for RC Frame Made of Polypropylene Fiber-Reinforced Concrete // Journal of Advanced Concrete Technology. 2018. Vol. 16(1). Pp. 36–45.
6. Лесовик В.С. Строительные материалы. Настоящее и будущее // Вестник МГСУ. 2017. № 1. С. 9–16.
7. Лесовик В.С., Строкова В.В., Кривенкова А.Н., Ходыкин Е.И. Композиционное вяжущее с использованием кремнистых пород. Вестник БГТУ им. Шухова. 2009. № 1. С. 25–27.
8. Fediuk R., Smoliakov A., Stoyushko N. Increase in composite binder activity // IOP Conference Series: Materials Science and Engineering. 2016 № 156(1). Pp. 012042.
9. Fediuk R.S. Mechanical Activation of Construction Binder Materials by Various Mills. IOP Conference Series: Materials Science and Engineering. 2016. № 125(1). Pp. 012019.

10. Abrishambaf A., Pimentel M., Nunes S. Influence of fibre orientation on the tensile behaviour of ultra-high performance fibre reinforced cementitious composites. Cement and Concrete Research. 2017. № 97. Pp. 28–40.
11. Yoo D.-Y., Banthia N. Mechanical properties of ultra-high-performance fiber-reinforced concrete: A review // Cement and Concrete Composites. 2016. № 73. Pp. 267–280.
12. Yoo D.-Y., Banthia N., Yoon Y.-S. Predicting service deflection of ultra-high-performance fiber-reinforced concrete beams reinforced with GFRP bars // Composites Part B: Engineering. 2016. № 99. Pp. 381–397.
13. Yang J.-M., Shin H.-O., Yoo D.-Y. Benefits of using amorphous metallic fibers in concrete pavement for long-term performance // Archives of Civil and Mechanical Engineering. 2017. No. 17(4). Pp. 750–760.
14. Ranjbar N., Behnia A., Alsubari B., Birgani P.M., Jumaat M.Z. Durability and mechanical properties of self-compacting concrete incorporating palm oil fuel ash // Journal of Cleaner Production. 2016. Vol. 112. Pp. 723–730.
15. Ranjbar N., Kuenzel C. Influence of preheating of fly ash precursors to produce geopolymers // Journal of American Ceramic Society. 2017. Vol. 00. Pp. 1–10.
16. Fediuk R.S., Yevdokimova Y.G., Smoliakov A.K., Stoyushko N.Y., Lesovik V.S. Use of geonics scientific positions for designing of building composites for protective (fortification) structures (Conference paper) // IOP Conference Series: Materials Science and Engineering. 2017. Vol. 221(1). Pp. 012011
17. Lesovik V.S., Urkhanova L.A., Gridchin A.M., Lkhasaranov S.A. Composite binders on the basis of pearlite raw material of Transbaikalia // Research Journal of Applied Sciences. 2014. Vol. 9(12). Pp. 1016–1020.
18. Ibragimov R.A., Bogdanov R.R. The influence of a complex modifying agent on the hydration and structure formation of self-compacting concrete // ZKG International. 2017. Vol. 70(4). Pp. 44–49.
19. Клюев С.В., Клюев А.В., Абакаров А.Д., Шорстова Е.С., Гафарова Н.Е. Влияние дисперсного армирования на прочностные и деформативые характеристики мелкозернистого бетона // Инженерно-строительный журнал. 2017. № 7(75). С. 66–75. DOI: 10.18720/MCE.75.6
20. Логанина В.И., Пышкина И.С., Мартяшин Г.В. Влияние добавки на основе гидросиликатов кальция на стойкость известковых покрытий // Инженерно-строительный журнал. 2017. № 4(72). С. 20–27. DOI: 10.18720/MCE.72.3
21. Pelin G., Pelin C.-E., Ştefan, A., Dincă I., Andronescu E., Ficai A. Mechanical and tribological properties of nanofilled phenolic-matrix laminated composites // Materiali in Tehnologije. 2017. Vol. 51(4). Pp. 569–575.
22. Shi C., Wu Z., Cao Z., Ling T.C., Zheng J. Performance of mortar prepared with recycled concrete aggregate enhanced by CO2 and pozzolan slurry // Cement and Concrete Composites. 2018. Vol. 86. Pp. 130–138.
23. Sata V., Jaturapitakkul C., Kiattikomol K. Influence of pozzolan from various by-product materials on mechanical properties of high-strength concrete // Construction and Building Materials. 2007. Vol. 21. Pp. 1589–1598.
24. Volodchenko A.A., Lesovik V.S., Volodchenko A.N., Glagolev E.S., Zagorodnjuk L.H., Pukharenko Y.V. Composite performance improvement based on non-conventional natural and technogenic raw materials // International Journal of Pharmacy and Technology. 2016 Vol. 8(3). Pp. 18856–18867.

Контактные данные:

Роман Сергеевич Федюк, +79502817945; эл. почта: roman44@yandex.ru
Валерий Станиславович Лесовик, +79103613263; эл. почта: naukavs@mail.ru
Юрий Леонидович Лисейцев, +79502817945; эл. почта: gera210307@ya.ru
Роман Андреевич Тимохин, +79502817945; эл. почта: gera210307@yandex.ru
Александр Васильевич Битуев, +79502817945; эл. почта: office@esstu.ru
Михаил Егорович Заяханов, +79502817945; эл. почта: roman44@ya.ru
Александр Викторович Мочалов, +79502817945; эл. почта: captainvmf@yandex.ru

Magazine of Civil Engineering. 2019. 85(1). Pp. 39–50
Инженерно-строительный журнал. 2019. № 1(85). С. 39–50

Magazine of Civil Engineering

ISSN 2071-0305

journal homepage: http://engstroy.spbstu.ru/

DOI: 10.18720/MCE.85.4

The critical ventilation velocity for transverse double fires in tunnel

Q. Zhang*[a]*, G. Pei*[b]**
[a] School of Civil Engineering and Architecture, Southwest Petroleum University, Chengdu, China
[b] School of Architectural Economics and Engineering Management, Hubei Business College, Wuhan, China
** E-mail: 570769297@qq.com*

Keywords: tunnel fire; numerical simulation; transverse double fires; critical velocity.

Abstract. The critical velocity of longitudinal ventilation is one of the most important parameters in tunnel fires. Most previous studies simulated fire scenarios in which only one fire source exists in the tunnel. However, the critical velocity will change under the condition of transverse double fires. In this study, the critical ventilation velocity under the transverse double-fire condition compared with the single fire source was analyzed by using the Fire Dynamics Simulator (FDS). The results show that the smoke movement for transverse double fires in the tunnel is affected by both the buoyant force and the shear stress of the sidewalls. As the distance between the double fires increases, the critical velocity decreases first, then increases and eventually decreases. When the double fire sources are both near the side walls, the critical velocity is approximately equal to the critical velocity for adjacent double fires at the center. Finally, relations between the influence coefficient of distance and the dimensionless transverse distance as well as correlations between the critical ventilation velocity with and without distances for double fires were developed. The presented correlation can provide reference value for smoke control and personnel evacuation in case of tunnel fires.

1. Introduction

In recent years, various railway tunnel, highway tunnel, and urban subway projects have been rapidly developed worldwide [1]. Fire safety is significantly important, particularly in tunnels. Many fire investigations have shown that the most dangerous factor leading to casualties is not the high temperature of the fire but the smoke produced by the fire, so smoke flow has a significant impact on fire-fighting strategy and personnel evacuation. The method of emergency plan and smoke control most currently applied in many tunnels is based on longitudinal ventilation produced mechanically [2]. The critical ventilation velocity is the minimum ventilation velocity that could force the smoke to stay at downstream of the fire source only. When ventilation velocity below the critical velocity is not sufficient to prevent the smoke from spreading against the direction of longitudinal ventilation air, the back-layering phenomenon (smoke back-layering length) will appear in the fire upstream, which is not conducive for personnel evacuation [3]. Therefore, one of the foremost parameters for managing the smoke movement effectively is the value of critical velocity.

The characteristics of smoke movement were studied by the earliest tunnel fire tests conducted in Switzerland. Subsequently, a series of large-scale fire experiments established in nine Western countries showed that smoke flow strongly depends on the ventilation velocity [4]. Currently, several different formulas to predict the critical velocity are developed by a theory based on the Froude number, and some scholars note that Thomas [5] was one of the first to engage in this study and set up the prediction determination for the critical velocity. The relationship between critical velocity and heat release rate was developed as

$$V_c = \left(\frac{gQH}{\rho_0 C_p T_f A} \right)^{1/3}, \tag{1}$$

where Q is the heat release rate, W;

Zhang, Q., Pei, G. The critical ventilation velocity for transverse double fires in tunnel. Magazine of Civil Engineering. 2019. 85(1). Pp. 39–50. DOI: 10.18720/MCE.85.4.

V_c is the critical velocity, m/s; g is the acceleration of gravity, m/s^2;

H is the tunnel height, m;

ρ_0 is the air density, kg/m^3;

C_p is the specific heat at constant pressure, J/kg·K;

T_f is the hot air temperature, K;

A is the cross-sectional area of the tunnel, m^2.

According to the dimension analysis, Oka and Athinson [6], Wu and Bakar [7], and Li et al. [8] proposed different prediction models for critical ventilation velocity. In terms of small-scale experimentation, Oka and Athinson [6] found that the critical velocity does not increase with the one-third power of the heat release rate with a high value, therefore, a new formula was established in dimensionless form through correlation of experimental results:

$$V_c^* = \begin{cases} K_v \left(\dfrac{Q^*}{0.12} \right)^{1/3} & Q^* \le 0.12, \\ K_v & Q^* > 0.12, \end{cases} \tag{2}$$

where $Q^* = Q / c_p \rho_0 T_a g^{1/2} H^{5/2}$,

$V^* = V / \sqrt{gH}$,

K_v is a constant value ranging from 0.22 to 0.38,

T_a is the ambient temperature, K.

Wu and Bakar [7] studied, by experiment and numerical simulation, the influence of different cross-section shapes on the critical ventilation velocity. From the model by Oka and Athinson [6], a new prediction model was expressed with the tunnel hydraulic height:

$$V_c^\bullet = \begin{cases} 0.4 \left(\dfrac{Q^\bullet}{0.2} \right)^{1/3} & Q^* \le 0.2, \\ 0.4 & Q^* > 0.2, \end{cases} \tag{3}$$

where $Q^* = Q / c_p \rho_0 T_a g^{1/2} \overline{H}^{5/2}$,

$V^* = V / \sqrt{g\overline{H}}$,

$\overline{H}$ is the tunnel hydraulic height, m.

Li et al. [8] carried out a series of small-scale experiments in two tunnels of 12 m length with diverse cross-sections to investigate the critical velocity, their prediction model is given as

$$V_c^\bullet = \begin{cases} 0.81 Q^{*1/3} & Q^* \le 0.15, \\ 0.43 & Q^* > 0.15, \end{cases} \tag{4}$$

where $Q^* = Q / c_p \rho_0 T_a g^{1/2} H^{5/2}$,

$V^* = V / \sqrt{gH}$.

In addition to the factor of cross-section shape, other elements, such as blockage and slope, also affect the critical velocity in a tunnel. Some authors have reported that the critical velocity decreases because of vehicle blockage [9–11]. Alva et al. [12] noted that the relative position between the fire source and blockage can increase the critical velocity compared with that of the same situation without vehicular blockage. For four slope values (0°, 3°, 6°, and 9°), Chow et al. [13] showed that the critical velocity for sloped tunnels is higher than that for horizontal tunnels. Yi et al. [14] suggested that the critical velocity decreases as slope value ranging from −3 % to 3 % increases gradually. In these studies, fires were always set on the centerline in the tunnel, but in reality, a fire can happen at any location in the transverse direction of tunnel. A “mirror” effect was considered by Hu et al. [15] to derive the ratio of the critical velocity for a fire next to a sidewall to that for a fire in the middle by theoretical analysis, the ratio value was estimated as 1.26. Furthermore, Zhong et al. [16] noted that the critical velocity would increase exponentially with decreasing distance between the fire and the sidewall. Wang et al. [17] revealed, using tunnel height as the characteristic length, that the critical velocity for a fire near a wall is distinctly higher than that for fire at other positions in the lateral direction, and the ratio is approximately equal to 1.2.

These previous studies have always focused on a single fire in the tunnel. In fact, under the congestion conditions caused by tunnel fire, a burning vehicle could easily ignite adjacent vehicles when the heat radiation grows adequately, at the same time, the critical velocity is influenced by the greater heat release rate and the distance between fire sources. Therefore, in this study, different conditions established by numerical simulation were used to investigate the critical velocity.

2. Methods

2.1. Physical model

In this study, a tunnel model measuring 15×1×0.25 m was established by using Fire Dynamics Simulator (FDS) version 6.6.0, as shown in Figure 1. The tunnel structure, including walls, ceiling, and floor, was modelled as concrete with thermal thickness, their boundary conditions were set to “CONCRETE” and the thermal properties of concrete were specified by the “MATL” command in FDS. The velocity at the walls, ceiling, and floor was assumed to be the default conditions by FDS. Two surfaces, including a portal set to “SUPPLY” and an exit called “OPEN” in FDS, were placed at both ends of the model tunnel, the longitudinal ventilation velocity was specified at the portal surface to introduce the air flow to the tunnel entry, and the open surface was connected with the atmospheric environment. The ambient temperature was 293 K and the atmospheric pressure was 101,325 Pa. The heat release rate was assigned as the heat release rate per unit area by using the “HRRPUA” command in FDS. The smoke produced by the burnable methane (CH_4) was used to model soot. Two identical rectangular fire sources were symmetrically placed on the floor of the tunnel center and horizontally moved to the sidewalls. In this study, X, Y, and Z represent the longitudinal, transverse, and vertical directions, respectively. All combinations are listed in Table 1.

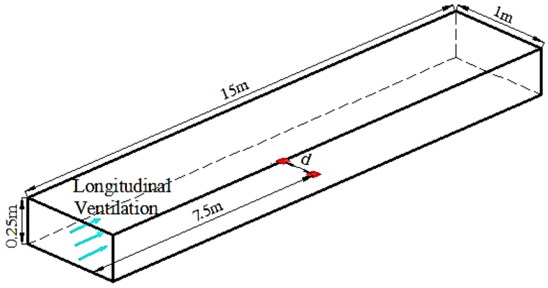

Figure 1. Diagram of the model tunnel.

Table 1. Relative position of transverse double fires.

Fire combination	Relative position of fire, m						
3 + 3 kW	0.1	0.2	0.3	0.4	0.5	0.6	0.7
6 + 6 kW	0.1	0.2	0.3	0.4	0.5	0.6	0.7
7.5 + 7.5 kW	0.1	0.2	0.3	0.4	0.5	0.6	0.7
12 + 12 kW	0.1	0.2	0.3	0.4	0.5	0.6	0.7

2.2. Large-eddy simulation

FDS is a computational fluid dynamics (CFD) model of fire-driven fluid flow to numerically solve a modality of the Navier-Stokes equations fit for speed with a low Mach number and smoke and heat transport by thermally-driven flow [18, 19]. The default combustion model used in the simulation was mix-controlled with infinitely fast chemistry. The turbulence model has four available models, including Deardorff, Vreman, constant Smagorinsky, and dynamic Smagorinsky for the subgrid-scale (sgs) turbulent viscosity [20], the default Deardorff model was applied in the simulation.

The default Deardorff turbulent viscosity is expressed as

$$(\mu_{LES} / \rho) = C_v \Delta \sqrt{k_{sgs}}, \tag{5}$$

where C_v = 0.1 and the sgs kinetic energy is taken from an algebraic relationship based on scale similarity [18, 19]. The filter width of Large-eddy simulation is taken as the geometric mean of the local mesh spacing in each direction,

$$\Delta = (\delta x \delta y \delta z)^{(1/3)},$$

where δx, δy, and δz are the dimensions of the smallest cell.

The thermal conductivity and material diffusivity are related to the turbulent viscosity by

$$k_{LES} = \frac{\mu_{LES} c_p}{Pr_t}; \tag{6}$$

$$(\rho D)_{LES} = \frac{\mu_{LES}}{Sc_t}. \tag{7}$$

The turbulent Prandtl number Pr_t and the turbulent Schmidt number Sc_t are assumed to be constant for a given scenario. The Pr_t and Sc_t have constant default values of 0.5, which can better simulate the fire smoke flow [11].

2.3. Grid independence test

Double fires (6 + 6 kw) at a distance of 0.1 m, as an example, were employed to test the grid independence. The grid region was divided into a left part (L) from 0 to 6 m, a middle part (M) from 6 to 9 m, and a right part (R) from 9 to 15 m in the x direction. The temperature measured under the tunnel ceiling was selected as the test parameter, and the longitudinal ventilation velocity was set to 0.35 m/s. The detailed information of four grid systems is shown in Table 2, the mesh number of the left part was the same as that of the right part, and the mesh of middle part was refined as the fire existed in each grid system. When the combustion reaches quasi-stable state, the simulation results are shown in Figure 2. Figure 2 indicates that as the mesh number increases, the temperature values between grid systems 3 and 4 are closest with an error of less than 5 %. Considering the economical efficiency of computing time, grid system 3, with a total mesh number of 975,000, was deemed as the most suitable meshing scheme for numerical simulation.

Table 2. Specific parameters of the grid system.

Grid system	Region	Mesh number			Mesh size			Total mesh number
		X	Y	Z	ΔX	ΔY	ΔZ	
1	L	300	50	10	0.02	0.02	0.025	425,000
	M	250	50	10	0.012	0.02	0.025	
	R	300	50	10	0.02	0.02	0.025	
2	L	300	80	10	0.02	0.0125	0.025	720,000
	M	300	80	10	0.01	0.0125	0.025	
	R	300	80	10	0.02	0.0125	0.025	
3	L	300	50	20	0.02	0.02	0.0125	975,000
	M	375	50	20	0.008	0.02	0.0125	
	R	300	50	20	0.02	0.02	0.0125	
4	L	300	80	20	0.02	0.0125	0.0125	1,920,000
	M	600	80	20	0.005	0.0125	0.0125	
	R	300	80	20	0.02	0.0125	0.0125	

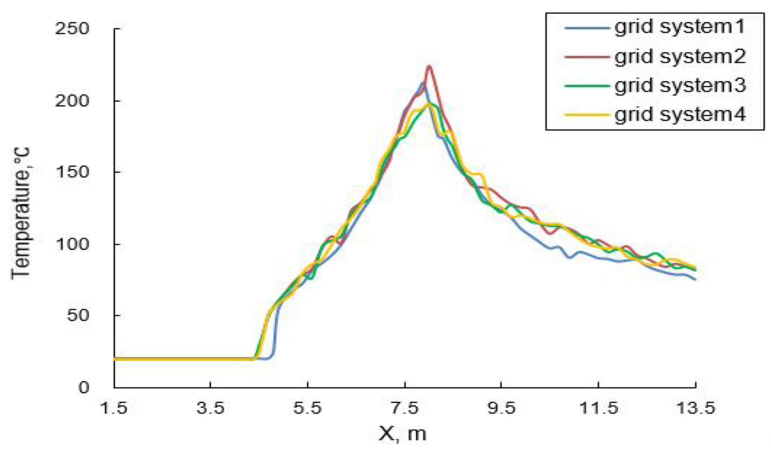

Figure 2. Temperature distribution of different grid systems along the *X* direction.

2.4. Convergence of simulation

The Courant- Friedrichs-Lewy (CFL) criterion was applied to justify the convergence of the CFD simulation. The criterion plays a significant role in large-scale calculations in FDS. The calculated velocities were examined at each time step to follow the CFL constraint [18,19]:

$$\mathrm{CFL} = \delta t \cdot \max\left(\frac{|u_{ijk}|}{\delta x}, \frac{|v_{ijk}|}{\delta y}, \frac{|w_{ijk}|}{\delta z}\right) < 1. \quad (8)$$

The initial time step is normally set automatically in FDS by dividing the size of a mesh cell by the characteristic velocity of the flow. During the calculation, the time step is varying and constrained by the convective and diffusive transport speeds to ensure that the CFL condition is satisfied at each time step. Figure 3 suggests that the CFL numbers during the iterations are in the range of 0.42 to 0.99, the CFL convergence criterion is satisfied because all of CFL numbers are less than the criteria value of 1. As seen in Figure 4, the time step eventually changes into a quasi-steady value with an average value of approximately 0.003 s when the fire reaches a quasi-steady state.

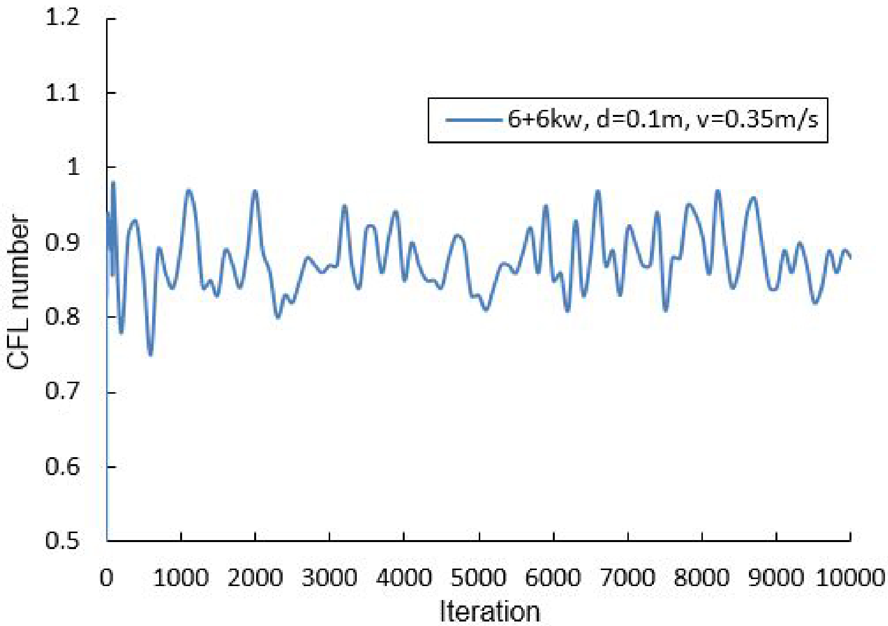

Figure 3. CFL number for FDS numerical simulation.

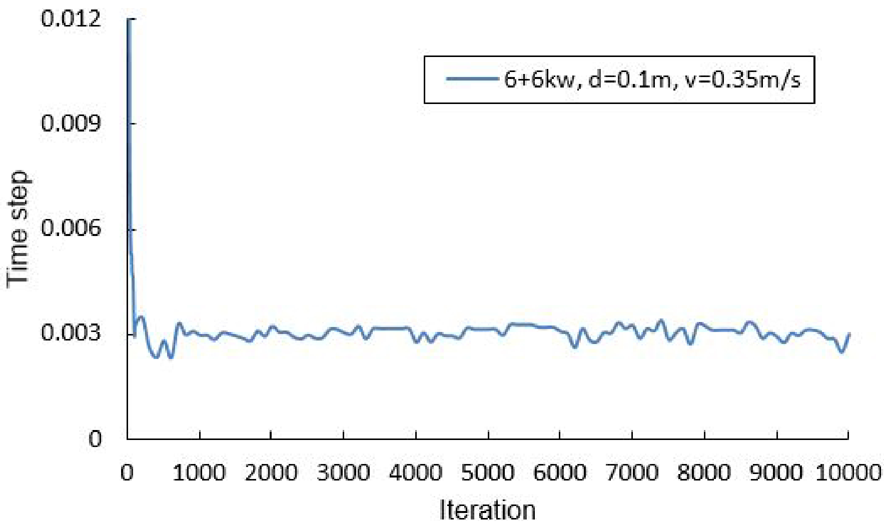

Figure 4. Time step for FDS numerical simulation.

2.5. Comparison with experiments

Wu and Bakar [7] implemented many experiments in five tunnels of 15 m length with different cross-section shapes to study the critical velocity on the basis of the small-scale method. The experimental data in tunnel D with dimensions 15×1×0.25 m were selected to prove the ability and reliability of the FDS model. In tunnel D, the burner was placed on the floor surface of the tunnel center, and the smoke temperature under the ceiling was detected by K-type thermocouples of diameter 0.25 mm. In order to detect the smoke temperature in the FDS model, thermocouples with an interval of 0.1 m were uniformly arranged below the top of the model tunnel centerline, the length ranged from 3.5 m to 11.5 m in the *x* direction, as shown in Figure 5. When the smoke flow approaches the quasi-steady state in the case of longitudinal ventilation, only the temperature of thermocouples located upstream of the fire source is close to the ambient temperature of 20 °C, at this time, the ventilation velocity is regarded as the critical ventilation velocity, as shown in Figure 6. As can be seen from Figure 7, the experimental and simulation values for critical velocity have the identical trend with minor error. Therefore, the FDS model can be used to study the critical velocity in tunnel fires.

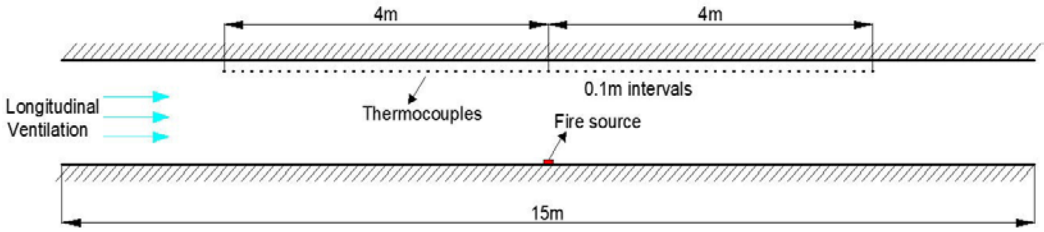

Figure 5. Layout of thermocouples in the FDS simulation for the validation.

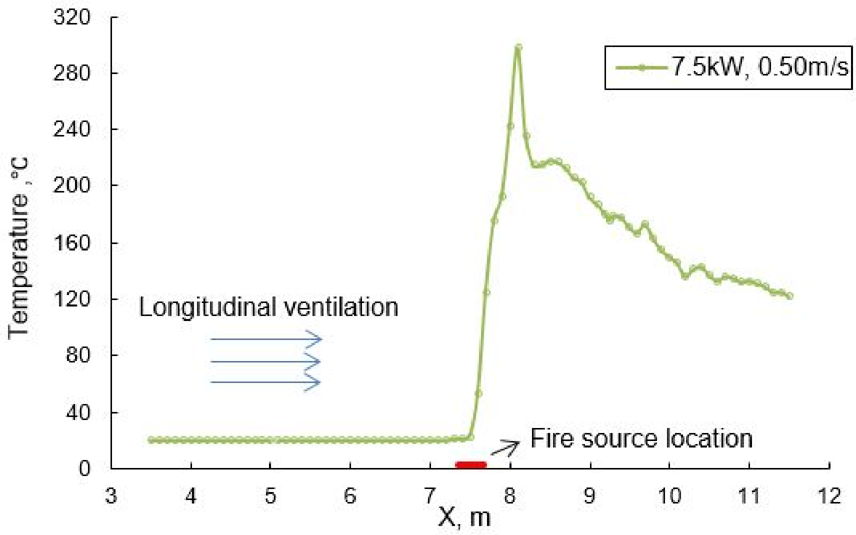

Figure 6. Smoke temperature with critical ventilation velocity.

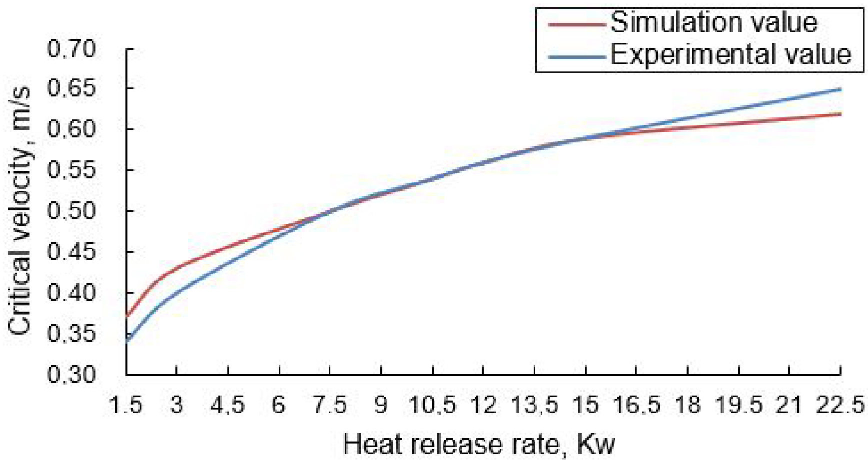

Figure 7. Comparison between the simulation values and experimental values in Wu and Bakar's study for critical ventilation velocity.

3. Results and Discussion

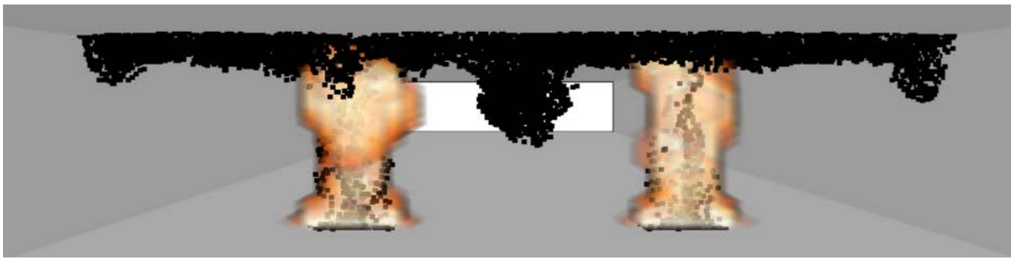

Figure 8. Schematic diagram of smoke flow at the junction between double fires.

Tracer particles were added to observe the situation because of the low carbon content of methane. In Figure 8, without longitudinal ventilation velocity, the smoke spreads freely to both sides in the transverse direction of the tunnel, and there is a distinct convection bonding part when the smoke of horizontal diffusion from the double fires meets.

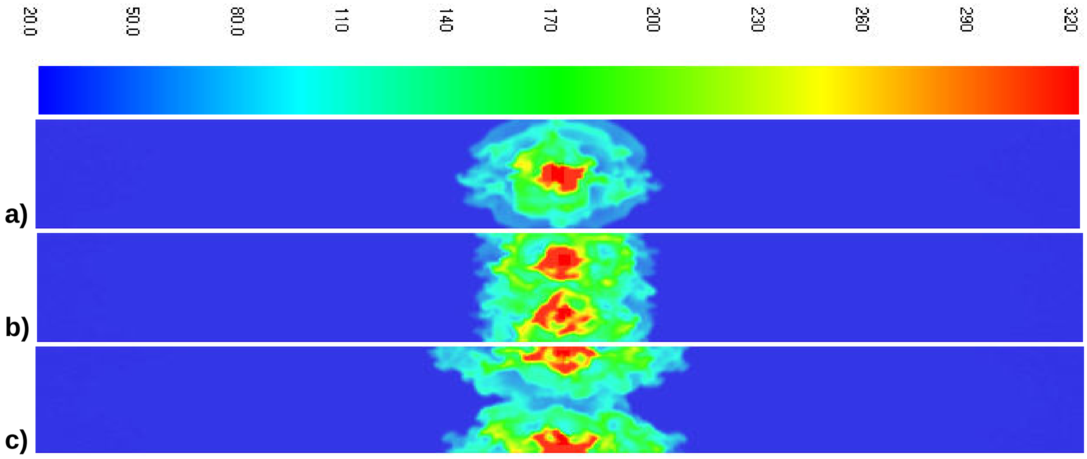

Figure 9. Temperature distribution of smoke (v = 0 m/s, t = 2 s) at d = (a) 0 m, (b) 0.4 m, and (c) 0.7 m.

In Figure 9, the temperature distribution is used to represent the smoke flow. From Figure 9 (a) to (c), when the distance between the two fires increases, the smoke length near the sidewall gradually increases and the smoke length in the centerline dwindles, thus, smoke flow is affected not only by buoyant force, but also simultaneously by the shear stress of the wall.

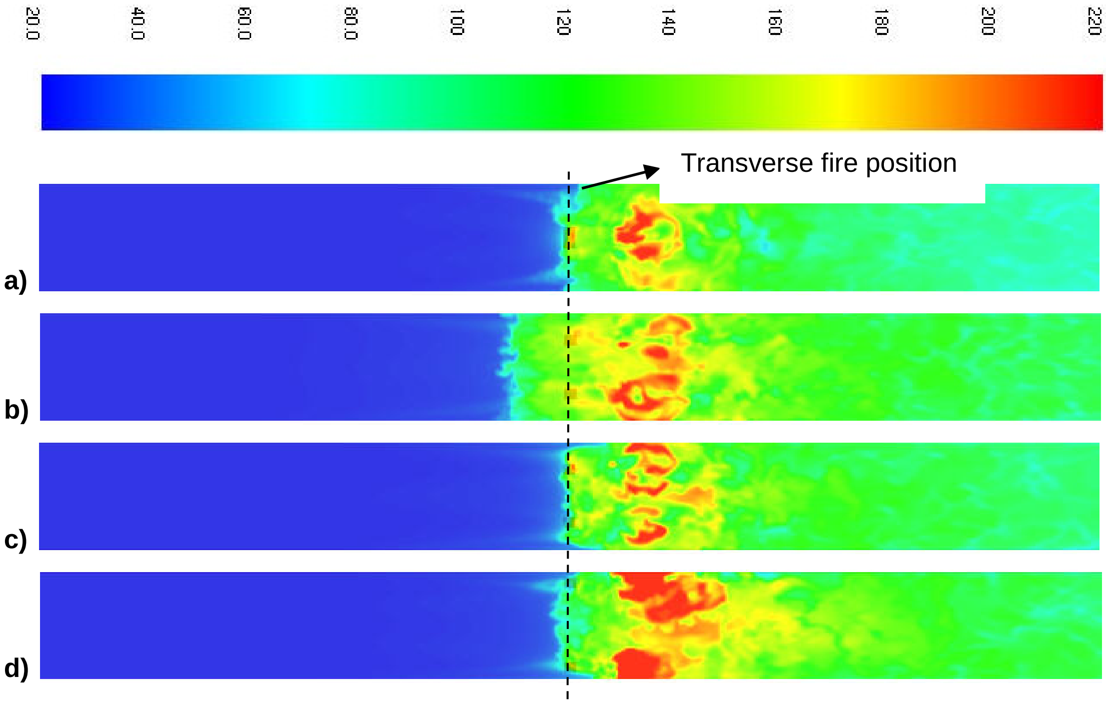

Figure 10. Temperature distribution of smoke (t = 70 s) at (a) d = 0 m, v = 0.56 m/s; (b) d = 0.4 m, v = 0.56 m/s; (c) d = 0.4 m, v = 0.60 m/s; and (d) d = 0.7 m, v = 0.56 m/s.

The temperature distributions under the quasi-stable state affected by different longitudinal ventilation velocities and different distances of double fire sources are shown in Figure 10. It is observed that the smoke back-layering length is 0 m when the longitudinal ventilation velocity is 0.56 m/s in Figures 10(a) and (d), which means that the longitudinal ventilation velocity is the critical velocity in these two conditions. However, as shown in Figure 10(b), smoke obviously lies at upstream of the fire sources under the same longitudinal velocity, but the upwind smoke is eliminated when the longitudinal ventilation velocity reaches to 0.6 m/s, so the critical velocity is not the same when the distance between double fires is different.

Table 3. Critical velocity of a single fire.

Heat release rate		Critical velocity, m/s				
		$d/2$ = 0 m	$d/2$ = 0.1 m	$d/2$ = 0.2 m	$d/2$ = 0.3 m	$d/2$ = 0.35 m
Single fire	Case (a): 3 kW	0.43	0.43	0.44	0.45	0.48
	Case (b): 6 kW	0.48	0.49	0.49	0.51	0.55
	Case (c): 7.5 kW	0.50	0.50	0.51	0.54	0.57
	Case (d): 12 kW	0.56	0.57	0.58	0.62	0.64
	24 kW	0.64	–	–	–	–

Table 4. Critical velocity of double fires.

Heat release rate		Critical velocity, m/s							
		d = 0 m	d =0.1 m	d =0.2 m	d = 0.3 m	d = 0.4 m	d = 0.5 m	d = 0.6 m	d = 0.7 m
Double fires	Case (1) : 3 + 3 kW	0.48	0.47	0.50	0.53	0.52	0.51	0.50	0.48
	Case (2) : 6 + 6 kW	0.56	0.54	0.57	0.61	0.60	0.59	0.58	0.56
	Case (3):7.5 +7.5 kW	0.59	0.57	0.60	0.63	0.62	0.61	0.60	0.59
	Case (4):12 +12 kW	0.64	0.62	0.65	0.68	0.66	0.65	0.64	0.66

As shown in Tables 3 and 4, when the heat release rate of a single fire is equal to the sum of that of adjacent double fires, the critical velocity for double fires adjacent to each other is equal to the critical velocity for the single fire. An increase of the transverse distance between the fires results in the critical velocity reaching a maximum value at d = 0.3 m. However, as two fires approach the walls, the critical velocity for which is approximately equal to that for double fires at d = 0 m. Between the case (1), case (2) and case (3), the critical velocity at d = 0.7 m is the same as that at d = 0 m. But in case (4), the critical velocity at d = 0.7 m is greater than that at d = 0 m, because the higher heat release rate, compared with other cases at d = 0.7 m, causes the interaction between the fire plumes force to still exist in the tunnel, therefore, greater inertia force is needed to overcome both the buoyant force and the shear stress of the sidewalls.

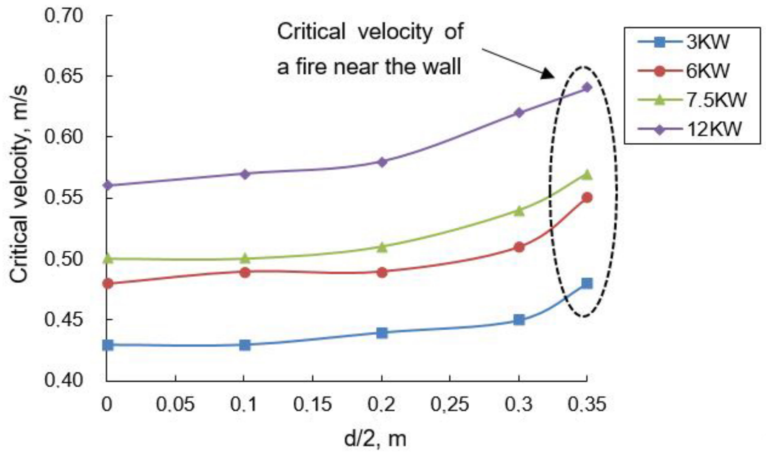

Figure 11. Critical velocity for a single fire at different locations from the tunnel center.

According to Figure 11, the critical velocity gradually grows as the distance between the single fire and the tunnel centerline increases. When the fire source is near the wall, the critical velocity increases obviously as the fire plume, limited by the wall, involves less air to result in a greater velocity for smoke front. By comparing Figures 11 and 12, it becomes apparent that the critical velocity for a single fire is obviously lower than that for double fires at d = 0, 0.4, 0.6, and 0.7 m, which suggests that the smoke movement for double fires is reinforced by both the buoyant force and the shear stress of the sidewalls in the tunnel, so a greater critical velocity is needed to prevent the upwind smoke.

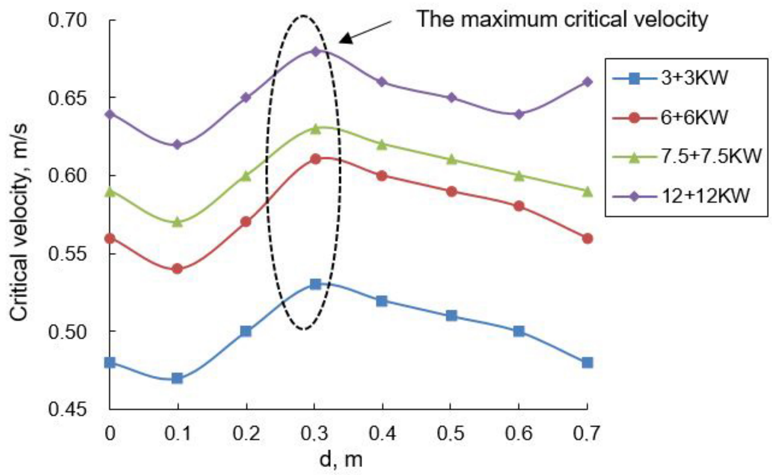

Figure 12. Critical velocity for double fires with different distances.

The simulated results show that the influence of distance between double fires on the critical velocity cannot be ignored. Therefore, the influence coefficient of distance was introduced as [21]:

$$a_i = \frac{\sum_{i=1}^{n}\left[(V^*{}_{double})_{i,j} / (V^*{}_{single})_j\right]}{n} \quad (i = 1, 2, 3, \ldots, n); \tag{9}$$

$$d^* = \frac{d}{H}; \tag{10}$$

$$V_c^* = \frac{V_c}{\sqrt{gH}}, \tag{11}$$

where $(V^*{}_{single})_j$ is the dimensionless critical velocity at d = 0 m,

$(V^*{}_{doulbe})_{i,j}$ is the dimensionless critical velocity at d > 0 m,

i is the condition with different distances between double fire sources,

j is the condition with different cases,

$d*$ represents the dimensionless distance between double fire sources.

The relationship between $(V^*{}_{doulbe})_{i,j}$ and $(V^*{}_{single})_j$ is shown in Figure 13 when the data in Tables 3 and 4 are processed by Eq. (11).

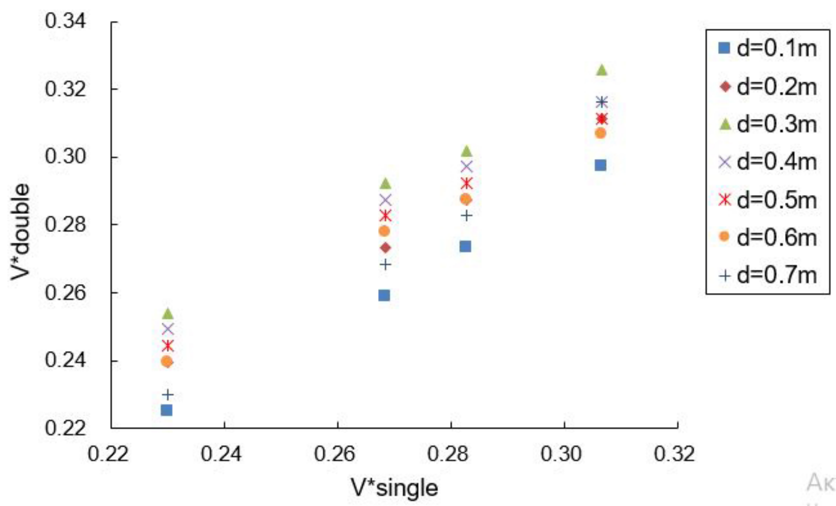

Figure 13. Comparisons of dimensionless critical velocity (d > 0 m) with dimensionless critical velocity (d = 0 m) for double fires.

Table 5. Relation between a_i and d^*.

d*	0.25	0.50	0.75	1.00	1.25	1.50	.1.75
***a**$_i$*	0.969	1.023	1.081	1.059	1.041	1.024	1.013

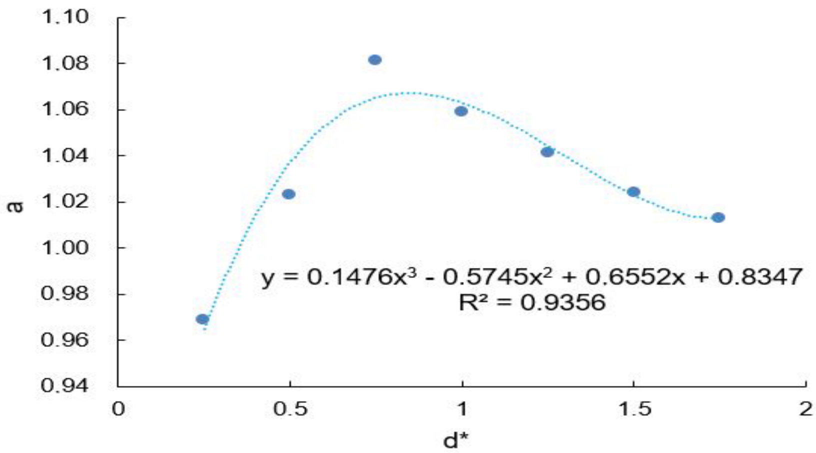

Figure 14. Relationship between the influence coefficient of distance and dimensionless distance for double fires.

The relationship between a_i and d^* is shown in Table 5 and Figure 14. It is observed that a_i increases first and then decreases with increasing d^*. The following expression between a and d^* can be obtained by data fitting:

$$a = 0.1476d^{*3} - 0.5745d^{*2} + 0.6552d^{*} + 0.8347 \tag{12}$$

and so

$$(V^*_{doulbe})_{i,j} / (V^*_{single})_j = 0.1476d^{*3} - 0.5745d^{*2} + 0.6552d^{*} + 0.8347. \tag{13}$$

In order to validate the reliability of Eq. (13), the other two cases of fire combination were simulated using FDS. The detailed comparison results between the simulation values and predicted values by Eq. (13) are shown in Figures 15 and 16, it can be seen that the difference is small and the trend is essentially identical. Figure 17 shows that the basic situation of the tunnel model with dimensions 7×0.6×0.6 m, the tunnel hydraulic height was 0.6 m, the position of the 4.5 + 4.5 kw double fires was 2.5 m from the tunnel entrance longitudinally, and the distance between the double fires increased in the lateral direction [22]. Comparison of the simulation values in reference [22] with the predicted values by Eq. (13) is shown in Figure 18.

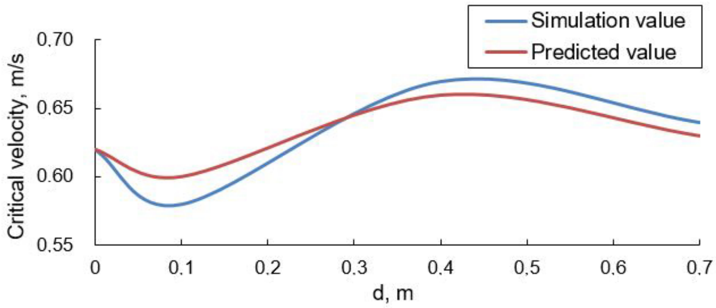

Figure 15. Critical velocity for 10 + 10 kw double fires.

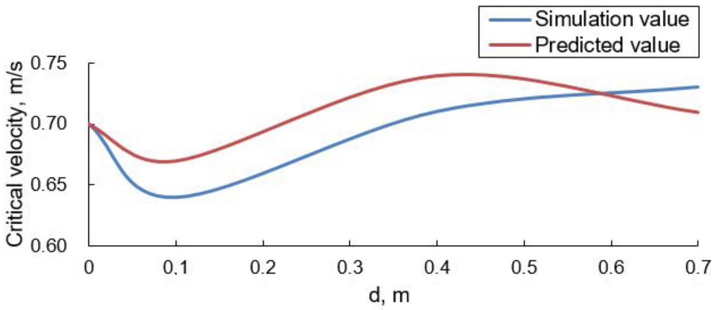

Figure 16. Critical velocity for 20 + 20 kw double fires.

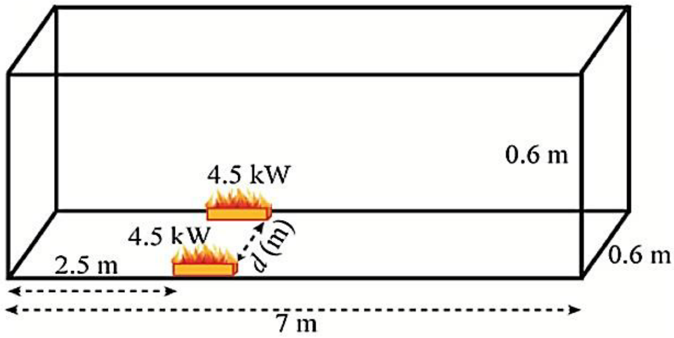

Figure 17. Diagram of the model tunnel [22].

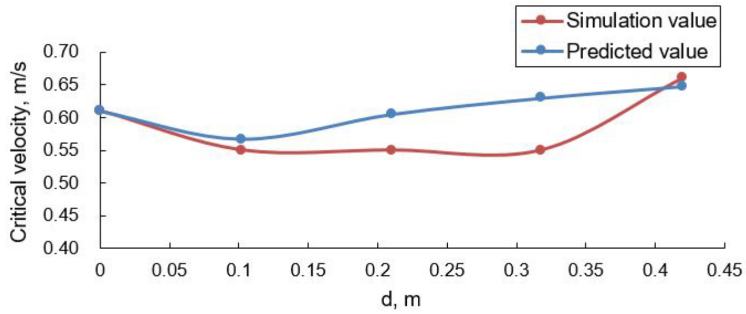

Figure 18. Comparison between the predicted values by Eq. (13) and the simulation values in reference [22].

According to Figure 18, when the double fires are away from each other, the trend of prediction values by Eq. (13) first decreases and then increases gradually, and the trend of simulation values in reference [22] first decreases, then remains constant and eventually increases, there is a clear difference between the simulation values and predicted values at d = 0.32 m, but the difference is small at the other points. The difference results from the diverse cross-section geometry and the position of the double fire sources in the longitudinal direction, in addition, the prediction model was obtained under the condition with different fire combinations and different distances between the double fires, so the prediction model in this study is considered reliable for predicting the critical velocity for double fire sources.

4. Conclusions

In this study, a numerical investigation of critical ventilation velocity for transverse double fires in a tunnel was carried out using FDS 6.6.0. The same double fire sources were placed on the floor of the tunnel center and moved horizontally to the sidewalls, and the effect of different distances of the double fires on critical velocity was analysed. The main conclusions are as follows:

(1) The smoke movement for transverse double fires is affected by both the buoyant force and the shear stress of the sidewalls in the tunnel, greater inertia force is needed to overcome both the buoyant force and the shear stress of the sidewalls, so the higher critical ventilation velocity compared with a fire is needed to prevent upwind smoke.

(2) When double fires are completely placed next to each other, the critical velocity is equal to the state that a single fire by the sum of the heat release rate of the double fires is burned in the tunnel. The critical velocity for several fire combinations reaches the maximum value at d = 0.3 m as the transverse distance between double fires increases. Nevertheless, as double fire sources become close to the sidewalls, the critical velocity is approximately equal to the critical velocity for double fires at d = 0 m.

(3) Relations between the influence coefficient of distance and the dimensionless transverse distance as well as correlations between the critical ventilation velocity with and without distances for double fires were developed. The presented correlation can provide a reference value for smoke control and personnel evacuation in case of tunnel fire.

5. Acknowledgement

This research was financially supported by the National Science and Technology Major Project of China (Grant No.2017ZX05013006). The authors are grateful to Professor Jianjun Liu for his constructive comments on this paper.

References

1. Vvedenskij, V.R., Gendler, S.G., Titova, T.S. Environmental impact of the tunnel construction. Magazine of Civil Engineering. 2018. No. 3. Pp. 140–149. DOI: 10.18720/MCE.79.15

2. Zhao, S., Liu, F., Wang, F., et al. A numerical study on smoke movement in a metro tunnel with a non-axisymmetric cross-section. Tunnelling and Underground Space Technology. 2018. Vol. 73. Pp. 187–202.
3. Li, Y.Z., Ingason, H. Effect of cross section on critical velocity in longitudinally ventilated tunnel fires. Fire Safety Journal, 2017.
4. Heselden, A., Hinkley, P. Smoke Travel in Shopping Malls Experiments in Co-Operation with Glasgow Fire Brigade–Part 1. Joint Fire Research Organization, Fire Research Note, 1970. Pp. 832.
5. Thomas, P.H. The Movement of Smoke in Horizontal Passages against Air Flow. Fire Research Technical Paper. 1963. Vol. 7. No. 1. Pp. 1–8.
6. Oka, Y., Atkinson, G.T. Control of smoke flow in tunnel fires. Fire Safety Journal, 1995. Vol. 25. No. 4. Pp. 305–322.
7. Wu, Y., Bakar M.Z.A. Control of smoke flow in tunnel fires using longitudinal ventilation systems – a study of the critical velocity. Fire Safety Journal, 2000. Vol. 35. No. 4. Pp. 363–390.
8. Li, Y.Z., Lei, B., Ingason, H. Study of critical velocity and backlayering length in longitudinally ventilated tunnel fires. Fire Safety Journal, 2010. Vol. 45. No. 6. Pp. 361–370.
9. Lee, Y.P., Tsai, K.C. Effect of vehicular blockage on critical ventilation velocity and tunnel fire behavior in longitudinally ventilated tunnels. Fire Safety Journal. 2012. Vol. 53. No. 10. Pp. 35-42.
10. Tang, W., Hu, L.H., Chen, L.F. Effect of blockage-fire distance on buoyancy driven back-layering length and critical velocity in a tunnel: An experimental investigation and global correlations. Applied Thermal Engineering. 2013. Vol. 60. No. 1-2. Pp. 7–14.
11. Gannouni, S., Maad, R.B. Numerical study of the effect of blockage on critical velocity and backlayering length in longitudinally ventilated tunnel fires. Tunnelling and Underground Space Technology. 2015. Vol. 48. Pp. 147–155.
12. Alva, W.U.R., Jomaas, G., Dederichs, A. The influence of vehicular obstacles on longitudinal ventilation control in tunnel fires. Fire Safety Journal. 2017. Vol. 87. Pp. 25–36.
13. Chow, W.K., Gao, Y., Zhao, J.H., et al. Smoke movement in tilted tunnel fires with longitudinal ventilation. Fire Safety Journal. 2015. Vol. 75. Pp. 14–22.
14. Yi, L., Xu, Q., Xu, Z., et al. An experimental study on critical velocity in sloping tunnel with longitudinal ventilation under fire. Tunnelling and Underground Space Technology. 2014. Vol. 43. Pp. 198–203.
15. Hu, L.H., Peng, W., Huo, R. Critical wind velocity for arresting upwind gas and smoke dispersion induced by near-wall fire in a road tunnel. Journal of Hazardous Materials. 2008. Vol. 150. No. 1. Pp. 68–75.
16. Zhong, W., Duanmu, W., Wang, T., et al. A Study of the Critical Velocity of Smoke Bifurcation Flow in Tunnel with Longitudinal Ventilation. Fire Technology. 2016. Vol. 53. No. 2. Pp. 1–19.
17. Wang, F., Wang, M. A computational study on effects of fire location on smoke movement in a road tunnel. Tunnelling & Underground Space Technology Incorporating Trenchless Technology Research. 2016. Vol. 51. Pp. 405–413.
18. McGrattan, K., Hostikka, S., McDermott, R., Floyd, J., Weinschenk, C., Overholt, K. Fire Dynamics Simulator Users' Guide (Version 6), NIST, Gaithersburg, MD, 2013a.
19. McGrattan, K., Hostikka, S., McDermott, R., Floyd, J., Weinschenk, C., Overholt, K. Fire Dynamics Simulator Technical Guide (Version 6), NIST, Gaithersburg, MD. 2013b.
20. Zadeh, S.E., Beji, T., Merci, B. Assessement of FDS 6 Simulation Results for a Large-Scale Ethanol Pool Fire. Combustion Science and Technology. 2016. Vol. 188. No. 4-5. Pp. 10.
21. Wei, Cun-xiang. Numerical simulation study on smoke exhaust effect of subway tunnel under multi-source fires. Safety engineering Institute, 2017.
22. Heidarinejad, G., Mapar, M., Pasdarshahri, H. A comprehensive study of two fire sources in a road tunnel: Considering different arrangement of obstacles. Tunnelling and Underground Space Technology. 2016. Vol. 59. Pp. 91–99.

Contacts:

Qiuyi Zhang, 0086+15228969340; luomusanchang@qq.com
Guihong Pei, 0086+15281073766; 570769297@qq.com

Magazine of Civil Engineering. 2019. 85(1). Pp. 51–58
Инженерно-строительный журнал. 2019. № 1(85). С. 51–58

Magazine of Civil Engineering

ISSN 2071-0305

journal homepage: http://engstroy.spbstu.ru/

DOI: 10.18720/MCE.85.5

The periodic temperature oscillations in a cylindrical profile with a large thickness

O.D. Samarin,
National Research Moscow State University of Civil Engineering, Moscow, Russia
E-mail: samarin-oleg@mail.ru

Keywords: hollow cylinder; thermal conductivity equation; Hankel function; finite-difference scheme; temperature wave; cylindrical symmetry; damping coefficient; civil engineering; building; construction industry

Abstract. A hollow cylinder with thick walls is one of the most complex objects to calculate the unsteady temperature field, so this field is the least studied. However, such objects are found in many modern constructions of systems of generation and distribution of heat. In the proposed work it deals with the study of propagation of temperature waves in the wall of the hollow cylinder with harmonic temperature change of external environment arising from its diurnal fluctuations. The approximate analytical solution is presented by separation of variables in the complex domain with the use of cylindrical functions. The algorithm of calculation of temperature fields numerically is shown using an explicit finite-difference scheme of high accuracy in conditions of cylindrical symmetry with boundary conditions of the first kind. The results of calculations according to the considered algorithm, depending on the time since the start of heat exposure and their comparison with the analytic solution are given for its implementation. Calculated radial profiles of the temperature in the cylindrical wall within the temperature waves and the analytical approximation relations for the description of its damping coefficient are presented. The results are compared with the existing analytical solution in rectangular coordinates and it is marked that they have some differences but the common results are found regardless of the material and geometry of the cylinder, as well as of temperatures of inner and outer environment. Presented dependences are invited to apply for the analytical evaluation of the temperature amplitude on the inner surface of the heated cylindrical structures that will allow the use of engineering methods to verify compliance with industrial safety requirements.

1. Introduction

In this article, an unsteady temperature profile of a hollow thick wall cylinder under periodic thermal influence is studied.

The problem of unsteady thermal conductivity in bodies of various geometric forms is studied for a long time. Moreover, currently, due to achievements of computational equipment, numerical methods of solving the problem are more attractive. Nevertheless, in most cases, they are either related to a single dimension case or consideration is done in rectangular coordinates. This rather corresponds to the most really existing problems in both unsteady and steady modes [1–2]. Under the condition of cylindrical symmetry, heating and cooling of solid hollow cylinders are the most developed issues [1].

Over the last years a number of researches, where such issues are studied in both analytic and numerical ways, is emerged. However, the results obtained by the authors are either very difficult for use in engineering practice [3, 4, 9, 14, 17] or too rough, contrary [11]. The other solution variants are related to specific types of constructions used in limited areas and functioning in super critical modes [8], in nuclear power industry [13] or composite material production [5–7, 10], as well as in case of phase transitions [12], [15, 16, 18] or fuel combustion [19], or for underground pipes [20].

Samarin, O.D. The periodic temperature oscillations in a cylindrical profile with a large thickness. Magazine of Civil Engineering. 2019. 85(1). Pp. 51–58. DOI: 10.18720/MCE.85.5.

Самарин О.Д. Периодические температурные колебания в цилиндрическом слое при большой толщине стенки // Инженерно-строительный журнал. 2019. № 1(85). С. 51–58. DOI: 10.18720/MCE.85.5

In the same time, the calculation of an unsteady temperature profile of thick walled hollow cylinders, including a periodic mode, is interesting. For instance, this can be useful for solving the problem of condensate formation either on the internal surface of fume stacks or on the external surface of thermal pipe insulation with daily fluctuation of ambient air temperature and heat carrier temperature. This is especially interesting for open-laid pipelines of heating systems with a significant moisture content of the outside air, which happens at a temperature close to zero and above, when it may be necessary to assess the conditions of freezing and thawing of atmospheric moisture and snow. In addition, such a calculation is needed to confirm the absence of condensation on the inner surface of the air ducts of exhaust ventilation systems with their outer gasket, which in some cases is allowed in case of structural necessity with the condition of their thermal insulation. The same applies to the outer surface of the air intake ducts, when they are laid as an exception inside the building, also in a heat-insulated form. Finally, the considered calculation may be required to assess the temperature fluctuations on the outer surface of cylindrical furnaces with changes in their operation mode in order to solve the question of the admissibility of this temperature for sanitary and hygienic requirements. The author of the published paper [21] has obtained a simple solution for thick walled cylinder cooling. However, the solution is related only to aperiodic mode conditions, whereas an analytic solution, but for a small diameter linear source is given in the paper [22]. Therefore, the relevance of the proposed research is in the necessity to search the precise and physically well-reasoned (in the same time acceptable for engineering usage) dependences of temperature alteration in periodically heated/ cooled cylindrical structures. Obtained results may be acceptable for a large number of energetic facilities of such structure.

The calculation of a temperature profile at harmonic fluctuations of ambient temperature near the external surface of a cylinder is the research purpose. Research tasks are as follows:

– building up an analytical solution for an equation of thermal conductivity in the cylinder wall for a regular mode;

– development of an algorithm, which implements finite-difference approximation of the equation;

– obtaining analytic dependences for temperature across cylinder cross section and temperature wave amplitude by results of correlating the theoretical results with software generation data.

2. Methods

Figure 1 shows a diagram of studied cylinder and some conventional symbols used further. The main of them are r_0 and r_1, i.e. the external and internal radii of a cylinder, m, respectively.

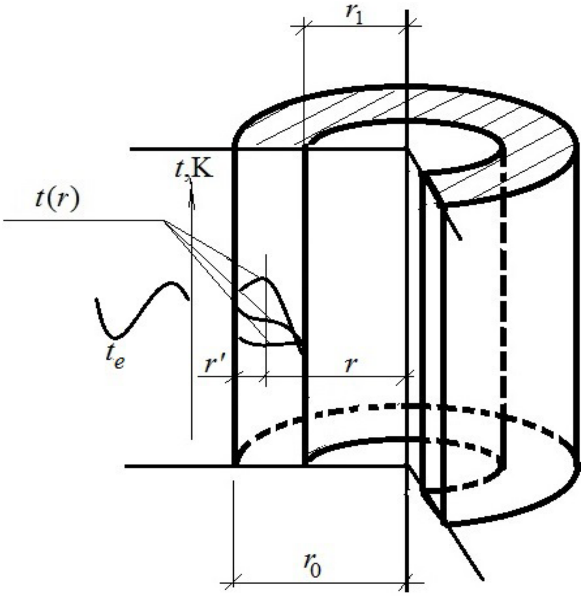

Figure 1. A diagram of a hollow cylinder and unsteady temperature profile in its wall.

Then a differential equation of unsteady heat conductivity for the cylindrical symmetry case may be written in the following way [1–2]:

$$\frac{\partial t}{\partial \tau} = a\left[\frac{\partial t}{r\partial r} + \frac{\partial^2 t}{\partial r^2}\right], \tag{1}$$

where $a = \dfrac{\lambda}{c\rho}$ – coefficient of cylinder body material heat conductivity, m^2/s;

λ is its thermal conductivity, W/(m·K);

c and ρ are specific heat capacity, J/(kg·K), and density, kg/m^3, respectively. The solution in this case will show a current temperature profile in the temperature wave distribution zone.

The boundary condition on the cylinder external surface for a periodic mode in the complex view of the harmonic oscillation simplest case may be written as follows:

$$t = A_{te}\exp(-i\omega\tau), \tag{2}$$

where A_{te} is oscillation amplitude of ambient air temperature t_e, K;

$\omega = 2\pi/T$ is wave circular frequency of t_e, s^{-1}. Here T is oscillation period, s. As the initial condition we may adopt $t(r) = 0$, considering an average period value $t_{e.av} = 0$, and, if it is not, we shall consider excessive temperature $\theta = t(r) - t_{e.av}$. Therefore, we adopt conditions of 1-st type, and in case of known heat exchange intensity on the surfaces, in first approximation it is possible to introduce additional layers with thickness equal to $\Delta r_{cond} = \lambda/\alpha$, where α – full heat exchange coefficient, W/(m^2·K), at a corresponding side.

Then we may search for solution of equation (1) by the method of dividing the variables as the production of cofactors depending respectively only on τ and r:

$$t = \exp(-i\omega\tau)\varphi(r'), \tag{3}$$

where $r' = r_0 - r$ is radial coordinate, with respect to the fact that a temperature wave distributes from outsides (see Figure 1). After substituting in (1) we obtained a regular differential equation for φ:

$$r'\frac{\partial^2\varphi}{\partial r'^2} + \frac{\partial\varphi}{\partial r'} + \frac{i\omega r'}{a}\varphi = 0. \tag{4}$$

Such equation is Bessel's equation in the complex area. The equation may be solved by Hankel cylindrical function of zero order first type $H_0^{(1)}$ [1] under applied boundary and initial conditions. The final shape of the function t may be found by substitution into (3):

$$t = A_{te}\exp(-i\omega\tau)H_0^{(1)}\left(r'\sqrt{\frac{i\omega}{a}}\right), \tag{5}$$

Through selecting a real component and using the known asymptotic approximation of the function $H_0^{(1)}$ at sufficiently large values of the argument, which may be used, since we are interested in the established oscillation process, we finally find:

$$\mathrm{Re}(t) = A_{te}\cdot 2\sqrt{\frac{1}{\pi r'}\sqrt{\frac{a}{\omega}}}\cos\left(\omega\tau - r'\sqrt{\frac{\omega}{2a}} + \frac{\pi}{n}\right)\exp\left(-r'\sqrt{\frac{\omega}{2a}}\right). \tag{6}$$

Therefore, unlike temperature waves in a flat wall, for a cylindrical wall it is more likely to have rapid decrease of amplitude as depth increases: not only due to the exponential factor, but also in a proportional way $1/\sqrt{r'}$. In this case, there is an additional shift of a phase in relation to oscillations t_e expressed by cosine argument summand equal to π/n. The theoretical value of the parameter n makes 1/8, however, taking into account the approximated character of the dependency (6), it is reasonable to clarify it through comparing with numeric calculation data based on the finite-differential approximation of the equation (1).

Since we need the obtained result precision, whereas used memory volume and quantity of made operations are not significant due to high computational resources of modern computers, a finite-differential diagram will be the most favorable due to its programming simplicity. Then a temperature value in i-n grid node at j+1-n time moment may be calculated according to the following expression:

$$t_{i,j+1} = Fo_\Delta\left(\frac{2i-1}{2i-2}t_{i+1,j} + \left(\frac{1}{Fo_\Delta} - 2\right)t_{i,j} + \frac{2i-3}{2i-2}t_{i-1,j}\right). \tag{7}$$

Here $t_{i,j}$, $t_{i-1,j}$ and $t_{i+1,j}$ are temperature values at *j*-n time moment in *i*-n node and two adjoining nodes on the right and left (node numbering from the cylinder axis to the external surface side); $Fo_\Delta = \frac{a\Delta\tau}{(\Delta r)^2}$ is dimensionless local Fourier criterion, where $\Delta\tau$, s and Δr, m is respectively, time and coordinate steps representing parameters of finite-differential diagram. As it is known [1–2], the adopted diagram converges at $Fo_\Delta \le 1/2$. In this case, the value $Fo_\Delta = 1/6$, providing high precision of 4-th order approximation by a space coordinate and 2-nd order approximation by a time coordinate, was chosen.

3. Results and discussion

Calculation results according to the formula (6) and author provided software in *Fortran* language according to the diagram (7) for $A_{te} = 1$ K, $r_0 = 1$ m, $a = 5.1 \cdot 10^{-7}$ m²/s and $\omega = 2\pi/86400 = 7.27 \cdot 10^{-5}$ s^{-1}, i.e. with daily oscillation period are given in Figure 2. On the internal radius $r_1 = 0.5$ m, temperature was kept constant.

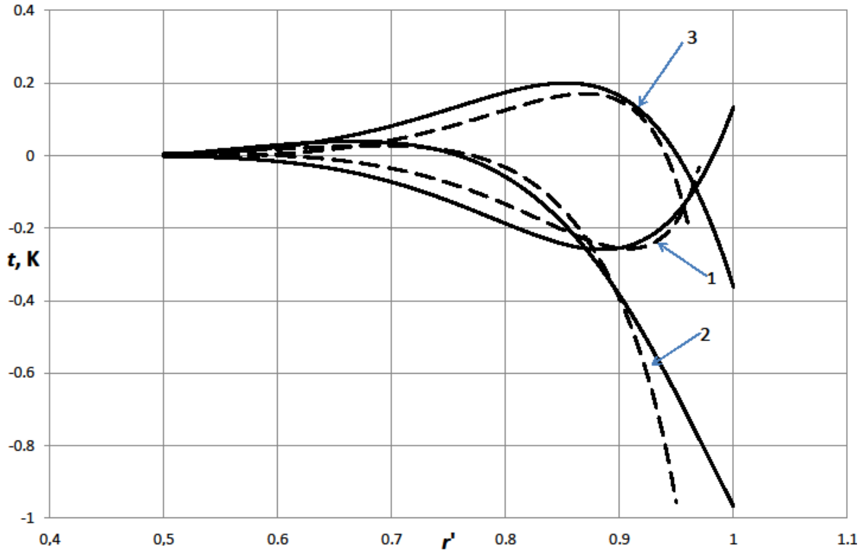

Figure 2. Temperature alteration along the cylinder radius (continuous lines – numeric calculation, dotted lines – according to the formula (6)); 1 – $\omega\tau$ = 23.7; 2 – $\omega\tau$ = 47.4; 3 – $\omega\tau$ = 71.1.

In this case, for maximal matching it is necessary to adopt the value $n = 32$, i.e. real additional phase shift at cylindrical symmetry is very insignificant. It is clear, that in general, correctness of the relation (6) is confirmed, except $r' < 0.05$. It is true that the function approximation $H_0^{(1)}$ used in the conclusion (6) poorly works in this area, however for the considered problem it is meaningless, since in most cases a value of the relation $\Delta r_{cond}/r_0$, showing relative radius of the additional external cylindrical layer with considered external heat exchange is more than 0.05 or, at least, equal to 0.05.

Since in practical problems, temperature fluctuation amplitude is interesting, it is possible to introduce its attenuation coefficient $\nu_r = A_{te}/A_t$, which may be associated with thermal inertia of a cylindrical layer D_r in the same way as in the single dimension problem. From (6) the following expression may be obtained for it:

$$\nu_r = \frac{\sqrt{\pi D_r}\,\exp\left(D_r/\sqrt{2}\right)}{2}, \text{ where } D_r = r'\sqrt{\frac{\omega}{a}}. \qquad (8)$$

It is not hard to see that the obtained dependency differs from the single dimension case [2] only by the additional factor $\frac{\sqrt{\pi D_r}}{2}$. It is clear that at $D_r > 4/\pi \approx 1.26$ this factor is more than 1, therefore damping in a cylindrical layer is really more significant. In the considered example for the entire cylinder $D_r = (1-0.5)\sqrt{\frac{7.27 \cdot 10^{-5}}{5.1 \cdot 10^{-7}}} = 5.965$, then $\nu_r = 147$, or 2.16 times more than for a flat wall with the same heat inertia. For illustrative purpose, the ratio between damping coefficients for a flat and cylindrical layers shown in Figure 3.

Since the ratio (8) is written in a dimensionless form, it is common, and having no dependency on actual air temperature values, cylinder radius, cylinder wall material, and the ratio r_1/r_0, at least at $r_1/r_0 > 0.5$, for which numeric calculations are done.

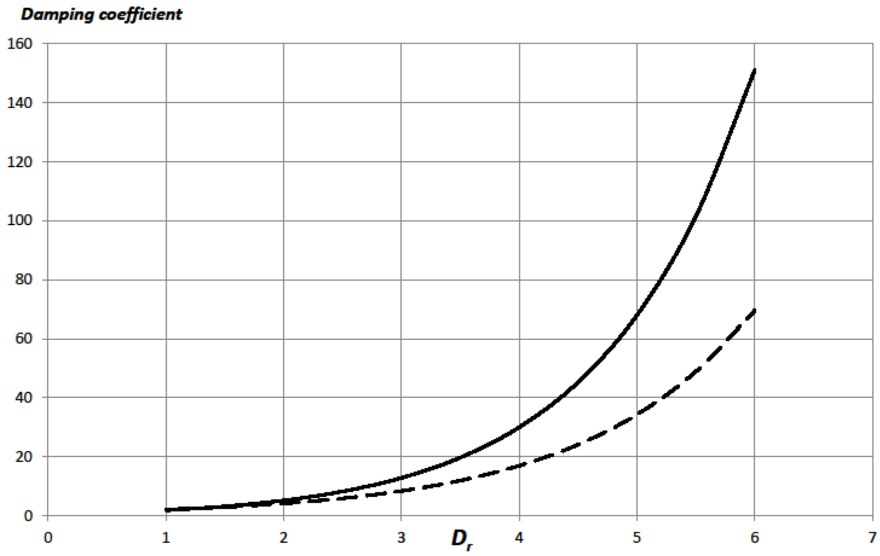

Figure 3. The dependence of the heat wave damping coefficient on heat inertia for a flat wall (dotted line) and cylindrical profile.

The results are principally matched with the data given in [2] for a flat wall with precision down to a factor $\frac{\sqrt{\pi D_r}}{2}$. Besides, a general form of calculated temperature profiles corresponds to results of some other authors, for instance, [15], whereas their analytical description discovers similarities in theoretical solutions of other sources, in particular, [13], [14].

To illustrate the practical use of the ratio (8), we calculate the temperature fluctuations in the insulation layer of an open air duct with the parameters r_1 = 0.25 m, r_0 = 0.35 m, i.e. with the insulation thickness of 100 mm, with the amplitude of the outdoor air temperature fluctuations A_{te} = 2.7 °C for the average conditions of the heating season. In this case the condition $r_1/r_0 > 0.5$ is satisfied. For thermal insulation of mineral wool λ = 0.044 W/(m·K), c = 840 J/(kg·K), ρ = 50 kg/m^3, so $a = 1.05 \cdot 10^{-6}$ m^2/s. Since we are primarily interested in the temperature on the inner surface of the air duct $t(r_1)$ from the point of view of assessing the possibility of condensation of water vapor, then $r' = r_0 - r_1$ = 0.1 m; and when the daily period of oscillations according to the formula (8) D_r = 0.83, where ν_r = 1.45, and therefore the oscillation amplitude of the fluctuations of $t(r_1)$ is equal to A_{te}/ν_r = 2.7/1.45 = 1.86 °C. This means that when checking the adequacy of the adopted thickness of the insulation will need to take into account that the minimum during the day the value of $t(r_1)$ will be below the average of 1.86 degrees.

4. Conclusion

– It is noted that temperature wave distribution is controlled by the same laws as in the single dimension case, but with a slightly different attenuation coefficient and phase shift.

– It is proved that unlike temperature waves in a flat wall, for a cylindrical wall it is more likely to have rapid decrease of amplitude as depth increases: not only due to the exponential factor, but also in reverse proportion to square root of a radial coordinate.

– It is shown that a real additional phase shift of temperature fluctuation at cylindrical symmetry in comparison with the single dimension case is very insignificant and equals to 1/32 of a period.

– It is shown that the ratio of the internal and external radii of a hollow cylinder does not explicitly influences on the temperature profile character in the temperature wave zone, at least, at $r_0/R > 0.5$.

– It is shown that temperature field distribution in the zone of temperature wave penetration into the cylinder, according to results of analytic and numeric solutions, coincides within engineering calculation limits, which means that the obtained dependences are correct.

–It is proposed to apply the ratios obtained in the research for analytic evaluation of temperature fluctuation amplitude on cylindrical surfaces of heated and cooled structures. It is necessary, first of all, to solve the problem of condensate formation on the internal surface of fume stacks in case of boiler unit load fluctuation or on the external surface of heat line insulation as well as on the surfaces of the open-laid heat-insulated air ducts in case of daily ambient temperature alteration and on the outer surface of cylindrical furnaces in variable operating modes. It will allow to use not only software methods, but also engineering methods to check meeting the industrial safety requirements.

References

1. Carslaw, H.S., Jaeger, J.C. Conduction of heat in solids. Oxford University Press, USA, 1986. 520 p.
2. Fokin, K.F. Stroitel'naya teplotekhnika ograzhdayushchikh chastey zdaniya [Thermal physics of building envelopes]. Under ed. of Yu.A. Tabunshchikov and V.G. Gagarin. 5th ed., revised. Moscow : AVOK-PRESS Publishers, 2006. 256 p. (rus)
3. Shokouhmand, H., Ghaffari, S. Investigation of cooling process of a high-temperature hollow cylinder in moving induction heat treatment. Journal of Thermal Science and Engineering Applications. 2012. Vol. 4. No. 1. Pp. 011002.
4. Kalynyak, B.M. Fredholm equations of the second kind for radial stresses aimed at the determination of the thermoelastic state of an inhomogeneous hollow long cylinder. Journal of Mathematical Sciences. 2015. Vol. 205. No. 5. Pp. 659–666.
5. Norouzi, M., Birjandi, A.K., Rahmani, H., Joneidi, A.A. A general exact analytical solution for anisotropic non-axisymmetric heat conduction in composite cylindrical shells. International Journal of Heat and Mass Transfer. 2016. Vol. 93. Pp. 41–56.
6. Norouzi, M., Shariati, M., Rezaei Niya, S.M., Karimi Demneh, M., Naghavi, M.S., Kayhani, M.H. Exact solution of unsteady conductive heat transfer in cylindrical composite laminates. Journal of Heat Transfer. 2012. Vol. 134. No. 10. Pp. 101301.
7. Shevchuk, V.A. Nonstationary one-dimensional problem of heat conduction for a cylinder with a thin multi-layer coating. Journal of Mathematical Sciences. 2012. Vol. 184. No. 2. Pp. 215–223.
8. Brunner, G. Heat transfer. Supercritical fluid science and technology. 2014. No. 5. Pp. 228–263.
9. Horikiri, K., Yao, Y., Yao, J. Modelling conjugate flow and heat transfer in a ventilated room for indoor thermal comfort assessment. Building and Environment. 2014. No. 77. Pp. 135–147.
10. Yun, T.S., Jeong, Y.J., Han, T.-S., Youm, K.-S. Evaluation of thermal conductivity for thermally insulated concretes. Energy and Buildings. 2013. No. 61. Pp. 125–132.
11. Gabrielaitiene, I. Numerical simulation of a district heating system with emphases on transient temperature behavior. Proceedings of the 8th International Conference «Environmental Engineering». Vilnius: VGTU Publishers. 2011. Vol. 2. Pp. 747–754.
12. Vasilyev, G.P., Gornov, V.F., Konstantinov, P.I., Kolesova, M.V., Korneva, I.A. Analysis of ground temperature variations, on the basis of years-long measurements. Magazine of Civil Engineering. 2017. 72(4). Pp. 62–72. DOI: 10.18720/MCE.72.8.
13. Loginov, V.S., Parpiev, A.T. Nestacionarnye temperaturnye rezhimy pologo cilindricheskogo aktivnogo elementa i paroperegrevatelya v parogeneratore [Non-stationary thermal regimes of the hollow cylindrical active element and the vapor superheater in the vapor generator]. Herald of the Sholom-Aleihem Amur State Univ. 2013. No. 2(13). Pp. 90–97 [Online]. URL: https://elibrary.ru/download/elibrary_21298568_86404092.pdf (date of treatment: 23.11.18). (rus)
14. Eliseev, V.N., Tovstonog, V.A., Borovkova, T.V. Algoritm resheniya obobshchennoy zadachi nestacionar-noy teploprovodnosti [Solution Algorithm of Generalized Non-Stationary Heat Conduction Problem in the Bodies of Simple Geometric Shapes]. Herald of the Bauman Moscow State Tech. Univ., Mech. Eng. 2017. No. 1. Pp. 112–128 [Online]. URL: https://elibrary.ru/download/elibrary_28415996_48648202.pdf (date of treatment: 23.11.18). (rus)
15. Vasilyev, G.P., Gornov, V.F., Peskov, N.V., Popov, M.P., Kolesova, M.V., Yurchenko, V.A. Ground moisture phase transitions: Accounting in BHE'S design. Magazine of Civil Engineering. 2017. 74(6). Pp. 102–117. DOI: 10.18720/MCE.74.9
16. Parfentyeva, N., Valancius, K., Samarin, O., Paulauskaite, S., Ciuprinskine J. Solving the problem of pipeline freezing with respect to external heat exchange. Mechanika. 2015. Vol. 21 (5). Pp. 393–396.
17. Liu, C.-S. An integral equation method to recover non-additive and non-separable heat source without initial temperature. International Journal of Heat and Mass Transfer. 2016. Vol. 97. Pp. 943–953.
18. Bahadori, A., Vuthaluru, H.B. Simple method for estimation of unsteady state conduction heat flow with variable surface temperature in slabs and spheres. International Journal of Heat and Mass Transfer. 2010. Vol. 53. Pp. 4536–4542.
19. Li, Y., Kong, S.-C. Coupling conjugate heat transfer with in-cylinder combustion modeling for engine simulation. International Journal of Heat and Mass Transfer. 2011. Vol. add.
20. Bouhacina, B., Saim, R., Oztop, H.F. Numerical investigation of a novel tube design for the geothermal borehole heat exchanger. Applied Thermal Engineering. 2015. No. 79. Pp. 153–162.
21. Samarin, O.D. The temperature waves motion in hollow thick-walled cylinder. Magazine of Civil Engineering. 2018. 78(2). Pp. 161–168. DOI: 10.18720/MCE.78.13
22. Podledneva, N.A., Krasnov, V.A., Magomadov, R.S. Opredeleniye koefficientov teploprovodnosti i tem-peraturoprovodnosti za odin opyt metodom lineynogo istochnika teploty postoyannoy moshchnosti [De-termination of coefficients of heat conductivity and heat diffusivity for one experience by a method of a linear source of heat of constant power]. Herald of Astrakhan State Technical University. 2013. No 2. Pp. 50–55 [Online]. URL: https://elibrary.ru/download/elibrary_20859905_11088693.pdf (date of treatment: 23.11.18). (rus)

Contacts:

Oleg Samarin, +7(916)107-77-01; samarin-oleg@mail.ru

Magazine of Civil Engineering

ISSN 2071-0305

journal homepage: http://engstroy.spbstu.ru/

DOI: 10.18720/MCE.85.5

Периодические температурные колебания в цилиндрическом слое при большой толщине стенки

О.Д. Самарин,
Федеральное государственное бюджетное образовательное учреждение высшего образования «Национальный исследовательский Московский государственный строительный университет», Москва, Россия
E-mail: samarin-oleg@mail.ru

Ключевые слова: полый цилиндр; уравнение теплопроводности; функция Ханкеля; конечно-разностная схема; цилиндрическая симметрия; коэффициент затухания; гражданское строительство; здание; строительная индустрия

Аннотация. Полый цилиндр с толстыми стенками является одним из наиболее сложных объектов для расчета нестационарного температурного поля, поэтому такое поле является наименее изученным. Вместе с тем подобные объекты встречаются во многих современных конструкциях систем генерации и распределения теплоты. В предлагаемой работе рассматривается исследование распространения температурной волны в стенке полого цилиндра при гармоническом изменении температуры наружной среды, возникающем при ее суточных колебаниях. Представлено приближенное аналитическое решение задачи методом разделения переменных в комплексной области с использованием цилиндрических функций. Показан алгоритм расчета температурного поля численным методом с помощью явной конечно-разностной схемы повышенной точности в условиях цилиндрической симметрии при граничных условиях первого рода. Приведены результаты вычислений по рассмотренному алгоритму в зависимости от времени с момента начала теплового воздействия и их сопоставление с аналитическим решением для осуществления его идентификации. Представлены рассчитанные радиальные профили температуры в стенке цилиндра в пределах температурной волны и предложены аналитические зависимости для коэффициента ее затухания. Полученные результаты сопоставлены с имеющимся аналитическим решением в прямоугольных координатах и отмечены их различия, а также общность найденных результатов независимо от материала и геометрии цилиндра, а также температур внутренней и наружной среды. Представленные зависимости предложено применять для аналитической оценки амплитуды колебаний температуры на внутренней поверхности цилиндрических нагреваемых конструкций, что позволит использовать инженерные методы проверки выполнения требований промышленной безопасности.

Литература

1. Carslaw H.S., Jaeger J.C. Conduction of heat in solids. Oxford University Press, USA, 1986. 520 p.
2. Фокин К. Ф. Строительная теплотехника ограждающих частей здания. / Под ред. Ю.А. Табунщикова, В.Г. Гагарина. 5-е изд., пересмотр. М.: АВОК-ПРЕСС, 2006. 256 с.
3. Shokouhmand H., Ghaffari S. Investigation of cooling process of a high-temperature hollow cylinder in moving induction heat treatment // Journal of Thermal Science and Engineering Applications. 2012. Vol. 4. No. 1. Pp. 011002.
4. Kalynyak B.M. Fredholm equations of the second kind for radial stresses aimed at the determination of the thermoelastic state of an inhomogeneous hollow long cylinder // Journal of Mathematical Sciences. 2015. Vol. 205. No. 5. Pp. 659–666.
5. Norouzi M., Birjandi A.K., Rahmani H., Joneidi A.A. A general exact analytical solution for anisotropic non-axisymetric heat conduction in composite cylindrical shells // International Journal of Heat and Mass Transfer. 2016. Vol. 93. Pp. 41–56.
6. Norouzi M., Shariati M., Rezaei Niya S.M., Karimi Demneh M., Naghavi M.S., Kayhani M.H. Exact solution of unsteady conductive heat transfer in cylindrical composite laminates // Journal of Heat Transfer. 2012. Vol. 134. No. 10. Pp. 101301.
7. Shevchuk V.A. Nonstationary one-dimensional problem of heat conduction for a cylinder with a thin multi-layer coating // Journal of Mathematical Sciences. 2012. Vol. 184. No. 2. Pp. 215–223.
8. Brunner G. Heat transfer // Supercritical fluid science and technology. 2014. No. 5. Pp. 228–263.
9. Horikiri K., Yao Y., Yao J. Modelling conjugate flow and heat transfer in a ventilated room for indoor thermal comfort assessment // Building and Environment. 2014. No. 77. Pp. 135–147.

10. Yun T.S., Jeong Y.J., Han T.-S., Youm K.-S. Evaluation of thermal conductivity for thermally insulated concretes // Energy and Buildings. 2013. No. 61. Pp. 125–132.
11. Gabrielaitiene I. Numerical simulation of a district heating system with emphases on transient temperature behavior // Proceedings of the 8th International Conference «Environmental Engineering». Vilnius: VGTU Publishers. 2011. Vol. 2. Pp. 747–754.
12. Васильев Г.П., Горнов В.Ф., Константинов П.И., Колесова М.В., Корнева И.А. Анализ изменения температуры грунта на основе многолетних измерений // Инженерно-строительный журнал. 2017. № 4(72). С. 62–72. DOI: 10.18720/MCE.72.8.
13. Логинов В.С., Парпиев А.Т. Нестационарные температурные режимы полого цилиндрического активного элемента и пароперегревателя в парогенераторе // Вестник Приамурского государственного университета им. Шолом-Алейхема. 2013. № 2(13). С. 90–97 [Электронный ресурс]. URL: https://elibrary.ru/download/elibrary_21298568_86404092.pdf (дата обращения: 23.11.18)
14. Елисеев В.Н., Товстоног В.А., Боровкова Т.В. Алгоритм решения обобщенной задачи нестационарной теплопроводности в телах простой геометрической формы // Вестник МГТУ им. Н.Э. Баумана. Сер. Машиностроение. 2017. № 1. С. 112–128 [Электронный ресурс]. URL: https://elibrary.ru/download/elibrary_28415996_48648202.pdf (дата обращения: 23.11.18)
15. Васильев Г.П., Горнов В.Ф., Песков Н.В., Попов М.И., Колесова М.В., Юрченко В.А. Фазовые переходы влаги в грунте. Учет при проектировании грунтовых теплообменников // Инженерно-строительный журнал. 2017. № 6(74). С. 102–117. DOI: 10.18720/MCE.74.9
16. Parfentyeva N., Valancius K., Samarin O., Paulauskaite S., Ciuprinskine J. Solving the problem of pipeline freezing with respect to external heat exchange // Mechanika. 2015. Vol. 21 (5). Pp. 393–396.
17. Liu C.-S. An integral equation method to recover non-additive and non-separable heat source without initial temperature // International Journal of Heat and Mass Transfer. 2016. Vol. 97. Pp. 943–953.
18. Bahadori A., Vuthaluru H. B. Simple method for estimation of unsteady state conduction heat flow with variable surface temperature in slabs and spheres // International Journal of Heat and Mass Transfer. 2010. Vol. 53. Pp. 4536–4542.
19. Li Y., Kong S.-C. Coupling conjugate heat transfer with in-cylinder combustion modeling for engine simulation // International Journal of Heat and Mass Transfer. 2011. Vol. add.
20. Bouhacina B., Saim R., Oztop H.F. Numerical investigation of a novel tube design for the geothermal borehole heat exchanger // Applied Thermal Engineering. 2015. No. 79. Pp. 153–162.
21. Самарин О.Д. Распространение температурных волн в пустотелом толстостенном цилиндре // Инженерно-строительный журнал. 2018. № 2(78). С. 161–168. DOI: 10.18720/MCE.78.13
22. Подледнева Н.А., Краснов В.А., Магомадов Р.С. Определение коэффициентов теплопроводности и температуропроводности за один опыт методом линейного источника теплоты постоянной мощности // Вестник Астраханского государственного технического университета. 2013. № 2. С. 50–55 [Электронный ресурс]. URL: https://elibrary.ru/download/elibrary_20859905_11088693.pdf (дата обращения: 23.11.18).

Контактные данные:

Олег Дмитриевич Самарин, +7(916)107-77-01; эл. почта: samarin-oleg@mail.ru

Magazine of Civil Engineering. 2019. 85(1). Pp. 59–70
Инженерно-строительный журнал. 2019. № 1(85). С. 59–70

Magazine of Civil Engineering

journal homepage: http://engstroy.spbstu.ru/

ISSN 2071-0305

DOI: 10.18720/MCE.85.6

Mechanical properties of the Crimean limestone, treated with material based on silicic acids

E.A. Korneeva[a], N.I. Vatin[b], A.E. Dontsova[b]*

[a] St. Petersburg State University of Architecture and Civil Engineering, St. Petersburg, Russia

[b] Peter the Great St. Petersburg Polytechnic University, St. Petersburg, Russia

** E-mail: anne.dontsoova@gmail.com*

Keywords: limestone; shell limestone; treatment; restoration; durability; consolidation.

Abstract. The paper describes shell-limestone treatment with stone strengthener Oxal NK 100. Aging impairs the mechanical characteristics of the stone and reduces its bearing capacity. The purpose of the study was to investigate the efficiency of the stone-strengthening composition Oxal NK 100. The composition is supposed to reduce water absorption and strengthen the stone. Cube samples of the Crimean shell-limestone were used. Several testing operations were made to reveal such specifications as absorption of water, compression capacity, freeze-thaw resistance, and porosity of the material. Tests were done on two kinds of samples: treated and non-treated. The results of the study indicated an improvement of mechanical properties of treated stone, compared to non-treated rock samples. The study proved the efficiency of the use of stone-strengthening materials for construction and restoration with shell-limestone.

1. Introduction

Crimean limestone is a sedimentary rock of organic origin. Extensive range of varieties of Crimean limestone includes stones from yellow porous shells to pink-brown breccias. Generally, limestones are divided into several groups: shells, marble limestones, bryozoan, and nummulite limestones. Nummulite limestone consists of small nummulite shells cemented together, bryozoan is composed of quite long branches of bryozoan colonies. Pieces and whole shells of small marine animals are involved in the formation of shell limestone. Limestones are widely used as building and facing blocks in accordance with Russian State Standards. Crimean limestones are common building materials in the south-western areas of the Russian Federation because of their low cost, ease of processing and high thermal performance. Nevertheless, weakness in load and weather resistance remains to be a major issue, concerned with shell limestones.

The literature survey indicates the relevance of the subject. Research papers related to strength characteristics investigation and improvement are published. Thus, factors that influence limestone durability and quality are reviewed in scientific works [1–6]. To date, wide variety of methods to improve characteristics of the stone material exists. The most common algorithms include appliance of epoxy-silica compositions, calcium or barium hydroxide, ethyl silicates and silicic acids. The ability of these substances to consolidate stone and mortar is examined in papers [7–10]. The comprehensive assessment of effectiveness of epoxy silica and silicone-based treatments as well as acrylic polymers confirmed by laboratory tests results is given in researches [11, 12]. Phosphate-based treatments and bacterial protection are innovative techniques described in studies [13, 14]. Also, the properties of nanomaterials have been comprehensively studied in recent years. The major advantage of such treatments is that nanoparticles penetrate deeper into the material and allow us to achieve the better consolidation effect. For instance, the performance of nanolime that is just a dispersion of lime nanoparticles in a solvent is observed in papers [15–17]. The effectiveness of calcium and barium hydroxide nanoparticles and sulfur-based nanoscale coatings is analysed in studies [18–20].

Korneeva, E.A., Vatin, N.I., Dontsova, A.E. Mechanical properties of the Crimean limestone, treated with material based on silicic acids. Magazine of Civil Engineering. 2019. 85(1). Pp. 59–70. DOI: 10.18720/MCE.85.6.

Корнеева Е.А., Ватин Н.И., Донцова А.Е. Механические характеристики крымского известняка, обработанного камнеукрепителем на основе кремниевых кислот // Инженерно-строительный журнал. 2019. № 1(85). С. 59–70. DOI: 10.18720/MCE.85.6

Comparative analysis of different treatments is given in article [21]. Consideration of aspects of the theory and practice of stone strengthening is given in the works [22, 23]. Despite the research is based on the investigation of concrete properties similar results can be found showing the efficiency of stone treatment methods in general. Therefore, application of a hydrophobic treatment on shell-limestone in the same way as on concrete to improve the mechanical properties is described in [24].

Need for restoration and conservation of cultural heritage objects is obvious and creates an area for research in the construction industry. Global warming and increase of exhaust gases concentration in the atmosphere accelerates the process of stone aging due to the leaching of mineral compounds from the stone. [2, 3]. The problem of new materials implementation for architectural heritage conservation remains.

In this paper the efficacy of the epoxy-silica consolidant on nummulite Crimean limestone is studied. This type of stone is historically widely used in low-rise construction, moreover, large number of Crimean historical buildings are made of limestone. Silicic acid-based treatment «Oxal NK 100» was used as stone strengthener.

The purpose of this research is to assess the mechanical properties of the limestone treated with Oxal NK 100. For a full and comprehensive assessment, the following tasks should be completed:

1. Literature analysis in the field of the research;
2. Performance characteristics measurement for treated and non-treated samples such as water drop absorption rate, compression capacity, freeze-thaw resistance and porosity;
3. Comparison of the test data and the overall conclusion about stone strengthener effectiveness.

2. Methods

Cubic samples of a nummulite Crimean limestone with dimensions $a = b = c = 50 \pm 2\ \mathrm{mm}$ were used for the tests. Samples were labeled in accordance with the tests (Figure 1).

Stone strengthening material was silicic acid-based treatment «Oxal NK 100». It was applied on several rock samples in accordance with the instructions. Samples were abundantly sprayed with the composition and naturally dried before all the tests.The best operating temperature for the treatment is 10°C to 20°C and optimal relative humidity is ≥ 40 %. Composition is recommended to apply wet in wet until no more material is absorbed from the substrate. The consumption varies between 0.5 and 1.5 l/m^3 and depends on the absorbency of the substrate.

Series of tests was performed in accordance with Russian State Standard GOST 30629-2011 «Facing materials and products made of natural stone. Test methods». Particularly, samples were tested for water absorption, freeze-thaw resistance, compression strength and porosity. The tests were carried out on samples, typical for the rock.

2.1. Equipment

During the tests, the following instruments and equipment were used:

- Dial desktop scales ((Russian State Standard GOST 29329);
- A vessel to saturate samples with water;
- A hydraulic jack with a force 100 to 500 kN with an adjustable speed of load application and deviation ≤ 2 % (Russian State Standard GOST 28840 or GOST 9753);
- A reference square (Russian State Standard GOST 3749);
- A froster achieving and maintaining a temperature of (20 ± 2) °C above zero;
- A vessel maintaining a temperature of 20±2 °C for samples thawing;
- A weighing bottle (Russian State Standard GOST 25336) or a porcelain cup (Russian State Standard GOST 9147);
- Sizing screen (5 mm and 1.25 mm; Russian State Standard GOST 6613).

2.2. Water absorption tests

Water absorption is measured by comparison of dry and wet samples weight. First, samples were put in water for 48h, then they were weighed. After that, limestone cubes were dried in the desiccator until they reached their constant weight and after that they were weighed again.

2.3. Compression strength test

Compression strength tests included measuring of compression resistance and liquostriction. Half of the stone cubes were treated with stone strengthener beforehand. All the samples were weighed in dry and moisturized condition.

During the tests the cubes were put under pressure (Figure 2). The load was increasing uniformly until wrecking.

Figure 1. Limestone sample.

Figure 2. The sample in the compression apparatus.

2.4. Freeze-thaw resistance test

Firstly, the samples were kept in water for at least 48h, then the cubes were put into a froster in a container for 4 hours with temperature (20±2) °C, after that the samples were put in a bath until a complete defrosting. The freeze-thaw cycle was repeated steadily. The cubes passed compression tests after 15, 25, 35, and 50 freeze-thaw cycles. At least 5 samples were compressed in each test.

2.5. Porosity and voids content measurements

Rock density is characterized by average and true specific density.

The samples were dried until fixed-mass, weighed and measured to find the average specific density. The volume of the cubes is taken as product of their sizes, and the average density is the ratio of mass to volume.

The true specific density was measured with a fast-track methodology using the Chatelier apparatus. We used the samples on which the average density had been determined to have an opportunity to compare the results. Generally, the samples were milled until the coarseness was less than 1.25 mm, then dried and cooled to room temperature. Two weighed portions 50g each were used for the tests.

In the start of the test, the Chatelier apparatus was filled with water to the lowest zero mark (the water level was determined with the concave-convex lens). Milled sample was put into the apparatus till the water reached 20 mm mark. The part of the sample that wasn't put into the apparatus, was weighed.

On the basis of true and average density values the rock porosity is determined

3. Results and Discussion

In the description of the results, the term "limestone" refers to untreated stone samples, and the term "limestone NK 100" refers to samples treated with Oxal NK 100 stone strengthening material.

3.1. Water absorption test

Water absorption for each sample is calculated by the formula:

$$W_{ab} = \frac{m_1 - m}{m} \cdot 100\,\%, \tag{1}$$

where m_1 is the mass of the sample in a water-saturated condition, g

m is the mass of the dry sample, g.

Calculation example for the untreated sample no. 1:

$$W_{ab} = \frac{253.88 - 227.97}{227.97} \cdot 100 = 11.37\,\%.$$

The average water absorption is calculated as the arithmetic average of the results for five rock samples:

$$W_{avg} = \frac{W_1 + W_2 + W_3 + W_4 + W_5}{5}. \quad (2)$$

Calculation example for untreated samples:

$$W_{avg} = \frac{11.37 + 12.23 + 11.59 + 10.67 + 11.61}{5} = 11.49\ \%.$$

The test results are shown in Table 1.

Table 1. The results of the water absorption test.

Sample number	Sample mass, g			Water absorption, %
	Before dehumidifying	After dehumidifying	After water saturation	
Limestone				
1	228.35	227.97	253.88	11.37
2	220.85	220.54	247.52	12.23
3	224.53	224.15	250.12	11.59
4	222.47	222.10	245.80	10.67
5	219.54	221.13	246.80	11.61
			$W_{ab\ avg}$	11.49±0.38
Limestone NK 100				
1	245.02	242.51	250.56	3.32
2	247.76	245.33	254.31	3.66
3	239.38	236.26	241.95	2.41
4	247.24	244.64	250.90	2.56
5	246.54	243.97	252.48	3.49
			$W_{ab\ avg}$	3.09±0.48

A comparative graph of water absorption for treated and untreated samples is shown in Figure 3.

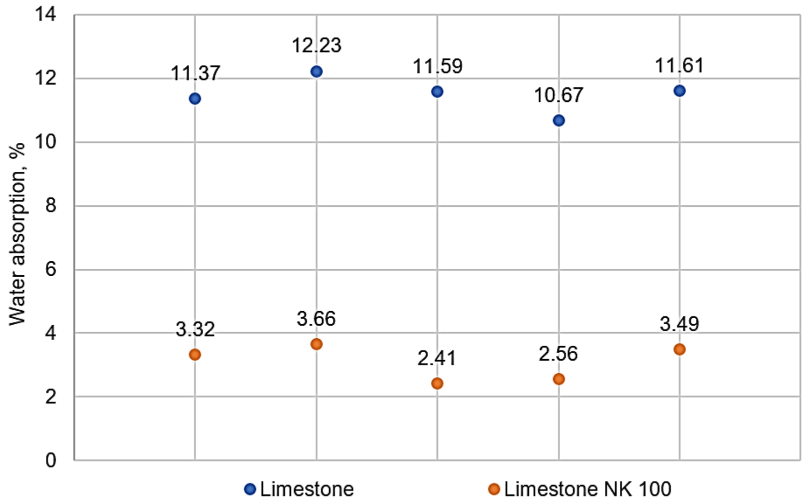

Figure 3. Water absorption of treated and untreated samples.

3.2. Compression strength test

The compressive strength in the dry condition R_{pr}, MPa, is calculated with an accuracy of 1 MPa by the formula:

$$R_{pr} = \frac{P}{F}, \quad (3)$$

where P is breaking strength, N;

F is cross-section area of sample, cm^2.

Average compressive strength is calculated as the arithmetic average of the test results of five samples:

$$R_{pr\ avg} = \frac{R_{pr_1} + R_{pr_2} + R_{pr_3} + R_{pr_4} + R_{pr_5}}{5}. \quad (4)$$

Calculation example for dry untreated samples:

$$R_{pr\ avg} = \frac{23.02 + 26.13 + 23.38 + 17.42 + 23.95}{5} = 22.78 \text{ MPa}.$$

Liquostriction of the rock ΔR, %, is calculated by the formula:

$$\Delta R = \frac{R_{pr\ avg} - R_{pr}}{R_{pr\ avg}} \cdot 100\ \%, \tag{5}$$

where $R_{pr\ avg}$ is average compressive strength of the samples, dried to fixed-mass, MPa;

R_{pr} is average compressive strength of wet samples, MPa.

Calculation example for untreated samples:

$$\Delta R = \frac{22.78 - 8.06}{22.78} \cdot 100 = 64.62\%.$$

Compression strength, R_{pr} had been determined automatically by compression apparatus. The test results are shown in Table 2.

Table 2. Compression strength test results.

Sample number	1	2	3	4	5	$R_{pr\ avg}$, MPa	ΔR
Dry samples							
Limestone	23.02	26.13	23.38	17.42	23.95	22.78±2.14	–
Limestone NK 100	21.07	34.93	32.81	26.58	31.82	29.44±4.49	–
Water saturated samples							
Limestone	7.3	8.5	6.9	7.7	9.9	8.06±0.91	64.62
Limestone NK 100	17.3	20.2	26.8	14.2	26.4	20.98±4.50	28.74

In graphical form, the results of compression strength test are shown in Figure 4.

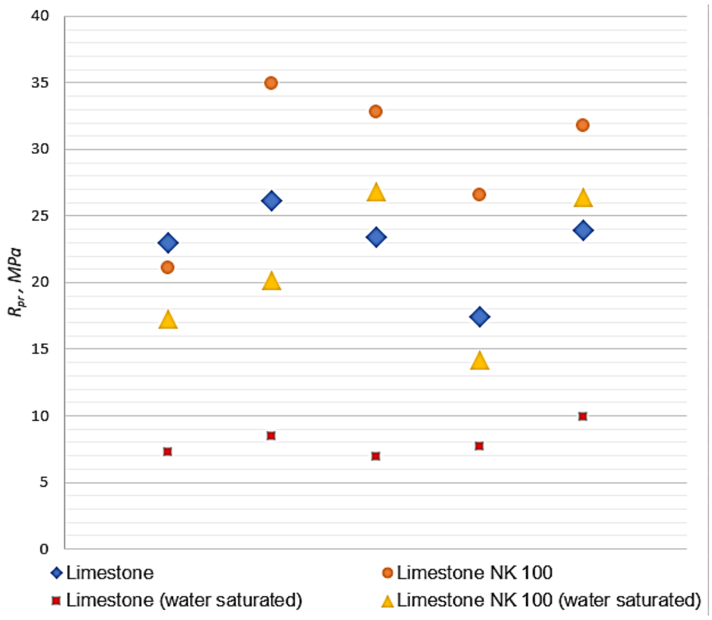

Figure 4. Compressive strength of dry and water-saturated, treated and untreated samples.

3.3. Freeze-thaw resistance test

Strength loss of samples ΔR, %, is determined by the formula:

$$\Delta R = \frac{R_{pr}^{w} - R_{pr}^{f}}{R_{pr}^{w}} \cdot 100\ \%, \tag{6}$$

where R_{pr}^{w} is the arithmetic average of the compressive strength of the samples in a water-saturated condition, MPa,

R_{pr}^{f} is the arithmetic average of the compressive strength of the samples after number of freeze-thaw cycles, MPa.

Average strength loss is calculated as the arithmetic average of the test results for five samples:

$$\Delta R_{avg} = \frac{\Delta R_1 + \Delta R_2 + \Delta R_3 + \Delta R_4 + \Delta R_5}{5}. \quad (7)$$

The freeze-thaw test results are shown in Table 3.

Table 3. Compression strength of the limestone after freeze-thaw cycles.

Sample number	1	2	3	4	5	$R_{pr\ avg}$, MPa	ΔR_{org}, %
15 cycles							
Limestone	8.5	9.7	9.8	11.3	10.1	9.88±0.66	-22.58
Limestone NK 100	19.2	16.5	21.9	18.3	22.5	19.68±2.02	6.20
25 cycles							
Limestone	9.3	7.7	10.2	10.8	11.7	9.94±1.15	-23.33
Limestone NK 100	15.5	18.7	19	17.8	15.8	17.36±1.37	17.25
35 cycles							
Limestone NK 100	6.3	15.3	25.4	19.3	14.5	16.16±4.95	22.97
50 cycles							
Limestone NK 100	10.1	7.2	12.2	13.4	12.8	11.14±1.99	46.90

The untreated samples had shown visible defects after 30 freeze-thaw cycles (Figures 5, 6). This samples were not tested anymore. The reason was their major damage after 30 cycles.

Figure 5. Cracks and delamination on the untreated sample.

Figure 6. Cracks on the untreated sample.

A comparative graph of the change in strength after each stage of freeze-thaw cycles is shown in Figure 7.

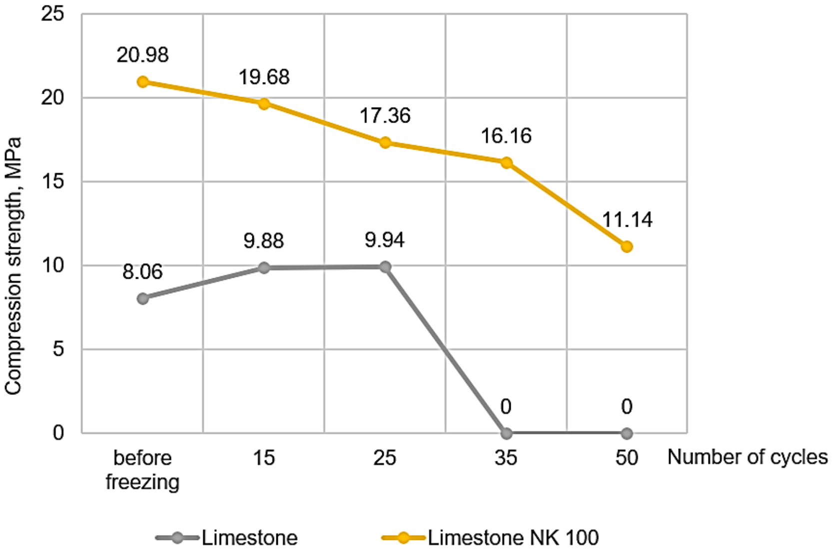

Figure 7. Changes of compression strength after freeze-thaw cycles.

3.4. Porosity and voids content measurements

Average density of the sample ρ_o, g/sm³, is calculated by the formula:

$$\rho_0 = \frac{m}{V}. \quad (8)$$

Example calculation for the untreated limestone sample no. 1:

$$\rho_0 = \frac{262.077}{128.49} = 2.04 \text{ g/sm}^3.$$

Average density of the rock is calculated as the arithmetic average of the average density of all samples:

$$\rho_{0\,avg} = \frac{\rho_{01} + \rho_{02} + \rho_{03} + \rho_{04} + \rho_{05}}{5}. \quad (9)$$

Example calculation of average density for the untreated samples:

$$\rho_{0\,avg} = \frac{2.04 + 2.49 + 2.19 + 2.18 + 2.08}{5} = 2.20 \text{ g/sm}^3.$$

True special density ρ, g/sm^3, is calculated by the formula:

$$\rho = \frac{m - m_1}{V}, \quad (10)$$

where m is mass of the dried milled sample, 100 g;

m_1 is mass of the part of the sample that wasn't put into the apparatus, g;

V is volume of water displaced by milled sample, 20 sm^3.

Example calculation of true density for the untreated sample no. 1:

$$\rho = \frac{100 - 46.546}{20} = 2.673 \text{ g/sm}^3.$$

Average true density is calculated as the arithmetic average of the true density of all samples:

$$\rho_{avg} = \frac{\rho_1 + \rho_2 + \rho_3 + \rho_4 + \rho_5}{5}. \quad (11)$$

Example calculation of true density for untreated limestones:

$$\rho_{avg} = \frac{2.673 + 2.842 + 2.823 + 2.827 + 2.796}{5} = 2.79 \text{ g/sm}^3.$$

The results of determination of average and true specific density are shown in Table 4.

Table 4. Average and true specific density of the limestone.

Sample number	Fixed mass of a sample, g	A, cm	B, cm	C, cm	V, cm^3	ρ_0	$\rho_{0\,avg}$	m_1	ρ	ρ_{avg}
Limestone										
1	262.077	5.14	5.05	4.95	128.49	2.04	2.20±0.12	46.546	2.673	2.79±0.05
2	319.108	4.99	5.03	5.11	128.26	2.49		43.16	2.842	
3	293.598	5.16	5.06	5.13	133.94	2.19		43.532	2.823	
4	294.258	5.14	5.07	5.18	134.99	2.18		43.462	2.827	
5	270.981	5.01	5.18	5.02	130.28	2.08		44.079	2.796	
Limestone NK 100										
1	284.015	5.15	5.11	5.12	134.74	2.11	2.14±0.09	47.542	2.623	2.70±0.04
2	292.585	4.98	4.96	5.16	127.46	2.30		45.012	2.749	
3	277.966	5.11	5.2	5.14	136.58	2.04		46.034	2.698	
4	276.661	5.15	5.04	5.18	134.45	2.06		45.178	2.741	
5	296.43	5.15	5.19	4.99	133.38	2.22		46.177	2.691	

The values of the average and true density are graphically presented in Figure 8.

Porosity V_{por}, %, is calculated by the formula:

$$V_{por} = \left(1 - \frac{\rho_0}{\rho}\right) \cdot 100\ \%. \quad (12)$$

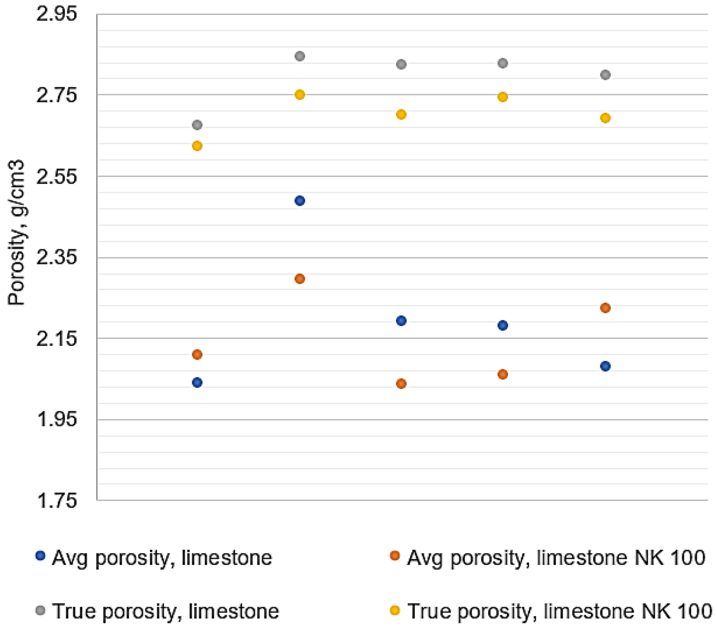

Figure 8. Average and true density of treated and untreated samples.

Porosity of the untreated limestone samples:

$$V_{por} = \left(1 - \frac{2.20}{2.79}\right) \cdot 100 = 21.36\ \%.$$

Porosity of the limestone NK 100 samples:

$$V_{por} = \left(1 - \frac{2.14}{2.70}\right) \cdot 100 = 20.62\ \%.$$

Limestone is a soft rock and is not immune to decay. There is a need for consolidation of limestone buildings and constructions. The works should be corroborated with theoretical studies. Modern methods used for restoration work are often non-effective.

The water absorption of the samples treated with Oxal NK 100 was 3.09 % while the water absorption of untreated stone was 11.49 %. Treatment with stone strengthening material reduced the water absorption of the samples by 4 times. The destruction of limestone because of weather conditions can be represented by the number of wetting and drying cycles, as described in [2]. Many cycles lead to salt weathering that can cause cracking and decay. To combat this phenomenon, swelling inhibitors, phosphate treatment and bacterial communities are used in civil engineering [2, 13, 14]. Reduce in the water absorption rate can slow down the salt weathering and can be an alternative to the described methods.

Dry samples of the limestone treated with Oxal NK 100 shown an increased compressive strength rate (23 % higher than dry untreated samples compressive strength). Liquostriction of treated samples turned out to be significantly (2.3 times) lower than liquostriction of untreated cubes. Generally, after the treatment of the stone, the compressive strength increased from 22.78 MPa to 29.44 MPa in the dry state and from 8.06 MPa to 20.98 MPa in water-saturated condition.

Most of the territory of the Russian Federation is in a subarctic climate area. The highest average January temperature is –5 °C. This means that in absolutely all regions the temperature falls below zero in winter [25]. Therefore, the freeze-thaw resistance of the material is always considered in the conditions of construction in Russia as well as the ways to improve it. The untreated stone had taken only 25 freeze-thaw cycles before cracking, while the treated samples withstood up to 50 cycles with a significant loss of compressive strength after 35 cycles. Limestone compressive strength decreased from 20.98 to 11.14 MPa. Samples treated with Oxal NK 100 stone strengthening material had handled twice as many freeze-thaw cycles as compared to untreated samples.

Porosity of the treated limestone reduced slightly comparing to untreated samples.

Increased compression strength, improved freeze-thaw cycle resistance and reduced water absorption have been noted by many authors in studies of the effectiveness of stone strengthening materials. Thus, the compressive strength of the samples changed from 20 MPa to 25.33 and 34.4 MPa after treatment of limestone with hydroxyapatite and strontium hydroxyapatite, respectively [26]. Based on these data, it is possible to consider silica-based stone consolidation more effective than compositions containing hydroxyapatites. At the same time, strontium stone processing showed a greater increase in the compressive strength of the samples.

The efficiency of treatment with silicic acids depends on the concentration in the solvent, which was studied using the ethyl silicate in [27]. During the study, it was found that the optimal concentration of ethyl silicate in the solvent is 25 %. It is possible that a change in the concentration of silicic acids in the Oxal NK 100 would increase the efficiency of the treatment.

It is also necessary to consider the effect of measurement error on the research results. Since the tests for each of the characteristics were carried out on only five samples, in some cases the relative error reached 30 % and taking the «worst» case into account significantly influenced the results.

Therefore, for the treated samples in the water absorption tests, the relative measurement error was 16 %, and for the untreated ones – 3 %. In the study of the "worst" outcome of events (minimum water absorption rate of untreated samples and maximum absorption rate of processed), the use of a stone-strengthening solution reduces the water absorption of the rock by 3.11 times.

During strength tests, a significant relative error (21 %) exists at the compressive strength of the water-saturated treated samples. The minimum value of the ultimate strength is 16.48 MPa, while the loss of strength ΔR would be 44 %.

The highest relative error in frost resistance tests is 31 % – for the compressive strength of the treated samples after 35 freeze-thaw cycles. The relative error after 50 cycles is 18 %. In the “worst” case, the compression strength of cubes after 35 freeze-thaw cycles would be 11.21 MPa, and after 50 cycles – 9.15 MPa. Loss of compression strength after 50 cycles in such case would be 56 %.

Finally, the errors in measuring the porosity of the material turned out to be small: from 1 % to 5 %.

An analysis of the literature on the chosen topic showed an increase in the number of publications in recent years, which can be explained by the growing interest of the scientific community in the use of stone strengthening materials for restoration and construction [28, 29]. The main methods of stone structures consolidation include treatment with epoxy-silica compositions and silicone-based materials. Stone strengthening material Oxal NK 100 is based on silicic acids and belongs to epoxy-silica compositions. Further research could be aimed to reveal the most effective material to strengthen the Crimean limestone. To reach this objective, it is necessary to compare the mechanical characteristics of the samples treated with different stone strengthening compositions, as was done, for instance, in papers [21, 27].

4. Conclusions

In the study, water absorption, compressive strength, freeze-thaw resistance, and porosity of the samples were tested. The untreated limestone cubes were examined as well as treated to get a comparative characteristic of the studied parameters. Limestone treated with the Oxal NK 100 showed higher strength parameters and freeze-thaw resistance and lower water absorption. The porosity of the treated and untreated samples varied slightly.

The water absorption of the samples treated with Oxal NK 100 was 3.09 % while the water absorption of untreated stone was 11.49 %. Dry samples of the limestone treated with Oxal NK 100 had shown a better result in compressive strength test (23 % stronger than dry untreated samples). Liquostriction of treated samples became 2.3 times lower than this characteristic of untreated cubes. The treated samples withstood up to 50 freeze-thaw cycles while the untreated stone had taken only 25 cycles. It is also possible that a change in the concentration of silicic acids in the Oxal NK 100 would increase the efficiency of the treatment.

During the study, the samples were sprayed with a stone-reinforcing composition, which ensured their uniform impregnation. This technology of application of the composition is recommended by the manufacturer. Changes in technology may lead to reduced improvements in mechanical performance. However, the use of injection treatment, by contrast, can improve test results. This is due to the mechanics of the action of silica-gel, which is a secondary porous material for limestone in this case of processing. Deeper penetration of silicic acid ester into the stone provides better protection, while at the same time it’s a more expensive solution. In any case, this application method must be tested experimentally.

This study is one of the first testing series with the use of stone-strengthening materials. Such solutions seem to become popular soon because of the need to increase reliability and durability of stone materials. The use of the stone-strengthening composition Oxal NK 100 has proven to be an effective method for improving the mechanical characteristics of limestone.

5. Acknowledgement

Acknowledgement is expressed to the Head of the laboratory Pestryakov I.I. (Educational laboratory of general engineering technologies) for provided equipment that was used for tests, and to the company «MC Bauchemie» Ltd. for the material samples given for testing.

References

1. Sassoni, E. Hydroxyapatite and other calcium phosphates for the conservation of cultural heritage: A review. Materials. 2018. No. 11(4). Pp. 557.
2. Jiménez-González, I., Rodríguez-Navarro, C., Scherer. G.W. Role of clay minerals in the physicomechanical deterioration of sandstone. J. Geophys. Res. Earth Surf. 2008. No. 113 (2). Pp. F02021.
3. Rodriguez-Navarro, C., Sebastian, E. Role of particulate matter from vehicle exhaust on porous building stones (limestone) sulfation. Sci. Total Environ. 1996. No. 187 (2). Pp. 79–91.
4. Baglioni, P., Giorgi, R., Dei, L. Soft condensed matter for the conservation of cultural heritage. Comptes Rendus Chim. 2009. No.12. Pp. 61–69.
5. Motornyi, N.I. Ocenka dolgovechnosti prirodnogo kamnya [Evaluation of the durability of natural stone]. Sci. Bull. Moscow State Min. Univ. 2012. No. 3. Pp. 68–76. (rus)
6. Kazaryan, J.A. Primer obsledovaniya kompleksa zdanij v istoricheskom centre Moskvy s rekomendaciyami po restavracii izvestnyakovyh fasadov i perspektivami primeneniya v krupnyh proektah [An example of a survey of buildings in the historical center of Moscow with recommendations]. Extr. Process. Use Nat. Stone. Magnitogorsk: Nosov Magnitogorsk State Technical University, 2017. Pp. 209–225. (rus)
7. Gómez-Laserna, O., Lanzafame, P., Papanikolaou, G., Olazabal, M.Á., Lo Schiavo, S., Cardiano, P. Analytical assessment to develop innovative nanostructured BPA-free epoxy-silica resins as multifunctional stone conservation materials. Sci. Total Environ. 2018. No. 645. Pp. 817–826.
8. Daehne, A., Herm, C. Calcium hydroxide nanosols for the consolidation of porous building materials – results from EU-STONECORE. Herit. Sci. 2013. No. 1. Pp. 11.
9. Slížková, Z., Drdácký, M., Viani, A. Consolidation of weak lime mortars by means of saturated solution of calcium hydroxide or barium hydroxide. J. Cult. Herit. 2015. No. 16. Pp. 452–460.
10. Cardiano, P., Ponterio, R.C., Sergi, S., Lo Schiavo, S., Piraino, P. Epoxy-silica polymers as stone conservation materials. Polymer. 2005. No. 46. Pp. 1857–1864.
11. Favaro, M., Mendichi, R., Ossola, F., Russo, U., Simon, S., Tomasin, P., Vigato, P.A. Evaluation of polymers for conservation treatments of outdoor exposed stone monuments. Part II. Polym. Degrad. Stab. 2006. No. 91. Pp. 3083–3096.
12. Cardiano, P. Hydrophobic properties of new epoxy-silica hybrids. J. Appl. Polym. Sci. 2008. No. 108. Pp.3380–3387.
13. Graziani, G., Sassoni, E., Scherer, G.W., Franzoni, E. Phosphate-based treatments for consolidation of salt-bearing Globigerina limestone. IOP Conf. Ser. Mater. Sci. Eng. 2018. No. 364 (1). Pp. 012082.
14. Jroundi, F., Schiro, M., Ruiz-Agudo, E., Elert, K., Martín-Sánchez, I., González-Muñoz, M.T., Rodriguez-Navarro, C. Protection and consolidation of stone heritage by self-inoculation with indigenous carbonatogenic bacterial communities. Nat. Commun. 2017. No. 8 (1). Pp. 279.
15. Borsoi, G., Lubelli, B., Van Hees, R., Veiga, R., Silva, A.S., Colla, L., Fedele, L., Tomasin, P. Effect of solvent on nanolime transport within limestone: How to improve in-depth deposition. Colloids and Surfaces A Physicochem. Eng. Asp. 2016. No. 497. Pp. 171–181.
16. Borsoi, G., Lubelli, B., Van Hees, R., Veiga, R., António, L., Silva, S. Optimization of nanolime solvent for the consolidation of coarse porous limestone. Applied Physics A: Materials Science and Processing. 2016. No. 122 (9). Pp. 846.
17. Rodriguez-Navarro, C., Ruiz-Agudo, E. Nanolimes: From synthesis to application. Pure Appl. Chem. 2018. No. 90. Pp. 523–550.
18. Giorgi, R., Ambrosi, M., Toccafondi, N., Baglioni, P. Nanoparticles for cultural heritage conservation: Calcium and barium hydroxide nanoparticles for wall painting consolidation. Chem. – A Eur. J. 2010. No. 16. Pp. 9374–9382.
19. Chelazzi, D., Poggi, G., Jaidar, Y., Toccafondi, N., Giorgi, R., Baglioni, P. Hydroxide nanoparticles for cultural heritage: Consolidation and protection of wall paintings and carbonate materials. J. Colloid Interface Sci. 2013. No. 392. Pp. 42–49.
20. Massalimov, I.A., Mustafin, A.G., Husainov, A.N., Chuykin, A.E. Protection of building materials and structures with sulfur-based nanoscale coatings. Stroit. Mater. Oborudovanie, Tekhnologii XXI Veka. 2012. No. 2 (157). Pp. 19–21. (rus)
21. Rodrigues, J.D., Ferreira Pinto, A.P., Nogueira, R., Gomes, A. Consolidation of lime mortars with ethyl silicate, nanolime and barium hydroxide. Effectiveness assessment with microdrilling data. J. Cult. Herit. 2018. No. 29. Pp. 43–53.
22. Massalimov, I.A., Yanakhmetov, M.R., Chuykin, A.E., Massalimov, B.I., Urakaev, F.H., Uralbekov, B.M. Hydrophobization of dense and fine concrete by polysulfide solutions. Nanotechnologies Constr. A Sci. Internet-Journal. 2016. No. 8. Pp. 85–99. (rus)
23. Yanakhmetov, M.R., Chuykin, A.E., Massalimov, I.A. Pore structure modification of cement concretes by impregnation with sulfur-containing compounds. Nanotechnologies Constr. A Sci. Internet-Journal. 2015. No. 7. Pp. 63–72. (rus)
24. Massalimov, I.A., Chuykin, A.E., Massalimov, B.I., Urakaev, F.H., Uralbekov, B.M., Burkitbaev, M.M. Improvement of operational properties of shell Limestone building materials by polysulfide. Solution impregnation. Nanotechnologies Constr. A Sci. Internet-Journal. 2017. No. 9. Pp. 66–80. (rus)
25. Federal State Statistics Service, Agriculture, hunting and hunting sector, forestry in Russia. [Online] System reqirements: AdobeAcrobatReader. URL: http://www.gks.ru (accessed November 15, 2018). (rus)
26. Ion, R., Turcanu-Carutiu, D., Fierascu, R., Fierascu, I. Chalk stone restoration with hydroxyapatite-based nanoparticles. Sci. Bull. Valahia Univ. – Mater. Mech. 2014. No. 9 (12). Pp. 24–28.
27. Cultrone, G., Sánchez-Ibáñez, V. Consolidation with ethyl silicate: How the amount of product alters the physical properties of the bricks and affects their durability. Mater. Constr. 2018. No. 68 (332). Pp. Y.
28. Korneeva, E., Mohamad, S. The water absorption of Crimean limestone treated with silicic acid-based material. MATEC Web of Conferences. 2018. Vol. 245. No. 03001. Pp. 1–4.
29. Korneeva, E., Mohamad, S. Strengthening the historical constructions made of limestone by treating with silicic acid-based material. MATEC Web of Conferences. 2018. Vol. 245. No. 01005. Pp. 1–4.

Contacts:

Elena Korneeva, +79633193218; linka360639020@yandex.ru
Nikolai Vatin, +79219643762; vatin@mail.ru
Anna Dontsova, +79811889300; anne.dontsoova@gmail.com

Инженерно-строительный журнал

ISSN 2071-0305

сайт журнала: http://engstroy.spbstu.ru/

DOI: 10.18720/MCE.85.6

Механические характеристики крымского известняка, обработанного камнеукрепителем на основе кремниевых кислот

Е.А. Корнеева[a], Н.И. Ватин[b], А.Е. Донцова[b*]

[a] Санкт-Петербургский государственный архитектурно-строительный университет, Санкт-Петербург, Россия

[b] Санкт-Петербургский политехнический университет Петра Великого, Санкт-Петербург, Россия

** E-mail: anne.dontsoova@gmail.com*

Ключевые слова: известняк; известняк-ракушечник; пропитка; реставрация; долговечность; укрепление.

Аннотация. В настоящее время ведется поиск новых решений для улучшения эксплуатационных характеристик каменного материала. Обработка фасадов и отдельных образцов различными пропитками показала себя эффективной. В статье описаны основные составляющие подобных растворов и исследованы механические характеристики обработанного камня. С камнями крымского известняка-ракушечника был проведен ряд испытаний: на водопоглощение, прочность на сжатие, морозостойкость. Была дана оценка пористости материала после обработки пропиткой. Сравнением характеристик обработанных и необработанных камней была проанализирована эффективность камнеукрепляющего материала Oxal NK 100. В результате было выявлено значительное улучшение параметров обработанных известняков. Водопоглощение обработанных известняков снизилось в 4 раза, предел прочности на сжатие в сухом состоянии увеличился на 23 %, а снижение прочности в водонасыщенном состоянии снизилось в 2,3 раза. Морозостойкость обработанных образцов увеличилась вдвое, а пористость изменилась незначительно (менее, чем на 2 %).

Литература

1. Sassoni E. Hydroxyapatite and other calcium phosphates for the conservation of cultural heritage: A review // Materials. 2018. 11(4). Pp. 557.
2. Jiménez-González, I., Rodríguez-Navarro C., Scherer G.W. Role of clay minerals in the physicomechanical deterioration of sandstone // J. Geophys. Res. Earth Surf. 2008. 113(2). Pp. F02021.
3. Rodriguez-Navarro C., Sebastian E. Role of particulate matter from vehicle exhaust on porous building stones (limestone) sulfation // Sci. Total Environ. 1996. 187(2). Pp. 79–91.
4. Baglioni P., Giorgi R., Dei L. Soft condensed matter for the conservation of cultural heritage // Comptes Rendus Chim. 2009. No.12. Pp. 61–69.
5. Моторный Н.И. Оценка долговечности природного камня // Научный вестник Московского Горного университета. 2012. №3. С. 68-76.
6. Казарян Ж.А. Пример обследования комплекса зданий в историческом центре Москвы с рекомендациями по реставрации известняковых фасадов и перспективами применения в крупных проектах // Добыча, обработка и применение природного камня. Магнитогоск: Магнитогорский государственный технический университет им. Г.И. Носова, 2017. С. 209–225.
7. Gómez-Laserna O., Lanzafame P., Papanikolaou G., Olazabal M.Á., Lo Schiavo S., Cardiano P. Analytical assessment to develop innovative nanostructured BPA-free epoxy-silica resins as multifunctional stone conservation materials // Sci. Total Environ. 2018. No. 645. Pp. 817–826.
8. Daehne A., Herm C. Calcium hydroxide nanosols for the consolidation of porous building materials – results from EU-STONECORE // Herit. Sci. 2013. No. 1. Pp. 11.
9. Slížková Z., Drdácký M., Viani A. Consolidation of weak lime mortars by means of saturated solution of calcium hydroxide or barium hydroxide // J. Cult. Herit. 2015. No. 16. Pp. 452–460.
10. Cardiano P., Ponterio R.C., Sergi S., Lo Schiavo S., Piraino P. Epoxy-silica polymers as stone conservation materials // Polymer. 2005. No. 46. Pp. 1857–1864.
11. Favaro M., Mendichi R., Ossola F., Russo U., Simon S., Tomasin P., Vigato P.A. Evaluation of polymers for conservation treatments of outdoor exposed stone monuments. Part II // Polym. Degrad. Stab. 2006. No. 91. Pp. 3083–3096.
12. Cardiano P. Hydrophobic properties of new epoxy-silica hybrids // J. Appl. Polym. Sci. 2008. No. 108. Pp. 3380–3387.

13. Graziani G., Sassoni E., Scherer G.W., Franzoni E. Phosphate-based treatments for consolidation of salt-bearing Globigerina limestone // IOP Conf. Ser. Mater. Sci. Eng. 2018. No. 364 (1). Pp. 012082.
14. Jroundi F., Schiro M., Ruiz-Agudo E., Elert K., Martín-Sánchez I., González-Muñoz M.T., Rodriguez-Navarro C. Protection and consolidation of stone heritage by self-inoculation with indigenous carbonatogenic bacterial communities // Nat. Commun. 2017. No. 8 (1). Pp. 279.
15. Borsoi G., Lubelli B., Van Hees R., Veiga R., Silva A.S., Colla L., Fedele L., Tomasin P. Effect of solvent on nanolime transport within limestone: How to improve in-depth deposition // Colloids and Surfaces A Physicochem. Eng. Asp. 2016. No. 497. Pp. 171–181.
16. Borsoi G., Lubelli B., Van Hees R., Veiga R., António L., Silva S. Optimization of nanolime solvent for the consolidation of coarse porous limestone // Applied Physics A: Materials Science and Processing. 2016. No. 122 (9). Pp. 846.
17. Rodriguez-Navarro C., Ruiz-Agudo E. Nanolimes: From synthesis to application // Pure Appl. Chem. 2018. No. 90. Pp. 523–550.
18. Giorgi R., Ambrosi M., Toccafondi N., Baglioni P. Nanoparticles for cultural heritage conservation: Calcium and barium hydroxide nanoparticles for wall painting consolidation // Chem. – A Eur. J. 2010. No. 16. Pp. 9374–9382.
19. Chelazzi D., Poggi G., Jaidar Y., Toccafondi N., Giorgi R., Baglioni P. Hydroxide nanoparticles for cultural heritage: Consolidation and protection of wall paintings and carbonate materials // J. Colloid Interface Sci. 2013. No. 392. Pp. 42–49.
20. Массалимов И.А., Мустафин А.Г., Хусаинов А.Н., Чуйкин А.Е. Защита строительных материалов и конструкций наноразмерными покрытиями на основе серы // Строительные материалы, оборудование, технологии XXI века. 2012. №.2 (157). С. 19–21.
21. Rodrigues J.D., Ferreira Pinto A.P., Nogueira R., Gomes A. Consolidation of lime mortars with ethyl silicate, nanolime and barium hydroxide. Effectiveness assessment with microdrilling data // J. Cult. Herit. 2018. No. 29. Pp. 43–53.
22. Массалимов И.А., Янахмедов М.Р., Чуйкин А.Е., Массалимов Б.И., Уракаев Ф.Х., Уралбеков Б.М., Буркитбаев М.М. Гидрофобизация плотного и мелкозернистого бетонов полисульфидными растворами // Нанотехнологии в строительстве: научный интернет-журнал. 2016. Т. 8. № 5. С. 85–99.
23. Янахметов М.Р., Чуйкин А.Е., Массалимов И.А. Модифицирование поровой структуры цементных бетонов пропиткой серосодержащими растворами // Нанотехнологии в строительстве: научный интернет-журнал. 2015. Т. 7. № 1. С. 63–72.
24. Массалимов И.А., Чуйкин А.Е., Массалимов Б.И., Уракаев Ф.Х., Уралбеков Б.М., Буркитбаев М.М. Улучшение эксплуатационных свойств строительных материалов из известнякаракушечника пропиткой полисульфидными растворами // Нанотехнологии в строительстве: научный интернет-журнал. 2017. Т. 9. № 3. С. 66-80.
25. Федеральная служба государственной статистики. Сельское хозяйство, охота и охотничье хозяйство, лесоводство в России. [Электронный ресурс]. Систем. требования: AdobeAcrobatReader. URL: http://www.gks.ru (дата обращения 15 ноября 2018)
26. Ion R., Turcanu-Carutiu D., Fierascu R., Fierascu I. Chalk stone restoration with hydroxyapatite-based nanoparticles // Sci. Bull. Valahia Univ. Mater. Mech. 2014. No. 9 (12). Pp. 24–28.
27. Cultrone G., Sánchez-Ibáñez V. Consolidation with ethyl silicate: How the amount of product alters the physical properties of the bricks and affects their durability // Mater. Constr. 2018. No. 68 (332). Pp. Y.
28. Korneeva E., Mohamad S. The water absorption of Crimean limestone treated with silicic acid-based material // MATEC Web of Conferences. 2018. Vol. 245. No. 03001. Pp. 1–4.
29. Korneeva E., Mohamad S. Strengthening the historical constructions made of limestone by treating with silicic acid-based material // MATEC Web of Conferences. 2018. Vol. 245. No. 01005. Pp. 1–4.

Контактные данные:

Елена Александровна Корнеева, +79633193218; эл. почта: linka360639020@yandex.ru
Николай Иванович Ватин, +79219643762; эл. почта: vatin@mail.ru
Анна Евгеньевна Донцова, +79811889300; эл. почта: anne.dontsoova@gmail.com

Magazine of Civil Engineering. 2019. 85(1). Pp. 71–91
Инженерно-строительный журнал. 2019. № 1(85). С. 71–91

Magazine of Civil Engineering

ISSN 2071-0305

journal homepage: http://engstroy.spbstu.ru/

DOI: 10.18720/MCE.85.7

Quasistaticity of the process of dynamic strain of soils

K.S. Sultanov*, P.V. Loginov, S.I. Ismoilova, Z.R. Salikhova
Institute of Mechanics and Seismic Stability of Structures Academy of Sciences of the Republik of Uzbekistan, Tashkent, Uzbekistan
* *E-mail: sultanov.karim@mail.ru*

Keywords: soil, dynamic loading, waves, stresses, quasi-statics, mechanical characteristics of soil.

Abstract. Mechanical characteristics of soil under static and dynamic strains are determined experimentally. Their accuracy and reliability depends on quasi-static nature of strain process in soil. The independence of experimental results on the wave processes is ensured. Laboratory devices of dynamic loading (DDL) have been used to determine the laws of dynamic strain and mechanical characteristics of soil. The quasi-static nature of strain process in soil on DDL is achieved solving the wave problem corresponding to experiment. Plane wave propagation in soil is considered; its statement is adequate to experiment on DDL. To describe the dynamic strain of soil, the G.M. Lyakhov elastic-viscoplastic model has been adopted. The system of differential equations in partial derivatives of hyperbolic type, describing the wave process, has been solved by the method of characteristics and finite difference method in an implicit scheme. The changes in wave parameters over time for different sections of soil layer have been obtained by numerical solution. The effect of layer thickness on wave parameters and on quasi-static process is shown by experiments. Quantitative and qualitative influence of mechanical characteristics of soil on wave parameters is determined. Analyzing results, it has been established that the main factors determining the quasi-static process are the parameters of dynamic load and the thickness of soil layer in DDL. The dependence of mechanical characteristics of soil on quasistatic nature of dynamic strain in DDL is shown. Conditions to ensure the quasi-static process of strain in soil sample under dynamic compression on DDL are obtained.

1. Introduction

Stability and seismic resistance of buildings and structures (especially earth and underground structures) are directly related to the strength of soil under static and dynamic loads. Therefore, the study of strength and mechanical properties of soil is a pressing issue throughout the world. Strength characteristics of soil, as is well known, mainly include the coefficient of cohesion and the angle or coefficient of internal friction of soil. In contrast to strength characteristics, mechanical characteristics of soils are related to the laws of soil strain. These include the modulus of elasticity, Poisson's ratio, modulus of unloading, soil viscosity coefficient, etc. These or other mechanical and strength characteristics of soil make it possible to determine and calculate strength and stability of soil as the foundations for the buildings and structures; of earth structures such as dams, dykes, the walls of open pits, slopes and dumps; of underground structures located in different soil conditions. The strength and mechanical characteristics of soil are determined experimentally.

A great amount of publications are devoted to experimental study of strength and mechanical characteristics of soil. Strength characteristics of various soils and rocks under static loads have been experimentally defined in [1–3].

In [1], strength characteristics of loess soils stabilized by silica nanoparticles were determined. It was shown that it increased the strength characteristics of soil. In [2], strength characteristics of soil were

Sultanov, K.S., Loginov, P.V., Ismoilova, S.I., Salikhova, Z.R. Quasistaticity of the process of dynamic strain of soils. Magazine of Civil Engineering. 2019. 85(1). Pp. 71–91. DOI: 10.18720/MCE.85.7.

Султанов К.С., Логинов П.В., Исмоилова С.И., Салихова З.Р. Квазистатичность процесса динамического деформирования грунтов // Инженерно-строительный журнал. 2019. № 1(85). С. 71–91. DOI: 10.18720/MCE.85.7

determined depending on water saturation by the direct shear test and the triaxial compression method. In [3], strength characteristics of soil were defined in relation to the stability of slopes.

Experimental determination of strength characteristics of soil under dynamic loads in field conditions was given in [4, 5]. In [4], the shear resistance of soft clay was determined at the free fall of a steel sphere of 0.25 m diameter into water. The measuring unit, located inside the sphere, measured the response to sphere motion at fall and penetration into soil. The obtained acceleration measurement data allowed determining strength characteristics of soil. In [5], by a method similar to the one in [4], strength characteristics of the seabed were determined at various velocities of the impact of a steel ball.

Experimental determination of mechanical characteristics of soil under static loads was given in [6–9]. In [6], the elastic modulus of a granular material was determined at low values of strain, depending on the diameter of the grain particles. It had been established that the Young modulus was practically independent of the diameter of particles of granular material. In [7], the strain modulus was determined by compressive and pressing tests of soil samples. Under triaxial cyclic loading, the strain characteristics of soil were defined in [8]. Mechanical viscoelastic characteristics of geosynthetic materials under static stresses were determined in [9].

Mechanical characteristics of soils and rocks under dynamic loads have been defined in [10–23] in laboratory and field conditions.

In [10], mechanical characteristics of brittle soils were determined under loading rates of axial stress equal to 0.05–10 kN/s in laboratory conditions. It was established that the modulus of elasticity of soil increased with an increase in loading rate. In [11], elastic properties of clay soil were determined by measuring the velocities of ultrasonic waves of various frequencies propagating in soil. The dynamic modulus obtained experimentally was compared to the static modulus. In [12], mechanical characteristics of soft clay were determined under dynamic loads by the centrifugal modeling method. In [13–15], dynamic parameters of friction and resistance at sliding of dry and water-saturated surfaces of soil and sand were experimentally determined. Mechanical characteristics of a prismatic marble block, pyroclastic rocks and clayey soil were studied by ultrasonic scanning in [16–18).

Mechanical characteristics of soil, based on specific elastic-viscoplastic models, under static and dynamic loads have been determined in [19–23] in laboratory and field conditions.

Complex laws of strain in soils and rocks were given in [24–28], the consideration of applied problems of fracture – in [29], a comparative analysis of mechanical characteristics determined by different methods – in [30] and nonlinear models of soil strain – in [31–35]. The emergence of non-one-dimensional problems of seismic stability of earth structures required experimental data on mechanical characteristics of soils and rocks, especially under dynamic loads.

The values of mechanical characteristics of soil when calculating seismic stability of underground structures were of particular relevance [23]. Without the knowledge of mechanical characteristics of soil under dynamic strain it is impossible to estimate the quantitative parameters of various waves in soil media and rocks [19–23, 33]. The reliability of the values of mechanical characteristics of soils when solving the problems of seismic resistance of aboveground and earth structures (soil dams, levees, walls of open pit, foundations) is very important [36–38].

In field experiments it is almost impossible to obtain repetitions of exactly the same tests in quantities and quality that allow static processing of results. The latter circumstance is very important to prove the reliability of experimental results.

In [21], the authors have created a special device for dynamic loading (DDL) to determine dynamic characteristics of soils. In this case, a soil sample of undisturbed or disturbed structure was tested for shock loads created by a falling weight. The DDL operated on the principle of a compression device for testing soils under static loads. Design description of the DDL and the principles of its operation were given in detail in [21]. The method of experimental determination of mechanical characteristics of soil proposed in [21] allowed serial experiments, the results of which were then processed using the methods of mathematical statistics. As a result, significantly reliable experimental data were obtained for determining mechanical characteristics of soil under dynamic loads [21].

However, in this case, when conducting experiments on dynamic compression of soil samples on the DDL, another problem arose. It laid in the fact that the stress measurement results were affected by the wave process that occurred in a soil sample when it was subjected to a shock load. To accurately measure the stresses in soil under dynamic uniaxial compression on the DDL, it was necessary to ensure the quasistatic nature of the process of soil strain. The quasistatic process of dynamic strain was realized under the conditions $\frac{d\sigma}{dx}=0$ and $\frac{d\varepsilon}{dx}=0$, where σ was the longitudinal stress along the compression x axis, ε was the longitudinal strain along the x axis.

In [21], the conditions for the quasistatic nature of the process of dynamic strain of soil were determined at some theoretical assumptions. According to these conditions, the ratio of the mass of soil sample and the mass of the DDL piston should satisfy the condition of a quasistatic nature given in [21]. The condition of the values of rise time of dynamic load from zero to the maximum should also be satisfied. In [21], the wave process occurring in soil under shock load was not investigated.

Based on the analysis of published sources [1-38], and, particularly, on the results obtained in [19–23, 34], the wave problem which corresponds to the statement of the experiment on the DDL is solved in this paper. In published sources, there is no solution to this problem. The object of the study is the wave process in soil under its dynamic compression and the dynamic stress-strain state of soil.

Theoretical substantiation of the validity of experimental results obtained in laboratory conditions on the device of the DDL type is an actual problem, since the accuracy of calculations on strength and seismic stability of soils and soil structures directly depends on the reliability of mechanical characteristics determined from the results of dynamic compression of soils.

The aim of this study is to theoretically investigate the wave process in a soil sample placed in the DDL soil receiving chamber and to determine the conditions for the quasistatic nature of the process of dynamic strain of a soil sample based on the analysis of wave parameters.

To achieve this goal, the following tasks are solved:

1. Choice and substantiation of the law of soil strain on the DDL. Determination of the basic equations of motion describing the process of dynamic compression of soil and the boundary conditions corresponding to the statement of the experiment on the DDL.

2. Choice of a numerical method for solving the obtained wave equations, its substantiation. Development of the principles for the construction of an algorithm and a program for solving a system of differential equations describing wave processes in soil.

3. Choice and substantiation of the initial values of mechanical characteristics of soil, of the parameters of dynamic load to carry out numerical calculations. Obtaining numerical results characterizing the changes in the parameters of waves in different sections of soil.

4. Analysis of the obtained numerical results of the changes in the parameters of waves in soil, depending on physical and mechanical characteristics of soil and its thickness.

5. Determination of the conditions for the quasistatic nature of dynamic strain in soil on the basis of studies, which ensure the reliability of the results of dynamic experiments on the DDL.

2. Methods

2.1. Statement of theoretical problem corresponding to the experiment on the DDL

The DDL-100 and DDL-150 devices described in [21] have a cylindrical soil receiving chambers with diameters of 0.1 or 0.15 m and a height of 0.03 m, into which a cylindrical soil sample of undisturbed or disturbed structure is placed. The bottom plane of the chamber, where the soil sample rests, is fixed. On the upper plane of the soil sample, there is a piston through which dynamic load created by the impact of load of a certain weight, freely falling along the guide bars, is transferred [21].

The wave pattern of experimental setup on the DDL is quite complicated. On the *x* axis of a cylindrical soil sample, a load acting from the upper piston varies from zero to maximum and then again to zero. According to the results obtained in [21], one of the conditions to ensure the quasi-static nature of the strain process is the ratio of the rise time of the load to the maximum and the fall time to zero. The rise time of the load should always be less than the fall time. This is a rigor condition to ensure the quasi-static nature of the process of soil strain on the DDL.

The load change is represented here as a half-sinusoid. In this case, the rise time equals to the fall time. This load uniformly acts on the upper plane of the soil layer located in the DDL soil-receiving chamber, which ensures the one-dimensional character of dynamic and static process of soil compression. The side walls of the soil-receiving chamber have sufficient smoothness, which allows the friction forces between soil and side wall to be zero. So, the forces of soil friction on the side surface are neglected.

A layer of soil 0.03 m thick is located at a distance $0-x_*$ along the *x* axis. At a distance $x = x_*$ there is an upper plane of the lower, absolutely rigid, fixed piston. This plane can be considered as a fixed obstacle.

According to the results of the above experiments, soil is considered to be an elastically viscous-plastic medium.

At $t=0$, load $\sigma=\sigma(t)$, varying by a sinusoidal law, begins to act on the soil layer. A wave is propagating in undisturbed soil. The front of this wave reaching the lower plane reflects from it. Under the effect of load $\sigma=\sigma(t)$ plastic strains are formed in soil. Consequently, a plastic wave propagates in soil [21].

After load $\sigma=\sigma(t)$ reaches its maximum, one more front is formed – the front of the maximum stress in soil, followed by unloading. At $\sigma=\sigma(t)=0$ the front of the wave of unloading propagates in soil. The above fronts, reflected from the lower piston ($x=x_*$) and from the upper piston ($x=0$) form a complex wave pattern.

Due to the fact that load $\sigma=\sigma(t)$ acting on the soil layer is continuous, these fronts are the lines of weak discontinuity, that is, the wave parameters do not have jumps (discontinuities) on these fronts. Only the first derivatives of the wave parameters on these fronts can have discontinuities; therefore, they are called weak discontinuity lines. This circumstance, as will be shown later, greatly simplifies the solution of the theoretical problem corresponding to the dynamic compression of the soil layer on the DDL.

The linearity of wave fronts mainly depends on the specific type of equation of state of soil and on the load. In case of linearity or even piecewise linearity of the equation of state of soil, which determines mechanical characteristics of soil, the wave fronts remain linear under continuous loading. In case of nonlinearity of the equation of state, these fronts are nonlinear. In case of nonlinearity of fronts, the problem of dynamic compression of a soil sample on the DDL is significantly complicated. The wave pattern and, therefore, the statement of the problem corresponding to the case under consideration, directly depends on the equation of state or the law of soil strain, on the basis of which mechanical characteristics of soil are determined.

In [21, 22, 33] it was shown that even at load values of 0.3–0.5 MPa, the process of dynamic strain in experiments demonstrated the elastic-viscoplastic properties of soil. Based on this, a soil model adequate to this process is chosen.

According to the analysis of the equation of state of soil [19–22, 33], the most complete law of soil strain, which takes into account the plastic strain of soil and its viscous properties under volume changes, is the law proposed in [22]. Let us consider this law in the process of strain in loess soil on the DDL, that is define mechanical characteristics of loess soil based on the model given in [22].

The model of an elastic-viscoplastic medium has the following form [22]:

$$\left.\begin{array}{c}
\dfrac{d\varepsilon}{dt}+\mu\varepsilon=\dfrac{d\sigma}{E_D dt}+\mu\dfrac{\sigma}{E_S}\quad at\quad \dfrac{d\sigma}{dt}>0,\ \dfrac{d\varepsilon}{dt}>0 \\
\dfrac{d\varepsilon}{dt}+\mu\varepsilon=\dfrac{d\sigma}{E_R dt}+\mu\sigma\left(\dfrac{1}{E_S}\quad\dfrac{1}{E_D}+\dfrac{1}{E_R}\right)+\mu\sigma_m\left(\dfrac{1}{E_D}\quad\dfrac{1}{E_R}\right)\quad at\quad \dfrac{d\sigma}{dt}<0,\ \dfrac{d\varepsilon}{dt}>0 \\
\dfrac{d\varepsilon}{dt}=\dfrac{d\sigma}{E_R dt}\quad at\quad \dfrac{d\sigma}{dt}<0,\ \dfrac{d\varepsilon}{dt}<0
\end{array}\right\} \tag{1}$$

where E_D is the modulus of dynamic compression of soil at $d\varepsilon/dt\to\infty$,

E_S is the modulus of static compression of soil at $d\varepsilon/dt\to 0$,

E_R is the unloading modulus, μ is the viscosity parameter, which is related to the viscosity coefficient by the ratio

$$\mu=\frac{E_D E_S}{\eta(E_D-E_S)} \tag{2}$$

where η is the coefficient of soil viscosity under volume changes,

σ_m is the maximum stress in soil particles. Equation (2) was obtained analytically in [22]. The principles and experimental grounds of the model construction (1) and relationship (2) were described in detail in [22].

The parameter η characterizes the dependence of the soil stresses on the strain rate $\dfrac{d\varepsilon}{dt}$. The value of η was determined experimentally [22, 34].

Strain ε, as applied to the experiments on the DDL-150, explicitly determines the volume change in the soil layer. Therefore, it can be considered as a volume strain, and σ as the pressure. In this case $\sigma = -P$, where P is the pressure. From this it follows that the equation of state of soil (1) is the law of variation of the spherical part of the stress tensor, that is, the law of the volume strain of soil. From (1) it is clear that in this case the basic mechanical characteristics of soil are E_D, E_S, E_R and μ.

Until now, the values of mechanical characteristics of soils mentioned above or other ones (based on other equations of soil state) have been determined directly from the results of experiments on the readings of the diagrams of soil compression.

However, dynamic compression of soil on the DDL is a rather complicated process; it is accompanied by a rather complex wave pattern. The values of stress and strain at different points of the soil sample along the *x* axis are affected by both the waves reflected from the lower and upper pistons and by their superposition. As a result, we can get the wrong values of mechanical characteristics of soil, just their apparent values, formed as a result of the superposition of incident and reflected waves.

Ensuring the quasi-static nature of the process of dynamic strain in soil eliminates the influence of wave processes on the values of mechanical characteristics of soil on the DDL. Despite the assessment of the quasi-static nature of the process of soil strain on the DDL [21], this condition needs to be assessed by studying the wave processes in a soil sample under dynamic load on the DDL.

To determine the quasistatic process of soil strain on the DDL, it is necessary to solve the equation of motion, which has the form:

$$\rho_0 \frac{\partial v}{\partial t} - \frac{\partial \sigma}{\partial x} = 0, \ \frac{\partial v}{\partial x} - \frac{\partial \varepsilon}{\partial t} = 0, \tag{3}$$

where ρ_0 is the initial density of soil,

v is the velocity of soil particles under compression.

The equation of one-dimensional soil motion in the DDL (3) is successively closed by the equations of state of soil (1). In the closed system of equations (3), (1), the unknowns are σ, ε and v, called the parameters of waves in soil or the parameters of stress-strain state of soil in the DDL.

To solve the system of differential equations (3), (1), it is necessary to state the initial and boundary conditions. The initial conditions of the problem are zero, since before the loading, the soil on the DDL is at rest, that is, it is considered undisturbed.

The boundary conditions of the problem, corresponding to the statement of the experiment, are the following: at $x = 0$ the upper plane of the soil layer in the DDL is affected by load $\sigma = \sigma(t)$ due to the motion of the upper piston; at $x = x_*$ the lower piston is fixed, that is $v = 0$, the velocity of the soil particles at this boundary is zero.

Mathematical formulation of the boundary conditions is as follows.

$$\left.\begin{aligned} &\sigma = \sigma(t) \ at \ \ x = 0, \ 0 < t < t_* \\ &\sigma = 0 \ \ at \ \ x = 0, \ t > t_* \\ &v = 0 \ \ at \ \ x = x_* \end{aligned}\right\} \tag{4}$$

where t_* is the duration of load.

On the front of the incident wave the following condition is met:

$$\begin{gathered} \langle \sigma \rangle = 0, \ \langle \varepsilon \rangle = 0, \ \langle v \rangle = 0 \\ at \ \ x = ct \end{gathered} \tag{5}$$

where c is the velocity of longitudinal wave propagation in soil,

$\langle \sigma \rangle$, $\langle \varepsilon \rangle$, $\langle v \rangle$ are the jumps in the wave parameters.

In case of the equations of state (1), the front line $x = ct$ and the lines of all other fronts are straight lines. This follows from the linearity of the equations that make up the law of soil strain (1).

Thus, the process of dynamic strain of a soil sample located in the DDL is described by the system of equations (1), (3). Having solved the system of equations (3), (1) with boundary conditions (4), (5) and zero initial conditions, the dynamic stress-strain state of soil can be determined.

2.2. Method and algorithm for solving the problem of dynamic compression of soil on the DDL

The system of equations (3), (1) is a hyperbolic one [22, 23]. At present, it is not possible to obtain an analytical solution for these equations. Therefore, we will use the numerical method of finite differences. First, following [22, 23], we will use the method of characteristics. The system of equations (3), (1) is a hyperbolic one and it has real characteristics and characteristic relations.

As a result of applying the method of characteristics, partial differential equations (3), (1) are reduced to ordinary differential equations. The application of the finite difference method to ordinary differential equations improves the accuracy of their solution compared to differential equations in partial derivatives [22, 23].

The successive closure of equations (3) by the equations of the law of soil strain (1) leads to three systems of equations that have the following characteristic relations on the characteristic lines:

$$\left.\begin{aligned} d\sigma - c\rho_0 dv &= c^2\rho_0\mu\left(\varepsilon - \frac{\sigma}{E_S}\right)dt,\ \frac{dx}{dt} = +c \\ d\sigma + c\rho_0 dv &= c^2\rho_0\mu\left(\varepsilon - \frac{\sigma}{E_S}\right)dt,\ \frac{dx}{dt} = -c \\ d\sigma - c\rho_0 dv &= c^2\rho_0\mu\left(\varepsilon - \frac{\sigma}{E_S}\right)dt,\ \frac{dx}{dt} = 0 \end{aligned}\right\} \tag{6}$$

$$\left.\begin{aligned} d\sigma - c_1\rho_0 dv &= c_1^2\rho_0\mu\left(\varepsilon - \sigma\left(\frac{1}{E_S}+\frac{1}{E_R}-\frac{1}{E_D}\right) - \sigma_m\left(\frac{1}{E_D}-\frac{1}{E_R}\right)\right)dt,\ \frac{dx}{dt} = +c_1 \\ d\sigma + c_1\rho_0 dv &= c_1^2\rho_0\mu\left(\varepsilon - \sigma\left(\frac{1}{E_S}+\frac{1}{E_R}-\frac{1}{E_D}\right) - \sigma_m\left(\frac{1}{E_D}-\frac{1}{E_R}\right)\right)dt,\ \frac{dx}{dt} = -c_1 \\ d\sigma + c_1^2\rho_0 d\varepsilon &= c_1^2\rho_0\mu\left(\varepsilon - \sigma\left(\frac{1}{E_S}+\frac{1}{E_R}-\frac{1}{E_D}\right) - \sigma_m\left(\frac{1}{E_D}-\frac{1}{E_R}\right)\right)dt,\ \frac{dx}{dt} = 0 \end{aligned}\right\} \tag{7}$$

$$\left.\begin{aligned} d\sigma - c_1\rho_0 dv = 0,\ \frac{dx}{dt} = +c_1 \\ d\sigma + c_1\rho_0 dv = 0,\ \frac{dx}{dt} = -c_1 \\ d\sigma - c_1^2\rho_0 d\varepsilon = 0,\ \frac{dx}{dt} = 0 \end{aligned}\right\} \tag{8}$$

where $c = \sqrt{E_D / \rho_0}$; $c_1 = \sqrt{E_R / \rho_0}$.

Using the method of characteristics, the system of differential equations (3), (1) is replaced by the system (6)–(8).

The derivation of the equations of characteristics and characteristic relations is given in detail in [22]. The system of equations (6)–(8) has been solved on a computer, with the transition to dimensionless variables and parameters using an implicit finite-difference scheme. The transition to dimensionless variables reduces the errors in numerical calculations associated with their accumulation in calculations when using large numbers.

The transition to dimensionless variables is carried out according to the formula:

$$\left.\begin{aligned} t^0 = \mu t,\quad x^0 = \mu x / c,\quad \sigma_0 = \sigma_0 / \sigma_{\max} \\ v^0 = v / v_{\max},\ \varepsilon^0 = \varepsilon / \varepsilon_{\max} \\ v_{\max} = \sigma_{\max} / c\rho_0,\ \varepsilon_{\max} = \sigma_{\max} / E_D \end{aligned}\right\} \tag{9}$$

where $\sigma_{\max}$ is the maximum value of the load acting at $x = 0$, that is, in the upper plane of the soil layer.

In dimensionless variables, the basic equations take the form

$$\frac{\partial \upsilon^0}{\partial t^0} - \frac{\partial \sigma^0}{\partial x^0} = 0, \quad \frac{\partial \upsilon^0}{\partial x^0} - \frac{\partial \varepsilon^0}{\partial t^0} = 0 \tag{10}$$

The laws of soil strain (1) in new variables is written as

$$\left.\begin{array}{c} \varepsilon^0 + \dfrac{d\varepsilon^0}{dt^0} = \dfrac{d\sigma^0}{dt^0} + \gamma\sigma^0 \\ \varepsilon^0 + \dfrac{d\varepsilon^0}{dt^0} = \beta\dfrac{d\sigma^0}{dt^0} + \sigma^0(\gamma + \beta - 1) + \sigma_m^0(1-\beta) \\ \dfrac{d\varepsilon^0}{dt^0} = \beta\dfrac{d\sigma^0}{dt^0} \end{array}\right\} \tag{11}$$

where $\gamma = E_D / E_S$, $\beta = E_D / E_R$.

The characteristic relations in the dimensionless form are determined by the following equations:

$$\left.\begin{array}{c} \text{at } d\sigma^0 / dt^0 > 0, \; d\sigma^0 / dt^0 < d\varepsilon^0 / dt^0 \\ d\sigma^0 \pm dv^0 = \left(\varepsilon^0 - \gamma\sigma^0\right)dt^0 \text{ along the lines } dx^0 / dt = \pm 1 \\ d\sigma^0 - d\varepsilon^0 = \left(\varepsilon^0 - \gamma\sigma^0\right)dt^0 \text{ along the lines } dx^0 / dt = 0 \end{array}\right\} \tag{12}$$

$$\left.\begin{array}{c} d\sigma^0 / dt^0 < 0, \quad d\sigma^0 / dt^0 < \beta d\varepsilon^0 / dt^0 \\ d\sigma^0 \pm \dfrac{dv^0}{\sqrt{\beta}} = \dfrac{1}{\beta}\left[\varepsilon^0 - (\gamma + \beta - 1)\sigma^0 - (1-\beta)\sigma_m^0\right]dt^0, \; dx^0 / dt^0 = \pm\dfrac{1}{\sqrt{\beta}} \\ d\sigma^0 - \dfrac{d\varepsilon^0}{\beta} = \dfrac{1}{\beta}\left[\varepsilon^0 - (\gamma + \beta - 1)\sigma^0 - (1-\beta)\sigma_m^0\right]dt^0, \; dx / dt = 0 \end{array}\right\} \tag{13}$$

$$\left.\begin{array}{l} \text{at } d\sigma^0 / dt^0 < 0, \quad d\sigma^0 / dt^0 = \beta d\varepsilon^0 / dt^0 \\ \sqrt{\beta} d\sigma^0 \pm d\upsilon^0 = 0, \; dx^0 / dt^0 = \pm\dfrac{1}{\sqrt{\beta}} \\ \sqrt{\beta} d\sigma^0 - d\varepsilon^0 = 0, \; dx^0 / dt^0 = 0 \end{array}\right\} \tag{14}$$

From equations (12)–(14) it is seen that the solution domains in plane x^0, t^0 have three sets of characteristic lines. Depending on the solution domain and conditions in (12)–(14), the incline of the characteristic lines varies, but they always remain straight lines.

The boundary conditions at dimensionless variables are:

$$\left.\begin{array}{c} \sigma^0 = \sigma(t) / \sigma_{\max} \;\; at \;\; x^0 = 0, \; 0 \le t^0 \le \mu t_* \\ \sigma(t) = \sigma_{\max}\sin(\pi t / t_*) \\ \sigma^0 = 0 \;\; at \;\; x^0 = 0, \; t^0 > \mu t \\ \sigma^0 = 0, \; \varepsilon^0 = 0, \; \upsilon^0 = 0 \;\; at \;\; x^0 = t^0 \\ v^0 = 0 \;\; at \;\; x^0 = x_0^* \end{array}\right\} \tag{15}$$

In case of the equation of state of soil (1) and boundary conditions (15), all front lines are the lines of weak discontinuity. There are no “jumps” in wave parameters on these fronts.

The absence of strong discontinuities at the wave fronts makes it possible to perform calculations on the time layers (Figure 1) by the “through” counting method, which does not take these fronts into account in the algorithm. This is the advantage of this statement of the problem.

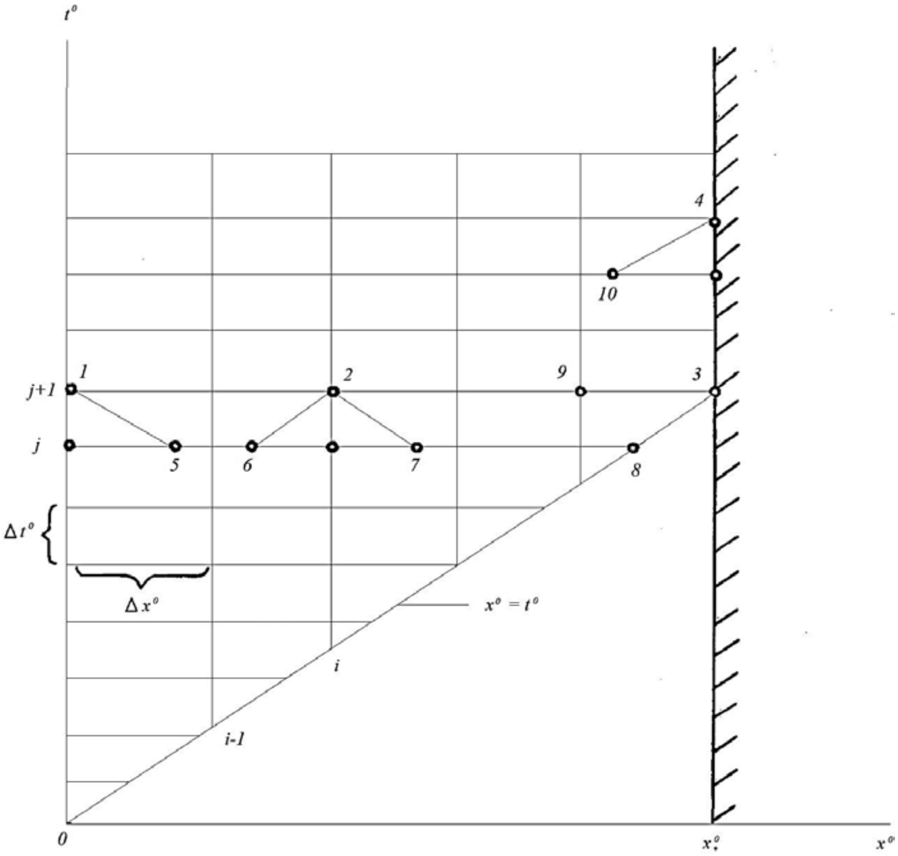

Figure 1. Discretization scheme for the solution domain and the types of calculation points.

In the calculation domain, in plane $x^0,\ t^0$ there are four types of calculation points 1–4: point 1 in cross section $x^0 = 0$, internal point 2, point 3 at the wave front, point 4 at the lower piston of the DDL. The wave parameters at these points are to be determined. Equation (12)–(14) are written in a difference form. For example, for point 2 in case of equation (12) they have the form:

$$\left.\begin{aligned}
&\left(\sigma_2^0-\sigma_6^0\right)+\left(v_2^0-v_6^0\right)=0.5\left[\varepsilon_2^0+\varepsilon_6^0-\gamma\left(\sigma_2^0+\sigma_6^0\right)\right]\Delta t^0\\
&\left(\sigma_2^0-\sigma_7^0\right)-\left(v_2^0-v_7^0\right)=0.5\left[\varepsilon_2^0+\varepsilon_7^0-\gamma\left(\sigma_2^0+\sigma_7^0\right)\right]\Delta t^0\\
&\left(\sigma_2^0-\sigma_i^0\right)+\left(\varepsilon_2^0-\varepsilon_i^0\right)=0.5\left[\varepsilon_2^0+\varepsilon_i^0-\gamma\left(\sigma_2^0+\sigma_i^0\right)\right]\Delta t^0
\end{aligned}\right\} \qquad (16)$$

Similarly, using the boundary conditions (15), the difference equations could be written for points 1, 3, 4 and for other cases. The values of the parameters in time layer j are considered known. Parameters at points 5, 6, 7, 8, 10 (Figure 1) are determined by linear interpolation. In time layer $j+1$, the parameter values are to be determined.

In the layer $j+1$, the parameters of the near-front point 9 are also determined by interpolation.

In computer-aided calculations, the values of Δt^0 and Δx^0 are given according to the Courant condition. For this problem it has the form:

$$\frac{\Delta x^0}{\Delta t^0} \geq 1/\sqrt{\beta} \qquad (17)$$

Condition (17) is necessary and sufficient so that the characteristics do not go beyond the boundaries of the quadrilateral cell. Otherwise, the stability of computer calculation is lost.

Thus, the solution of a system of equations (12) – (14) with boundary conditions (15) is reduced to solving a system of linear algebraic equations of (16) type. In (16), $\sigma_2^0,\ \varepsilon_2^0,\ v_2^0$ are the unknowns.

First, equation (16) is solved relative to these unknowns. Further, using these solutions and similar solutions for other types of points, an algorithm for solving the problem is built.

On the basis of the above algorithm and the solution of the problem shown in calculation scheme in Figure 1, a program for solving the problem has been compiled in the Pascal algorithmic language in the DELPHI environment. The developed program is implemented on a computer. The stability of the algorithm of problem solution is verified by a numerical experiment using different values of Δt^0 and Δx^0 and initial parameters of the problem. The results of numerical experiments have shown that the stability of computational scheme and algorithm is fully ensured by the Courant condition. The reliability and accuracy of the methods used for solving equations (1) – (2), i.e. the method of characteristics with the successive application of the finite difference method according to an implicit scheme is considered in [22, 34]. The drawn up program in each cell of the discrete grid (Figure 1) is controlled by the condition (17). The results of comparison of numerical solutions of the problem of plane wave propagation in elastic-viscoplastic medium (1) with an analytical solution in elastic and elastic-plastic media are given in [34]. These results [34] show that the method used makes it possible to obtain numerical solutions of wave problems with high accuracy and reliability.

2.3. Validation of the algorithm and program for problem solution

The algorithm and program for problem solution developed above are verified by comparing the results of numerical solutions and experiments. To do this, the full-scale experiment given in [34] is chosen. In [34], the propagation of an explosive wave in loess soil has been studied experimentally in full-scale (field) conditions. The statement of the experiment in [34] is one-dimensional. The behavior of loess soil is described by equations (1)–(3). The initial conditions in the experiment are zero, the boundary conditions (4), in this case, have the following form [34]:

$$\begin{aligned} &\sigma = \sigma_{\max}(1 - t/\theta)^3 && 0 \le t \le \theta \\ &\sigma = 0 && t \ge \theta \end{aligned} \tag{18}$$

where $\sigma_{\max} = 30 \cdot 10^5$ Pa is the maximum value, and $\theta = 10^{-2}$ is the time of action of explosive load. Mechanical characteristics of soil, as an elastic-viscoplastic medium (1), have been determined on the basis of field experiments in [34]. They are as follows: $\gamma = 4, \beta = E_D / E_R = 0.4;$ μ = 1000 s^{-1}, $\mu\theta = 10$.

Load (18) in a dimensionless form, on the basis of equations (9) has the form

$$\begin{aligned} &\sigma^0 = (1 - t^0/\mu\theta)^3 && 0 \le t^0 \le \mu\theta \\ &\sigma^0 = 0 && t^0 \ge \mu\theta \end{aligned} \tag{19}$$

Numerical solution of the problem of explosive wave propagation in soil initiated by load (19) is obtained using the algorithm and program developed above. Dimensionless numerical solutions are converted to dimensional ones, taking into account the experimental values of parameters $\varepsilon_{\max} =$ 0.116; $c =$ 100 m/s; $\rho_0 =$ 1500 kg/m^3, $\sigma_{\max} =$ 30·10^5 Pa, E_D = 280·10^5 Pa, E_s =70·10^5 Pa, E_R = 700·10^5 Pa, given in [34].

In calculation program for solving experimental problem, the distance from the initial section of soil to the obstacle x_* is taken as sufficiently large ($x_* =$ 100 m), then, the statements of the experiment and theoretical problem completely coincide. The statement of the experiment and the results obtained are given in detail in [34].

Figures 2 and 3 show the graphs of dependences $\sigma(t)$ and $\varepsilon(t)$. Curves 1 and 2 correspond to experiments [34] related to distances $x =$ 0.2 m and 0.6 m from the initial section of soil $x =$ 0, where the load acts (19). Curves 1* and 2* refer to the results of numerical calculations obtained according to the developed algorithm and program.

Figure 4 shows the results of comparisons of soil compression diagram $\sigma(\varepsilon)$, constructed using experimental and theoretical (numerical calculations) dependences $\sigma(t)$ and $\varepsilon(t)$, shown in Figures 2 and 3. Here curve 1 is an experiment, curve 2 is a numerical solution obtained based on the program for solving the problem under consideration.

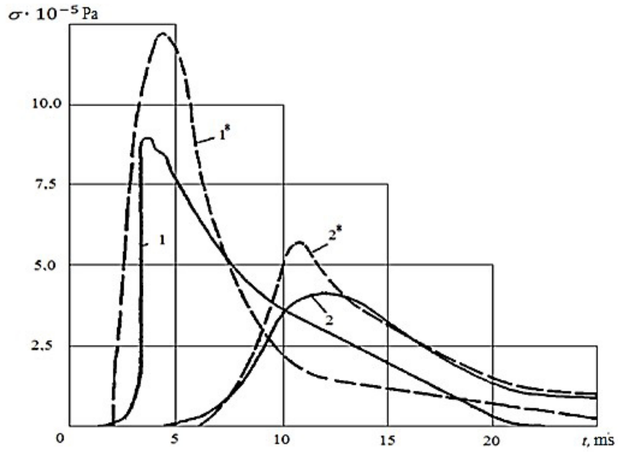

Figure 2. Change in stresses over time. Solid lines – experiment, dotted lines – theory.

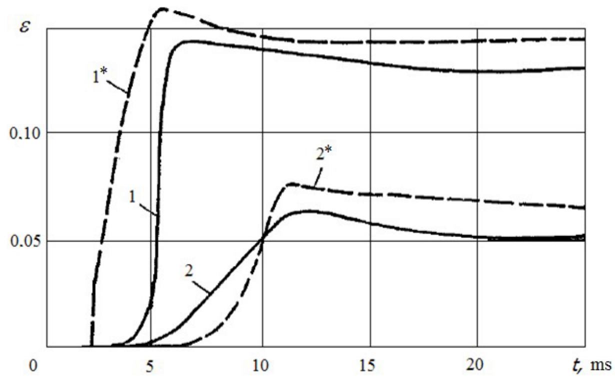

Figure 3. Change in strain over time. Solid lines – experiment, dotted lines – theory.

From Figures 2–4 it can be seen that the experiment and the numerical solution obtained on the basis of the algorithm and computer program developed above coincide qualitatively and satisfactory. The maximum stress values differ by 30 %, and the maximum strain values by 15–20 %, which is quite satisfactory and is within the limits of experimental accuracy. The scatter of data is 15–30 %. This result is quite acceptable for testing the theory and a full-scale experiment in the dynamics of soil [18–23].

Thus, the results of comparison of theoretical calculations with the data of a full-scale experiment show that the developed algorithm and program for calculating the problem in question give quite satisfactory results. This means that the algorithm and program developed above for solving the problem in question allow the study of wave processes in soil within the limits of the problem statement, described by equations (1)–(3).

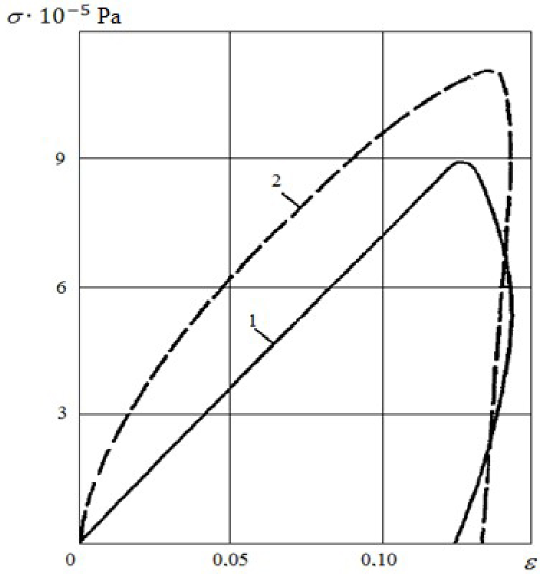

Figure 4. Diagram σ (ε), curve 1 – experiment, curve 2 – numerical solution.

3. Results and Discussion

3.1. Results of calculations of wave parameters and patterns of strain of loess soil samples, placed in the DDL

The patterns of plane wave propagation in soil as in an elastic-viscoplastic medium were theoretically investigated in [22, 23, 36]. Theoretical problem according to the above method, in case when soil is a linear viscoelastic medium (a standard-linear body), has been numerically solved using the method of characteristics [22, 34]. In [22, 34], the problems of wave interaction with a moving non-deformable obstacle in a viscoplastic medium – soil – were considered. The wave interaction with a deformable obstacle in a viscoelastic medium was studied in [23].

The interaction of a continuous compression wave with a rigidly fixed obstacle in an elastic-visco-plastic medium has not yet been studied. So, the solution to the problem considered here is obtained for the first time.

The considered problem of the interaction of a continuous plane compression wave with a rigidly fixed obstacle in an elastic-viscous-plastic medium – soil – is studied on the DDL to determine the conditions of quasistatic process of dynamic strain of soil. The compiled algorithm and the program for solving the problem make it possible to investigate (on the results of numerical solutions) the change in wave parameters in soil and the patterns of soil strain, not only in relation to the DDL tests.

The main parameters (initial data) of the problem to conduct the calculations are:

– soil characteristics – $\gamma = E_D / E_S$, $\beta = E_D / E_R$, ρ_0, c, μ;

– load characteristics – $\sigma_{\max}$, t_*;

– distances from the initial section of soil to the obstacle – x_*.

Table 1. Options for computer calculations at various values of the parameters.

№ of option	γ	β	x_*, m	t_*, s	μ, s^{-1}
1	2	0.5	2.8	0.1	100
2	4	0.5	2.8	0.1	100
3	2	0.5	0.28	0.1	100
4	2	0.5	0.03	0.1	100
5	4	0.5	0.03	0.1	100
6	1.05	0.5	0.03	0.1	1000
7	2	0.25	0.03	0.01	100
8	2	0.5	0.03	0.01	100
9	2	0.5	0.03	0.001	100

Options for computer calculations at various values of the parameters are given in Table 1. They are selected based on the parameters of seismic load in loess soils [23]. Based on the results of experiments [23], the value of maximum load $\sigma_{\max}$ for all the options is taken as equal to 0.5 MPa. The initial density of soil ρ_0 is 1500 kg/m^3, the velocity of longitudinal wave propagation is $c = 100$ m/s. Values of ρ_0 and c for option 6 have been changed: $\rho_0 =$ 2000 kg^3/m, $c = 1000$ m/s. Option 6 corresponds to elastic-plastic soil, where the density of soil and, accordingly, the velocity of longitudinal wave propagation in soil are more significant than in elastic-viscoplastic soil [23].

When choosing the options listed in Table 1, possible values of $\gamma, \beta, x_*, t_*, \mu$ have been taken into account [21–23].

The value of the modulus of dynamic compression E is determined by formula $E_D = c^2 \rho_0$, the static compression modulus by $E_S = E_D / \gamma$, and the unloading modulus by $E_R = E_D / \beta$.

Numerical solution of the problem is obtained in a dimensionless form. Then, using relations (9), they are transformed into dimensional ones.

Let us consider the results of computer calculations.

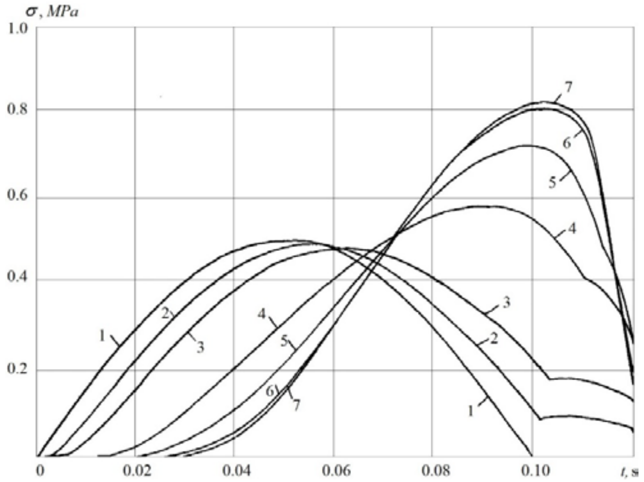

Figure 5. Stress variations in soil sections: 1) $x = 0$; 2) $x = 0.28$; 3) $x = 0.56$; 4) $x = 1.15$; 5) $x = 1.2$; 6) $x = 2.55$; 7) $x = 2.8$ m.

Figure 5 shows the longitudinal stress σ variation over time t for different sections of soil for option 2 (Table 1). Curves 1-7 refer to the sections of soil at x = 0; 0.28; 0.56; 1.15; 1.2; 2.55 and 2.8 m, respectively. At $x = x_* = 2.8$ m there is a fixed and non-deformable obstacle.

In theoretical calculations there is a possibility of arbitrary positioning of the lower piston of device. In option 2, the obstacle (lower piston) is specifically set aside at a distance of $x_* = 2.8$ m to consider the pattern of change in wave parameters in soil.

Note that in dependencies $\sigma(t)$, hereinafter, the stress σ should be understood as the compression stress. In the figures, a negative sign in front of σ is omitted for simplicity. Similarly, the strain under compression is taken as positive.

As seen from Figure 5, under conditions (15), at $x = 0$ a half-period of sinusoidal load is acting on soil (curve 1). At a distance of $x = 2.83$ m there is an obstacle. In this option, at $t_* = 0.1$ s of load action, the wave 3.5 times runs to the obstacle and back. As a result of the superposition of waves reflected from the lower and upper boundaries, different values of stresses are observed on different sections of the soil layer. On the obstacle, the maximum stress is 1.6 times greater than in the initial section (curve 7). In other sections of soil, the maximum stress value is also greater than in the initial section. A similar picture is observed at dependencies $\varepsilon(t)$ (Figure 6). Here, the maximum strain is reached on the obstacle (curve 7). The values of residual strains in soil sections are significant. Curves 1–7 refer to the same distances as shown in Figure 5.

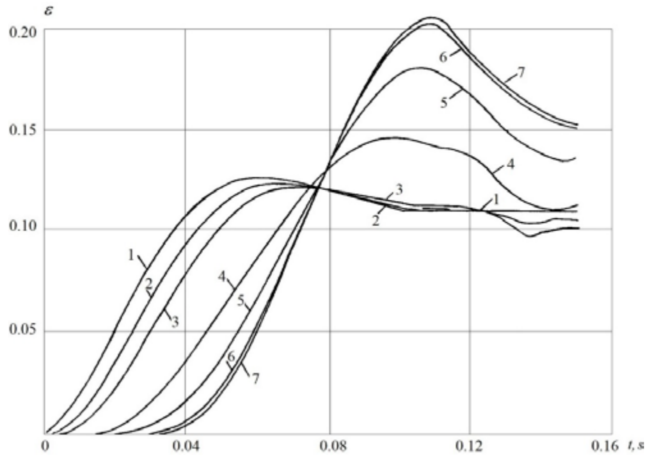

Figure 6. Strain variation in soil sections: 1) $x = 0$; 2) $x = 0.28$; 3) $x = 0.56$; 4) $x = 1.15$; 5) $x = 1.2$; 6) $x = 2.55$; 7) $x = 2.8$ m.

Dependences $\sigma(t)$ and $\varepsilon(t)$ given in Figures 5 and 6 show that the changes in stress and strain in different sections of soil under dynamic loads differ. This circumstance should be taken into account when determining mechanical characteristics of soil from similar experiments.

The change in velocity (mass velocity) over time at the same sections of soil for option 2 is shown in Figure 7. Here, the maximum velocity is reached in the cross section $x = 0$. Later, it decreases, and on the obstacle the values of velocities are zero (line 7).

The change in soil displacements at different sections of soil is shown in Figure 8. The initial section of soil under loading, as expected, shows significant displacements (curve 1). Subsequent sections of soil are less displaced (curves 2-6), and on the obstacle the displacement of soil is naturally absent (line 7).

As seen from Figures 5–8 the wave processes in soil, in this option, are of significant importance. When conducting similar experiments (at considerable thickness of the soil layer) to define mechanical characteristics of soil under dynamic load, it is necessary to take into account the effect of wave processes on the values of stress and strain in soil.

Compression diagrams for soil sections (option 2) are shown in Figure 9. Here elastic-viscoplastic strain of soil is observed in all sections of soil. However, quantitatively these dependences $\sigma(\varepsilon)$ for different sections of soil differ. At the values of initial data of option 2, significant residual strains of soil have been observed. The maximum stress values are slightly behind the maximum strain values. As seen from Figure 9, the soil compression diagrams on sections x=0 and x=2.8 m differ significantly. Mechanical characteristics of soil, determined on the basis of these diagrams, will also differ significantly.

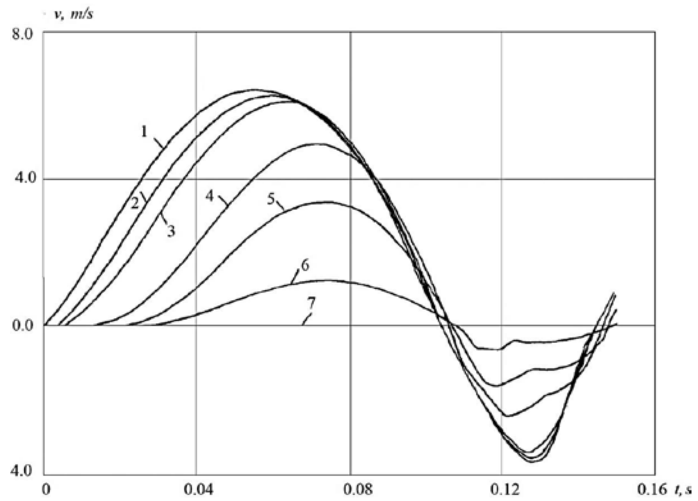

Figure 7. Changes in particle velocity in soil sections: 1) $x = 0$; 2) $x = 0.28$; 3) $x = 0.56$; 4) $x = 1.15$; 5) $x = 1.2$; 6) $x = 2.55$; 7) $x = 2.8$ m.

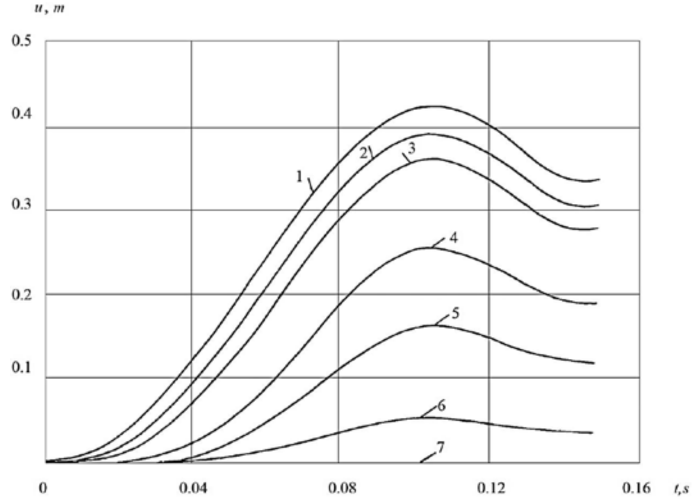

Figure 8. Displacements of soil particles in sections: 1) $x = 0$; 2) $x = 0.28$; 3) $x = 0.56$; 4) $x = 1.15$; 5) $x = 1.2$; 6) $x = 2.55$; 7) $x = 2.8$ m.

In this case, the values of mechanical characteristics of soil are influenced by the wave process in soil. These mechanical characteristics of soil are not true. To obtain true values of mechanical characteristics of soil, it is necessary to exclude the effect of wave processes on the stress-strain state of soil under dynamic loading. That is, the soil compression diagrams in all sections of soil should be identical.

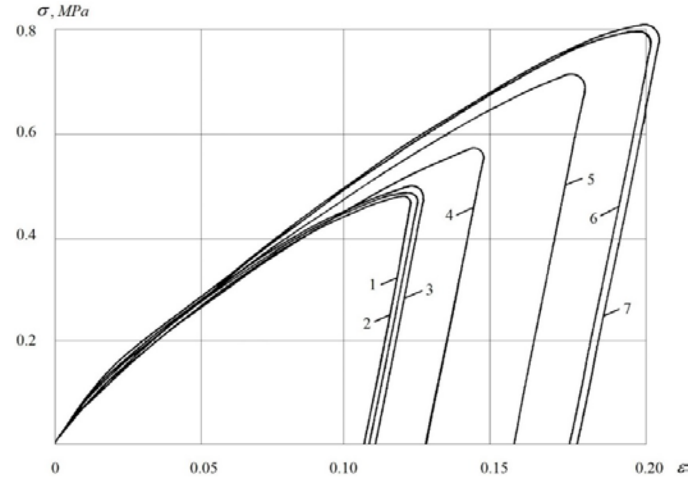

Figure 9. Stress-strain dependences for soil sections: 1) $x = 0$; 2) $x = 0.28$; 3) $x = 0.56$; 4) $x = 1.15$; 5) $x = 1.2$; 6) $x = 2.55$; 7) $x = 2.8$ m.

Results of calculations for option 2 at $\gamma = 4$ (Figures 5–9) show that an increase in γ corresponding to an increase in viscous properties of soil leads to a decrease in the maximum stress values as compared to option 1. The values of maximal and residual strains increase with increase in γ. The increase in γ also leads to an increase in the velocity values of soil particles. Accordingly, the values of soil displacement increase.

At increase in γ, the compression diagrams $\sigma(\varepsilon)$ for considered soil sections do not qualitatively change, but they differ quantitatively as compared to option 1. In option 2, the values of maximum stresses are less, the values of residual strains are greater, and the lag of maximum strains from maximum stresses is greater as compared to option 1. In quantitative terms, the double increase in γ of considered sections of soil leads to 1.1 times decrease in maximum stresses, to approximately 2 times increase in maximum strains and residual strains, to approximately 1.5 times increase in velocity and displacement.

In case of 10 times reduction of the distance from initial section to the obstacle (option 3) at γ = 2, β = 0.5, a significantly different wave pattern is observed in the soil layer as compared to options 1 and 2 (Figure 10).

Figure 10 shows the stress changes for the sections of soil layer at $x_* = 0$; 0.028; 0.056; 0.15; 0.2; 0.254 and 0.28 m for curves 1-7, respectively. Here $x_* = 0.28$ m, that is, the obstacle is at a distance of 0.28 m from the initial section of soil. As seen from Figure 10, in this case the stress values in all sections of the soil layer are almost the same (curves 1-7). At decrease in x^*, the strain values for all cross sections merge into one curve (Figure 11).

The change in velocity of soil particles for the considered cross sections with decreasing distance to the obstacle becomes more complex (Figure 12). Here the results of multiple wave reflections from the rigid surfaces of the upper and lower pistons are observed. During the time of load effect the wave 35 times runs back and forth from the initial section to the obstacle. The value of displacements in this case is important; it is about 10 times less than in options 1 and 2. Under the same dynamic load, a decrease in thickness of the soil layer leads to a decrease in soil displacement, while the strains remain almost the same in all sections of soil (Figure 11). As expected from Figures 10 and 11, for option 3 the dependences $\sigma(\varepsilon)$ for all cross sections of the layer become identical.

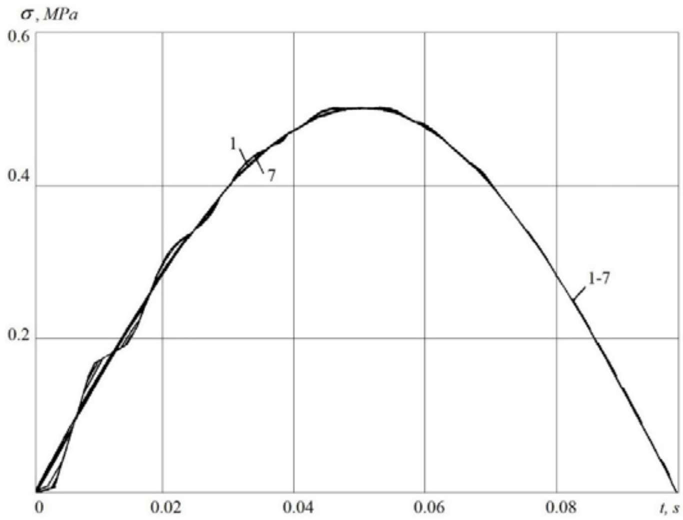

Figure 10. Stress variation in soil sections at x_* = 0.28 m.

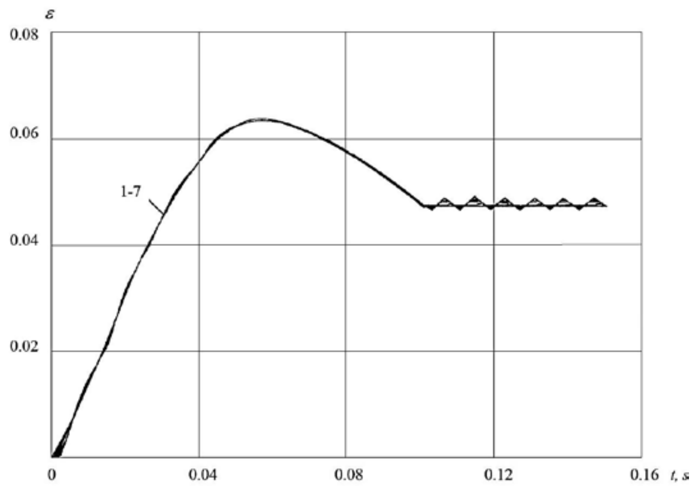

Figure 11. Strain variation in soil sections at x_* = 0.28 m

The results of calculations of option 3 (Figures 10–12) show that even at the soil layer thickness x_* = 0.28 m the conditions for quasi-static nature of soil compression for a given dynamic load are met, that is, the stress and strain values for all soil sections become identical. However, this circumstance depends not only on the thickness of the soil layer, but also on the parameters of dynamic load.

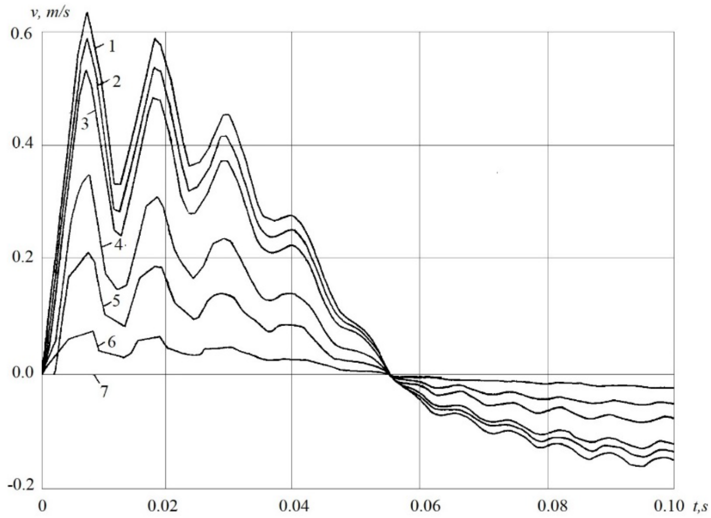

Figure 12. Velocity variation in soil sections: 1) $x = 0$; 2) $x = 0.028$; 3) $x = 0.056$; 4) $x = 0.15$; 5) $x = 0.2$; 6) $x = 0.255$; 7) $x = 0.28$ m.

In general, the patterns of changes in wave parameters in soil, as shown by the results of the above numerical solutions, depend on the characteristics of soil, on the thickness of the soil layer and, of course, on the characteristics of dynamic load. The latter is especially important to ensure the quasi-static nature of the process of soil strain in experiments. The study of this issue is considered on the examples for options 4–9 (Table 1).

3.2. Quasistatic nature of the process of soil strain on the DDL

As shown above, the quasistatic process of dynamic strain in soil on the DDL depends on the thickness of the soil layer. At considerable thicknesses of the layer $x_* > 0.3$ m and the time of load action $t_* \leq 0.1$ sec, we can assume that the quasistatic nature of the process of soil strain is not ensured (options 1 and 2). This means that the values of stress and strain in different sections of soil differ significantly. To refer these differences in experiments to the scattering of experimental data will be incorrect and will lead to incorrect results in statistical processing.

So, it is very important to exclude the differences in dependences $\sigma(t)$ and $\varepsilon(t)$ related to the effect of waves reflected from the lower piston. In experiments, complete agreement of dependences $\sigma(t)$ and $\varepsilon(t)$, fixed by sensors installed above and below the soil layer, is necessary. This is ensured, first of all, by the condition of a quasi-static process of dynamic strain in soil. In other words, when dynamic load is applied, the soil layer strains almost statically, that is, in all its points stress and strain values are identical. Such dynamic strain in soil is called a quasi-static strain.

The thickness of the soil layer in the experiments on the DDL equals to $x_* = 0.03$ m [21]. Based on this, when choosing options 4–9 (Table 1), x_* is taken as equal to 0.03 m. Using as example the calculation of option 4, consider the change in wave parameters in soil layer of 0.03 m thick and load time of $t_* =$ 0.1 s.

In options 4–9, the changes in wave parameters are given in the sections of soil layers: $x = 0$; 0.0028; 0.0056; 0.015; 0.02; 0.0255 and 0.03 m.

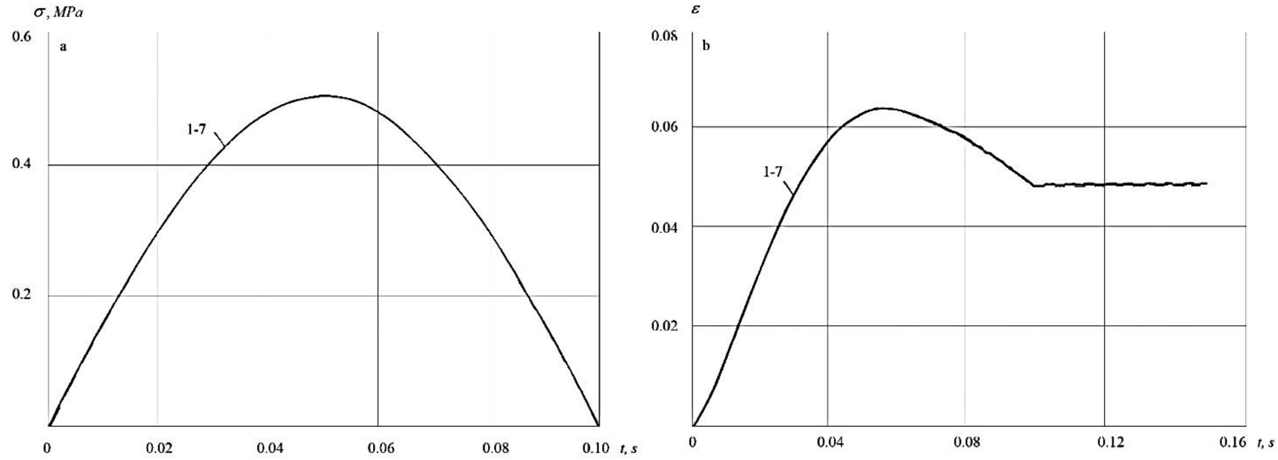

Figure 13. Variation in stress (a) and strain (b) in soil sections at x_* = 0.03 m.

Figure 13a shows the dependencies $\sigma(t)$ related to the above distances (curves 1–7) for option 4 (Table 1). As seen from Figure 13a, at time of load action $t_* = 0.1$ s, the dependences $\sigma(t)$ for all sections of soil are exactly the same. This proves the complete quasistatic nature of the process of soil strain on the DDL at a given dynamic load. In option 4, the dependences $\varepsilon(t)$ for the considered sections of the soil layer also completely agree (Figure 13b).

The changes in particle velocity are completely different for the considered soil sections. At time of load action of 0.1 s (option 4), the wave 333 times runs back and forth in the soil layer. As a result of multiple reflections of waves from the upper and lower pistons and their superposition, we have a complex pattern of velocities. The displacements of soil particles in the considered soil sections are also different. In this case, the maximum displacement of the upper piston is approximately 0.002 m.

Increasing the value of γ at constant values of other parameters (option 5) does not affect the dependencies $\sigma(t)$. Dependencies $\varepsilon(t)$ change quantitatively. Maximum and residual values of strains increase. Dependencies $v(t)$ become less sensitive to the reflected waves. The maximum values of the velocity of soil particles increase by an order of magnitude.

At increase in γ, the compression diagram $\sigma(\varepsilon)$ remains the same for all sections of soil. The increase in γ (which corresponds to an increase in viscous and plastic properties of the medium) does not affect the quasi-static nature of the process of soil strain on the DDL, as the results of calculations show.

A decrease in γ, which corresponds to an increase in elastic properties of soil, does not affect the quasi-static nature of the process of soil strain on the DDL as well. This case is considered on the example of option 6. Here γ = 1.05, accordingly: c = 1000 m/s and μ = 1000 s^{-1}. The other parameters remain unchanged. At the loading time of $t_* = 0.1$ s, the wave more than 3000 times runs through a layer of soil of 0.03 m thick. Dependencies $\sigma(t)$ and $\varepsilon(t)$ for all sections of soil are completely identical.

It is characteristic that with an increase in elastic properties of soil, the value of residual strain at the lower piston is about two times less than in other sections. This is due to the increase in number of wave reflections from the lower piston. In this case, the displacements of soil particles become significantly smaller than in cases when γ = 2 and γ = 4.

At γ = 1.05, the soil compression diagram $\sigma(\varepsilon)$ corresponds to the diagram of elastic-plastic medium. Here the values of residual strains decrease, the maximum values of stresses and strains coincide over time. However, the quasistatic nature of the process of soil strain is not violated.

The effect of an increase in parameter $\sigma(\varepsilon)$ on the calculation results is shown on the example of option 7. Here, β = 0.25. The remaining values of the parameters are the same as in option 4. A decrease in β, which corresponds to an increase in plastic properties of soil, leads to an increase in residual strain of soil. A decrease of β does not affect the values of the maximum displacements.

According to the soil compression diagram, a decrease in β does not affect the quasi-static process of soil strain on the DDL.

Reducing the load time t_* by 10 times (option 8) leads to a noticeable violation of the quasi-static nature of the process of soil strain. In this case, the stress values in the sections of soil layer differ by 10–15 %. Similar differences are observed in the values of strains. In dependencies $v(t)$ and $u(t)$ high-frequency oscillations associated with a much shorter load time are observed. Violation of the quasi-static nature of the process is also observed in dependencies $\sigma(\varepsilon)$. The quasi-static nature of the process is noticeably disturbed in the stage of unloading of the soil layer.

Reducing the load time t_* by 100 times (option 9), as compared to option 4, leads to an explicit violation of quasi-static process of soil strain on the DDL. At $t_* = 0.001$ s, the values of stresses and strains in the considered sections of the soil layer differ significantly. On the upper and lower pistons, their values differ about twice. At a decrease in time of action of dynamic load, the values of stress and strain are significantly affected by the waves reflected from the lower piston. At $t_* = 0.001$ s, the pattern of changes in dependencies $v(t)$ and $u(t)$ has also changed. There are no high-frequency oscillations.

At $t_* = 0.001$ s, dependencies $\sigma(\varepsilon)$ change significantly. The process of soil strain becomes an elastic-plastic one. The quasistatic nature of the process is completely violated under soil unloading.

The results of calculations of the options listed in Table 1 allow us to estimate the quasistatic nature of the process of soil strain on the DDL. To do this, let us determine half the wavelength, propagating in soil on the DDL:

$$\lambda = ct_*. \tag{20}$$

Introduce the ratio of half the wavelength λ to the thickness of the soil layer. The data obtained for options 1–9 are shown in Table 2.

Table 2. The data obtained for options 1–9.

№ of option	c, m/s	t_*, s	x_*, m	λ, m	λ / x_*
1	100	0.1	2.8	10	3.5
2	100	0.1	2.8	10	3.5
3	100	0.1	0.28	10	35
4	100	0.1	0.03	10	333
5	100	0.1	0.03	10	333
6	1000	0.1	0.03	100	3333
7	1000	0.1	0.03	10	333
8	100	0.01	0.03	1	33
9	100	0.001	0.03	0.1	3.3

According to the results of calculations (options 1–9), for options 1, 2, 9, the quasistatic process of soil strain on the DDL is not observed. For options 3 and 8, the quasistatic process is observed satisfactorily. For options 4–7, the quasi-static process is observed with high accuracy.

Based on the data of Table 2, to maintain the quasi-static nature, the following condition must be met:

$$\lambda / x_* = \lambda / \delta_o > 50 \tag{21}$$

When the ratio of half the wavelength to the thickness of the soil layer δ is more than 50, the quasi-static nature of the process of soil strain under dynamic compression on the DDL is fully ensured. The greater the ratio λ / δ, the more accurate the quasi-static nature of the process of soil strain. Consequently, the reliability of the results of experiments obtained on the DDL increases.

4. Conclusions

1. A problem on propagation and interaction of plane waves with a rigidly fixed obstacle is set; the problem corresponds to dynamic compression of soil samples on a device of dynamic loading (DDL), designed to define the laws of dynamic strain and on their basis to determine mechanical characteristics of soil.

2. An algorithm and a program for solving the wave problem on a computer using the characteristic method, the finite difference method in an implicit scheme have been developed. The stability conditions of the algorithm and the program for solving the problem are determined and realized on a computer.

3. For known physical-mechanical characteristics of loess soils and parameters of the DDL-150, numerical results have been obtained in the form of changes in stress, strain, particle velocity and displacements over time for different sections of soil.

4. The changes in the stress-strain state have been analyzed for different values of dynamic load, of the soil layer thickness in the DDL and physical-mechanical characteristics of soil.

5. The conditions for the quasistatic nature of dynamic strain in soil on the DDL have been determined depending on the parameters of load, the wavelength and the thickness of the soil layer in the DDL. It is established that when the ratio of half the wavelength to the thickness of the soil layer in the DDL is 50 or more, the quasi-static nature of the process of dynamic strain in soil on the DDL is fully ensured.

References

1. Qingfend, L., Chengrui, C., Benhai, Z., Bo, M.. Loess Soil Stabillization by Means of SiO2 Nanoparticles. Soil Mechanics and Foundation Engineering. 2017. Vol. 54. No. 6. Pp. 409–413.
2. Nguyen, F.Z. Issledovaniya zavisimosti prochnostnykh svoystv grunta ot yego fizicheskogo sostoyaniya [Study of Dependence of Soil Strength Properties on its Physical State]. Magazine of Civil Engineering. 2012. No. 9 (35). Pp. 23–28. (rus)
3. Goldin, A.L., Nguyen, F.Z. Postroyeniye trayektorii napryazheniy dlya nenasyshchennogo grunta pri konsolidirovanno-nedrenirovannykh ispytaniyakh v stabilometre [Construction of a Stress Trajectory for Unsaturated Soil in Consolidated-Un-drained Tests in a Stabilometer]. Magazine of Civil Engineering. 2012. No. 9 (35). Pp. 35–40. (rus)
4. Morton, J.P., O'Loughlin, C.D., White, D.J. Estimation of soil strength in fine-grained soils by in strumented free-fall sphere tests. Géotechnique. 2016. Vol. 66. No. 12. Pp. 959–968.
5. Chow, S.H., Airey, D.W. Soil strength characterisation using free-falling penetrometers. Géotechnique. 2013. Vol. 63. No. 13. Pp. 1131–1143.
6. Tadao, E. Effects of grading and particle characteristics on small strain properties of granular materials. Soils and Foundations. 2016 Vol. 56. No. 4. Pp. 745–750.
7. Ignatova, O.I. Deformation characteristics of the Jurassic clayey soils of Moscow. Soil Mechanics and Foundation Engineering. 2009. Vol. 46. No. 5. Pp. 196–201.
8. Aleksandrov, A.S. Plasticheskoye deformirovaniye granodiortovogo shchebnya i peschano-graviynoy smesi pri vozdeystvii trekhosnoy tsiklicheskoy nagruzki [Plastic Strain of Granodiorite Crushed Stone and Sand- Gravel Mix under the Influence of a Three-Axis Cyclic Load]. Magazine of Civil Engineering. 2013. No. 4(39). Pp. 22–34. (rus)
9. Loginova, I.I., Artomonova, D.A., Stolyarov, O.N., Melnikov, B.Ye. Structure Effect on Viscoelastic Properties of Geosynthetic Material. Magazine of Civil Engineering. 2015. No. 4(56). Pp. 11–18. DOI: 10.5862/MCE.56.2 (rus)
10. Hui, Zhou, Yanshuang, Yang, Chuanqing, Zhang, Dawei, Hu. Experimental investigations on loading-rate dependency of compressive and tensile mechanical behaviour of hard rocks. European Journal of Environmental and Civil Engineering. 2015. Vol. 19. No. s1. Pp. s70–s82.
11. LamineIghil, Ameur, Guillaume, Robin, Mahdia, Hattab. Elastic properties in a clayey material under mechanical loading – an estimation through ultrasonic propagations. European Journal of Environmental and Civil Engineering. 2016. Vol. 20. No. 9. Pp. 1127–1146.
12. Chow, S.H., O'loughlin, C.D., Randolph, M.F. Soil strength estimation and pore pressure dissipation for free-fall piezocone in soft clay. Géotechnique. 2014. Vol. 64. No. 10. Pp. 817–827.
13. Kostas, Senetakis, Anastasios, Anastasiadis, Kyriazis, Pitilakis. Normalized shear modulus reduction and damping ratio curves of quartz sand and rhyolitic crushed rock. Soils and Foundations. 2013. Vol. 53. No. 6. Pp. 879–893.
14. Yumin, Chen, Hanlong, Liu, Haiqing, Wu. Laboratory study on flow characteristics of liquefied and post-liquefied sand. European Journal of Environmental and Civil Engineering. 2013. Vol. 17. No. s1. Pp. s23–s32.
15. Maheshwari, B., Kale, S., Kaynia, A. Dynamic properties of Solani sand at large strains: a parametric study. International Journal of Geotechnical Engineering. 2012. Vol. 6. No. 3. Pp. 353–358.
16. Cengiz, Kurtulus, Maral, Üçkardeş, Umut, Sarır, Onur Güner, Ş. Experimental studies in wave propagation across a jointed rock mass. Bulletin of Engineering Geology and the Environment. 2011. Vol. 71. No. 2. Pp. 231–234.
17. Wang, Y., Li, X., Zheng, B. Experimental study on mechanical properties of clay soil under compression by ultrasonic test. European Journal of Environmental and Civil Engineering. 2018. Vol. 22. No. 6. Pp. 666–685.
18. Verrucci, L., Lanzo, G., Tommasi, P., Rotonda, T. Cyclic and dynamic behaviour of a soft pyroclastic rock. Géotechnique. 2015. Vol. 65. No. 5. Pp. 359–373.
19. Vovk, A.A, Zamyshlyayev, B.V., Yevterev, L.S., Belinskiy, I.V., Mikhalyuk, A.V. Povedeniye gruntov pod deystviyem impulsivnykh nagruzok [Behavior of Soils under the Influence of Impulse Loads]. Kiyev: Naukova dumka, 1984. 286 p. (rus)
20. Zamyshlyayev, B.V., Yevterev, L.S. Modeli dinamicheskogo deformirovaniya i razrusheniya gruntovykh sred [Models of Dynamic Strain and Damage of Soil Medium]. Moscow: Nauka, 1990. 216 p. (rus)
21. Rykov, G.V., Skobeyev, A.M. Izmereniye napryazheniy v gruntakh pri kratkovremennykh nagruzkakh [Stress Measurement in Soils under Short-Term Loads]. Moscow: Nauka, 1978. 168 p. (rus)
22. Lyakhov, G.M. Osnovy dinamiki vzryvnykh voln v gruntakh i gornykh porodakh [Fundamentals of the Dynamics of Blast Waves in Soils and Rocks]. Moscow: Nedra, 1974.192 p. (rus)
23. Sultanov, K.S. Volnovaya teoriya seysmostoykosti podzemnykh sooruzheniy [Wave Theory of Seismic Resistance of Underground Structures]. Tashkent: Fan, 2016. 392 p. (rus)
24. Mojtaba, E.Kan, Hossein, Taiebat, Nasser, Khalili. A Simplified Mapping Rule for Bounding Surface Simulation of 2 Complex Loading Paths in Granular Materials. International Journal of Geomechanics. 2014. Vol. 14. No. 2. Pp. 239–253.
25. Giuseppe, Buscarnera, Giuseppe, Dattola. Mathematical capture of failure processes in elastoplastic geomaterials. Soils and Foundations. 2016. Vol. 56. No. 1. Pp. 1–18.
26. Monnet, J. Elasto-plastic analysis of the pressuremeter test in granular soil. Part I: theory. European Journal of Environmental and Civil Engineering. 2012. Vol. 16. No. 6. Pp. 699–714.
27. Monnet, J. Elasto-plastic analysis of the pressuremeter test in granular soil. Part 2: numerical study. European Journal of Environmental and Civil Engineering. 2012. Vol. 16. No. 6. Pp. 715–729.
28. Shashkin, A.G. Moldeling the performance of masses of weak clayey soils. Soil Mechanics and Foundation Engineering. 2011. Vol. 48. No. 4. Pp. 138–147.

29. Mirsayapov, I.T., Koroleva, I.V. Strength and deformability of clay soil under different triaxial load regimes that consider crack formation. Soil Mechanics and Foundation Engineering. 2016. Vol. 53. No. 1. Pp. 5–11.
30. Levandovskiy, A.N., Melnikov, B.E., Shamkin, A.A. Modeling of porous material fracture. Magazine of civil Engineering. 2017. No. 1 (69). Pp. 3–22.
31. Kalugina, Ju.A., Keck, D., Pronozin, Ya.A. Determination of soil deformation moduli after National Building Codes of Russia and Germany. Magazine of civil Engineering. 2017. No. 7 (75). Pp. 139–149.
32. Sultanov, K.S. A Non-Linear Law of the Deformation of Soft Soil. Journal Applied Mathematics and Mechanics. 1998. Vol. 62. No. 3. Pp. 465–472.
33. Sultanov, K.S., Khusanov, B.E. State equation for Soils Prone to Slump-type Settlement with Allowance for Degree of Wetting. Soil Mechanics and Foundation Engineering. 2001. Vol. 38. No. 3. Pp. 80–86.
34. Lyakhov, G.M. Volny v gruntakh i poristykh mnogokomponentnykh sredakh [Waves in Soils and Porous Multi-Component Media]. Moscow: Nauka, 1982. 238 p. (rus)
35. Sultanov, K.S., Khusanov, B.E. Determination of the Slump-Type Settlement of a Nonlinearly Deformable Soil Mass during Wetting. Soil Mechanics and Foundation Engineering. 2002. Vol. 39. No. 3. Pp. 81–84.
36. Sultanov, K.S. The Attenuation of Longitudinal Waves in Non-Linear Visco-Elastic Media. Journal Applied Mathematics and Mechanics. 2002. Vol. 66. No. 1. Pp. 115–122.
37. Mirsaidov, M.M., Godovannikov, A.M. Seysmostoykost sooruzheniy [Seismic Stability of Structures]. Tashkent: Uzbekistan, 2008. 220 p. (rus)
38. Mirsaidov, M.M. Teoriya i metody rascheta gruntovykh sooruzheniy na prochnost i seysmostoykost [Theory and Methods of Calculation of Soil Structures for Strength and Seismic Resistance]. Tashkent: Fan, 2010. 312 p. (rus)

Contacts:

Karim Sultanov, +998909702535; sultanov.karim@mail.ru
Pavel Loginov, +998909801765; lopavi88@mail.ru
Sabida Ismoilova, +998946204598; ismailova.sabida@mail.ru
Zulfiya Salikhova, +998909296665; zulfiya6665@gmail.com

Инженерно-строительный журнал

ISSN
2071-0305

сайт журнала: http://engstroy.spbstu.ru/

DOI: 10.18720/MCE.85.7

Квазистатичность процесса динамического деформирования грунтов

К.С. Султанов*, П.В. Логинов, С.И. Исмоилова, З.Р. Салихова
Институт механики и сейсмостойкости сооружений Академии наук Республики Узбекистан, г. Ташкент, Узбекистан
* *E-mail: sultanov.karim@mail.ru*

Ключевые слова: грунт, динамическое нагружение, волны, напряжения, квазистатика, механические характеристики грунтов.

Аннотация. Механические характеристики грунтов при их статическом и динамическом деформировании определяются экспериментально. Точность и достоверность определения механических характеристик грунтов при динамических нагружениях зависит от квазистатичности процесса деформирования грунта. Для этого необходимо обеспечит независимости результатов опытов от волновых процессов в грунте при воздействии на нее динамических нагрузок. Существуют лабораторные установки динамических нагружений (УДН) для проведения опытов по определению законов динамического деформирования, и на их основе механических характеристик грунтов. Проверка квазистатичности процесса динамического деформирования грунта в УДН, достигается решением соответствующей к постановке эксперимента волновой задачи. В связи с этим, рассмотрена задача о распространении плоской волны в грунте, постановка которой адекватно к постановке эксперимента на УДН. Для описания динамическое деформирование грунтов принять упруго – вязкопластическая модель Г.М. Ляхова. Система дифференциальных уравнений в частных производных гиперболического типа, описывающая волновой процесс в грунте, решена методом характеристик с последующим применением численного метода конечных разностей по неявной схеме. Численным решением получены изменения параметров волн (напряжения, деформация и скорости частиц) по времени для разных сечений грунтового слоя. Показаны влияния толщины слоя грунта в УДН на параметры волн, следовательно, на квазистатичность процесса динамического деформирования грунтов в экспериментах. Определены также, степени количественного и качественного влияния механических характеристик грунта на параметры волн. На основе анализа полученных результатов установлена, что главными факторами определяющими квазистатичность волнового процесса являются – толщина грунтового слоя в УДН и параметры динамической нагрузки. Показана зависимость механических характеристик грунта от квазистатичности динамического деформирования грунтового слоя в УДН. Получена на основе результатов численного решения волновой задачи и их анализа условия обеспечения квазистатичности процесса деформирования образца грунта при ее динамическом сжатии в УДН.

Литература

1. Qingfend L., Chengrui C., Benhai Z., Bo M. Loess Soil Stabillization by Means of SiO2 Nanoparticles // Soil Mechanics and Foundation Engineering. 2017. Vol. 54. No.6. Pp. 409–413.
2. Нгуен Ф.З. Исследования зависимости прочностных свойств грунта от его физического состояния // Инженерно-строительный журнал. 2012. № 9 (35). С. 23–28.
3. Гольдин А.Л., Нгуен Фыонг Зунг. Построение траектории напряжений для ненасыщенного грунта при консолидированно-недренированных испытаниях в стабилометре // Инженерно-строительный журнал. 2012. № 9 (35). С. 35–40.
4. Morton J.P., O'Loughlin C.D., White D.J. Estimation of soil strength in fine-grained soils by in strumented free-fall sphere tests // Géotechnique. 2016. Vol. 66. No. 12. Pp. 959–968.
5. Chow S.H., Airey D.W. Soil strength characterisation using free-falling penetrometers // Géotechnique. 2013. Vol. 63. No. 13. Pp. 1131–1143.
6. Tadao E. Effects of grading and particle characteristics on small strain properties of granular materials // Soils and Foundations. 2016 Vol. 56. No. 4. Pp. 745–750.
7. Ignatova O.I. Deformation characteristics of the Jurassic clayey soils of Moscow // Soil Mechanics and Foundation Engineering. 2009. Vol. 46. No. 5. Pp. 196–201.

8. Александров А.С. Пластическое деформирование гранодиортового щебня и песчано-гравийной смеси при воздействии трехосной циклической нагрузки // Инженерно-строительный журнал. 2013. № 4 (39). С. 22–34.
9. Логинова И.И., Артомонова Д.А., Столяров О.Н., Мельников Б.Е. Влияние структуры на вязкоупругие свойства геосинтетических материалов // Инженерно-строительный журнал. 2015. № 4 (56). С. 11–18. DOI: 10.5862/MCE.56.2
10. Hui Zhou, Yanshuang Yang, Chuanqing Zhang, Dawei Hu. Experimental investigations on loading-rate dependency of compressive and tensile mechanical behaviour of hard rocks // European Journal of Environmental and Civil Engineering. 2015. Vol. 19. No. s1. Pp. s70–s82.
11. LamineIghil Ameur, Guillaume Robin, Mahdia Hattab. Elastic properties in a clayey material under mechanical loading – an estimation through ultrasonic propagations // European Journal of Environmental and Civil Engineering. 2016. Vol. 20. No. 9. Pp. 1127–1146.
12. Chow S.H., O'loughlin C.D., Randolph M.F. Soil strength estimation and pore pressure dissipation for free-fall piezocone in soft clay // Géotechnique. 2014. Vol. 64. No. 10. Pp. 817–827.
13. Kostas Senetakis, Anastasios Anastasiadis, Kyriazis Pitilakis. Normalized shear modulus reduction and damping ratio curves of quartz sand and rhyolitic crushed rock // Soils and Foundations. 2013. Vol. 53. No. 6. Pp. 879–893.
14. Yumin Chen, Hanlong Liu, Haiqing Wu. Laboratory study on flow characteristics of liquefied and post-liquefied sand // European Journal of Environmental and Civil Engineering. 2013. Vol. 17. No. s1. Pp. s23–s32.
15. Maheshwari B., Kale S.,Kaynia A. Dynamic properties of Solani sand at large strains: a parametric study // International Journal of Geotechnical Engineering // 2012. Vol. 6. No. 3. Pp. 353–358.
16. Cengiz Kurtulus, Maral Üçkardeş, Umut Sarır, Ş. Onur Güner. Experimental studies in wave propagation across a jointed rock mass // Bulletin of Engineering Geology and the Environment. 2011. Vol. 71. No. 2. Pp. 231–234.
17. Wang Y., Li X., Zheng B. Experimental study on mechanical properties of clay soil under compression by ultrasonic test // European Journal of Environmental and Civil Engineering. 2018. Vol. 22. No. 6. Pp. 666–685.
18. Verrucci L.,Lanzo G.,Tommasi P., Rotonda T. Cyclic and dynamic behaviour of a soft pyroclastic rock // Géotechnique. 2015. Vol. 65. No. 5. Pp. 359–373.
19. Вовк А.А, Замышляев Б.В., Евтерев Л.С., Белинский И.В., Михалюк А.В. Поведение грунтов под действием импульсивных нагрузок. Киев: Наукова думка, 1984. 286 с.
20. Замышляев Б.В., Евтерев Л.С. Модели динамического деформирования и разрушения грунтовых сред. М.: Наука, 1990. 216 с.
21. Рыков Г.В., Скобеев А.М. Измерение напряжений в грунтах при кратковременных нагрузках. М.: Наука, 1978. 168 с.
22. Ляхов Г.М. Основы динамики взрывных волн в грунтах и горных породах. М.: Недра, 1974.192 с.
23. Султанов К.С. Волновая теория сейсмостойкости подземных сооружений. Ташкент: Фан, 2016. 392 с.
24. Mojtaba E. Kan, Hossein Taiebat, Nasser Khalili. A Simplified Mapping Rule for Bounding Surface Simulation of 2 Complex Loading Paths in Granular Materials // International Journal of Geomechanics. 2014. Vol. 14. No. 2. Pp. 239–253.
25. Giuseppe Buscarnera, Giuseppe Dattola. Mathematical capture of failure processes in elastoplastic geomaterials // Soils and Foundations. 2016. Vol. 56. No. 1. Pp. 1–18.
26. Monnet J. Elasto-plastic analysis of the pressuremeter test in granular soil. Part I: theory // European Journal of Environmental and Civil Engineering. 2012. Vol. 16. No. 6. Pp. 699–714.
27. Monnet J. Elasto-plastic analysis of the pressuremeter test in granular soil. Part 2: numerical study // European Journal of Environmental and Civil Engineering. 2012. Vol. 16. No. 6. Pp. 715–729.
28. Shashkin A.G. Moldeling the performance of masses of weak clayey soils // Soil Mechanics and Foundation Engineering. 2011. Vol. 48. No. 4. Pp. 138–147.
29. Mirsayapov I.T., Koroleva I.V. Strength and deformability of clay soil under different triaxial load regimes that consider crack formation // Soil Mechanics and Foundation Engineering. 2016. Vol. 53. No. 1. Pp. 5–11.
30. Levandovskiy A.N., Melnikov B.E., Shamkin A.A. Modeling of porous material fracture // Magazine of civil Engineering. 2017. No. 1 (69). Pp. 3–22.
31. Kalugina Ju., A., Keck D., Pronozin Ya., A. Determination of soil deformation moduli after National Building Codes of Russia and Germany // Magazine of civil Engineering. 2017. No. 7 (75). Pp. 139–149.
32. Sultanov K.S. A Non-Linear Law of the Deformation of Soft Soil // Journal Applied Mathematics and Mechanics. 1998. Vol. 62. No. 3. Pp. 465–472.
33. Sultanov K.S., Khusanov B.E. State equation for Soils Prone to Slump-type Settlement with Allowance for Degree of Wetting // Soil Mechanics and Foundation Engineering. 2001. Vol. 38. No.3. Pp. 80–86.
34. Ляхов Г.М. Волны в грунтах и пористых многокомпонентных средах. М.: Наука, 1982. 238 с.
35. Sultanov K.S., Khusanov B.E. Determination of the Slump-Type Settlement of a Nonlinearly Deformable Soil Mass during Wetting // Soil Mechanics and Foundation Engineering. 2002. Vol. 39. No. 3. Pp. 81–84.
36. Sultanov K.S. The Attenuation of Longitudinal Waves in Non-Linear Visco-Elastic Media // Journal Applied Mathematics and Mechanics. 2002. Vol. 66. No.1. Pp.115–122.
37. Мирсаидов М.М., Годованников А.М. Сейсмостойкость сооружений. Ташкент: Узбекистан, 2008. 220 с.
38. Мирсаидов М.М. Теория и методы расчета грунтовых сооружений на прочность и сейсмостойкость. Ташкент: Фан, 2010. 312 с.

Контактные данные:

Карим Султанович Султанов, +998909702535; эл. почта: sultanov.karim@mail.ru
Павел Викторович Логинов, +998909801765; эл. почта: lopavi88@mail.ru
Сабида Исроиловна Исмоилова, +998946204598; эл. почта: ismailova.sabida@mail.ru
Зулфия Рустамовна Салихова, +998909296665; эл. почта: zulfiya6665@gmail.com

Magazine of Civil Engineering. 2019. 85(1). Pp. 92–106
Инженерно-строительный журнал. 2019. № 1(85). С. 92–106

Magazine of Civil Engineering

ISSN 2071-0305

journal homepage: http://engstroy.spbstu.ru/

DOI: 10.18720/MCE.85.8

Fire Design Methods for Structures with Timber Framework

M.V. Gravit[a], D. Serdjuks[b]*, A.V. Bardin[a], V. Prusakov[c], K. Buka-Vaivade[b],
[a] Peter the Great St. Petersburg Polytechnic University, St. Petersburg, Russia
[b] Riga Technical University, Riga, Latvia
[c] LTD «PROMIZOL», Tomilino, Lyubertsy district of Moscow region, Russia
** E-mail: Dmitrijs.Serdjuks@rtu.lv*

Keywords: glued load-bearing timber framework, trapezium timber truss, glued timber decking, reduced cross-sections method, reduced properties method, actual fire resistance.

Abstract. Timber structures are environmentally friendly in terms of decreasing the impact of human activity on the planet. Reliability of timber structures can be provided by the corresponding fire resistance so as fire risk is one of the most significant disadvantages of timber structures. Development of new method for calculation of actual fire resistance is a topical issue. The first draft of method for calculation of actual fire resistance and classes of fire risk for load-bearing timber structures based on Russian national standard, was compared with fire design methods based on European norm. The structure of one-storey glued load-bearing timber framework for sports hall of Corporative University of Sberbank was used as an example for the comparison. The main load bearing structure of the framework in the transversal direction is two-hinge glued laminated timber frame with the span equal to 24 m, consisting of the two columns with rectangular glued cross-sections and trapezium truss with triangular lattice system and two cantilevers. It was stated, that methods based on European norm and method based on Russian national standard enable to obtain comparable results for evaluation of fire resistance for glued laminated load-bearing timber frameworks structure. However, the method based on Russian national standard did not contain information for evaluation of fire resistance of joints of timber structures, which often is determinant for the timber frameworks. Therefore, adding of the chapter including approach to evaluation of fire resistance of the joints of timber structures is possible direction for further development of the method based on Russian national standard.

1. Introduction

The problem of limited raw material and energy resources is one of the most actual in the world. It can be solved by decreasing the structural dead weight, increase of span and durability of load carrying structures so as by the replacement of non-renewable structural materials by renewable ones [1–3]. The rapid rise of CO2 emissions is caused by the technological development mainly. The production of the concrete, which is the most widely used structural material, is already responsible for from 5 % to 8 % of global greenhouse gas emissions. The production of steel requires about 4 % of global energy use [4]. Replacement of reinforced concrete and steel structures by the timber ones is one of the modern tendencies in civil engineering. Timber structures are environmentally friendly. Using of timber structures enables to decrease the anthropogenic impact on the planet [5]. Structural members from glued laminated timber, cross-laminated timber and other timber-based materials are widely used for one-storey and multi-storey buildings [4, 6–9]. Timber as a structural material has a potential for substitution of concrete and steel in it major applications. Not so far timber use for the multi-storey buildings was mentioned as the most significant limitation of it use as a structural material. However, nowadays, this limitation was deleted due to the development of new timber based structural materials such as cross-laminated timber. At Norway has completed the frame of the tallest timber building in the world – The Mjos Tower, which has 18 floors. However, possibility to create more than 30-storey timber building was stated [10]. The structure of sports hall of Corporative University of Sberbank can be considered as an example of the modern one-storey

Gravit, M.V., Serdjuks, D., Bardin, A.V., Prusakov, V., Buka-Vaivade, K. Fire Design Methods for Structures with Timber Framework. Magazine of Civil Engineering. 2019. 85(1). Pp. 92–106. DOI: 10.18720/MCE.85.8.

Гравит М.В., Сердюк Д.О., Бардин А.В., Прусаков В.А., Бука-Вайваде К. Методы определения огнестойкости конструкций деревянного каркаса // Инженерно-строительный журнал. 2019. № 1(85). С. 92–106. DOI: 10.18720/MCE.85.8

residential building with the timber framework (Figure 1.*a)*). Residential building in London can be considered as an example of multi-storey timber buildings [4] (Figure 1.*b)*).

a) *b)*

Figure 1. One-storey and multi-storey timber buildings: *a)* The structure of sports hall of Corporative University of Sberbank; *b)* Residential building in London.

However, at the same time reliability of timber structures can be provided by the corresponding fire resistance so as fire risk is one of the most significant disadvantages of timber structures. Timber fire safety assessment is complicating due to it anisotropy [6]. Fire resistance of timber structures can be determined by fire tests, advanced calculations and simplified design methods [11–13]. Typically, fire test is very expensive, but advanced calculations require a lot of additional parameters that complicate calculations and make calculations more work and time-consuming, so, development of new simplified design method for calculation of actual fire resistance and classes of fire risk for load-bearing timber structures is a topical issue [14–20].

The first draft of method based on Russian national standard for calculation of actual fire resistance and classes of fire risk for load-bearing timber structures, which is based on the Federal Law No. 123-FZ “Technical regulations on fire safety requirements” in part of fire resistance and fire risk of building structures, was prepared up till now [21]. A certain interest cause comparison of the developed variant of method for calculation of actual fire resistance and classes of fire risk for load-bearing timber structures with just existing ones and exactly with the reduced section and reduced properties methods reflected in the European norm EN 1995-1-2, which are used in the most of European states now. The methods of reduced section and reduced properties are used in the case of standard fire action and recommended for practical application. Parametric design method, which also is used in European states, should be used in the case of full fire analyse.

Therefore, the aim of the paper is comparison of the methods for fire resistance evaluation on the base of European norm EN 1995-1-2, such as reduced cross-section method, known also as effective cross-sectional method and reduced properties method, and method based on Russian national standard for calculation of actual fire resistance and classes of fire risk for load-bearing timber structures, which is based on the Federal Law No. 123-FZ «Technical regulations on fire safety requirements” [21]. The comparison can indicate possible supplements and improvements for the developed method. The structure of one-storey glued load-bearing timber framework for sports hall of Corporative University of Sberbank will be used as an example for the comparison of fire resistances, obtained by the method based on Russian national standard and methods based on European norm.

2. Methods

2.1. Determination of fire resistance for timber structures by EN 1995-1-1 and EN 1995-1-2

The fire resistance of structures of glued load-bearing timber framework for sports hall of Corporative University of Sberbank should be analysed by the reduced section method and reduced propertied methods so as both the methods are mentioned in the EN 1995-1-2 and reduced section method was mentioned as a recommended one. The main load bearing structure of the framework in the transversal direction is two-hinge glued laminated timber frame consisting of the two columns with rectangular glued cross-sections and trapezium truss with triangular lattice system and two cantilevers (Figure 2).

Top and bottom chords of the truss so as the elements of the lattice have rectangular glued sections. The spatial stability of the frame is provided by the moment cornice joints of the columns with the truss in plane of the frame so as by horizontal and vertical bracings in zone of the trusses so as by glued timber decking. The structure of the roof including a glued timber decking joined with the top chord of the truss and providing it from the lateral torsional buckling. The system of vertical bracings between the trusses and columns provide stability of the frame in the perpendicular plane. The fire resistance of the glued laminated timber frame is evaluated as the minimum fire resistance of it load-bearing members and joints. Influence of the timber decking and system of bracing is taken into account.

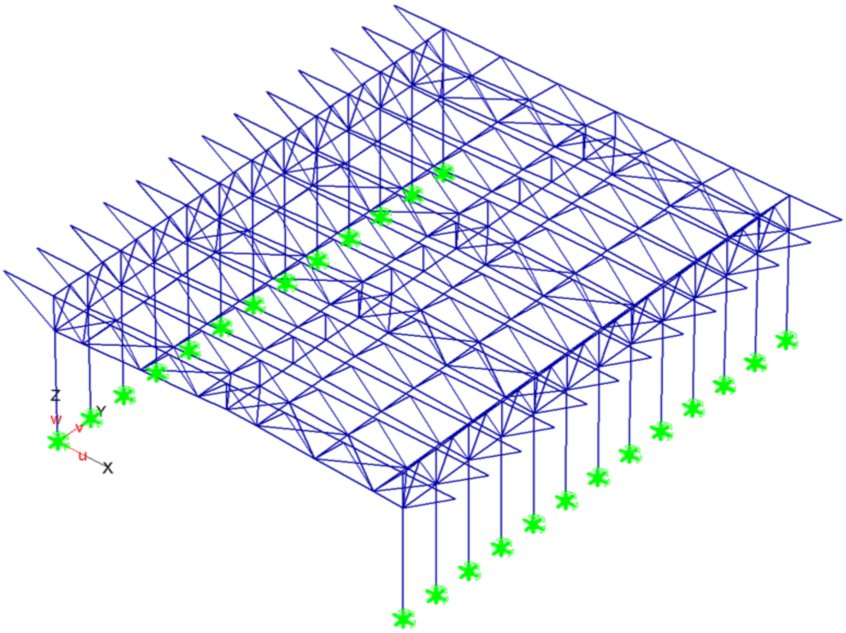

Figure 2. Structures of load-bearing framework of sports hall of Corporative University of Sberbank.

The members of glued laminated timber frame are subjected to the action of axial force in combination with the bending moment and axial force. The top chord of the truss and the columns are subjected to compression with the bending. Bottom chord of the truss is subjected to tension with the bending. Elements of the lattice of the truss are subjected to axial tension or compression. Glued timber decking is subjected to flexure. Therefore, conditions of strength and stability, which are explained in the points 6.1.6., 6.2.3, 6.2.4, 6.3.2 and 6.3.3 of EN 1995-1-1 are used for determination of fire resistances of glued timber decking, columns, chords of the truss so as elements of the lattice of the truss.

The fire resistance of joints of the truss must be checked by the controlling of the constructional requirements satisfaction for the bolted connections in course of the fire exposure. The structural requirements to the bolted connections are explained in the point 8.5 of EN 1995-1-1. Guidelines for evaluation of fire resistance for unprotected connections with the unprotected side members of wood by the simplified method are given in point 6.2.1.1. of EN 1995-1-2.

2.2. Reduced cross-section method

An effective cross-section of the members of glued timber frame should be determined by reducing the initial cross-section by the effective charring depth d_{ef} [22].

$$d_{ef} = d_{char,n} + k_0 d_0, \tag{1}$$

where: d_0 is thickness of pyrolyzed layer after 20 minutes of fire exposure (d_0 = 7 mm);

$d_{\text{char,n}}$ is the notional design charring depth, which should be determined as a product of β_n notional design charring rate, the magnitude of which includes for the effect of corner rounding and fissures, and t time of fire exposure;

k_0 is parameter, which take into account decrease the thickness of pyrolyzed layer in the case of fire exposure less than 20 minutes.

The cases, when the structural members are subjected to fire action from four, three and one sides should be considered (Figure 3). The columns of the frame, bottom chord of the truss and elements of the lattice are subjected to fire action from four sides. Top chord of the truss is subjected to fire action from three sides so as it top side is protected from the fire action by the glued timber decking.

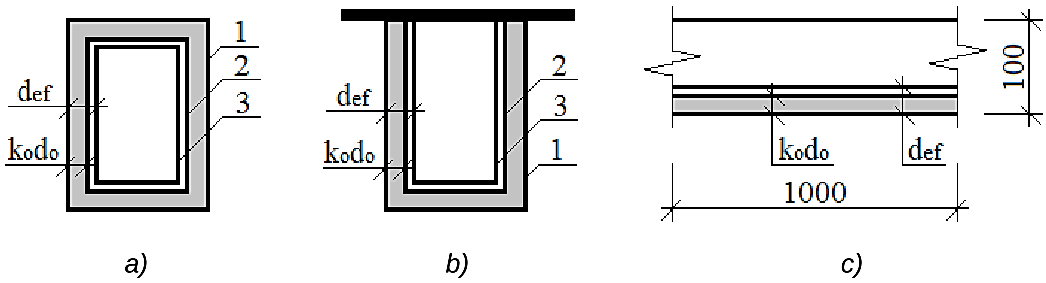

Figure 3 Reduced cross-section of the member for the cases [22]: *a)* structural member is subjected to the fire action from four sides; *b)* structural member is subjected to the fire action from three sides; *c)* structural member is subjected to the fire action from one side; 1 – initial surface of the member; 2 – border of residual cross-section; 3 – border of effective cross-section; d_{ef} – effective charring depth; $k_0 d_0$ – thickness of pyrolyzed layer.

The glued timber decking is considered as a section with the width equal to 1 m. It is subjected to fire action from the bottom only. The column and top chord of the truss are analysed at the fire action taking in to account strength and stability conditions so as the members are subjected to the action of axial compression forces and bending moment. The values of bending moment and axial forces in case of fire action are determined as a product of the forces obtained from the analysis at normal temperature for the fundamental combination of actions [23] and the reduction factor for the design load in the fire situation. As a simplification, the recommended value for the reduction factor for the design load in the fire situation was taken equal to 0.6 [22]. The strength condition is checked by the equations (2), (3) [24].

$$\left(\frac{\sigma_{c,0,d,fi}}{f_{c,0,d,fi}}\right)^2+\frac{\sigma_{m,y,d,fi}}{f_{m,y,d,fi}}+k_m\cdot\frac{\sigma_{m,z,d,fi}}{f_{m,z,d,fi}}\le 1; \tag{2}$$

$$\left(\frac{\sigma_{c,0,d,fi}}{f_{c,0,d,fi}}\right)^2+k_m\cdot\frac{\sigma_{m,y,d,fi}}{f_{m,y,d,fi}}+\frac{\sigma_{m,z,d,fi}}{f_{m,z,d,fi}}\le 1, \tag{3}$$

where $\sigma_{c,0,d,fi}$ is design compressive stress along the grain in case of fire action,

$\sigma_{m,y,d,fi}$ is design bending stress about the principal *y*-axis in case of fire action,

$\sigma_{m,z,d,fi}$ is design bending stress about the principal *z*-axis in case of fire action,

$f_{c,0,d,fi}$ is design compressive strength in case of fire action,

$f_{m,y,d,fi}$ is design bending strength about the principal *y*-axis in case of fire action,

$f_{m,z,d,fi}$ is design bending strength about the principal *z*-axis in case of fire action,

k_m is factor, considering redistribution of bending stress in cross-section.

The stability of column and top chord of the truss was checked by the equations (4) and (5) [24] as for members subjected to compression with the bending.

$$\left(\frac{\sigma_{c,0,d,fi}}{k_{c,y,fi}\cdot f_{c,0,d,fi}}\right)^2+\frac{\sigma_{m,y,d,fi}}{f_{m,y,d,fi}}+k_m\cdot\frac{\sigma_{m,z,d,fi}}{f_{m,z,d,fi}}\le 1; \tag{4}$$

$$\left(\frac{\sigma_{c,0,d,fi}}{k_{c,z,fi}\cdot f_{c,0,d,fi}}\right)^2+k_m\cdot\frac{\sigma_{m,y,d,fi}}{f_{m,y,d,fi}}+\frac{\sigma_{m,z,d,fi}}{f_{m,z,d,fi}}\le 1, \tag{5}$$

where $k_{c,y,fi}$ – instability factor about the principal *y*-axis in case of fire action,

$k_{c,z,fi}$ – instability factor about the principal *z*-axis in case of fire action; other designations as for equations (2) and (3).

The bottom chord of the truss is analysed at the fire action by the strength condition taking in to account axial tension force and bending moment by the equation (6), (7) [24].

$$\left(\frac{\sigma_{t,0,d,fi}}{f_{t,0,d,fi}}\right)^2+\frac{\sigma_{m,y,d,fi}}{f_{m,y,d,fi}}+k_m\cdot\frac{\sigma_{m,z,d,fi}}{f_{m,z,d,fi}}\le 1; \tag{6}$$

$$\left(\frac{\sigma_{t,0,d,fi}}{f_{t,0,d,fi}}\right)^2 + k_m \cdot \frac{\sigma_{m,y,d,fi}}{f_{m,y,d,fi}} + \frac{\sigma_{m,z,d,fi}}{f_{m,z,d,fi}} \le 1, \tag{7}$$

where $\sigma_{t,0,d,fi}$ is design tensile stress along the grain in case of fire action,

$f_{t,0,d,fi}$ is design tensile strength in case of fire action, other designations as for the equations (2) and (3).

The members of the lattice of the truss are analysed at the fire action taking in to account strength and stability conditions as the members subjected to the action of axial forces. The strength conditions are checked by the equations (8) and (9) for the axially tensioned and compressed elements of the lattice, correspondingly [24].

$$\frac{\sigma_{t,0,d,fi}}{f_{t,0,d,fi}} \le 1; \tag{8}$$

$$\frac{\sigma_{c,0,d,fi}}{f_{c,0,d,fi}} \le 1, \tag{9}$$

where designations as for the equations (2) and (6).

Stability of lattice of the truss, was checked by the equations (10) and (11) [24] as for the members subjected to compression.

$$\frac{\sigma_{c,0,d,fi}}{k_{c,y,fi} \cdot f_{c,0,d,fi}} \le 1; \tag{10}$$

$$\frac{\sigma_{c,0,d,fi}}{k_{c,z,fi} \cdot f_{c,0,d,fi}} \le 1, \tag{11}$$

where designations as for the equations (4) and (5).

The strength of the glued timber decking subjected to flexure, was checked by the equations (12) and (13).

$$\frac{\sigma_{m,y,d,fi}}{f_{m,y,d,fi}} + k_m \cdot \frac{\sigma_{m,z,d,fi}}{f_{m,z,d,fi}} \le 1; \tag{12}$$

$$k_m \cdot \frac{\sigma_{m,y,d,fi}}{f_{m,y,d,fi}} + \frac{\sigma_{m,z,d,fi}}{f_{m,z,d,fi}} \le 1, \tag{13}$$

where designations as for the equations (4) and (5).

The design strength and stiffness properties of the effective cross-section should be calculated with factor $k_{\mathrm{mod,fi}}$ = 1.0.

2.3. Reduced properties method

The design strength and stiffness properties of the effective cross-section by the reduced properties method should be calculated with factor $k_{\mathrm{mod,fi}}$, which should be determined by the dependences (14)–(16) or taken by the graphical dependence 4.3 [22].The values of the factor $k_{\mathrm{mod,fi}}$ will be differed dependently from the inner forces acting in the considered structural members. The value of $k_{\mathrm{mod,fi}}$ should be determined for bending strength:

$$k_{mod,fi} = 1.0 - \frac{1}{200} \cdot \frac{p}{A_r}. \tag{14}$$

The value of $k_{\mathrm{mod,fi}}$ should be determined for compression strength:

$$k_{mod,fi} = 1.0 - \frac{1}{125} \cdot \frac{p}{A_r}. \tag{15}$$

The value of $k_{\mathrm{mod,fi}}$ should be determined for tensile strength:

$$k_{mod,fi} = 1.0 - \frac{1}{330} \cdot \frac{p}{A_r}, \tag{16}$$

where p is the perimeter of the fire exposed residual cross-section, in meters, A_r is the area of the residual cross-section, in m^2.

The dependences (14)–(16) should be used in case if time of fire exposure is bigger or equal to 20 minutes. For time of fire exposure equal to zero $k_{\text{mod,fi}}$ = 1.0. The value of $k_{\text{mod,fi}}$ should be determined by the linear interpolation in case if time of fire exposure will be within the limits from 0 to 20 minutes.

The residual cross-section of the considered structural members should be determined by the point 3.4 [22]. The fire resistance of the joints was evaluated as for connections with the side members of timber, which are described in the point 6.2 [22]. The fire resistance of unprotected timber-to-timber connections where spacings, edge and end distances and side member dimensions satisfy the requirements given in EN 1995-1-1 section 8, were taken from the table 6.1 [22].

2.4. Determination of fire resistance for timber structures by method for calculation of actual fire resistance and classes of fire risk

The method contains the major requirements for calculation of actual fire resistance and classes of fire risk for load-bearing timber structures with solid and glued cross-sections. Changing of mechanical properties and geometrical parameters of the members cross-sections are taken into account. The method can be used for the development of technical solutions during designing of timber structures in accordance with the requirements of the Federal Law No. 123-FZ “Technical regulations on fire safety requirements”. The method was developed on the base of results of experimental tests [25]. The statements of existing analytical methods for evaluation of fire resistance of building constructions were taken into account [26]. The design statements of the method are a number of semi-empirical dependences which were obtained basing on the results of fire testing of structures under load by the method, which is described in GOST 30247.0-94 and GOST 30247.1-94. Evaluation of fire resistance of timber structures joined with the determination of time of losing of it load-bearing capacity by taking into account time-temperature curve in case of standard fire [27]. The charring rates were taken constant and equal to 0.7 mm/min if the cross-sections linear dimensions of the member are not less than 120 mm and 1 mm/min for the members with linear dimensions of cross-sections less than 120 mm. The time of loosing of load-bearing capacity of timber structural members in general case is calculated by formula (17).

$$\tau_{\text{p}} = \tau_{\text{kp}} + \tau_{\text{з}} = \tau_{\text{kp}} + 5\ \text{min}, \tag{17}$$

where τ_{kp} is time till the moment of critical cross-section development;

$\tau_{\text{з}}$ is time of delay, which is taken equal to 5 min.

The time till the moment of critical cross-section development dependently from the heating conditions for the structural members should be determined by the formula (18) in case, if the structure is subjected to fire action from three sides.

$$\tau_{\text{kp}} = B - \frac{b}{2\beta} = H - \frac{h}{\beta}, \tag{18}$$

where B is initial width of cross-section before heating, mm;

H is initial depth of cross-section before heating, mm;

b is width of critical cross-section, mm;

h is depth of critical cross-section, mm;

β is charring rate.

The time till the moment of critical section development should be determined by the formula (19) in case if structure is subjected to fire action from four sides.

$$\tau_{\text{kp}} = B - \frac{b}{2\beta} = H - \frac{h}{2\beta}, \tag{19}$$

where designations as for formula (18).

The rounding of corners and decrease of mechanical properties of timber are taken into account by the coefficient ξ, which should be taken from the table 1 of the method dependently from the internal forces acting in the considered structural member [21]. The coefficient ξ is equal to 0.6, 0.7 and 0.85 for the members subjected to flexure, compression parallel to fibres and tension parallel to fibres, correspondingly. The depths and widths of critical cross-sections should be determined by the formulas (20) and (21).

$$R_{\text{m,d}} \cdot \xi = \frac{6M_{\text{d}}}{bh^2}, \tag{20}$$

where M_{d} is maximum bending moment from the action of actual load;

ξ is coefficient, which takes into account decrease of mechanical properties of timber and rounding of corners;

$R_{\mathrm{m,d}}$ is design resistance of timber in bending;

b is width of critical cross-section, mm;

h is depth of critical cross-section, mm.

$$R_{\mathrm{c/t,0,d}} \cdot \xi = \frac{N_{\mathrm{c/t,\,d}}}{bh}, \tag{21}$$

where $N_{\mathrm{c/t,0,d}}$ is maximum axial force (compression/tension) acting parallel to the grain from the action of actual load;

$R_{\mathrm{c/t,0,d,}}$ is design resistance of timber in compression or tension; other designations as in formula (18).

The depth and width of critical cross-sections for elements subjected to compression with the bending should be calculated by the summing of right parts of formulas (20) and (21).

The time till the moment of critical section development can be determined by the simplified approach with using of nomographs.

The nomographs were obtained on the base of experimental data for glued timber members subjected to axial compression parallel to grains and flexure. The nomographs obtained for the beams are shown on Figure 4. The nomographs obtained for the columns have the similar shapes. The rounding of the corners of the member and decrease of mechanical properties of timber are taken into account. The nomographs are linear dependences of coefficient of cross-section use before heating and relation of critical time to the initial depth of cross-section, which changes within the limits from 0.2 to 1.0

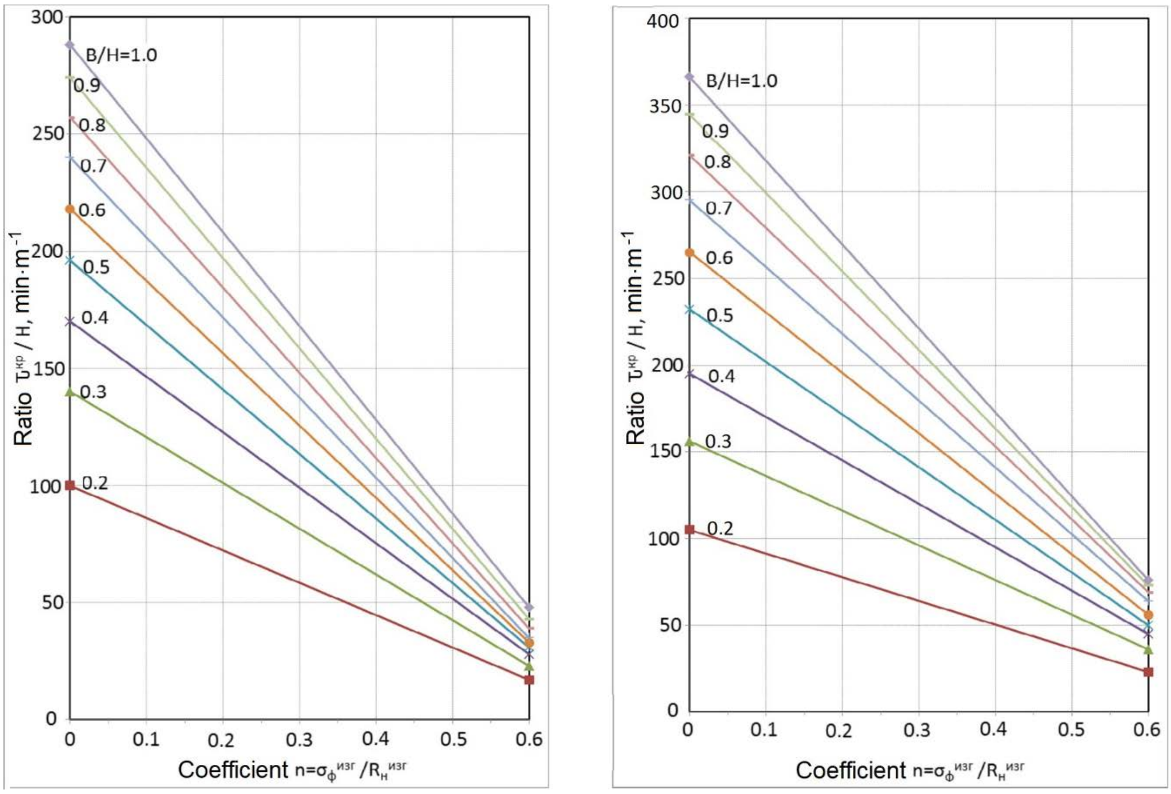

a) *b*)

Figure 4. Nomograph obtained for the beams: *a)* subjected to fire action from three sides; *b)* subjected to fire action from four sides [21].

The nomographs were obtained for the beams and columns subjected to fire action from three and four sides.

3. Results and discussions

3.1. Determination of fire resistance of timber framework by EN 1995-1-1 and EN 1995-1-2

The fire resistance of structure of glued laminated load-bearing framework for sports hall of Corporative University of Sberbank was determined by the reduced cross-section and reduced properties methods. The fire resistance of structure of glued laminated load-bearing framework was determined as the smallest from the fire resistances of columns, trusses and glued timber decking. The fire resistance of trapezium truss was determined as a minimum from the fire resistances of top and bottom chords so as members of lattice and joints. The scheme of the two-hinge glued laminated timber frame is shown on the Figure 5. Span of the frame is equal to 24 m and its bay is equal to 2.4 m. Heights of the truss at supports and in the middle of the span are equal to 2.9 and 2.5 m, correspondingly.

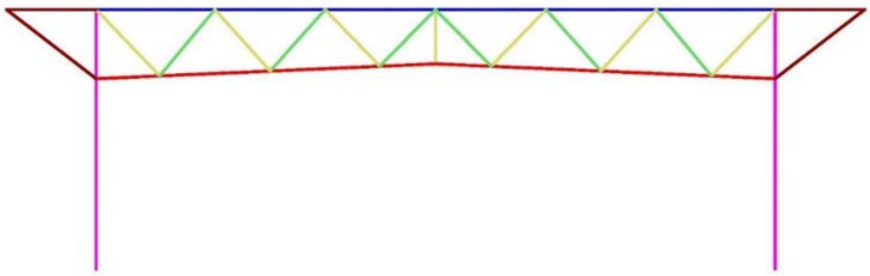

Figure 5. Scheme of the two-hinge glued laminated timber frame with coloured indication of members cross-sections, the colours descriptions are given in the Table 1.

The dimensions of cross-sections of all members of the two-hinge glued laminated timber frame so as some mechanical properties of used glued laminated timber are given in the Table 1.

Table 1. Parameters of members of the frame.

Member of the frame	Colour identification	Cross-section ($b*h$), mm	Modulus of elasticity, kN/m^2	Density, kg/m^3	Poisson ratio
Top chord		240*400	1e+007	600.00	0.45
Cantilevers		300*300	1e+007	600.00	0.45
Rising braces		200*200	1e+007	600.00	0.45
Lowering braces and central strut		150*220	1e+007	600.00	0.45
Bottom chord		320*420	1e+007	600.00	0.45
Columns and support struts		240*600	1e+007	600.00	0.45

3.1.1. Fire resistance of glued laminated timber decking

The glued timber decking is a structural member which is supported by the top chords of the trapezium trusses. The glued timber decking is developed by the squared boards with the depth of cross-section equal to 100 mm. Thickness of the glued timber decking is also equal to 100 mm. The softwood with the design resistance in 13 MPa was considered as a structural material for the glued timber decking. It was stated, that corresponding strength class of the timber is C20 [28]. The design scheme of the glued timber decking was five span continuous beam with the spans in 2.4 m. It was loaded by the uniformly distributed load with intensity in 7 kN/m (Figure 6).

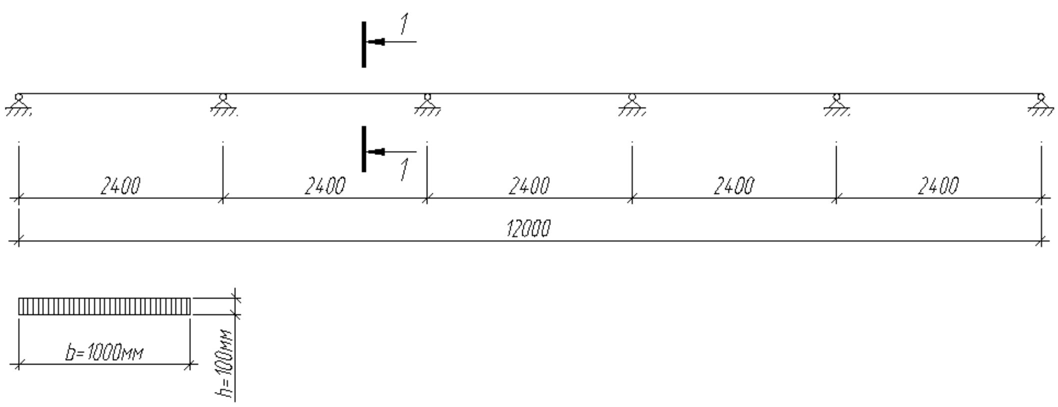

Figure 6. Design scheme of glued timber decking.

The intensities of surface permanent and snow loads are equal to 5.2 and 1.8 kPa, correspondingly. The growing of normal stresses in the cross-section, where act the maximum bending moment, was analysed in the case of normal fire by the reduced properties and reduced section methods. The maximum bending moment acts on the second support and was equal to 4.24 kNm when the structure is loaded by the snow and permanent load and fire action is not taken in to account. The value of bending moment in case of fire action was determined as a product of the forces obtained from the analysis at normal temperature and the reduction factor for the design load in the fire situation. The reduction factor was taken equal to 0.6 [22]. The value of bending moment in case of fire action was equal to 2.54 kNm. Relation of the maximum normal stresses acting in the cross-sections to the design resistance of the timber was considered as a level of cross-section use in case of fire. The cross-section of glued timber decking was considered as subjected to fire from one side as it is shown on the Figure 3, c). The dependences of the level of cross-section use, as a function from the time of the fire action, were obtained and shown on the Figure 7.

Fire resistance of the glued timber decking was evaluated as R85 and R106 by the reduced section and reduced properties methods, correspondingly. Fire resistance of cantilever part of the glued timber decking was evaluated as R82 and R103 by the reduced section and reduced properties methods, correspondingly. Therefore, the fire resistance of glued timber decking can be evaluated as R85, so as cantilever parts of the decking did not influence on the behaviour of the structure in general.

3.1.2. Fire resistance of glued timber columns

The glued laminated timber column with the dimensions of cross-section 600x200 mm with the hinge joints with the truss and foundation was analysed. Length of the column is equal to 11030 mm. The strength class of glued laminated timber was taken as GL28h [29]. Transversal frame of the building was loaded by the permanent, snow and wind loads. Characteristic value of wind pressure was taken as 0.23 kPa. The maximum values of bending moment and axial compression force in case of fire action were equal to 172.8 kN and 37.35 kNm, correspondingly. The cross-section of glued laminated timber column was considered as a subjected to fire from four sides, as it is shown on the Figure 3 a). Fire resistance of glued laminated timber column was analysed by the equations (2)–(5). The dependences of the level of cross-section use of the glued laminated timber column as a function from the time of the fire action were obtained and shown on the Figure 8.

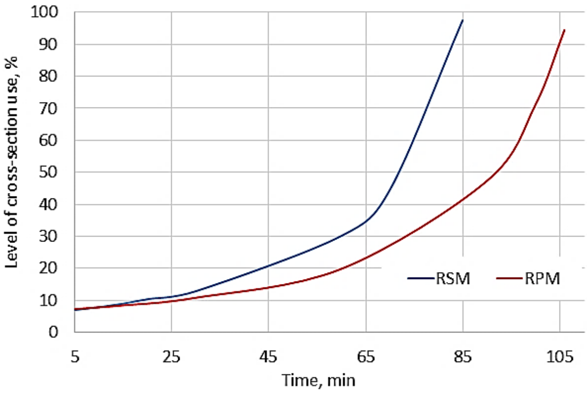

Figure 7. The dependences of the level of cross-section use as a function from the time of the fire action for glued timber decking: RSM – obtained by the reduced section method; RPM – obtained by the reduced properties method.

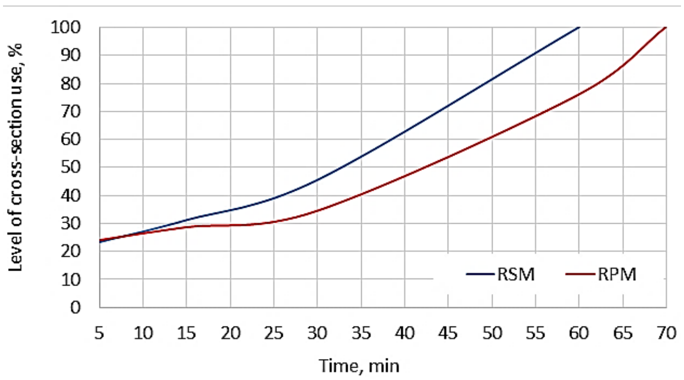

Figure 8. The dependences of the level of cross-section use as a function from the time of the fire action for glued laminated timber column: designations as in Figure 7.

Fire resistance of the glued laminated timber column was evaluated as R60 and R70 by the reduced section and reduced properties methods, correspondingly.

3.1.3. Fire resistance of timber truss

Fire resistance of the timber truss was evaluated as the minimum fire resistance of glued laminated timber top and bottom chords and members of the lattice. The timber truss has a span equal to 24 m. The glued laminated timber top chord of the truss has cross-section in 400x240 mm. It effective length is equal to the length of the panel in the both planes. The length of the panel of the top chord of the truss is equal to 4 m. The maximum values of the bending moment and axial compression forces in case of fire action were equal to 15.16 kNm and 332.12 kN, correspondingly. The cross-section of glued laminated timber top chord was considered as a subjected to fire from three sides, as it is shown on the Figure 3 b). The upper side of the top chord was protected by the decking. Fire resistance of glued timber top chord was analysed by the equations (2)–(5). Fire resistance of the glued laminated timber top chord was evaluated as R85 and R106 by the reduced section and reduced properties methods, correspondingly.

The glued laminated timber bottom chord of the truss has cross-section in 420×320 mm. The maximum values of the bending moment and axial tension forces in case of fire action were equal to 6 kNm and 342.60 kN, correspondingly. The cross-section of glued laminated timber bottom chord was considered as a subjected to fire from four sides, as it is shown on the Figure 3, a). Fire resistance of glued laminated timber bottom chord was analysed by the equations (6)–(7). It is significantly bigger than that of the top chord so as bottom chord is not subjected to the action of compressive forces. Safety storage in 68 % will take place for the bottom chord at the moment, when the buckling of the top chord occurs.

The dependences of the level of cross-section use, as a function from the time of the fire action for the top chord and most compressed brace of the truss, were obtained and shown on the Figure 9.

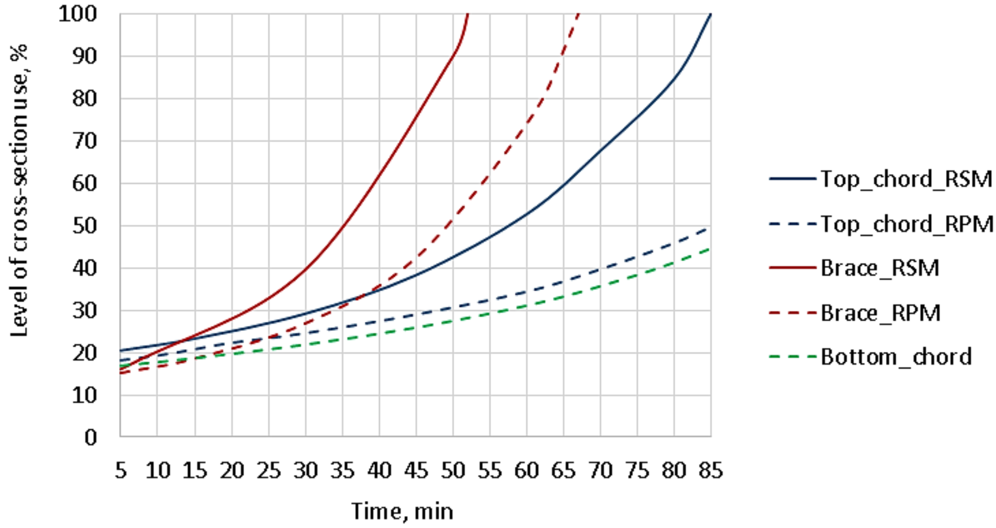

Figure 9. The dependences of the level of cross-section use as a function from the time of the fire action for glued laminated timber truss elements, where RSM – reduced section method, RPM – reduced properties method, Top_chord – the dependence obtained for the top chord, Brace – the dependence obtained for the most compressed brace; Bottom_chord – the dependence obtained for the bottom chord by the reduced properties method.

The lattice of the truss is presented by the compressed and tensioned braces. The most loaded compressed and tensioned braces of the truss are subjected to axial forces equal to 150.60 and 137.40 kN, correspondingly. The most loaded compressed and tensioned braces are the first and second braces from the support. The first from the support glued laminated timber brace has cross-section in 200x200mm and considered as a subjected to fire from four sides as it is shown on the Figure 3 a). Fire resistance of glued laminated timber brace was analysed by the equations (8)–(11) and evaluated as R52 and R65 by the reduced section and reduced properties methods, correspondingly. The fire resistance of tensioned brace is significantly bigger.

The fire resistance of the trusses joints was evaluated as R15 as bolted joints without fire protection. Therefore, overall fire resistance of the timber truss and glued laminated timber framework at all was determined as R15.

3.2. Determination of fire resistance of timber framework by method based on Russian national standard

Fire resistance of the timber structures is dependent from parameters of cross-section and density of timber. Therefore, more massive timber structure possesses a higher fire resistance. As it was mentioned before, determination of fire resistance of massive and glued laminated timber structures is joined with the determination of time R, when in case of fire cross-section of the structure decreases till the critical value, when the structure loose it load-carrying capacity. Decrease of the cross-section of the structure is joined with the development of the layer of coal on the surface of the structure in case of fire action.

The fire resistance of timber framework, described in the subchapter 3.2, was determined by the method based on Russian national standard [21]. The method was described in details in the sub-chapter 2.2. The structure in case of fire is subjected to the action of permanent and imposed loads – dead weight of structures and snow load (III snow region).

The fire action on the structure corresponds to the standard curve, which is described by the dependence (22).

$$T = T_0 + 345 \cdot \lg(8t + 1), \tag{22}$$

where T is temperature corresponding to time t, °C;

T_0 is initial temperature of fire action °C (T_0 =20 °C);

t is time from the initial moment of fire action.

Actual stresses acting in the structural members should be determined to find fire resistance which is reflected by the critical time from the initial moment of fire action till the moment, when structure loose it load-carrying capacity. Top and bottom chords of the truss so as support compressed brace were considered for evaluation of fire resistance of the glued laminated timber frame.

For support compressed brace coefficient of cross-section use before heating so as relation of initial width to depth of the cross-section are equal to 0.2 and 1.0, correspondingly. Relation of critical time to depth of the brace cross-section was determined by the nomograph and is equal to 230 min/m. Corresponding critical time is equal to 46 min. Therefore, the fire resistance of support compressed brace is equal to 51 min taking in to account time of charring delay, which is equal to 5 min.

The bottom chord of the truss is a member subjected to the action of tension force with the bending moment. For bottom chord coefficient of cross-section use before heating so as relation of initial width to depth of the cross-section are equal to 0.04 and 0.76, correspondingly as for the member subjected to flexure. The coefficient of cross-section use before heating and relation of initial width to depth of the cross-section are equal to 0.039 and 0.76, correspondingly, as for the member subjected to tension. Relations of critical time to depth of the top chord cross-section was determined by the nomographs and are equal to 241 min/m and 258 min/m by the nomograph for the bending moment and tension force, correspondingly. Corresponding critical times are equal to 101 and 108 min as for the member subjected to flexure and tension, correspondingly. Therefore, the fire resistance of the bottom chord of the truss is equal to 106 min taking in to account time of charring delay, which is equal to 5 min.

The fire resistance for the top chord of the truss was determined by the same approach as for the bottom once. For top chord coefficient of cross-section use before heating so as relation of initial width to depth of the cross-section are equal to 0.064 and 0.60, correspondingly. Relation of critical time to depth of the top chord cross-section was determined by the nomograph and is equal to 200 min/m by the nomograph for the bending moment. Corresponding critical time is equal to 80 min. Therefore, the fire resistance of support compressed brace is equal to 85 min.

The fire resistance for timber column was determined by the approach to compressed elements. For timber column coefficient of cross-section use before heating so as relation of initial width to depth of the cross-section are equal to 0.2 and 0.4, correspondingly. Relation of critical time to depth of the column cross-section was determined by the nomograph and is equal to 360 min/m. Corresponding critical time is equal to 72 min. Therefore, the fire resistance of the column is equal to 77 min taking in to account time of charring delay. Fire resistances for support compressed brace, top and bottom chords so as column are given on the Figure 10.

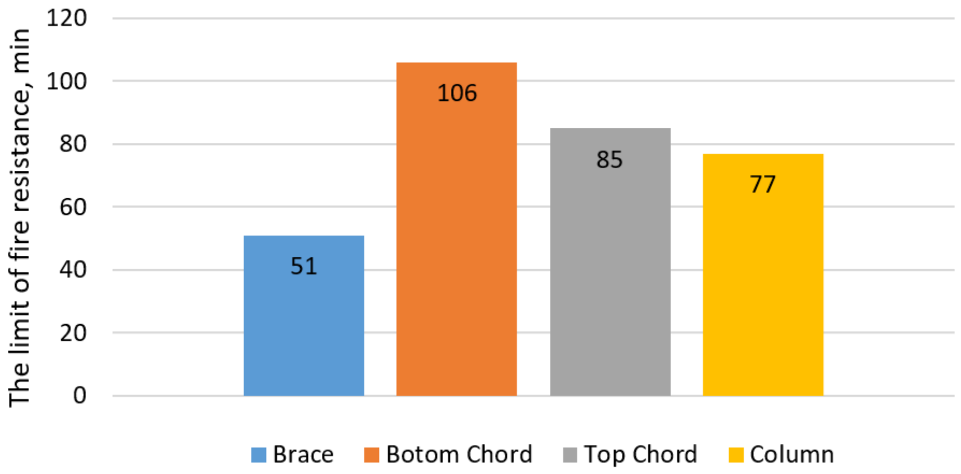

Figure 10. Value of the limit of fire resistance for part of timber frame.

Therefore, fire resistance of glued laminated timber frame is accepted as lowest value for timber frame and evaluated as R51.

3.3. Discussions

Comparison of results obtained for glued laminated load-bearing structures of timber framework for sports hall of Corporative University of Sberbank enables to make a conclusion that both methods allow to evaluate fire resistance of the major load bearing members with the comparable precision. The determinant structural member for evaluation of fire resistance for glued laminated load-bearing frameworks structure was timber truss in the case, if fire resistance of the joints is neglected. The fire resistance of glued timber top chord was evaluated by the reduced section method, reduced properties method and by method based on Russian national standard [21, 22]. The obtained values of fire resistance of glued timber top chord are evaluated as R85, R106 and R85, correspondingly. Fire resistance of glued laminated timber brace was analysed by the above-mentioned methods [21, 22] and evaluated as R52, R65 and R51 by the reduced section method, reduced properties method and by method based on Russian national standard. The fire resistances obtained for the glued laminated timber column were evaluated as R60, R70 and R77, correspondingly. Fire resistance of the glued timber bottom chord was evaluated as exceeding R106.

Therefore, it can be stated, that reduced section method, reduced properties method and method based on Russian national standard [21, 22] enable to obtain comparable results for evaluation of fire resistance for glued laminated load-bearing timber frameworks structure. The fire resistances obtained by the reduced section method and by method based on Russian national standard for the structure for sports hall of Corporative University of Sberbank were evaluated as R52 and R51, correspondingly. The differences between the results obtained for the glued laminated timber column by the method based on Russian national standard, reduced section method and reduced properties method were equal to 22.08 and 9.09 %, correspondingly. However, at the same moment, fire resistance of the trusses joints was evaluated as R15 as bolted joints without fire protection. Therefore, overall fire resistance of the timber truss and glued laminated timber framework was evaluated as R15 as for connections with the side members of timber, which are described in the point 6.2 [22]. However, the method based on Russian national standard did not contain information for evaluation of fire resistance of joints of timber structures. Therefore, adding of the chapter including approach to evaluation of fire resistance of the joints of timber structures is possible direction for further development of the method [21].

4. Conclusions

The methods for fire resistance evaluation on the base of European norm EN 1995-1-2 and method based on Russian national standard for calculation of actual fire resistance and classes of fire risk for load-bearing timber structures, which is based on the Federal Law No. 123-FZ «Technical regulations on fire safety requirements" were compared numerically for one-storey glued load-bearing timber framework. It was shown that the difference between the results obtained by the method based on Russian national standard and methods based on European norm is within the limits from 1,96 to 27.45 %. It was stated, that the method based on Russian national standard did not contain information for evaluation of fire resistance of joints of timber structures, which is determinant for the considered one-storey glued load-bearing timber framework so as it overall fire resistance was evaluated as R15 as for connections with the side members of timber. Therefore, adding of the chapter including approach for evaluation of fire resistance of the joints of timber structures is possible direction for further development of the method based on Russian national standard.

References

1. Suzuki, J., Mizukami, T., Naruse, T., Araki, Y. Fire resistance of timber panel structures under standard fire exposure. Fire Technology. 2016. No. 52. Pp. 1015–1034. DOI: 10.1007/s10694-016-0578-2
2. Goremikins, V., Serdjuks, D., Buka-Vaivade, K., Pakrastins, L., Vatin, N.I. Interaction of Prestressed Cable Truss and Cross-Laminated Timber Deck in Suspension Bridge. The Baltic Journal of Road and Bridge Engineering. 2017. Vol. 12. No. 4. Pp. 234–240. DOI: 10.3846/bjrbe.2017.29
3. Goremikins, V., Serdjuks, D., Buka-Vaivade, K., Pakrastins, L. Choice of Rational Structural Solution for Smart Innovative Suspension Structure. Proceedings of the 3nd International Conference on Innovative Materials, Structures and Technologies. IOP Conf. Series: Materials Science and Engineering. 2017. Vol. 251. Pp. 1–8. DOI: 10.1088/1757-899X/251/1/012083
4. Green, M., Taggart, J. Tall Wood Buildings Design, Construction and Performance. Birkhauser. 2017. 176 p. DOI: 10.1080/24751448.2018.1497379
5. Smith, R.E. Interlocking Cross-laminated Timber: Alternative Use of Waste Wood in Design and Construction. Proceedings of the BTES Conference – Convergence And Confluence. 2011. Pp. 1–22.
6. O'Neill, J.W., Abu, A.K., Carradine, D.M., Moss, P.J., Buchanan, A.H. Modelling the fire performance of structural timber floors. Journal of Structural Fire Engineering. 2014. Vol. 5. No. 2. Pp. 113–124. DOI: 10.1260/2040-2317.5.2.113
7. Klippel, M., Leyder, C., Frangi, A., Fontana, M., Lam, F., Ceccotti, A. Fire Tests on Loaded Cross-laminated Timber Wall and Floor Elements. Fire Safety Science. 2014. Vol. 11. Pp. 626–639. DOI: 10.3801/IAFSS.FSS.11-626
8. Frangi, A., Fontana, M. Fire Performance of Timber Structures under Natural Fire Conditions. Fire Safety Science. 2005. Pp. 279–290. DOI: 10.3801/IAFSS.FSS.8-279
9. Wiesner, F., Bisby, L.A., Bartlett, A.I., Hidalgo, J.P., Santamaria, S., Deeny, S., Hadden, R.M. Structural capacity in fire of laminated timber elements in compartments with exposed timber surfaces. Engineering Structures. 2019. Vol. 179. Pp. 284–295. DOI: 10.1016/j.engstruct.2018.10.084
10. Green, M. The case for tall wood buildings. MGB. 2012. 237 p.
11. Nedryshkin, O., Gravit, M., Grabovyy, K. Modeling fires in structures with an atrium in the FDS field model, MATEC Web of Conferences. 2018. Vol. 193. 03023. DOI: 10.1051/matecconf/201819303023
12. Gravit, M., Dmitriev, I., Ishkov, A. Quality control of fireproof coatings for reinforced concrete structures. IOP Conference Series: Earth and Environmental Science. 2017. Vol. 90. 012226. DOI: 10.1088/1755-1315/90/1/012226

13. Krivtcov, A., Gravit, M., Zimin, S., Nedryshkin, O., Pershakov, V. Calculation of limits of fire resistance for structures with fire retardant coating. MATEC Web of Conferences. 2016. Vol. 53. 01032. DOI: 10.1051/matecconf/20165301032
14. Tiso, M., Just, A., Schmid, J., Klippel, M. Effective cross-sectional method for timber frame assemblies—definition of coefficients and zero-strength layers. Fire and Materials. 2018. Vol. 42. No. 8. Pp. 897–913. DOI: 10.1002/fam.2645
15. Schmid, J., Klippel, M., Just, A., Frangi, A., Tiso, M. Simulation of the Fire Resistance of Cross-laminated Timber (CLT). Fire Technology. 2018. Vol. 54. No. 5. Pp. 1113–1148. DOI: 10.1007/s10694-018-0728-9
16. Roszkowski, P., Sulik, P., Sedlak, B. Fire resistance of timber stud walls. Forestry and Wood Technology. 2015. No. 92. Pp. 368–372.
17. Polishchuk, E.Yu., Sivenkov, A.B., Kenzhehan, S.K. Heating and charring of timber constructions with thin-layer fire protection. Magazine of Civil Engineering. 2018. Vol. 81. No. 5. Pp. 3–14. DOI: 10.18720/MCE.81.1.
18. Saknite, T., Serdjuks, D., Goremikins, V., Pakrastins, L., Vatin, N.I. Fire Design of Arch-type Timber Roof. Magazine of Civil Engineering. 2016. Vol. 64(4). Pp. 26–39. DOI: 10.5862/MCE.64.3
19. Kinjo, H., Katakura, Y., Hirashima, T., Yusa, S., Saito, K. Deflection behavior and load-bearing period of structural glued laminated timber beams in fire including cooling phase. Journal of Structural Fire Engineering. 2018. Vol. 9. No. 4. Pp. 287–299. DOI: 10.1108/JSFE-01-2017-0009
20. Östmana, B., Brandonb, D., Frantzichc, H. Fire safety engineering in timber buildings. Fire Safety Journal. 2017. Vol. 91. Pp. 11–20. DOI: 10.1016/j.firesaf.2017.05.002
21. Metodika ocenki predelov ognestojkosti i klassov pozharnoj opasnosti nesuschih derevjannyh konstrukcij [Method for calculation of actual fire resistance and classes of fire risk for load-bearing timber structures]. Moscow: FGBU VNIIPO, 2018. 19 p. (rus)
22. Eurocode 5: Design of timber structures – Part 1–2: General – Structural fire design
23. EN 1990: Basis of structural design
24. Eurocode 5: Design of timber structures – Part 1–1: General – Common rules and rules for buildings
25. Mosalkov, I.L. Ognestoykost stroitelnyh konstrukciy [Fire resistance of building constructions]. Moscow: ZAO «SPECTEHNIKA», 2001. 490 p. ISBN 5-901018-13-3. (rus)
26. Posobie po opredeleniyu predelov ognestojkosti stroitel'nyh konstrukcij, parametrov pozharnoj opasnosti materialov. Poryadok proektirovaniya ognezashchity. Spravochnyj material [Allowance to determine the fire resistance of building structures, parameters of fire hazard materials. fire protection design procedure. Reference material]. Moscow: JSC Research Center of Construction, 2013. 38 p. (rus)
27. International standart of Commonwealth of Independent States GOST 30247.0 Konstruktsii stroitelnyye. Metody ispytaniy na ognestoykost. Obshchiye trebovaniya [Elements of building constructions. Fire-resistance test methods. General requirements]. (rus)
28. EN 338: Structural timber. Strength classes
29. EN 14080: Timber structures. Glued laminated timber and glued solid timber. Requirements

Contacts:

Marina Gravit, +79129126407; marina.gravit@mail.ru
Dmitrijs Serdjuks, +37126353082; Dmitrijs.Serdjuks@rtu.lv
Aleksei Bardin, +79313546847; kmkbav@gmail.com
Vasiliy Prusakov, +79129126407; info@tdpromizol.com
Karina Buka-Vaivade, +37126353082; karina.buka.vaivade@gmail.com

Инженерно-строительный журнал

ISSN 2071-0305

сайт журнала: http://engstroy.spbstu.ru/

DOI: 10.18720/MCE.85.8

Методы определения огнестойкости конструкций деревянного каркаса

М.В. Гравит[a], Д.О. Сердюк[b]*, А.В. Бардин[a], В.А. Прусаков[c], К. Бука-Вайваде[b],

[a] Санкт-Петербургский политехнический университет Петра Великого, Санкт-Петербург, Россия

[b] Рижский технический университет, г. Рига, Латвия

[c] ООО «ПРОМИЗОЛ», г. Томилино, Люберецкий район Московской области, Россия

** E-mail: Dmitrijs.Serdjuks@rtu.lv*

Ключевые слова: клееный несущий деревянный каркас, трапециевидная деревянная ферма, клееный деревянный настил, метод уменьшенных сечений, метод уменьшенной прочности, огнестойкость.

Аннотация. Использование деревянных конструкций позволяет снизить негативное воздействие человеческой деятельности на окружающую среду. Надежность деревянных конструкций может быть обеспечена путем достижения соответствующей огнестойкости так как опасность пожара является одним из главных недостатков деревянных конструкций. Разработка новых методов определения огнестойкости деревянных конструкция является актуальным вопросом. В настоящий момент на основе российского национального стандарта разработана первая редакция методики оценки пределов огнестойкости и классов пожарной опасности несущих деревянных конструкций. Результаты, полученные при помощи данной методики для определения огнестойкости несущих деревянных конструкций здания спортзала Корпоративного университета Сбербанка, сравнены с результатами, полученными при помощи расчетных методов, описанных в европейских нормах. Несущие деревянные конструкции здания спортзала Корпоративного университета Сбербанка представлены двухшарнирной клееной деревянной рамой , состоящей из трапециевидной фермы с треугольной решеткой, двумя консолями, а так же клееными колоннами и клееным деревянным настилом. В результате сравнения, получено, что методика оценки пределов огнестойкости и классов пожарной опасности несущих деревянных конструкций на основе российского национального стандарта дает результаты сопоставимые с результатами, полученными при помощи методов, описанных в европейских нормах. В то же время следует отметить, что отсутствие информации по определению огнестойкости узлов конструкций является существенным недостатком методики на основе российского национального стандарта, так как именно узлы часто являются звеном, определяющим огнестойкость деревянных конструкций. Дополнение методики на основе российского национального стандарта информацией по определению огнестойкости узлов является рекомендацией по ее улучшению.

Литература

1. Suzuki J., Mizukami T., Naruse T., Araki Y. Fire resistance of timber panel structures under standard fire exposure. Fire Technology. 2016. No. 52. Pp. 1015–1034. DOI: 10.1007/s10694-016-0578-2
2. Goremikins V., Serdjuks D., Buka-Vaivade K., Pakrastins L., Vatin N.I. Interaction of Prestressed Cable Truss and Cross-Laminated Timber Deck in Suspension Bridge. The Baltic Journal of Road and Bridge Engineering. 2017. Vol. 12. No. 4. Pp. 234–240. DOI: 10.3846/bjrbe.2017.29
3. Goremikins V., Serdjuks D., Buka-Vaivade K., Pakrastins L. Choice of Rational Structural Solution for Smart Innovative Suspension Structure. Proceedings of the 3nd International Conference on Innovative Materials, Structures and Technologies. IOP Conf. Series: Materials Science and Engineering. 2017. Vol. 251. Pp. 1–8. DOI: 10.1088/1757-899X/251/1/012083
4. Green M., Taggart J. Tall Wood Buildings Design, Construction and Performance. Birkhauser. 2017. 176 p. DOI: 10.1080/24751448.2018.1497379
5. Smith R.E. Interlocking Cross–laminated Timber: Alternative Use of Waste Wood in Design and Construction. Proceedings of the BTES Conference – Convergence And Confluence. 2011. Pp. 1–22.
6. O’Neill J.W., Abu A.K., Carradine D.M., Moss P.J., Buchanan A.H. Modelling the fire performance of structural timber floors. Journal of Structural Fire Engineering. 2014. Vol. 5. No. 2. Pp. 113–124. DOI: 10.1260/2040-2317.5.2.113
7. Klippel M., Leyder C., Frangi A., Fontana M., Lam F., CeccottiA. Fire Tests on Loaded Cross-laminated Timber Wall and Floor Elements. Fire Safety Science. 2014. Vol. 11. Pp. 626–639. DOI: 10.3801/IAFSS.FSS.11-626

8. Frangi A., Fontana M. Fire Performance of Timber Structures under Natural Fire Conditions. Fire Safety Science. 2005. Pp. 279–290. DOI: 10.3801/IAFSS.FSS.8-279
9. Wiesner F., Bisby L.A., Bartlett A.I., Hidalgo J.P., Santamaria S., Deeny S., Hadden R.M. Structural capacity in fire of laminated timber elements in compartments with exposed timber surfaces. Engineering Structures. 2019. Vol. 179. Pp. 284–295. DOI: 10.1016/j.engstruct.2018.10.084
10. Green M. The case for tall wood buildings. MGB. 2012. 237 p.
11. Nedryshkin O., Gravit M., Grabovyy K. Modeling fires in structures with an atrium in the FDS field model, MATEC Web of Conferences. 2018. Vol. 193. 03023. DOI: 10.1051/matecconf/201819303023
12. Gravit M., Dmitriev I., Ishkov A. Quality control of fireproof coatings for reinforced concrete structures. IOP Conference Series: Earth and Environmental Science. 2017. Vol. 90. 012226. DOI: 10.1088/1755-1315/90/1/012226
13. Krivtcov A., Gravit M., Zimin S., Nedryshkin O., Pershakov V. Calculation of limits of fire resistance for structures with fire retardant coating. MATEC Web of Conferences. 2016. Vol. 53. 01032. DOI: 10.1051/matecconf/20165301032
14. Tiso M., Just A., Schmid J., Klippel M. Effective cross-sectional method for timber frame assemblies—definition of coefficients and zero-strength layers. Fire and Materials. 2018. Vol. 42. No. 8. Pp. 897–913. DOI: 10.1002/fam.2645
15. Schmid J., Klippel M., Just A., Frangi A., Tiso M. Simulation of the Fire Resistance of Cross-laminated Timber (CLT). Fire Technology. 2018. Vol. 54. No. 5. Pp. 1113–1148. DOI: 10.1007/s10694-018-0728-9
16. Roszkowski P., Sulik P., Sedlak B. Fire resistance of timber stud walls. Forestry and Wood Technology. 2015. No. 92. Pp. 368–372.
17. Polishchuk E.Yu., Sivenkov A.B., Kenzhehan S.K. Heating and charring of timber constructions with thin-layer fire protection. Magazine of Civil Engineering. 2018. Vol. 81. No. 5. Pp. 3–14. DOI: 10.18720/MCE.81.1.
18. Saknite T., Serdjuks D., Goremikins V., Pakrastins L., Vatin N.I. Fire Design of Arch-type Timber Roof. Magazine of Civil Engineering. 2016. Vol. 64(4). Pp. 26–39. DOI: 10.5862/MCE.64.3
19. Kinjo H., Katakura Y., Hirashima T., Yusa S., Saito K. Deflection behavior and load-bearing period of structural glued laminated timber beams in fire including cooling phase. Journal of Structural Fire Engineering. 2018. Vol. 9. No. 4. Pp. 287–299. DOI: 10.1108/JSFE-01-2017-0009
20. Östmana B., Brandonb D., Frantzichc H. Fire safety engineering in timber buildings. Fire Safety Journal. 2017. Vol. 91. Pp. 11–20. DOI: 10.1016/j.firesaf.2017.05.002
21. Методика оценки пределов огнестойкости и классов пожарной опасности несущих деревянных конструкций. Москва: ФГБУ ВНИИПО, 2018. 19 с.
22. Eurocode 5: Design of timber structures – Part 1–2: General – Structural fire design
23. EN 1990: Basis of structural design
24. Eurocode 5: Design of timber structures – Part 1–1: General – Common rules and rules for buildings
25. Мосалков И.Л. Огнестойкость строительных конструкций. Москва: ЗАО «СПЕЦТЕХНИКА», 2001. 490 с. ISBN 5-901018-13-3
26. Пособие по определению пределов огнестойкости строительных конструкций, параметров пожарной опасности материалов. Порядок проектирования огнезащиты. Справочный материал. Москва: ОАО НИЦ «Строительство», 2013. 38 с.
27. Межгосударственный стандарт ГОСТ 30247.0. Конструкции строительные. Методы испытаний на огнестойкость. Общие требования.
28. EN 338: Structural timber. Strength classes
29. EN 14080: Timber structures. Glued laminated timber and glued solid timber. Requirements

Контактные данные:

Марина Викторовна Гравит, +79129126407; эл. почта: marina.gravit@mail.ru
Дмитрий Олегович Сердюк, +37126353082; эл. почта: Dmitrijs.Serdjuks@rtu.lv
Алексей Владимирович Бардин, +79313546847; эл. почта: kmkbav@gmail.com
Василий Алексеевич Прусаков, +79129126407; эл. почта: info@tdpromizol.com
Карина Бука-Вайваде, +37126353082; эл. почта: karina.buka.vaivade@gmail.com

Magazine of Civil Engineering. 2019. 85(1). Pp. 107–122
Инженерно-строительный журнал. 2019. № 1(85). С. 107–122

Magazine of Civil Engineering

ISSN 2071-0305

journal homepage: http://engstroy.spbstu.ru/

DOI: 10.18720/MCE.85.9

Calculation method of bending plates with assuming shear deformations

Yu. Ya. Tyukalov*,
Vyatka State University, Kirov, Russia
** E-mail: yutvgu@mail.ru*

Keywords: bending plates, shear deformations, stresses, finite elements.

Abstract. The problem of calculating bending plates by the finite element method with considering of shear deformations is considered. The bending plates are widely used as common structures of various objects of civil and industrial construction. The solution was obtained on the basis of the principles of the minimum of additional energy and possible displacements. For approximation of moment fields, piecewise constant functions are used. Shear forces can be approximated by constant or piecewise constant functions. The necessary relations for rectangular and triangular finite elements are obtained. It is shown that the proposed method can be used in combination with traditional finite elements for thin plates obtained by the finite element method in displacements. A comparison of the solutions, obtained by the proposed method, with other known solutions for bending plates, with assuming of shear deformations, is given. A numerical estimate of the accuracy and convergence of the proposed method, when crushing the finite element mesh, is given.

1. Introduction

The bending plates are widely used as common structures of various objects of civil and industrial construction. Often, in modern constructions thick and multi-layered slabs are used. In calculating, such thick slabs, we should consider, besides the bending deformations, the shear strains, which can significantly affect the values of the plate displacements. The classical theory of Kirchhoff plate bending is based on assumption of the direct normals assumption and, therefore, does not allow for the shear deformations. The finite elements, which are developed based on the Kirchhoff theory, are can used only for the calculation of thin plates [1–2]. Therefore, Timoshenko–Mindlin theory of bending plates [3–4] are widely application for calculating thick plates. According to this theory, angles of rotation of the normals and the vertical displacements are considered as independent variables. Such an approach lowers the maximum order of derivatives in the strains energy functional and makes it possible to use the first-order function-forms for approximating the displacements. Studies have shown that the direct use of the Timoshenko–Mindlin theory for constructing finite elements in displacements leads to the effect of «locking», or to the impossibility of using these finite elements to calculate thin plates.

To overcome the «locking» effect, various procedures are used, such as putting the assumption of direct normals at discrete points or applying high order shift theories [5–6]. The finite elements based on the putting the assumption of direct normals in the middle points of the finite element sides are widely used in program complexes. The new methods for considering for shear deformations, based on equations in displacements, are also offered in [7–8]. In [9–10], nonlinear solutions for rod systems with considering for shear deformations of cross sections are considered. The high order shear theories, when deformations along a cross section change by to a law other than linear, are used in constructing analytical solutions to bending problems of rectangular plates [11–12]. To construct finite elements, that considering shear deformations, the theory of the third order is successfully applied [13–14]. In [14], the quadrangular finite element is presented, that has seven degrees of freedom at each node: three displacements along the axes of coordinates, two shear angles and

Tyukalov, Yu.Ya. Calculation method of bending plates with assuming shear deformations. Magazine of Civil Engineering. 2019. 85(1). Pp. 107–122. DOI: 10.18720/MCE.85.9.

Тюкалов Ю.Я. Метод расчета изгибаемых плит с учетом деформаций сдвига // Инженерно-строительный журнал. 2019. № 1(85). С. 107–122. DOI: 10.18720/MCE.85.9

two angles of rotation of the normals. This approach allows us to more accurately consider shear deformations, when the properties of the material change in various directions.

The procedure for introduction shear deformations in existing finite elements designed for the calculation of thin plates is proposed in [15]. The deformations of the transverse shear can be accounting since the direct use of the equations of the three-dimensional theory of elasticity. This method and the Galerkin's method in a weak form is used to construct a quadrilateral finite element [16]. Also, the Galerkin's method is used to construct triangular and quadrangular finite elements according to the Timoshenko-Mindlin theory in [17].

Another way to construct finite elements with accounting shear deformations is the use of mixed and hybrid variational formulations [18–20]. This approach, on the one hand, simplifies the consideration of shear deformations due to the use of transverse forces and moments as unknowns, together with displacements. On the other hand, in order to ensure convergence of solution, it is necessary to agree on approximations of displacements and forces. Note the work [21–23], in which the solution of the problem of plate bending with consider the shear deformations, the modified Mindlin's theory is used. The modification of the Mindlin's theory consists in the introduction of an additional unknown parameter in the form of an angle of rotation in the plane of the plate.

Thus, construction the models with considering shear deformations, which are alternatives by the finite element method in displacements, is actual for the bending plates. The purpose of this work is to develop the method for calculating the plates with accounting shear deformations based on the functional of additional energy and the principle of possible displacements [24–27], as well as comparing the solutions obtained for plates with different support conditions with solutions of the other methods.

2. Methods

Solving the problems of plate bending with considering the shear deformations due to transverse forces, we will obtain based on the functional of additional energy for an isotropic plate (for simplicity, we assume that there are no specified displacements) [1]:

$$\Pi^c = \frac{1}{2}\left(\frac{12}{E\cdot t^3}\right)\int\left(M_x^2 + M_y^2 - 2\nu M_x M_y + 2(1+\nu)M_{xy}^2\right)\mathrm{d}\Omega + \frac{1}{2}\left(\frac{2k(1+\nu)}{E\cdot t}\right)\int\left(Q_x^2 + Q_y^2\right)\mathrm{d}\Omega \to \min. \quad (1)$$

E is the modulus of elasticity of the material; t is the plate thickness; ν is Poisson's ratio; k is coefficient, which considering the parabolic law of change of the tangential stresses across the thickness of the plate. The functional (1), also called the Castigliano's functional, is also considered in [2]. In [1] it was shown that in the linear theory of elasticity the value Π^c for the equilibrium state is minimal.

We write the functional (1) in matrix form that is more convenient for solving by the finite element method:

$$\Pi^c = \frac{1}{2}\int\{M\}^T[E]^{-1}\{M\}\mathrm{d}\Omega + \frac{1}{2}\int\{Q\}^T[E_{sh}]^{-1}\{Q\}\mathrm{d}\Omega \to \min. \quad (2)$$

In expression (2) the following notation is entered:

$$\{M\} = \begin{Bmatrix} M_x \\ M_y \\ M_{xy} \end{Bmatrix},\quad \{Q\} = \begin{Bmatrix} Q_x \\ Q_y \end{Bmatrix},\quad [E]^{-1} = \frac{12}{E\cdot t^3}\begin{bmatrix} 1 & -\nu & 0 \\ -\nu & 1 & 0 \\ 0 & 0 & 2(1+\nu) \end{bmatrix},\quad [E_{sh}]^{-1} = \frac{12(1+\nu)}{5E\cdot t}\begin{bmatrix} 1 & 0 \\ 0 & 1 \end{bmatrix}. \quad (3)$$

In the functional (2), the first member is associated with the bending deformations of the plate, the second – with shear deformations by transverse forces. M_x and Q_x are the bending moment directed along the X axis and the corresponding shear force; M_y and Q_y are the bending moment directed along the Y axis and the corresponding shear force; M_{xy} is torque. The bending moments are positive if the lower fibers of the plate are stretched.

In accordance with the principle of minimum of additional energy, the functions of moments and shear forces must satisfy the corresponding differential equations of equilibrium and static boundary conditions. Since, in the general case, it is almost impossible to select such functions, we will operate as follows. Divide the plate into rectangular or triangular finite elements. On the region of the finite element, we approximate the moment and shear force fields by piecewise constant functions (Figure 1a). Below we show that transverse forces can also be approximated by the functions, which are constant over the finite element region (Figure 1b).

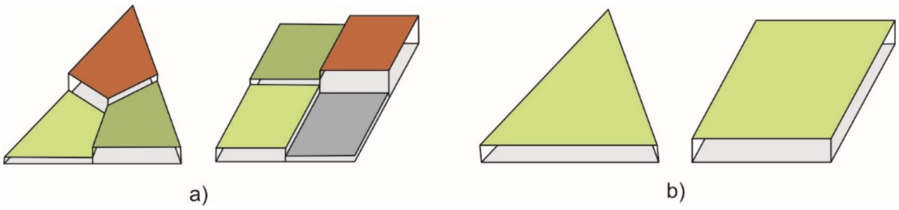

Figure 1. Approximation of moments and shear forces in the region of finite elements: a) piecewise constant moments and shear forces; b) constant transverse forces.

Then the functional (2) can be written in the following form:

$$\Pi^c = \frac{1}{2}\{M\}^T[D]\{M\} + \frac{1}{2}\{Q\}^T[D_{sh}]\{Q\} \to \min. \tag{4}$$

$\{M\}$ is vector of unknown nodal moments for the whole system;

$[D]$ is flexibility matrix for the whole system under bending;

$[D_{sh}]$ is flexibility matrix for the whole system under shear.

Then, using the principle of possible displacements, we are construct algebraic equilibrium equations of the nodes of the grid of finite elements. In this case, independently, possible displacements causing only a bending state and possible displacements causing only a shift are considered. In Figure 2, it is showing such possible displacements by the example of beam elements. Under the possible bend (Figure 2a), the cross sections rotate and remain perpendicular to the neutral axis, and the nodal moments do the work. Under shear (Figure 2b), the cross sections remain vertical and only transverse forces perform a work. For triangular and rectangular finite elements of a plate, possible states are like to those shown in Figure 2.

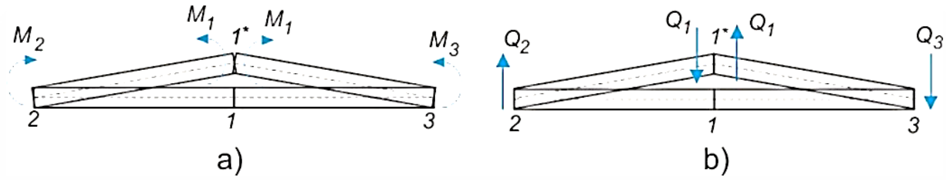

Figure 2. Possible displacements of node 1: a) bending state; b) shear state.

Under bending, the equilibrium equations are expressed through the nodal moments and can be represented in the following matrix form:

$$\{C_i\}^T\{M_i\} + \bar{P}_i = 0, \quad i \in \Xi_z. \tag{5}$$

Static boundary conditions we write in the following form:

$$M_{n,i} = M_{x,i}\cos^2\varphi_i + M_{y,i}\sin^2\varphi_i - 2M_{xy,i}\sin\varphi_i\cos\varphi_i - \bar{M}_{n,i} = 0,$$
$$M_{ns,i} = \left(-M_{x,i} + M_{y,i}\right)\sin\varphi_i\cos\varphi_i + M_{xy,i}\left(\cos^2\varphi_i - \sin^2\varphi_i\right) - \bar{M}_{ns,i} = 0, \quad i \in \Xi_\Gamma$$

Under shear, the equilibrium equations are expressed only through the transverse forces and are represented in follow form:

$$\{C_{sh,i}\}^T\{Q_i\} + \bar{P}_i = 0, \quad i \in \Xi_z. \tag{6}$$

Static boundary conditions for transverse forces are as follows:

$$Q_{n,i} = Q_{x,i}\cos\varphi_i + Q_{y,i}\sin\varphi_i - \bar{Q}_{n,i} = 0, \quad i \in \Xi_\Gamma,$$

φ_i is the angle between the tangent to the border at node i and the axis X; $\bar{M}_{n,i}$, $\bar{Q}_{n,i}$ are the values of setting moments and shear forces, which are normal to the boundary; $\bar{M}_{ns,i}$ is the values of the setting moments, which are tangent to the boundary; $M_{x,i}, M_{y,i}, M_{xy,i}$ are unknown nodal moments; $Q_{x,i}$, $Q_{y,i}$ are unknown nodal shear forces; $\{M_i\}, \{Q_i\}$ are vectors of unknown nodal moments and shear forces of all finite elements adjoining to node i; Ξ_z are set of nodes that have free displacement along the vertical axis Z; Ξ_Γ

are set of nodes lying on the border; $\overline{P}_i$ is the generalized force corresponding to the potential of external loads under single possible displacement of the node i along the Z axis; $\{C_i\}$, $\{C_{sh,i}\}$ are vectors, which contain coefficients at unknown nodal moments and at shear forces in the equilibrium equations of node i along the vertical axis Z. Algebraic equilibrium equations provide the equilibrium of moments and shear forces in a discrete sense.

Thus, we have obtained the problem of minimizing quadratic function of several variables (4) with constraints in the form of system of linear algebraic equations. Unknown parameters are nodal moments and shear forces. To solve this problem, we use the well-known Lagrange multipliers method for account the equilibrium equations and static boundary conditions. Then, we get the following expression of the extended functional:

$$\begin{aligned}
&\Pi^c = \frac{1}{2}\{M\}^T[D]\{M\} + \frac{1}{2}\{Q\}^T[D_{sh}]\{Q\} + \\
&\sum_{i\in\Xi_z} w_i\left(\{C_i\}^T\{M_i\} + \overline{P}_i\right) + \sum_{i\in\Xi_z} w_{sh,i}\left(\{C_{sh,i}\}^T\{Q_i\} + \overline{P}_i\right) + \\
&\sum_{i\in\Xi_\Gamma} \lambda_{1,i}\left(M_{x,i}\cos^2\varphi_i + M_{y,i}\sin^2\varphi_i - 2M_{xy,i}\sin\varphi_i\cos\varphi_i - \overline{M}_{n,i}\right) + \\
&\sum_{i\in\Xi_\Gamma} \lambda_{2,i}\left(\left(M_{y,i} - M_{x,i}\right)\sin\varphi_i\cos\varphi_i + M_{xy,i}\left(\cos^2\varphi_i - \sin^2\varphi_i\right) - \overline{M}_{ns,i}\right) + \\
&\sum_{i\in\Xi_\Gamma} \lambda_{3,i}\left(Q_{x,i}\cos\varphi_i + Q_{y,i}\sin\varphi_i - \overline{Q}_n\right) \to \min.
\end{aligned} \tag{7a}$$

Static boundary conditions can also be considered using the penalty function method, then we get

$$\begin{aligned}
&\Pi^c = \frac{1}{2}\{M\}^T[D]\{M\} + \frac{1}{2}\{Q\}^T[D_{sh}]\{Q\} + \\
&\sum_{i\in\Xi_z} w_i\left(\{C_i\}^T\{M_i\} + \overline{P}_i\right) + \sum_{i\in\Xi_z} w_{sh,i}\left(\{C_{sh,i}\}^T\{Q_i\} + \overline{P}_i\right) + \\
&\sum_{i\in\Xi_\Gamma} \alpha\left(M_{x,i}\cos^2\varphi_i + M_{y,i}\sin^2\varphi_i - 2M_{xy,i}\sin\varphi_i\cos\varphi_i - \overline{M}_{n,i}\right)^2 + \\
&\sum_{i\in\Xi_\Gamma} \alpha\left(\left(M_{y,i} - M_{x,i}\right)\sin\varphi_i\cos\varphi_i + M_{xy,i}\left(\cos^2\varphi_i - \sin^2\varphi_i\right) - \overline{M}_{ns,i}\right)^2 + \\
&\sum_{i\in\Xi_\Gamma} \alpha\left(Q_{x,i}\cos\varphi_i + Q_{y,i}\sin\varphi_i - \overline{Q}_n\right)^2 \to \min.
\end{aligned} \tag{7b}$$

w_i is vertical displacement of the node i, associated with the bend of the plate; $w_{sh,i}$ is vertical displacement of the node i, associated with the shear of the plate cross sections; α is penalty parameter (large number). Obviously, the total displacement will be equal to the sum of these two values.

The use of penalty functions to account for static boundary conditions eliminates the introduction of additional unknowns, as compared to the Lagrange multipliers method. The calculation of the derivatives of the penalty functions along the unknown nodal forces leads to the appearance of additional addends to the elements of the flexible matrix $[D]$ and to the elements of the load vectors $\{F^M\}$ and $\{F^Q\}$. If the static boundary conditions are zero, then the elements of the vectors $\{F^M\}$ and $\{F^Q\}$ are equal to zero. With considering the static boundary conditions, the matrix of flexibility will be denoted with the index Γ - $[D^\Gamma]$.

Then, the expression of the functional (7) can be represented in a more compact matrix form:

$$\begin{aligned}
&\Pi^c = \frac{1}{2}\{M\}^T[D^\Gamma]\{M\} + \frac{1}{2}\{Q\}^T[D_{sh}^\Gamma]\{Q\} + \{M\}^T\{F^M\} + \{Q\}^T\{F^Q\} + \\
&\{w\}^T\left(\{F\} - [L]\{M\}\right) + \{w_{sh}\}^T\left(\{F\} - [L_{sh}]\{Q\}\right) \to \min.
\end{aligned} \tag{8}$$

$\{w\}$, $\{w_{sh}\}$ are vectors of global displacements of nodes, associated with bending and shearing, respectively; $\{F\}$ is the loads vector, whose elements are equal to the works of external forces on the single vertical displacements of nodes; $[L]$, $[L_{sh}]$ are matrices of equilibrium equations, the rows of which are formed from the vectors $\{C_i\}$ and $\{C_{sh,i}\}$, respectively.

Equating to zero the derivatives of the functional Π^c along the vectors $\{M\}$ and $\{w\}$, we obtain the system of equations, consisting of the equations of the compatibility of deformations and the equilibrium equations for bending:

$$\begin{bmatrix} [D^{\Gamma}] & -[L]^T \\ -[L] & [0] \end{bmatrix} \begin{Bmatrix} \{M\} \\ \{w\} \end{Bmatrix} = \begin{Bmatrix} -\{F^M\} \\ -\{F\} \end{Bmatrix}. \tag{9}$$

If piecewise constant approximations are used for the moment fields, then the we easily get inverse matrix $[D^{\Gamma}]^{-1}$ analytically. Therefore, we can easily express the vector $\{M\}$ from the first matrix equation:

$$\{M\} = [D^{\Gamma}]^{-1}[L]^T\{w\}. + [D^{\Gamma}]^{-1}\{F^M\}. \tag{10}$$

Substituting expression (10) into the second matrix equation of (9), we obtain the system of linear algebraic equations for determining the vector $\{w\}$:

$$[K]\{w\} = \{F\} + [L][D^{\Gamma}]^{-1}\{F^M\}, \quad [K] = [L][D^{\Gamma}]^{-1}[L]^T. \tag{11}$$

The expressions for the elements of the vector $\{F\}$, matrices $[D]$, $[L]$, the algorithm of their formation and examples of the calculation of bent plates corresponding to the Kirchhoff theory, are given in [27].

To determine the displacement vector $\{w_{sh}\}$ and the vector of transverse forces $\{Q\}$ associated with shear deformations, we equate to zero the derivatives of the functional Π^c along the vectors $\{Q\}$ and $\{w_{sh}\}$. Then we get the following system of equations, like the system of equations (9):

$$\begin{bmatrix} [D^{\Gamma}_{sh}] & -[L_{sh}]^T \\ -[L_{sh}] & [0] \end{bmatrix} \begin{Bmatrix} \{Q\} \\ \{w_{sh}\} \end{Bmatrix} = \begin{Bmatrix} -\{F^Q\} \\ -\{F\} \end{Bmatrix}. \tag{12}$$

The solution of the system of equations (12) can be performed in the following sequence:

$$\begin{gathered} [K_{sh}] = [L_{sh}][D^{\Gamma}_{sh}]^{-1}[L_{sh}], \quad [K_{sh}]\{w_{sh}\} = \{F\} + [L_{sh}][D^{\Gamma}_{sh}]^{-1}\{F^Q\}, \\ \{Q\} = [D^{\Gamma}_{sh}]^{-1}[L_{sh}]^T\{w_{sh}\} + [D^{\Gamma}_{sh}]^{-1}.\{F^Q\}. \end{gathered} \tag{13}$$

Thus, solving the minimization problem of the functional (7) is reduced to solving two independent systems of linear algebraic equations (9) and (12). This allows, if necessary, to analyze the state of bending and state of shear of plates separately from each other. For example, one can solve the problem of plate bending, without considering the shear, by the finite element method in displacements, and the additional displacements, associated with the shear of cross sections, can be determined from the solution of the system of equations (12).

We will obtain the necessary expressions for the elements of the matrix $[D_{sh}]$, $[L_{sh}]$ and vector $\{F\}$, when using the rectangular and triangular finite elements for the discretization of the subject area (Figure 3). To approximate the fields of transverse forces on a finite element region, we consider piecewise-constant (Figure 1a) and constant (Figure 1b) functions.

Consider the variant of piecewise constant approximations of transverse forces. We introduce the following notation: $\{\overline{Q}_i\} = \begin{Bmatrix} \overline{Q}_{x,i} \\ \overline{Q}_{y,i} \end{Bmatrix}$ is vector of shear forces at node i in the local coordinate system X_1OY_1. $\{Q_i\} = \begin{Bmatrix} Q_{x,i} \\ Q_{y,i} \end{Bmatrix}$ is vector of shear forces at node i in the global coordinate system XOY.

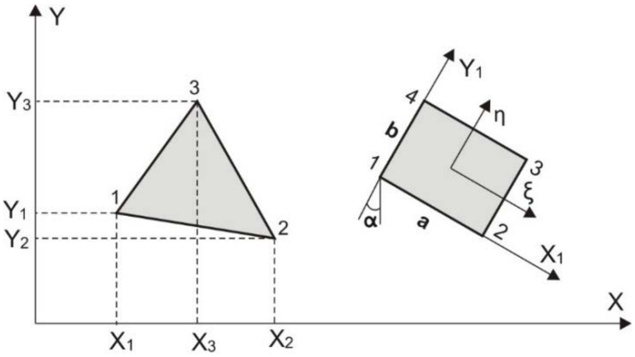

Figure 3. Triangular and rectangular finite elements.

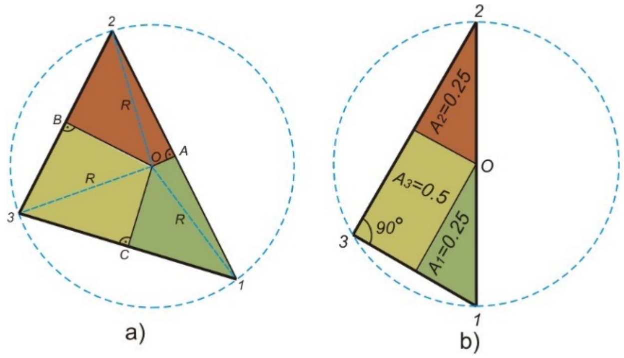

Figure 4. The division of triangular finite element into areas with constant transverse forces: a) arbitrary triangle; b) orthogonal triangle.

If the shear forces are piecewise constant, the expression of the additional strain energy in the global coordinate system can be written as simple sum:

$$U^* = \frac{1}{2}\sum\nolimits_{i=1}^{m} A_i \{Q_i\}^T [E_{sh}]^{-1}\{Q_i\}, \tag{14}$$

$$A_i = \sum\nolimits_{s=1}^{n_{i,R}} \frac{1}{4}A^s + \sum\nolimits_{s=1}^{n_{i.T}} A_i^s. \tag{15}$$

m is total number of nodes;

$n_{i,R}$ is the number of rectangular elements adjoined to node i;

$n_{i,T}$ is the number of triangular elements adjoined to node i;

A^s is area of the s-th finite element;

A_i^s is the area of the part s-th of the triangular finite element with constant transverse forces, adjoined to the node i (Figure 4a).

For rectangular finite element, the division of the finite element into regions with constant moments is uniquely – into four equal regions. For triangular element, each side must be divided equally, but there must also be the point, inside the element, at which the three areas connected to the nodes intersect. This point can be defined as the intersection point of perpendiculars drawn from the middle of the sides (Figure 4a). If the greatest angle of the triangle is more than 90 degrees, then such the point will lie outside the triangle. In this case, the triangle is divided into zones by lines passing through the midpoints of the sides. These lines will be parallel to the sides of the triangle. The proposed division of the triangular element into regions with constant moments, allows to obtain more accurate results, than when simply dividing into three equal parts – $\frac{1}{3}A^s$.

In Figure 4a point O is the center of the circle, described around triangle. OA, OB, OC *are* perpendiculars, which drawn from the midpoints of the corresponding sides of the triangle. Denote the lengths of the sides of the triangle as l_{12}, l_{23}, l_{31}. From geometric scheme in Figure 4a we get:

$$\begin{gathered} R = \frac{l_{12}l_{23}l_{31}}{4A^s}, \quad A_1^s = \frac{l_{12}}{4}\sqrt{R^2 - \frac{l_{12}^2}{4}} + \frac{l_{31}}{4}\sqrt{R^2 - \frac{l_{31}^2}{4}}, \\ A_2^s = \frac{l_{12}}{4}\sqrt{R^2 - \frac{l_{12}^2}{4}} + \frac{l_{23}}{4}\sqrt{R^2 - \frac{l_{23}^2}{4}}, \quad A_3^s = \frac{l_{23}}{4}\sqrt{R^2 - \frac{l_{23}^2}{4}} + \frac{l_{31}}{4}\sqrt{R^2 - \frac{l_{31}^2}{4}}. \end{gathered} \tag{16}$$

Obviously, for orthogonal triangle (Figure 4b) we get – $A_1^s = A_2^s = \frac{1}{4}A^s$, $A_3^s = \frac{1}{2}A^s$. If one of the corners of the triangle is greater than 90°, then, as well as for orthogonal triangle, we get: $A_1^s = A_2^s = \frac{1}{4}A^s$, $A_3^s = \frac{1}{2}A^s$. In addition, it is obvious, that it is better not to use too long triangles.

We introduce the notation for the flexible matrix $\left[D_{sh,i}\right]$ of "neighborhoods" of node i and for the global flexible matrix for the whole system $\left[D_{sh}\right]$, which consists of matrices for all nodes of the system:

$$\left[D_{sh,i}\right] = A_i\left[E_{sh}\right]^{-1}, \quad \left[D_{sh}\right] = \begin{bmatrix} \left[D_{sh,1}\right] & & \\ & \ddots & \\ & & \left[D_{sh,m}\right] \end{bmatrix}. \tag{17}$$

The matrix $\left[D_{sh}\right]$ has the block-diagonal form and is easily invertible analytically.

$$\left[D_{sh}\right]^{-1} = \begin{bmatrix} \left[D_{sh,1}\right]^{-1} & & \\ & \ddots & \\ & & \left[D_{sh,m}\right]^{-1} \end{bmatrix}. \tag{18}$$

If the shear forces are constant on the finite element region (Figure 1b), then

$$U^* = \frac{1}{2}\sum\nolimits_{k=1}^{n} A_k \left\{Q_k\right\}^T \left[E_{sh}\right]^{-1}\left\{Q_k\right\},$$

where A_k is the area of the finite element;

n is the total number of finite elements;

$\left\{Q_k\right\} = \begin{Bmatrix} Q_{x,k} \\ Q_{y,k} \end{Bmatrix}$ is vector of unknown transverse forces of the finite element in the global coordinate system. In this case, the flexible matrix for the whole system is determined by formulas like formulas (17)–(18), with the replacement of the index m by the index n.

We obtain the equilibrium equation for the possible displacement of a node of the rectangular finite element in the local coordinate system (Figure 3). For the rectangular finite element, we also introduce the local coordinate system, associated with its center, and the functions, which are expressed in normalized local coordinates in the following form:

$$N_i(x,y) = \frac{(1+\xi_i\xi)(1+\eta_i\eta)}{4}, \quad \xi = \frac{2x}{a}, \quad \eta = \frac{2y}{b}, \quad i = 1,2,3,4. \tag{19}$$

The index i denotes the local node of the finite element; x, y are coordinates of the node along the axes X_1 and Y_1, respectively; ξ_i, η_i are local normalized coordinates of node i, taking values of 1 or –1. Nodes are numbered counterclockwise, starting with the lower left node.

Possible displacements of the points of the finite element, for the possible shearing displacement of a node, are expressed in the following form:

$$\delta w_{sh,i} = \frac{(1+\xi_i\xi)(1+\eta_i\eta)}{4}. \tag{20}$$

As a result of the possible displacement of the node, such shear deformations will arise in sections:

$$\delta\gamma_{xz} = \frac{\partial(\delta w_{sh,i})}{\partial x} = \frac{\xi_i(1+\eta_i\eta)}{2a}, \quad \delta\gamma_{yz} = \frac{\partial(\delta w_{sh,i})}{\partial y} = \frac{\eta_i(1+\xi_i\xi)}{2b}. \tag{21}$$

Then, for the case of piecewise constant approximations, the work of internal transverse forces for finite element k, on possible displacements of node i, can be expressed as follows:

$$\delta U_{i,z}^{k}=\frac{ab}{4}\int_{-1}^{1}\int_{-1}^{1}\left(\delta\gamma_{xz}Q_x+\delta\gamma_{yz}Q_y\right)d\xi d\eta=\sum_{j=1}^{4}\left(\frac{b\xi_i}{8}\left(1+\frac{\eta_i\eta_j}{2}\right)\overline{Q}_{x,j}+\frac{a\eta_i}{8}\left(1+\frac{\xi_i\xi_j}{2}\right)\overline{Q}_{y,j}\right). \quad (22)$$

Substituting in (22) i equal to from 1 to 4, we obtain, for the considered finite element, expressions for the work of internal transverse forces for possible displacements of nodes, from the first to the fourth.

Unite the nodal transverse forces, expressed in the local coordinate system, for the finite element k into the vector $\left\{\overline{Q}^{k}\right\}$.

$$\left\{\overline{Q}^{k}\right\}^{T}=\left(\overline{Q}_{x,1}\quad \overline{Q}_{y,1}\quad \overline{Q}_{x,2}\quad \overline{Q}_{y,2}\quad \overline{Q}_{x,3}\quad \overline{Q}_{y,3}\quad \overline{Q}_{x,4}\quad \overline{Q}_{y,4}\right). \quad (23)$$

Also, we introduce vector combining the values of the work of internal transverse forces for possible displacements of all nodes of the finite element:

$$\left\{\delta U_{z}^{k}\right\}^{T}=\left(\delta U_{1,z}^{k}\quad \delta U_{2,z}^{k}\quad \delta U_{3,z}^{k}\quad \delta U_{4,z}^{k}\right). \quad (24)$$

Then, we can write the following expression:

$$\left\{\delta U_{z}^{k}\right\}=\left[\overline{L}_{sh}^{k}\right]\left\{\overline{Q}^{k}\right\}. \quad (25)$$

Using (22) we get the expressions of the elements of matrix $\left[\overline{L}^{k}\right]$.

$$\left[\overline{L}_{sh}^{k}\right]=\frac{1}{16}\begin{bmatrix}-3b & -3a & -3b & -a & -b & -a & -b & -3a\\ 3b & -a & 3b & -3a & b & -3a & b & -a\\ b & a & b & 3a & 3b & 3a & 3b & a\\ -b & 3a & -b & a & -3b & a & -3b & 3a\end{bmatrix}. \quad (26)$$

Nodal forces $\left\{\overline{Q}_{i}^{k}\right\}$, expressed in the local coordinate system, and $\left\{Q_{i}^{k}\right\}$, expressed in the global coordinate system, are connected by the matrix of direction cosines

$$[l]=\begin{bmatrix}\cos\alpha & \sin\alpha\\ -\sin\alpha & \cos\alpha\end{bmatrix}. \quad (27)$$

α – the angle between the Y_1 axis and the Y axis (Figure 3). Using (27) we obtain the matrix of direction cosines for the finite element

$$\left[S^{k}\right]=\begin{bmatrix}[l] & & & \\ & [l] & & \\ & & [l] & \\ & & & [l]\end{bmatrix}. \quad (28)$$

The work of the internal forces (25) can be represented as follows:

$$\left\{\delta U_{z}^{k}\right\}=\left[L_{sh}^{k}\right]\left\{Q^{k}\right\},\quad \left[L_{sh}^{k}\right]=\left[\overline{L}_{sh}^{k}\right]\left[S^{k}\right]. \quad (29)$$

The matrix $\left[L_{sh}^{k}\right]$, conditionally, can be called as local «equilibrium» matrix of finite element for shearing in the global coordinate system. From matrices for finite elements $\left[L_{sh}^{k}\right]$, in accordance with the numbering of the nodes and elements, the global matrix $\left[L_{sh}\right]$ for the whole system is formed (see (12)).

Consider the case, when the transverse forces are approximated, in finite element region, by constant functions (Figure 1b). Then, the work of internal transverse forces for finite element k on the possible displacement of node i can be expressed as follows:

$$\delta U_{i,z}^{k}=\frac{ab}{4}\int_{-1}^{1}\int_{-1}^{1}\left(\delta\gamma_{xz}Q_x+\delta\gamma_{yz}Q_y\right)d\xi d\eta=\frac{b\xi_i}{2}\overline{Q}_{x,k}+\frac{a\eta_i}{2}\overline{Q}_{y,k}. \quad (30)$$

$\overline{Q}_{x,k}$, $\overline{Q}_{y,k}$ are transverse forces for finite element, expressed in the local coordinate system, are combined into the vector of unknowns for finite element $\{\overline{Q}^k\}^T = (\overline{Q}_{x,k} \quad \overline{Q}_{y,k})$. The matrix $[\overline{L}^k]$, in this case, will have the following form:

$$[\overline{L}_{sh}^k] = \frac{1}{2}\begin{bmatrix} -a & -b \\ a & -b \\ a & b \\ -a & b \end{bmatrix}. \tag{31}$$

The matrix of directional cosines will coincide with the matrix $[l]$ (see (27)).

The potential of the external concentrated and uniformly distributed loads, for possible displacements of the node i along the global coordinate axis, is determined by (32).

$$\delta V_i = P_i + \frac{1}{4}q^k ab = R_i. \tag{32}$$

P_i is force concentrated in node;

q^k is uniformly distributed load.

The generalized forces R_i, in accordance with the numbering of nodes, are placed in the vector $\{F\}$ (see (12)).

We obtain the equilibrium equations for triangular finite elements. The equilibrium equation for possible displacement of node of the triangular finite element can be obtained directly in the global coordinate system. For this, the possible displacements of the points of the finite element k on shearing will express using the triangular coordinates:

$$\delta w_{sh,i}(x,y) = T_i, \quad i = 1,2,3 \quad T_i = \frac{1}{2A^k}(a_i + b_i x + c_i y). \tag{33}$$

$$a_i = x_{i+1}y_{i+2} - x_{i+2}y_{i+1}, \quad b_i = y_{i+1} - y_{i+2}, \quad c_i = x_{i+2} - x_{i+1}. \tag{34}$$

A^k is area of the triangular element;

x_i, y_i are coordinates of the node i (Figure 3). Triangular coordinates are natural coordinates of triangular area.

The function T_i takes the value 1 at node i and the value zero at other two nodes. With the possible displacement of node, constant shear deformations arise in cross sections:

$$\delta\gamma_{xz} = \frac{\partial(\delta w_{sh,i})}{\partial x} = \frac{b_i}{2A^k}, \quad \delta\gamma_{yz} = \frac{\partial(\delta w_{sh,i})}{\partial y} = \frac{c_i}{2A^k}. \tag{35}$$

Consider the case of piecewise constant approximations of transverse forces in finite element region. The vector of nodal forces for triangular finite element, expressed in the global coordinate system, will have the following form:

$$\{Q^k\}^T = (Q_{x,1} \quad Q_{y,1} \quad Q_{x,2} \quad Q_{y,2} \quad Q_{x,3} \quad Q_{y,3}). \tag{36}$$

The work of the internal transverse forces of the k-th finite element on the possible displacement of the node i is expressed as an integral:

$$\delta U_{i,z}^k = \int_{A^k}(\delta\gamma_{xz}Q_x + \delta\gamma_{yz}Q_y)dA = \frac{b_i}{2A^k}\sum_{j=1}^3 Q_{x,j}A_j^k + \frac{c_i}{2A}\sum_{j=1}^3 Q_{y,j}A_j^k. \tag{36}$$

A_j^k is area of part of k-th triangular finite element is adjoined to the node j (Figure 4a) and is determined by (16). We introduce the vector, that combines the values of the works of transverse forces on possible displacements of finite element nodes:

$$\left\{\delta U_z^k\right\}^T = \left(\delta U_{1,z}^k \quad \delta U_{2,z}^k \quad \delta U_{3,z}^k\right). \tag{37}$$

Then we get

$$\left\{\delta U_z^k\right\} = \left[L_{sh}^k\right]\left\{Q^k\right\}, \tag{38}$$

$$\left[L_{sh}^k\right] = \frac{1}{2A^k}\begin{bmatrix} b_1A_1^k & c_1A_1^k & b_1A_2^k & c_1A_2^k & b_1A_3^k & c_1A_3^k \\ b_2A_1^k & c_2A_1^k & b_2A_2^k & c_2A_2^k & b_2A_3^k & c_2A_3^k \\ b_3A_1^k & c_3A_1^k & b_3A_2^k & c_3A_2^k & b_3A_3^k & c_3A_3^k \end{bmatrix}. \tag{39}$$

In the case of using constant approximations of transverse forces, the vector of unknowns for the triangular element will have the following form:

$$\left\{Q^k\right\}^T = \left(Q_{x,k} \quad Q_{y,k}\right). \tag{40}$$

Calculating the integral (36), we get:

$$\left[L_{sh}^k\right] = \frac{1}{2}\begin{bmatrix} b_1 & c_1 \\ b_2 & c_2 \\ b_3 & c_3 \end{bmatrix}. \tag{41}$$

From matrices $\left[L_{sh}^k\right]$ for triangular finite elements, in accordance with the numbering of the nodes and the elements, the global matrix $\left[L_{sh}\right]$ for the whole system is formed (see (12)).

The potential of the external concentrated and uniformly distributed loads for possible displacements of the node i, along the global axis of coordinates, is calculated by (42).

$$\delta V_i = P_i + \frac{1}{3}q^k A^k = R_i. \tag{42}$$

The global «equilibrium» matrix $\left[L_{sh}\right]$ for the whole system will have tape structure of nonzero elements. The number of rows of the matrix $\left[L_{sh}\right]$ is equal to of the number of loose nodes of the system. Numbering of unknown are assigned according to the numbering of nodes and finite elements. Therefore, the width of the tape of nonzero elements of the matrix $\left[L_{sh}\right]$ will be determined by the maximum difference in the numbers of nodes of all finite elements adjoined to the node. After calculating the width of the tape for each of the rows, its maximum value $l_{\max}$ is determined. Then, for the elements of the matrix $\left[L_{sh}\right]$, you can use a rectangular array consisting of columns $l_{\max}$ and *m* rows. The tape structure of nonzero elements is used in constructing the matrix multiplication algorithm, when we calculate the elements of matrix $\left[K_{sh}\right]$. Note, using constant approximations of transverse forces in finite element region, the value of $l_{\max}$ and, thus, the width of the tape of matrix will be significantly smaller.

3. Results and discussion

To assess the accuracy of the proposed method, rectangular plates were calculated with different conditions for supporting the sides (Figure 5) on the action of uniformly distributed load.

In Figure 5, the dashed line and the letter S denote the hinged supported side along the X axis, the skew hatch and the letter C denote the clamped side, the letter F denote the free side. Table 1 presents the results of calculations of the SS plate, given in [8] for various theories, and the results obtained by the proposed method – SFEM. For approximation of shear forces, piecewise constant functions were used (Figure 1a). For crushing the plates, square finite elements with a side size of 0.05 m. were used. And the size b = 6 m. Poisson's ratio is $\nu = 0.3$. The results of calculations in Table 1 are presented in the dimensionless form:

$$\bar{w} = \frac{Et^3}{qa^4} w\left(\frac{a}{2}, \frac{b}{2}\right), \quad \bar{\tau}_{yz} = \frac{t}{qa}\tau_{yz}\left(\frac{a}{2}, 0\right), \quad \bar{\tau}_{xz} = \frac{t}{qa}\tau_{xz}\left(0, \frac{b}{2}\right), \quad \tau_{yz} = \frac{3Q_{yz}}{2t}, \quad \tau_{xz} = \frac{3Q_{xz}}{2t}. \tag{43}$$

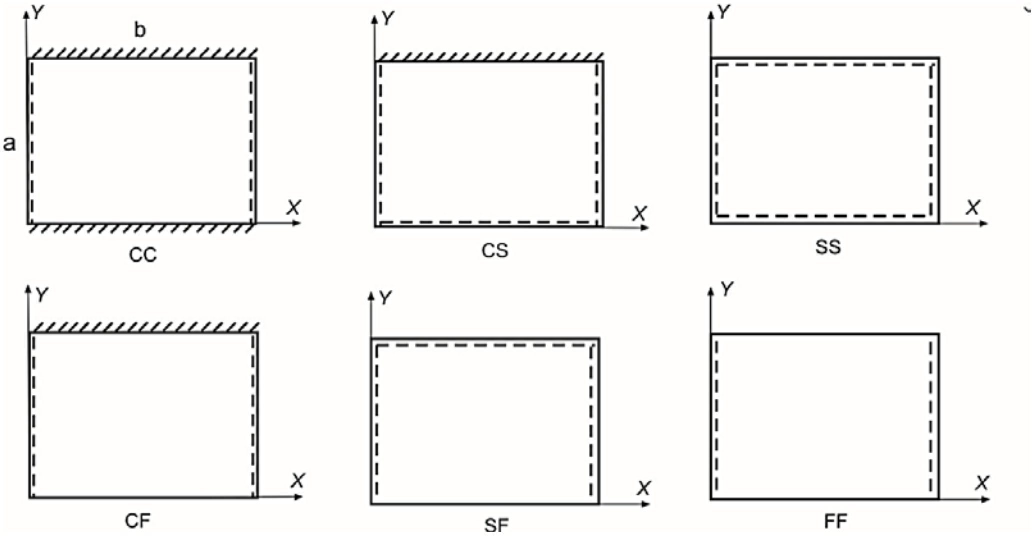

Figure 5. Conditions of supports and the sizes of sides of the Levi's plates.

Table 1. Displacements and stresses for the SS plate under the action of uniformly distributed load.

b/a	a/t	Methods	$\bar{w}$	$\bar{\tau}_{yz}$	$\bar{\tau}_{xz}$
1	5	ABACUS	0.0536		
		CRT	0.0444	0.4909	0.4909
		FSDT	0.0536	0.4909	0.4909
		TSDT	0.0535	0.3703	0.3703
		Analytical [8]	0.0536	0.4909	0.4909
		SFEM	0.0536	0.5064	0.5064
	10	ABACUS	0.0467		
		CRT	0.0444	0.4909	0.4909
		FSDT	0.0467	0.4909	0.4909
		TSDT	0.0467	0.4543	0.4543
		Analytical [8]	0.0467	0.4909	0.4909
		SFEM	0.0467	0.5064	0.5064
	100	ABACUS	0.0444		
		CRT	0.0444	0.4909	0.4909
		FSDT	0.0444	0.4909	0.4909
		TSDT	0.0444	0.4909	0.4905
		Analytical [8]	0.0444	0.4909	0.4909
		SFEM	0.0444	0.5064	0.5064
2	5	ABACUS	0.1248		
		CRT	0.1106	0.5240	0.6813
		FSDT	0.1248	0.5240	0.6813
		TSDT	0.1248	0.4569	0.5615
		Analytical [8]	0.1248	0.5240	0.6813
		SFEM	0.1249	0.5541	0.6969
	10	ABACUS	0.1141		
		CRT	0.1106	0.5240	0.6813
		FSDT	0.1142	0.5240	0.6813
		TSDT	0.1142	0.5051	0.6448
		Analytical [8]	0.1142	0.5240	0.6813
		SFEM	0.1146	0.5541	0.6969
	100	ABACUS	0.1106		
		CRT	0.1106	0.5240	0.6813
		FSDT	0.1106	0.5240	0.6813
		TSDT	0.1106	0.5238	0.6809
		Analytical [8]	0.1106	0.5240	0.6813
		SFEM	0.1107	0.5541	0.6969

Table 1 shows the results of calculations performed: by the ABACUS program; according to the classical Kirchhoff plate theory (CRT); according to the theory of plate bending with first order shear theory (FSDT); according to the theory of plate bend with third order shear (TSDT); by an analytical method, based on the third-order shear theory [8].

Comparison of calculation results shows, that the proposed calculation method (SFEM) in stresses, allows us to obtain solutions of the same accuracy for both thin and thick plates. This indicates the absence of a «locking» effect, which does not allow to obtain correct results for thin plates, when we use some types of finite elements. The values of displacements, obtained by the proposed method in stresses, practically coincide with the values obtained by other methods, that considering the shear deformations.

It should also be noted that the values of tangential stresses (in dimensionless form), obtained by the proposed method, do not depend on the thickness of the plate. For square plates, the maximum tangential stresses, obtained by the proposed method, are larger than the corresponding values, obtained by other methods, by about 3 %. For rectangular plates: the maximum tangential stresses, obtained along the short side of the slab, are 5.7 % larger, than the values obtained by other methods, and values along the long side are 2.2 % larger, than the values, obtained by other methods. Accounting for shear deformations is most important, when calculating flexural plates on stability, and, when determining the frequencies of free vibrations of plates. The values of the critical forces and frequencies of free oscillations will be affected by a decrease in the rigidity of the plates, due to additional shear deformations, therefore the accuracy and correctness of considering shear deformations is important. The proposed method for considering shear deformations is based on the fundamental principles of the minimum of additional energy and possible displacements. No additional techniques, such as the satisfaction of the Kirchhoff hypothesis at individual points (DKT – elements), or double approximation of displacements (MITS – elements), are not used in the proposed method.

Table 2. Displacement the center of the plate $\overline{w} = w \times 100D/\left(qa^4\right)$ ***for different conditions of supporting of sides, under the action of uniformly distributed load (*** $b = 2a = 6m$ ***).***

a/t	Methods	Bounders conditions					
		CC	CS	SS	CF	SF	FF
5	ABACUS	1.0000	1.0703	1.1429	1.2089	1.2842	1.4280
	FCDT	1.0000	1.0704	1.1430	1.2090	1.2844	1.4283
	Analytical [8]	0.9357	1.0373	1.1430	1.1757	1.2849	1.4293
	SFEM	0.9792	1.0617	1.1474	1.1992	1.2876	1.4325
10	ABACUS	0.8850	0.9637	1.0453	1.0980	1.1827	1.3225
	FCDT	0.8850	0.9637	1.0454	1.0981	1.1829	1.3228
	Analytical [8]	0.8673	0.9546	1.0454	1.0893	1.1834	1.3239
	SFEM	0.8813	0.9637	1.0495	1.0964	1.1848	1.3248
25	ABACUS	0.8511	0.9329	1.0180	1.0663	1.1545	1.2935
	FCDT	0.8511	0.9330	1.0181	1.0664	1.1547	1.2938
	Analytical [8]	0.8481	0.9314	1.0181	1.0651	1.1550	1.2944
	SFEM	0.8539	0.9363	1.0221	1.0676	1.1561	1.2947
1000	ABACUS	0.8445	0.9270	1.0128	1.0604	1.1494	1.2884
	FCDT	0.8445	0.9270	1.0129	1.0605	1.1496	1.2887
	Analytical [8]	0.8445	0.9270	1.0129	1.0605	1.1496	1.2887
	SFEM	0.8485	0.9311	1.0169	1.0613	1.1496	1.2877

Table 2 presents the results of determining the displacement of the center of a rectangular slab, for different variants of supporting the sides, and, for different ratios of the slab thickness to the size of short side of the slab. For crushing the slab, square finite elements with a side size of 0.05m were also used. For ratio $a/t = 5$, when the effect of shear deformations is greatest, the displacements, obtained by the proposed method (SFEM), differ from the displacements, obtained by the ABACUS program and the FCDT method by, no more than 2 %. At the same time, for some boundary conditions, the obtained values of displacements, are larger, and for others, less, than the compared ones. For thinner plates, the values of displacements for all the methods listed in Table 2, differ a little.

Table 3. Displacement of the center of the hinge plate under the action of uniformly distributed load $q = 10\ kN/m^2$***.***

b/a	n_a	n_b	Constant Q		Piecewise-constant Q	
			Rectangular elements	Triangle elements	Rectangular elements	Triangle elements
1	5	5	0.28875	0.28610	0.28842	0.28534
	10	10	0.28214	0.28184	0.28205	0.28155
	20	20	0.28049	0.28050	0.28047	0.28042
	30	30	0.28020	0.28021	0.28019	0.28017
2	5	10	0.69531	0.69810	0.69515	0.69724
	10	20	0.68753	0.68869	0.68749	0.68840
	20	40	0.68559	0.68539	0.68558	0.68531
	30	60	0.68523	0.68544	0.68523	0.68536

Table 3, to assess the convergence of the proposed solution, for different numbers of finite elements along the sides (n_a and n_b) presents the results for plate 0.6 m thick. The modulus of elasticity

$E = 10000\, kN / m^2$ and Poisson's ratio $\nu = 0.3$. Piecewise-constant and constant approximations of shear forces, as well as rectangular and triangular finite elements were considered. The grid of triangular finite elements was formed by dividing rectangular finite elements into two triangular elements. For the square hinged plate (b / a = 1) in [28], an analytical solution was obtained for displacement of the center of plate with considering for shear deformations:

$$w = 0.00406 \frac{a^4 q \left(1 + 4.6 \left(\frac{t}{a}\right)^2\right) \cdot 12\left(1 - \nu^2\right)}{Et^3} = 0.2785\, m. \tag{44}$$

Comparison with the values from Table 3 shows, that the values, getting by the proposed method, differs from the analytical value by less than 1 % for fine grid, and by about 4 %, for the coarsest grid. Note, that the results differ very slightly, both when using rectangular and triangular finite elements. The influence of the choice of the type of approximation of transverse forces is also insignificant. Thus, for solving using the proposed method, one can use constant approximations of transverse forces, which are more convenient for calculating branched systems.

4. Conclusion

1. The method for considering shear deformations, when bending plates are calculating by the finite element method, is proposed. The method is based on the fundamental principles of the minimum of additional energy and possible displacements and is applicable for the calculation of both thin and thick plates.

2. For approximation of shear forces, piecewise constant and constant approximations in finite element region can be used. To calculate branched systems, one can use constant approximations of shear forces without loss of accuracy.

3. Displacements from shear deformations are determined independently of bending-related displacements, therefore, the proposed method can be used in combination with traditional finite elements for thin plates, which was obtained by the finite element method in displacements.

4. Comparison of the solutions, obtained by the proposed method, with other known solutions for bending plates, considering shear cross sections, shows its good accuracy and convergence, when crushing the finite element mesh.

References

1. Gallager, R. Metod konechnykh elementov. Osnovy [Finite element method. The basics]. Moskow: Mir, 1984. 428 p. (rus)
2. Slivker, V.I. Stroitelnaya mekhanika. Variatsionnyye osnovy [Structural mechanics. Variational bases]. Moskow: Izdatelstvo Assotsiatsii stroitelnykh vuzov, 2005. 736 p. (rus)
3. Timoshenko, S.P., Voynovskiy-Kriger, S. Plastiny i obolochki [Plates and shells]. Moskow: Nauka, 1966. 636 p. (rus)
4. Fallah, N. On the use of shape functions in the cell centered finite volume formulation for plate bending analysis based on Mindlin–Reissner plate theory. Computers & Structures. 2006. Vol. 84. Pp. 1664–1672.
5. Katili, I., Batoz, J.L., Maknun, I.J., Hamdouni, A., Millet, O. The development of DKMQ plate bending element for thick to thin shell analysis based on the Naghdi/Reissner/Mindlin shell theory. Finite Elements in Analysis and Design. 2015. Vol. 100. Pp. 12–27.
6. Khezri, M., Gharib, M., Rasmussen, K.J.R. A unified approach to meshless analysis of thin to moderately thick plates based on a shear-locking-free Mindlin theory formulation. Thin-Walled Structures. 2018. Pp. 161–179.
7. Yaghoubshahi, M., Alinia, M.M. Developing an element free method for higher order shear deformation analysis of plates. Thin-Walled Structures. 2015, Vol. 94. Pp. 225–233.
8. Thai, H.-T., Nguyen, T.-K., Vo, T.P., Ngo, T. A new simple shear deformation plate theory. Composite Structures. 2017. Vol. 171. Pp. 277–285.
9. Lalin, V.V., Zdanchuk, Ye.V., Kushova, D.A., Rozin, L.A. Variatsionnyye postanovki nelineynykh zadach s nezavisimymi vrashchatelnymi stepenyami svobody [Variational statements of nonlinear problems with independent rotational degrees of freedom]. Magazine of Civil Engineering. 2015. No. 4(56). Pp. 54–65. (rus)
10. Lalin, V.V., Belyayev, M.O. Izgib geometricheski nelineynogo konsolnogo sterzhnya. Resheniye po teoriyam Kirkhgofa i Kossera – Timoshenko [Bending geometrically nonlinear cantilever rod. Decision on theories of Kirchhoff and Cossera – Tymoshenko]. Inzhenerno-stroitelnyy zhurnal. 2015. No. 1(53). Pp. 39–55. (rus)
11. Park, M., Choi, D.-H. A two-variable first-order shear deformation theory considering in-plane rotation for bending, buckling and free vibration analysis of isotropic plates. Applied Mathematical Modelling. 2018. Vol. 61. Pp. 49–71.
12. Kumara, R., Lala, A., Singhb, B.N., Singhc, J. New transverse shear deformation theory for bending analysis of FGM plate under patch load. Composite Structures. 2019. Vol. 208. Pp. 91–100.
13. Thai, H.-T., Choi, D.-H. Finite element formulation of various four unknown shear deformation theories for functionally graded plates. Finite Elements in Analysis and Design. 2013. Vol. 75. Pp. 50–61.
14. Doa, T.V., Nguyenb, D.K., Ducc, N.D., Doanc, D.H., Buie, T.Q. Analysis of bi-directional functionally graded plates by FEM and a new third-order shear deformation plate theory. Thin-Walled Structures. 2017. Vol. 119. Pp. 687–699.

15. Mulcahy, N.L., McGuckin, D.G. The addition of transverse shear flexibility to triangular thin plate elements. Finite Elements in Analysis and Design. 2012. Vol. 52. Pp. 23–30.
16. Karttunen, A.T., Hertzen, R., Reddy, J.N., Romanoff, J. Shear deformable plate elements based on exact elasticity solution. Computers & Structures. 2018. Vol. 200. Pp. 21–31.
17. Duan, H., Ma, J. Continuous finite element methods for Reissner-Mindlin plate problem. Acta Mathematica Scientia. 2018. Vol. 38. Pp. 450–470.
18. Zenkour, AM. Exact mixed-classical solutions for the bending analysis of shear deformable rectangular plates. App. Math. Model. 2003. Vol. 27. Pp. 515–534.
19. Erkmen, R.E. Shear deformable hybrid finite-element formulation for buckling analysis of thin-walled members. Finite Elements in Analysis and Design. 2014. Vol. 82. Pp. 32–45.
20. Özütok, A., Madenci, E. Static analysis of laminated composite beams based on higher-order shear deformation theory by using mixed-type finite element method. International Journal of Mechanical Sciences. 2017. Vol. 130. Pp. 234–243
21. Senjanović, I., Vladimir, N., Hadžić, N. Modified Mindlin plate theory and shear locking free finite element formulation. Mechanics Research Communications. 2014. Vol. 55. Pp. 95–104.
22. Sukhoterin, M.V., Baryshnikov, S.O., Potekhina, Ye.V. O raschetakh plastin po sdvigovym teoriyam [About plate calculations based on shear theories]. Vestnik gosudarstvennogo universiteta morskogo i rechnogo flota im. admirala S.O. Makarova. 2015. No. 2 (30). Pp. 81–89. (rus)
23. Sukhoterin M.V., Baryshnikov, S.O., Knysh, T.P. Stress-strain state of clamped rectangular Reissner plates. Magazine of Civil Engineering. 2017. 76(8). Pp. 225–240. DOI: 10.18720/MCE.76.20
24. Tyukalov, Yu.Ya. Finite element models in stresses for plane elasticity problems. Magazine of Civil Engineering. 2018. 77(1). Pp. 23–37. DOI: 10.18720/MCE.77.3
25. Tyukalov, Yu.Ya. The functional of additional energy for stability analysis of spatial rod systems. Magazine of Civil Engineering. 2017. 70(2). Pp. 18–32. DOI: 10.18720/MCE.70.3
26. Tyukalov, Yu.Ya. Stress finite element models for determining the frequencies of free oscillations. Magazine of Civil Engineering. 2016. 67(7). Pp. 39–54. DOI: 10.5862/MCE.67.5
27. Tyukalov, Yu.Ya. Finite element models in stresses for bending plates. Magazine of Civil Engineering. 2018. 82(6). Pp. 170–190. DOI: 10.18720/MCE.82.16
28. Donnell, L.G. Balki, plastiny i obolochki [Beams, plates and shells]. Moskow: Nauka, 1982. 568 p. (rus)

Contacts:

Yury Tyukalov, +7(912)8218977; yutvgu@mail.ru

Инженерно-строительный журнал

ISSN 2071-0305

сайт журнала: http://engstroy.spbstu.ru/

DOI: 10.18720/MCE.85.9

Метод расчета изгибаемых плит с учетом деформаций сдвига

Ю.Я. Тюкалов**,
Вятский государственный университет, г. Киров, Россия
** E-mail: yutvgu@mail.ru*

Ключевые слова: изгибаемые плиты, деформации сдвига, напряжения, конечные элементы.

Аннотация. Рассмотрена задача расчета изгибаемых плит методом конечных элементов с учетом деформаций сдвига. Изгибаемые плиты широко применяются для различных объектов гражданского и промышленного строительства. Решение задачи получено на основе принципов минимума дополнительной энергии и возможных перемещений. Для аппроксимации полей моментов используются кусочно-постоянные функции. Поперечные силы могут быть аппроксимированы постоянными или кусочно-постоянными функциями. Получены необходимые соотношения для прямоугольных и треугольных конечных элементов. Показано, что предлагаемый метод может использоваться в сочетании с традиционными конечными элементами для тонких пластин, полученными методом конечных элементов в перемещениях. Приведено сравнение решений, полученных по предлагаемому методу, с другими известными решениями для изгибаемых плит с учетом сдвига. Дана численная оценка точности и сходимости предлагаемого метода при измельчении сетки конечных элементов.

Литература

1. Галлагер Р. Метод конечных элементов. Основы. М.: Мир, 1984. 428 с.
2. Сливкер В. И. Строительная механика. Вариационные основы. М.: Изд-во Ассоциации строительных вузов. 2005. 736 с.
3. Тимошенко С.П., Войновский-Кригер С. Пластины и оболочки. М.: Наука, 1966. 636 с.
4. Fallah N. On the use of shape functions in the cell centered finite volume formulation for plate bending analysis based on Mindlin–Reissner plate theory // Computers & Structures. 2006. Vol. 84. Pp. 1664–1672.
5. Katili I., Batoz J.L., Maknun I.J., Hamdouni A., Millet O. The development of DKMQ plate bending element for thick to thin shell analysis based on the Naghdi/Reissner/Mindlin shell theory // Finite Elements in Analysis and Design. 2015. Vol. 100. Pp. 12–27.
6. Khezri M., Gharib M., Rasmussen K. J. R. A unified approach to meshless analysis of thin to moderately thick plates based on a shear-locking-free Mindlin theory formulation. Thin-Walled Structures. 2018. Pp. 161–179.
7. Yaghoubshahi M., Alinia M.M. Developing an element free method for higher order shear deformation analysis of plates // Thin-Walled Structures. 2015, Vol. 94. Pp. 225–233.
8. Thai H.-T., Nguyen T.-K., Vo T.P., Ngo T. A new simple shear deformation plate theory // Composite Structures. 2017. Vol. 171. Pp. 277–285.
9. Лалин В.В., Зданчук Е.В., Кушова Д.А., Розин Л.А. Вариационные постановки нелинейных задач с независимыми вращательными степенями свободы // Инженерно-строительный журнал. 2015. № 4(56). С. 54–65.
10. Лалин В.В., Беляев М.О. Изгиб геометрически нелинейного консольного стержня. Решение по теориям Кирхгофа и Коссера–Тимошенко // Инженерно-строительный журнал. 2015. №1(53). С. 39–55.
11. Park M., Choi D.-H. A two-variable first-order shear deformation theory considering in-plane rotation for bending, buckling and free vibration analysis of isotropic plates // Applied Mathematical Modelling. 2018. Vol. 61. Pp. 49–71.
12. Kumara R., Lala A., Singhb B.N., Singhc J. New transverse shear deformation theory for bending analysis of FGM plate under patch load // Composite Structures. 2019. Vol. 208. Pp. 91–100.
13. Thai H.-T., Choi D.-H. Finite element formulation of various four unknown shear deformation theories for functionally graded plates // Finite Elements in Analysis and Design. 2013. Vol. 75. Pp. 50–61.
14. Doa T.V., Nguyenb D.K., Ducc N.D., Doanc D.H., Buie T.Q. Analysis of bi-directional functionally graded plates by FEM and a new third-order shear deformation plate theory // Thin-Walled Structures. 2017. Vol. 119. Pp. 687–699.
15. Mulcahy N.L., McGuckin D.G. The addition of transverse shear flexibility to triangular thin plate elements // Finite Elements in Analysis and Design. 2012. Vol. 52. Pp. 23–30.
16. Karttunen A.T., Hertzen R., Reddy J.N., Romanoff J. Shear deformable plate elements based on exact elasticity solution // Computers & Structures. 2018. Vol. 200. Pp. 21–31.
17. Duan H., Ma J. Continuous finite element methods for Reissner-Mindlin plate problem // Acta Mathematica Scientia. 2018. Vol. 38. Pp. 450–470.

18. Zenkour AM. Exact mixed-classical solutions for the bending analysis of shear deformable rectangular plates // App. Math. Model. 2003. Vol. 27. Pp. 515–534.
19. Erkmen R.E. Shear deformable hybrid finite-element formulation for buckling analysis of thin-walled members // Finite Elements in Analysis and Design. 2014. Vol. 82. Pp. 32–45.
20. Özütok A., Madenci E. Static analysis of laminated composite beams based on higher-order shear deformation theory by using mixed-type finite element method // International Journal of Mechanical Sciences. 2017. Vol. 130. Pp. 234–243
21. Senjanović I., Vladimir N., Hadžić N. Modified Mindlin plate theory and shear locking free finite element formulation // Mechanics Research Communications. 2014. Vol. 55. Pp. 95–104.
22. Сухотерин М.В., Барышников С.О., Потехина Е.В. О расчетах пластин по сдвиговым теориям // Вестник государственного университета морского и речного флота им. адмирала С.О. Макарова. 2015. № 2 (30). С. 81–89.
23. Сухотерин М.В., Барышников С.О., Кныш Т.П. Напряженно-деформированное состояние защемленной прямоугольной пластины Рейсснера // Инженерно-строительный журнал. 2017. № 8 (76). С. 225–240. DOI: 10.18720/MCE.76.20
24. Тюкалов Ю.Я. Конечно-элементные модели в напряжениях для задач плоской теории упругости // Инженерно-строительный журнал. 2018. № 1(77). С. 23–37. DOI: 10.18720/MCE.77.3
25. Тюкалов Ю.Я. Функционал дополнительной энергии для анализа устойчивости пространственных стержневых систем // Инженерно-строительный журнал. 2017. № 2(70). С. 18–32. DOI: 10.18720/MCE.70.3
26. Тюкалов Ю.Я. Определение частот свободных колебаний методом конечных элементов в напряжениях // Инженерно-строительный журнал. 2016. № 7(67). С. 39–54. DOI: 10.5862/MCE.67.5
27. Тюкалов Ю.Я. Конечно элементные модели в напряжениях для изгибаемых пластин // Инженерно-строительный журнал. 2018. № 6(82). С. 170–190. DOI: 10.18720/MCE.82.16
28. Доннелл Л.Г. Балки, пластины и оболочки. М.: Наука, 1982. 568 с.

Контактные данные:

Юрий Яковлевич Тюкалов, +7(912)8218977; эл. почта: yutvgu@mail.ru

Magazine of Civil Engineering. 2019. 85(1). Pp. 123–135
Инженерно-строительный журнал. 2019. № 1(85). С. 123–135

Magazine of Civil Engineering

journal homepage: http://engstroy.spbstu.ru/

ISSN 2071-0305

DOI: 10.18720/MCE.85.10

Modified water-cement ratio rule for the design of air-entrained concrete

L.I. Dvorkin,
National University of Water Environmental Engineering, Rivne, Ukraine
E-mail: dvorkin.leonid@gmail.com

Keywords: Modified C/W; the volume of air entrained; cement consumption; strength and frost resistance of concrete; pore volume of aggregate; composition of lightweight concrete.

Abstract. Designing concrete compositions, containing entrained air, is usually done by means of empirical proportioning, which is quite a laborious and lengthy process. In the article design formulae are experimentally justified with rule of modified C/W, which is complex due to known empirical dependencies, and allow us to find the content of concrete components with desired strength, frost resistance, and density properties. Conducted experimental studies are: compression method for determining the volume of entrained air as well as standard methods for determining the strength and frost resistance of concrete. Lastly, generated formula was verified on an example for calculating the compositions of heavy concrete with a given strength and frost resistance and structural claydite-concrete with desired strength and density.

1. Introduction

One of the fundamental fields in concrete science is methodology of concrete compositions design, aimed at achieving concrete with a set of desired properties.

D. Abrams has for the first time proposed two approaches [1] for concrete compositions design: a so-called 'trial method' or experimental proportioning and a «preliminary calculations method» and considered that both approaches should be based on a water-cement ratio rule (low). Practice has confirmed this condition proved by Abrams however many subsequent researches have shown [2–5] that Abrams's statement that concrete strength for given materials and their processing conditions is defined just by the ratio between the water and cement volumes, used for manufacturing the concrete mixture' is some exaggeration and the word 'just' should be replaced by 'mainly' or 'basically'. In addition to the water-cement – W/C (or cement-water – C/W) ratio and cement strength or its activity (R_{cem}), in calculating the concrete composition it is necessary to take into account additional factors affecting the properties of concrete.

In 1920, having processed more than 50000 tests, Abrams proposed an empirical formula:

$$f_{cm} = \frac{k}{A^X}, \tag{1}$$

where k and A are coefficients;

X is the water to cement volume ratio for cement with a density of 1500 kg/m^3.

Many studies were carried out to specify the water-cement ratio rule and increase the number of factors, considered in equations for predicting concrete strength [6–12]. The most important investigations in this field

Dvorkin, L.I. Modified water-cement ratio rule for the design of air-entrained concrete. Magazine of Civil Engineering. 2019. 85(1). Pp. 123–135. DOI: 10.18720/MCE.85.10.

Дворкин Л.И. Модифицированное правило водоцементного соотношения для проектирования бетонов, содержащих воздух // Инженерно-строительный журнал. 2019. № 1(85). С. 123–135. DOI: 10.18720/MCE.85.10

are based on structural approach. In these studies the initial preconditions are based on hypotheses of interrelation of concrete strength and its structure, though these hypotheses are essentially different.

There is a number of design equations for concrete strength, trying to consider the complex interaction mechanism between aggregates and cement matrix at heterogeneous material's collapse [1, 6, 13]. These equations represent a big interest to studying possibilities of predicting concrete strength variation due to changes in strength and deformation characteristics of phases composing the material. However, at present time using these equations for concrete compositions design is usually inconvenient or impossible.

An attempt to increase the number of factors, considered in concrete compositions design and to consider the influence of aggregates features resulted in the «real» W/C theory [6] $(W/C)_r$:

$$(W/C)_r = \frac{W - W_S S - W_{cr.s} Cr.S}{C}, \tag{2}$$

where W and C are total content of water and cement; W_s and $W_{cr.s}$ are water demand of fine and coarse aggregates; S and $Cr.S$ are mass content of fine and coarse aggregates respectively.

Water demand parameters of fine and coarse aggregates characterize the water quantity that should be added to cement paste per unit of its mass in order to obtain a corresponding mortar mixture with $C:S$ (cement:sand) = 1:2 composition or a concrete mixture with C:S:Cr.S (cement:sand:crushed stone) = 1:2:3.5 composition, having the same slump after mixing as cement paste with normal consistency [6].

In opinion of some researchers [6], "real" W/C characterizes the cement paste in concrete after immobilization of water by the aggregates through a certain structure formation period. In our opinion «real» W/C can be interpreted as W/C of cement paste in concrete mixture at the moment of equal moisture carrying potentials.

Using the $(W/C)_r$ concept for concrete with constant entire W/C value enabled to estimate the dependence of concrete strength on some factors that affect redistribution of water between the cement paste and aggregates. At the same time the algorithm of using $(W/C)_r$ in the concrete design is complex and requires additional assumptions.

Great opportunities to take into account various factors affecting the properties of concrete when design the its composition open experimental models obtained using statistical methods for the processing of experimental data [14–24]. However these models are usually local and fair under the specified conditions of the experiments.

Presently for predicting concrete strength and for concrete composition design the following typical formula is widely used [1]:

$$f_{cm} = AR_{cem}(C/W - b), \tag{3}$$

where f_{cm} is the concrete strength at 28 days;

C and W are the masses of cement and water per 1 m^3 of the concrete mix;

A and b are empiric coefficients, depending on the initial materials features and structural type of concrete; R_{cem} is the compressive cement strength at 28 days.

Still Bolomey has mentioned that linear formula for prediction concrete strength $f_{cm} = k(C/W - 0.5)$ is valid just if C/W = 0.9...2.5 [1]. For wider diapason a nonlinear version of the formula was proposed. The general nonlinear function $f_{cm} = f(C/W)$ is often replaced in practice with linear piecewise dependences, proposed and proved by B. Skramtaev and Y. Bazhenov [1]. Alongside with Eq. (3) a number of other formulas, based on a water-cement rule are known (Table 1). They, however, are almost not applied because a relatively more complex structure and necessity of additional data. Another reason for limited use of these formulas is lack of essential increase in prediction accuracy.

It is more convenient to consider the factors, along with C/W, which significantly affect the strength of concrete, the system of amendments ΔAi for the coefficient A in formula (3). Such a system was developed by V. Sizov [1].

A number of computational and experimental dependencies [12, 24–27] were proposed to take into account the characteristics of aggregates and additives in the designation of concrete compositions.

Table 1. Main design formulas for predicting concrete strength, used for concrete compositions design [1].

Authors	Relation for strength prediction		Notations
R. Feret	$f_{cm} = k\left(\frac{V_{cem}}{V_{cem}+V_w+V_{air}}\right)^2$	(4)	V_{cem} – absolute cement volume, V_w – water volume, V_{air} – volume of air voids in concrete, k – coefficient, depending on materials quality, used for concrete, manufacturing and curing conditions,
N. Belyaev	$f_{cm} = \frac{R_{cem}}{A(W/C)^{3/2}}$	(5)	R_{cem} – ultimate cement strength
American Concrete Institute Manual of Concrete Practice [8]	$f_{cm} = 117.07e^{-2.572W/C}$	(6)	$W/C = 0.41-0.82$
B.Skramtaev, Y.Bazhenov	$f_{cm} = AR_{cem}\left(C/W-0.5\right)$ for $\mathrm{W}/C \geq 0.4$, $f_{cm} = A_1R_{cem}\left(C/W+0.5\right)$ for $\mathrm{W}/C < 0.4$	(7)	A – coefficient, depending on aggregates quality.
M. Simonov	$f_{cm} = 0.49AR_{cem}\left(\frac{3.1C/W}{3.1+C/W}\right)^2$	(8)	
L.Kaiser, R.Chehova	$f_{cm} = \frac{\left(2.3\,R_{cem}+100\right)\,\mathrm{C}/W-80}{10}$	(9)	
I.Rybiev	$f_{cm} = \frac{R^*}{\left(\frac{W/C}{(W/C)^*}\right)^n}$	(10)	$(W/C)^*$ – water-cement ratio of maximum possible cement stone strength, $R*$ – maximum possible cement stone strength, n – coefficient, depending on features of concrete macrostructure and applied aggregates.
I.Ahverdov	$f_{cm} = \frac{KR_{cem}}{0.95\frac{1+1.65K_{n.c}}{K_{n.c}}\left(W/C\right)-1.65K_{n.c}}$	(11)	$K_{n.c}$ – normal consistency of cement paste.
V.Shmigalsky	$f_{cm} = R_{cem}\frac{0.6-0.0014W}{\left(W/C\right)^{1/3}}$	(12)	

To take into account the influence of mineral additives and the entrained air on the strength of concrete, it was suggested [1] to use the modified Bolomey formula:

$$f_{cm} = K_b\left(\frac{C+K_{c.e}Ad}{W+V_{air}}-0.5\right), \tag{13}$$

where f_{cm} is the compressive strength,

K_b is the constant of Bolomey,

C is mass of cement,

Ad is the mass of mineral additive,

W is the mass of used water,

V_{air} is the volume occupied by the entrained air equivalent the mass of water,

$K_{c.e.}$ is the coefficient of «cementing efficiency» or «cement equivalent» of 1 kg additive.

The formula (14) reflects a depending that can be considered the "*rule of modified W/C*" (or C/W). In accordance with this rule the strength of concrete additionally to the effect of the ratio of cement and water content by weight can be affected the ratio of equivalent amounts of active mineral additives and entrained air. The ratio of the total content of these components of concrete uniquely determines the strength of concrete.

Based on this rule, a number of studies of concrete compositions design with fly ash and other mineral additives were performed [1, 7, 25, 28, 29]. At the same time for concrete, containing entrained air, this rule, insufficiently experimentally substantiated.

The purpose of the research, the results of which are given in the article, was to determine the possibility the applicability of the calculated dependencies of concrete strength based on the modified C/W for design of concrete compositions take into account the volume of air entrained by the addition of the surface-active substances (SAS) and porous aggregates.

2. Methods

As an air-entraining additive was used air-entraining resin (neutralized Vinsol) – a product of neutralization of the wood resin by caustic soda after extraction of turpentine from it. The additive introduced into concrete mixtures in an amount of 0.01...0.03 % by weight of cement, previously dissolved in water at t = 30...40 °C. The volume of entrained air in concrete mixtures was determined by compression method based on the law Boyle-Marriott, establishing the relationship between the volume of air and the applied pressure at a constant temperature (EN 206-1).

For the manufacture of concrete mixtures used Portland cement CEM II/ A-S with the mineralogical composition of clinker, %: C_3S – 57.10; C_2S – 21.27; C_3A – 6.87; C_4AF – 12.9. Specific surface of cement – 340 m^2/kg. The compressive strength of cement corresponded to the class of 42.5 N (EN 197-1). Fine aggregate of concrete served the quartz sand with a modulus of fineness M_k = 1.95 and a content of dust and clay impurities of 2.1 %. As a coarse aggregate of the normal weight concrete, granite crushed stone of fraction 5...20 mm was used, light concrete – claydite gravel of fraction 5...20 mm with bulk density of 500...800 kg/m^3.

Testing the strength of concrete was carried out on control samples-cubes with a fin length of 100 mm in accordance with GOST 10180-2012 (EN 12390-3:2009).

The frost resistance of concrete was determined by the ultrasonic method (Russian State standard GOST 26134-2016). The tests are carried out until the “ultrasound-velocity-number of cycles” line will break, after that the reduction in ultrasound velocity will have higher intensify.

Experimental researches were carried out in the research laboratory of the building materials tests of the National University of Water Environmental Engineering (Ukraine, Rovno).

3. Experimental results and discussion

Concrete with entrained air. When calculating the compositions of concrete with entrained air, the formula (13) with Ad = 0 can be brought to mind:

$$f_{cm} = AR_{cem}\left(\frac{C}{W+V_{air}} - 0.5\right), \tag{14}$$

were A is coefficient taking into account the quality of raw materials [1];

R_{cem} is compressive strength of cement, MPa;

C and W is cement and water consumption in concrete mix by weight, kg/m^3;

V_{air} is the volume of entrained air V_{air}, l/m^3.

An analysis of the effect of the volume of entrained air on formula (15) on the strength of concrete for various values of C/W and W is shown in Figure1.

On average, the calculated decrease in concrete strength for each percentage of air involved is 3.5...4.5 %. A tendency to a decrease in the relative effect of entrained air on strength is observed at C/W = const with an increase in water consumption in concrete. The calculated data are close to experimental (Figure 1).

The main purpose of air-entraining additives in concrete is to increase its frost resistance by creating a system of uniformly distributed closed air pores. This fact has been convincingly proved by the practice of construction and numerous studies. Processing our experimental data [1] included results of concrete frost resistance measurements in freezing cycles at –15...–20 °C and thawing at +15...±5 °C until strength decreases no more than 5 % for a rather wide compositions diapason ($f_{cm}^{28} = 15...40$ MPa, $W = 140...220$ l/m^3, $V_{air} = 0.8...6.5$ %). The data are approximised by a formula that has the following type:

$$F = A_1 f_{cm}^{28 A_2} \exp^{A_3 V_{air}} . \quad (15)$$

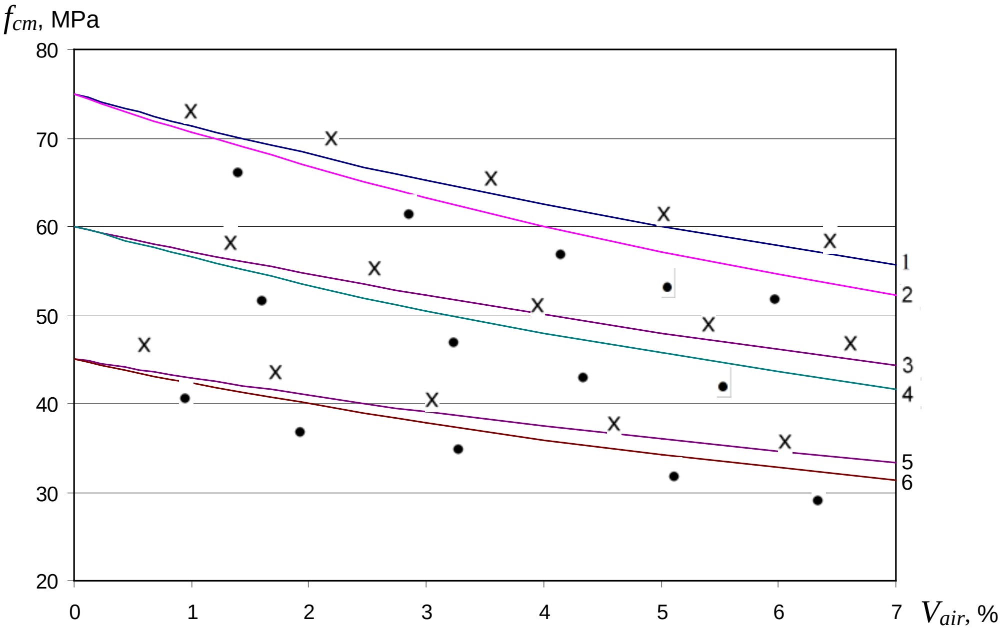

Figure 1. Influence of the volume of entrained on the concrete compressive strength
1 – C/W = 1.5; W = 200 l/m³. 2 – C/W = 1.5; W = 160 l/m³. 3 – C/W = 2; W = 200 l/m³. 4 – C/W = 2; W = 160 l/m³. 5 – C/W = 2.5; W = 200 l/m³. 6 – C/W = 2.5; W = 160 l/m³
(A = 0.6; R_{cem} = 50 MPa)
Experimental results: x – W = 200 l/m³; • – W = 160 l/m³.

For the investigated concrete A_3 = 0.35, A_1 and A_2 are varied depending on the water demand and correspondingly mixtures workability (Table 2).

As it follows from analyzing Eq. (15), at entrained air content of 3…5 % the concrete frost resistance increases by 3…6 times (Figure 2). For concrete strength above 30…40 MPa the relative increase of critical number of freezing-thawing cycles, achieved by entraining air a little increases. It can be explained by higher influence of closed pores of contraction origin.

Table 2. Values of coefficients A_1 and A_2 in Eq. (16) for concrete mixtures with various workability.

Concrete mixtures workability	A_1	A_2
Plastic concrete mixtures (Slump Sl = 9…12 cm)	0.34	1.68
Low-plastic concrete mixtures (Slump Sl = 1…4 cm)	0.91	1.47
Non-plastic concrete mixtures	2.48	1.25

As the empirical data on the values of parameters A_1 and A_2 is accumulated, Eq. (15) can be widely used either for predicting frost resistance or for concrete compositions design.

The required entrained air volume in % can be found according to a formula, obtained from Eq. (15):

$$V_{air} = \frac{\ln\left(\dfrac{F}{A_1 f_{cm}^{A_2}}\right)}{0.35}. \quad (16)$$

At the same time when designing concrete compositions with an air-entraining additive at given values of its strength and frost resistance, along with a significant increase in the latter the necessity of certain overestimating of the given concrete strength, depending on the entrained air volume, should be considered (Figure 3). The overall positive effect of reducing the consumption of cement can be quite significant, especially in concrete with high values of frost resistance and a moderate normalized value of strength. From Figure 4, in particular, it follows that f_{cm} = 20 MPa and F200 are provided without the addition of entrained air at W/C = 0.5 (C/W = 2) with the introduction of entrained air – W/C = 0.62 (C/W = 1.61).

Using the formula (14) at the design stage of concrete compositions and having previously determined the water consumption by reference or laboratory data, it is possible to calculate C/W, V_{air} and C values to ensure the specified indicators of concrete strength and frost resistance. The consumptions of aggregates and their ratio are using known recommendations [1–6].

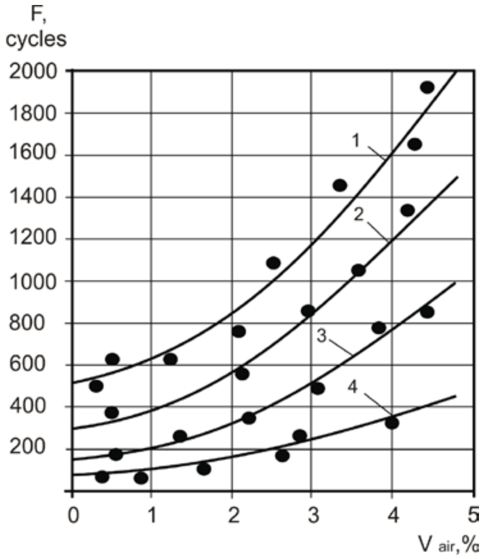

Figure 2. Affect of entrained air on concrete frost resistance (for concrete mixtures with Slump Sl = 1...4 cm) : *1* – $f_{cm}^{28} = 70$ MPa; *2* – $f_{cm}^{28} = 50$ MPa; *3* – $f_{cm}^{28} = 35$ MPa; *4* – $f_{cm}^{28} = 20$ MPa .

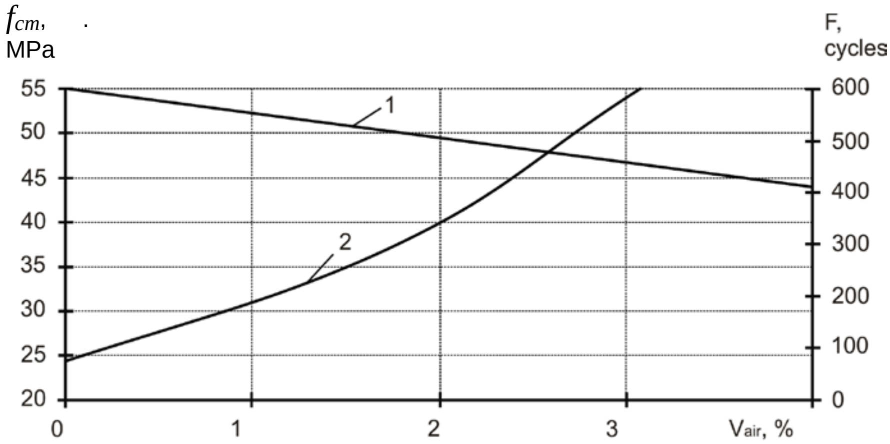

Figure 3. Dependence between the entrained air volume, concrete strength (f_{cm}) (*1*) and frost resistance (F) (2).

Note: concrete strength is calculated using a formula (14), concrete frost resistance (15).

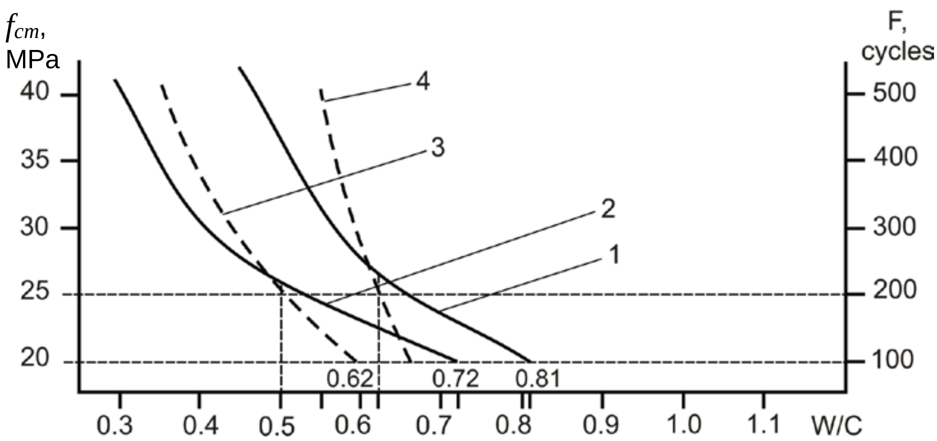

Figure 4. Relationship between W/C and given values of concrete strength (R_c) and frost resistance (F).

***1* – f_{cm} without entrained air; *2* – f_{cm} with 20 *l* of entrained air;**

***3* – F without entrained air; *4* – F with 20 *l* of entrained air.**

Example 1

Calculate the required values of the cement-water ratio (C/W), the volume of entrained air (V_{air}) and cement consumption to produce concrete with compressive strength at 28 days $f_{cm}^{28} = 30MPa$ and frost resistance F = 300 cycles. Apply Portland cement with compressive strength of 50 MPa, ordinary aggregates. Slump of the concrete mix – Sl = 1…4 cm.

1. According to the formula (16) we find the required volume of entrained air. The values of the coefficients A_1 and A_2 will be determined by the Table 2.

$$V_{air} = \frac{\ln\left(\frac{300}{0.34 \cdot 30^{1.68}}\right)}{0.35} = \frac{\ln(2.91)}{0.35} = 3.05\,\%\left(30.5\text{ l/m}^3\right).$$

2. Using the formula (14), taking the value of the coefficient A = 0.6 and the water consumption of 200 l/m^3 will determine the required value of C and C/W:

$$f_{cm} = 0.6 \cdot 50\left(\frac{C}{W + V_{air}} - 0.5\right);$$

$$C = \frac{\left(f_{cm} + 0.5AR_c\right)\left(W + V_{air}\right)}{AR_c} = \frac{(30 + 0.5 \cdot 0.6 \cdot 50)(200 + 30.5)}{0.6 \cdot 50} = 345.75\text{ kg/m}^3;$$

$$C/W = C:W = 345.75:200 = 1.73.$$

Lightweight Concrete. As known, for lightweight concrete on porous aggregates the water-cement ratio rule in its traditional formulation is unacceptable, as strength of such concrete is determined not just by cement stone density and accordingly strength, but also by strength and volumetric concentration of porous aggregates. Many formulas were suggested for calculating lightweight concrete strength [7]. Part of them characterized linear relation between concrete strength and cement consumption or C/W, considering the influence of mechanical and structural features of aggregates by generalized coefficients. Other formulas directly considered physic-mechanical parameters of porous aggregates, but were only indirectly related with composition parameters. These formulas require complicated calculations and provide approximate results.

Existing empirical formulas are of interest, mainly, for comparing materials based on various types of porous aggregates, but have low potential for concrete composition design. The existing practice of lightweight concrete composition design is based usually on using average tabulated data with subsequent experimental validation for given initial materials.

An integral parameter that takes into account both C/W and, indirectly, through pore volume of the aggregate, its strength, can be the parameter Z:

$$Z = \frac{V_{cem}}{V_w + (P_{ag} - W_{ab.ag})V_{ag} + V_{air}}, \quad (17)$$

were V_{cem}, V_w, V_{ag}, V_{air} are volumes of cement, water, aggregates and air, l/m^3;

P_{ag} is aggregate porosity,

$W_{ab.ag}$ is aggregate water absorption.

Claydite concrete compositions with compressive strength (f_{cm}) of 10...30 MPa at 28-days, density (ρ_c) of 1500...1800 kg/m^3 were calculated using recommendations given in [33] for claydite gravel with bulk density (ρ_{cl}^b) 600...800 kg/m^3 and water absorption ($W_{ab.cl}$) 0.18…0.22. Quartz sand was used as fine aggregate. The obtained results, presented in Table 3 and Figure 5, enable to approximate the dependence $R_c = f(Z)$ by a linear equation:

$$f_{cm} = AR_cZ, \quad (18)$$

where A = 1.7.

Experiments have confirmed the formula and accordingly the assumed physical preconditions (Table 4). The average strength deviation between experimental results and those calculated according Eq. (18) was 6 %.

Table 3. Calculation results for parameter Z and strength of claydite concrete.

No.	ρ_c, kg/m³	ρ_{cl}^{b}, kg/m³	W, kg/m³	V^{*}_{cl}, l/m³	$W_{ab.cl}^{vl}$	C, kg/m³	Z	f_{cm}, MPa	C/W
Claydite porosity P_{cl} = 0.4									
1	1500	800	197	507	0.22	230	0.257	17.50	1.17
2	1800	800	197	344	0.22	205	0.255	17.37	1.04
3	1500	800	197	507	0.22	320	0.358	24.35	1.62
4	1800	800	197	344	0.22	270	0.336	22.87	1.37
5	1600	800	197	468	0.22	380	0.436	29.64	1.93
6	1800	800	197	344	0.22	340	0.424	28.80	1.73
7	1600	800	197	468	0.22	450	0.516	35.10	2.28
8	1800	800	197	344	0.22	400	0.498	33.89	2.03
P_{cl} = 0.55									
9	1500	600	207	437	0.22	240	0.220	14.99	1.16
10	1800	600	207	274	0.22	210	0.228	15.49	1.01
11	1500	800	197	507	0.22	320	0.283	19.27	1.62
12	1800	500	212	252	0.18	300	0.317	21.56	1.42
13	1500	700	202	472	0.19	420	0.364	24.77	2.08
14	1800	600	207	274	0.22	360	0.390	26.55	1.74
15	1600	600	207	388	0.22	480	0.462	31.43	2.32
16	1800	700	202	300	0.19	420	0.437	29.72	2.08
P_{cl} = 0.7									
17	1500	800	197	507	0.22	230	0.168	11.46	1.17
18	1800	600	207	274	0.22	210	0.200	13.61	1.01
19	1500	600	207	437	0.22	340	0.263	17.90	1.64
20	1800	600	207	274	0.22	290	0.276	18.79	1.40
21	1500	800	197	507	0.22	400	0.293	19.93	2.03
22	1800	800	197	344	0.22	340	0.303	20.60	1.73
23	1500	800	197	507	0.22	470	0.344	23.41	2.39
24	1800	700	202	300	0.19	420	0.382	25.95	2.08

V^{*}_{cl} – volume of claydite gravel.

Table 4. Experimental and calculated values of claydite concrete strength.

No.	Calculated concrete strength, MPa	Concrete density, kg/m³	Materials consumptions, kg/m³			Volume of entrained air, %	Z	Experimental concrete strength, MPa
			cement	claydite	sand			
1	15	1500	224	767 / 800	479	3.2	0.222	15.1
2	15	1600	243	440 / 600	882	2.8	0.222	14.9
3	20	1500	369	380 / 500	691	2.7	0.296	19.8
4	20	1600	289	708 / 800	563	2.3	0.296	19.8
5	30	1600	477	572 / 700	477	2.1	0.445	29.4
6	30	1800	392	520 / 800	835	1.8	0.445	30.1

Notes: 1. Denominator shows the bulk density of claydite (Cl). 2. Slump for all compositions was 5 cm, 28-day strength of cement was 40 MPa.

From equations (18) and (19) it can be found that when is used for lightweight concrete, dense sand without air-entraining additives cement consumption:

$$V_{cem} = \frac{f_{cm}\left(V_w + (P_{ag} - W_{ab.ag})V_{ag} + V_{air}\right)}{AR_{ц}}; \tag{19}$$

$$C = V_{cem}\rho_{cem}, \tag{20}$$

were ρ_{cem} – density of cement ($\rho_{cem} \approx 3.1$).

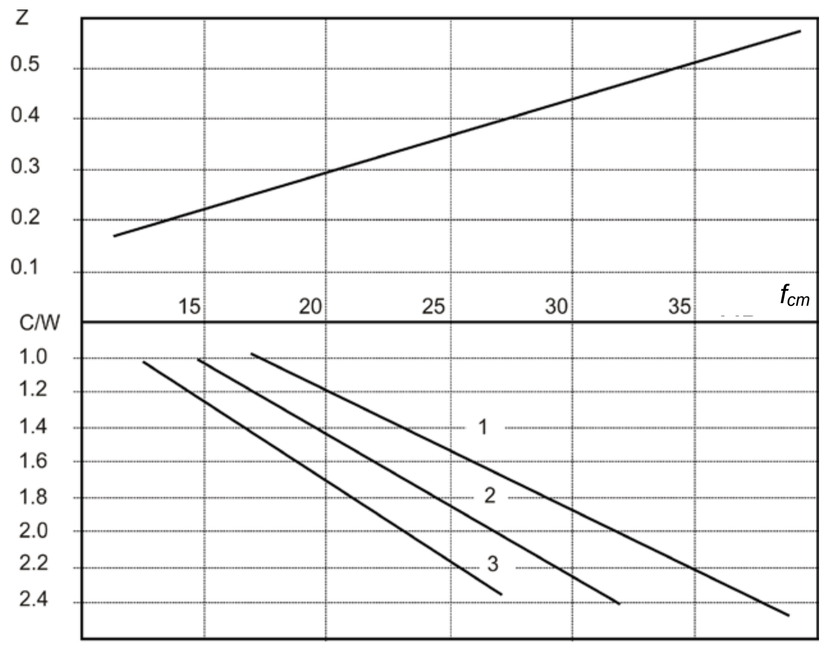

Figure 5. Dependence of claydite concrete strength (f_{cm}) on C/W and parameter Z:
1 **– claydite porosity is 0.4;** ***2*** **– 0.55;** ***3*** **– 0.7.**

Using parameter Z in formula for lightweight concrete strength enables to propose rather simple its composition design method.

Example 2

Determine the consumption of cement to obtain claydite concrete with a strength 25 MPa and a density of 1700 kg/m^3 on claydite gravel with a bulk density of ρ^b_{cl} = 700 kg/m^3 and quartz sand. The slump of the mixture Sl = 5 cm. The strength of cement R_{cem} = 50 MPa. Intergranular hollowness of claydite P^0_{cl} = 0.44. Claydite porosity P_{cl} = 53 %, water absorption $W_{ab.cl}$ = 20 %, V_{air} = 15 l/m^3.

1. Determine the desired "modified C/W" (parameter Z) to ensure the specified strength of concrete from the formula (17):

$$Z = \frac{25}{1.7 \cdot 50} = 0.294.$$

2. Determine the required water content to achieve the desired workability of the concrete mixture according to the empirical formula [1, 6]:

$$W = 2.33Sl - 0.04\rho_{cl} + 230;$$

$$W = 2.33 \cdot 5 - 0.04 \cdot 700 + 230 = 214 \text{ l/m}^3.$$

3. Calculate the volume concentration of φ and the volume content of V_{cl} the claydite gravel in concrete, using the formula:

$$\varphi = 1 - P^0_{cl}\alpha,$$

$$V_\alpha = 1000\varphi,$$

were α – coefficient of moving apart of coarse aggregate grains by cement-sand mortar (according to reference data [1] for concrete with a density of ρ_c = 1700 and a bulk density of claydite ρ^b_{cl} = 700, α = 1.45).

$$\varphi = 1 - 0.44 \cdot 1.45 = 0.362.$$

Craydite consumption:

$$V_{cl} = 1000 \cdot 0.362 = 362 \text{ l/m}^3.$$

4. Cement consumption is found by the formulas (19), (20)

$$V_{cem} = 0.294 \cdot (214 + (0.53 - 0.2) \cdot 362) + 15 = 113 \text{ l/m}^3;$$

$$C = 113 \cdot 3.1 = 350.3 \text{ kg/m}^3.$$

4. Conclusions

1. Modifying C/W taking into account of the influence of entrained air allows to correct of the strength of concrete calculated dependence that can be used for design concrete compositions with normalized values of concrete compressive strength under compression and frost resistance.

For light concrete, modifying C/W is advisable in view of the air volume contained in the pores of the porous aggregate. Using the proposed parameter Z, it is possible to calculate the composition of light weight concretes, taking into account the influence of both the cement-water ratio and the porosity of the aggregates.

References

1. Dvorkin, L., Dvorkin, O. Basics of concrete science: optimum design of concrete mixtures. Saint-Peterburg: Amason (Kindle edition) Stroi-Beton, 2006. 692 p.
2. Brandt, M. Optimization Methods for Material Design of Cement – Based Compozites. CRC Press. Roca Raton, 2014. 328 p. [Online]. URL: https://www.crcpress.com/Optimization-Methods-for-Material-Design-of-Cement-based-Composites/Brandt/p/book/9780419217909
3. Larrard, F. Concrete mixture – proportioning a scientific approach. CRC Press, London, 1999. 448 p. [Online]. URL: https://epdf.tips/queue/concrete-mixture-proportioning-a-scientific-approach.html
4. Kosmatka, S., Kerkhoff, B. Panarese, W. Design and Control of Concrete Mixture. 14th Edition. PSA, Skokie, Illinois, 2014. 358 p. [Online]. URL: https://www.researchgate.net/profile/Steven_Kosmatka/publication/284663491_Design_and_Control_of_Concrete_Mixtures/links/5655d8f908aefe619b1c5f2b/Design-and-Control-of-Concrete-Mixtures.pdf
5. Sonebi, M., Bassuoni, M., Yahia, A. Previous Concrete: Mix Design, Properties and Applications. RILEM Technical Letters, l, 2016. Pp. 109–115 [Online]. URL: http://dx.doi.org/10.21809/rilemtechlett.2016.24
6. Bazhenov, Yu.M., Demyanova, V.S., Kalashnikov, V.I. Modifitsirovannyye vysokokachestvennyye betony [Modified high-quality concretes] M.: Izdatelstvo: Assotsiatsiya stroitelnykh VUZov, 2006. 368 s. [Online]. URL: http://mirknig.su/knigi/stroitelstvo_i_remont/110641-modificirovannye-vysokokachestvennye-betony.html (rus)
7. Dvorkin, L., Dvorkin, O., Ribakov, Y. Multi-Parametric Concrete Compositions Design. Nova Science Publishers, Inc. New York, 2013. 223 p. [Online]. URL: https://www.bookdepository.com/Multi-Parametric-Concrete-Compositions-Design-Leonid-Dvorkin/9781624179112
8. Design and Control of Concrete Mixtures. 15th edition, Portland Cement Association. 2011. 460 p. [Online]. URL: https://faculty.uml.edu/ehajduk/Teaching/14.310/documents/EB001.15.pdf
9. Kett, I. Engineered Concrete Mix Design and Test Methods. 2th Edition 2009. CRC Press, 264 p. [Online]. URL: https://www.crcpress.com/Engineered-Concrete-Mix-Design-and-Test-Methods-Second-Edition/Kett/p/book/9781420091014
10. Day, K. Concrete Mix Design. Quality Control and Specification. 4th Edition 2017. CRC Press, 349 p. [Online]. URL: https://www.crcpress.com/Concrete-Mix-Design-Quality-Control-and-Specification/Day-Aldred-Hudson/p/book/9781138073531
11. Sabnis Cement Concrete Mix – Design Principles &Practice with CD. 6th Edition. 2017. V.Prakashan. 422 p.
12. Neville, A. Properties of concrete. 5-th edition 2011. Wiley, 620 p [Online]. URL: https://igitgeotech.files.wordpress.com/2014/10/properties-of-concrete-by-a-m-neville.pdf
13. Popovics, S, Contribution to the concrete strength versus water-cement ratio relationship. Mater. Civil. Eng., 2008, 20, Pp. 459–463. DOI: 10.1061/(ASCE)0899-1561(2008)20:7(459).
14. Dvorkin, L., Dvorkin, O., Ribakov, Y. Mathematical experiments planning in concrete technology. Nova Science Publishers, New York, 2012. 173 p. [Online]. URL: https://www.researchgate.net/publication/293205467_Mathematical_experiments_planning_in_concrete_technology
15. Kheder G., Gabhan A., Suhad Mathematical model for the prediction of cement compressive strength of the ages of 7 and 28 days. Mater. Struct., 36, 2003. Pp.693-701 [DOI:10.1007/BF02479504].
16. Hwang, K., Noguchi, T., Tomosava, F. Prediction model of compressive strength of fly-ash concrete. Cement Concrete Res., 34, 2004. Pp. 2269–2276. [Online]. URL: ftp://ftp.ecn.purdue.edu/olek/PTanikela/To%20Prof.%20Olek/Data/Strength%20Activity%20Index/INFORMATION/strength%20as%20a%20function%20of%20blaines.pdf
17. Hamid-Zaden, N., Jamili, A., Nariman-Zadeh, A., Akbar-Zadeh. A polynomial model for concrete compressive strength prediction using GMDH – type neural networks and genetic algorithem. Proceedings of the 5th International Conference of System Science, Canary Islands, Spain, 2006. Pp. 16–18. [Online]. URL: https://www.researchgate.net/publication/254457742_A_Polynomial_Model_for_Concrete_Compressive_Strength_Prediction_using_GMDH-type_Neural_Networks_and_Genetic_Algorithm
18. Zain, M., Abd, S. Multiple regression model for compressive strength prediction of high performance concrete. J. Applied Sci. 2009. No. 9. Pp. 155–160. DOI: 10.3923/jas.2009.155.160
19. Saadoon, T., Gomes-Meijide B., Garcia A. New predictive methodology for the apparent activation energy and strength of conventional and rapid hardening concretes. Cement and Concrete Research. January 2019. Vol. 115. Pp. 264–273. DOI: 10.1016/j.cemconres.2018.10.020.
20. DeRousseau, M., Kaspzyk, J., Srubar, W. Computational design optimization of concrete mixtures: A revier Cement and Concrete Reseach. Vol. 109. 2018. Pp. 42–53. [Online]. URL: https://doi.org/10.1016/j.cemconres.2018.04.007
21. Mayercsik, N., Vandamme, M., Kurtis, K. Asessing the efficiency of entrained air voids for freeze-thaw durability through modeling. Cement and Concrete research. 2016. Vol. 88. Pp. 43–59. DOI: 10.1016/j.cemconres.2016.06.004.
22. Jiao, D., Shi, C., Yuan, Q., An, X., Liu, Yu. Mixture design of concrete using simplex centroid design method. Cement and Concrete Composites. 2018. Vol. 89. Pp. 76–88. DOI: 10.17632/xhss7xv6wz.1.
23. Dvorkin, L., Zhitkovsky, V., Stepasiuk, Y. A method for design of high strength concrete composition considering curing temperature and duration. Construction and Building Materials. 2018. Vol. 186. Pp. 731–739. DOI: 10.1016/j.conbuildmat.2018.08.014.
24. Larsen, O.A., Narut, V.V. Samouplotnyayushchiysya beton s karbonatnym napolnitelem dlya obyektov transportnoy infrastruktury [Self-compacting concrete with limestone powder for transport infrastructure]. Inzhenerno-stroitelnyy zhurnal. 2016. № 8(68). S. 76–85. DOI: 10.5862/MCE.68.8. (rus)

25. Dvorkin, L., Zhitkovsky V., Ribakov Y. Concrete and mortar production using stone siftings, 2018, CRC Press, Roca Raton, London, New York. 155 p.

26. Furmanov, N.Ye. Blagopriyatnyy sostav betona dlya izgotovleniya vodonepronitsayemykh konstruktsiy po sisteme «Belaya vanna» [The favorable composition of concrete for the manufacture of waterproof structures using the «White Bath» system]. Inzhenerno-stroitelnyy zhurnal. 2009. № 3 (5). C. 11–16. [Online]. URL: http://engstroy.spbstu.ru/index_2009_03/furmanov_gidroizoliaciya.pdf (rus)

27. Barabanshchikov, Yu.G., Belyayeva, S.V., Arkhipov, I.Ye., Antonova, M.V, Shkolnikova, A.A, Lebedeva, K.S. Vliyaniye superplastifikatorov na svoystva betonnoy smesi [Influence of superplasticizers on the concrete mix properties]. Inzhenerno-stroitelnyy zhurnal. 2017. № 6(74). S. 140–146. DOI: 10.18720/MCE.74.11. (rus)

28. Hedegaord, S., Hansen, T. Modified water/cement ratio law for compressive strength of fly ash concretes. Materials and Structure. 1992. Vol. 25. Pp. 273–283. DOI: 10.1007/BF02472668.

29. Abdulahi, M., Ojeade G. Modified water-cement ratio law for compressive strength of rice husk ash concrete. Nigerian Journal of Technology. 2017. Vol. 36. No. 2. Pp. 373–379. DOI:10.4314/njt.v36i2.8.

Contacts:

Leonid Dvorkin, +38(068)3533338; dvorkin.leonid@gmail.com

Инженерно-строительный журнал

ISSN 2071-0305

сайт журнала: http://engstroy.spbstu.ru/

DOI: 10.18720/MCE.85.10

Модифицированное правило водоцементного соотношения для проектирования бетонов, содержащих воздух

Л.И. Дворкин,
Национальный университет водного хозяйства и природопользования, г. Ровно, Украина
E-mail: dvorkin.leonid@gmail.com

Ключевые слова: Модифицированное Ц/В; объем вовлеченного воздуха; расход цемента; прочность и морозостойкость бетона; объем пор заполнителя; состав легких бетонов.

Аннотация. Проектирование составов бетона, содержащего вовлеченный воздух, обычно выполняется с помощью эмпирических подборов, что является довольно трудоемким и длительным процессом. В статье экспериментально обоснованы расчетные формулы с помощью правила модифицированного Ц/В, которое основано на известных эмпирических зависимостях и позволяет находить содержание компонентов бетона с заданными параметрами прочности, морозостойкости и плотности. Приведены результаты экспериментальных исследований, выполненных с помощью компрессионного метода определения объема вовлеченного воздуха, а также стандартных методов определения прочности и морозостойкости бетона. Полученные формулы проверены на примерах расчета составов тяжелого бетона с заданной прочностью и морозостойкостью и конструкционного керамзитобетона с заданными значениями прочности и плотности.

Литература

1. Dvorkin L., Dvorkin O. Basics of concrete science: optimum design of concrete mixtures. Saint-Peterburg: Amason (Kindle edition) Stroi-Beton, 2006. 692 p.
2. Brandt M. Optimization Methods for Material Design of Cement – Based Compozites. CRC Press. Roca Raton, 2014. 328 p. [Электронный ресурс]. URL: https://www.crcpress.com/Optimization-Methods-for-Material-Design-of-Cement-based-Composites/Brandt/p/book/9780419217909
3. Larrard F. Concrete mixture – proportioning a scientific approach. CRC Press, London, 1999. 448 p. [Электронный ресурс]. URL: https://epdf.tips/queue/concrete-mixture-proportioning-a-scientific-approach.html
4. Kosmatka S., Kerkhoff B. Panarese W. Design and Control of Concrete Mixture. 14th Edition. PSA, Skokie, Illinois, 2014. 358 p. [Электронный ресурс]. URL: https://www.researchgate.net/profile/Steven_Kosmatka/publication/284663491_Design_and_Control_of_Concrete_Mixtures/links/5655d8f908aefe619b1c5f2b/Design-and-Control-of-Concrete-Mixtures.pdf
5. Sonebi M., Bassuoni M., Yahia A. Previous Concrete: Mix Design, Properties and Applications. RILEM Technical Letters, I, 2016. Pp. 109-115. [http://dx.doi.org/10.21809/rilemtechlett.2016.24
6. Баженов Ю.М., Демьянова В.С., Калашников В.И. Модифицированные высококачественные бетоны [Modified high-quality concretes] М.: Изд-во: Ассоциация строительных ВУЗов, 2006. 368 с. [Электронный ресурс]. URL: http://mirknig.su/knigi/stroitelstvo_i_remont/110641-modificirovannye-vysokokachestvennye-betony.html
7. Dvorkin L., Dvorkin O., Ribakov Y. Multi-Parametric Concrete Compositions Design. Nova Science Publishers, Inc. New York, 2013. 223 p. [Электронный ресурс]. URL: https://www.bookdepository.com/Multi-Parametric-Concrete-Compositions-Design-Leonid-Dvorkin/9781624179112
8. Design and Control of Concrete Mixtures. 15th edition, Portland Cement Association. 2011. 460 p. [Электронный ресурс]. URL: https://faculty.uml.edu/ehajduk/Teaching/14.310/documents/EB001.15.pdf
9. Kett I. Engineered Concrete Mix Design and Test Methods. 2th Edition 2009. CRC Press, 264 p. [Электронный ресурс]. URL: https://www.crcpress.com/Engineered-Concrete-Mix-Design-and-Test-Methods-Second-Edition/Kett/p/book/9781420091014
10. Day K. Concrete Mix Design. Quality Control and Specification. 4th Edition 2017. CRC Press, 349 p. [Электронный ресурс]. URL: https://www.crcpress.com/Concrete-Mix-Design-Quality-Control-and-Specification/Day-Aldred-Hudson/p/book/9781138073531
11. Sabnis Cement Concrete Mix – Design Principles &Practice with CD. 6th Edition. 2017. V. Prakashan. 422 p.
12. Neville A. Properties of concrete. 5-th edition 2011. Wiley, 620 p. [Электронный ресурс]. URL: https://igitgeotech.files.wordpress.com/2014/10/properties-of-concrete-by-a-m-neville.pdf
13. Popovics S. Contribution to the concrete strength versus water-cement ratio relationship // Mater. Civil. Eng. 2008. No. 20. Pp. 459–463. DOI: 10.1061/(ASCE)0899-1561(2008)20:7(459).

14. Dvorkin L., Dvorkin O., Ribakov Y. Mathematical experiments planning in concrete technology. Nova Science Publishers, New York, 2012. 173 p. [Электронный ресурс]. URL: https://www.researchgate.net/publication/293205467_Mathematical_experiments_planning_in_concrete_technology
15. Kheder G., Gabhan A., Suhad Mathematical model for the prediction of cement compressive strength of the ages of 7 and 28 days // Mater. Struct. 2003. No. 36. Pp. 693–701. DOI: 10.1007/BF02479504.
16. Hwang K., Noguchi T. and Tomosava F. Prediction model of compressive strength of fly-ash concrete // Cement Concrete Res. 2004. No. 34, Pp. 2269–2276. [Электронный ресурс]. URL: ftp://ftp.ecn.purdue.edu/olek/PTanikela/To%20Prof.%20Olek/Data/Strength%20Activity%20Index/INFORMATION/strength%20as%20a%20function%20of%20blaines.pdf
17. Hamid-Zaden N., Jamili A., Narim-Zadeh A., Akbar-Zadeh. A polynomial model for concrete compressive strength prediction using GMDH – type neural networks and genetic algorithem. Proceedings of the 5th International Conference of System Science, Canary Islands, Spain, 2006. Pp. 16–18. [Электронный ресурс]. URL: https://www.researchgate.net/publication/254457742_A_Polynomial_Model_for_Concrete_Compressive_Strength_Prediction_using_GMDH-type_Neural_Networks_and_Genetic_Algorithm
18. Zain M., Abd S. Multiple regression model for compressive strength prediction of high performance concrete // J. Applied Sci. 2009. No. 9. Pp. 155–160. DOI: 10.3923/jas.2009.155.160.
19. Saadoon T., Gomes-Meijide B., Garcia A. New predictive methodology for the apparent activation energy and strength of conventional and rapid hardening concretes // Cement and Concrete Research. January 2019. Vol. 115. Pp. 264–273. DOI: 10.1016/j.cemconres.2018.10.020.
20. DeRousseau M., Kaspzyk J., Srubar W. Computational design optimization of concrete mixtures: A revier // Cement and Concrete Reseach. Vol. 109. 2018. Pp. 42–53 [Электронный ресурс]. URL: https://doi.org/10.1016/j.cemconres.2018.04.007
21. Mayercsik N., Vandamme M., Kurtis K. Asessing the efficiency of entrained air voids for freeze-thaw durability through modeling // Cement and Concrete research. 2016. Vol 88. Pp. 43–59. DOI: 10.1016/j.cemconres.2016.06.004.
22. Jiao D., Shi C., Yuan Q., An X., Liu Yu. Mixture design of concrete using simplex centroid design method // Cement and Concrete Composites. 2018. Vol. 89. Pp. 76–88. DOI: 10.17632/xhss7xv6wz.1.
23. Dvorkin L., Zhitkovsky V., Stepasiuk Y. A method for design of high strength concrete composition considering curing temperature and duration // Construction and Building Materials. 2018. Vol. 186. Pp. 731–739. DOI: 10.1016/j.conbuildmat.2018.08.014.
24. Ларсен О.А., Наруть В.В. Самоуплотняющийся бетон с карбонатным наполнителем для объектов транспортной инфраструктуры // Инженерно-строительный журнал. 2016. № 8(68). С. 76–85. DOI: 10.5862/MCE.68.8.
25. Dvorkin L., Zhitkovsky V., Ribakov Y. Concrete and mortar production using stone siftings, 2018, CRC Press, Roca Raton, London, New York, 155 p.
26. Фурманов Н.Е. Благоприятный состав бетона для изготовления водонепроницаемых конструкций по системе «Белая ванна» // Инженерно-строительный журнал. 2009. № 3 (5). С. 11–16 [Электронный ресурс]. URL: http://engstroy.spbstu.ru/index_2009_03/furmanov_gidroizoliaciya.pdf
27. Барабанщиков Ю.Г., Беляева С.В., Архипов И.Е., Антонова М.В, Школьникова А.А, Лебедева К.С. Влияние суперпластификаторов на свойства бетонной смеси [Influence of superplasticizers on the concrete mix properties] // Инженерно-строительный журнал. 2017. № 6(74). С. 140–146. DOI: 10.18720/MCE.74.11.
28. Hedegaord S., Hansen T. Modified water/cement ratio law for compressive strength of fly ash concretes // Materials and Structure. 1992. Vol 25. Pp. 273–283. DOI: 10.1007/BF02472668.
29. Abdulahi M., Ojeade G. Modified water-cement ratio law for compressive strength of rice husk ash concrete // Nigerian Journal of Technology. 2017. Vol. 36, No. 2. Pp. 373–379. DOI: 10.4314/njt.v36i2.8.

Контактные данные:

Леонид Иосифович Дворкин, +38(068)3533338; эл. почта: dvorkin.leonid@gmail.com

Magazine of Civil Engineering. 2019. 85(1). Pp. 136–145
Инженерно-строительный журнал. 2019. № 1(85). С. 136–145

Magazine of Civil Engineering

ISSN 2071-0305

journal homepage: http://engstroy.spbstu.ru/

DOI: 10.18720/MCE.85.11

Structural health monitoring of a concrete-filled tube column

A. Younesi*[a]*, O. Rezaifar*[a]**, M. Gholhaki*[a]*, A. Esfandiari*[b]*,
[a]Semnan University, Semnan, Iran
[b]AmirKabir University, Tehran, Iran
** E-mail: orezayfar@semnan.ac.ir*

Keywords: CFT column; modal data; damage identification; Structural Health Monitoring; CWT.

Abstract. Structural Health Monitoring (SHM) has provided an opportunity to assess the reliability and integrity of civil engineering structures. Damage in the structure reduces the hardness and modal properties of the structures. Therefore, changes in dynamic behavior and modal data can be used to identify damage. This study identifies the existence and location of damage in the CFT column based on vibrational analysis techniques. The method for damage detection is based on dynamic analysis on the modal data (mode shape, frequency and damping) of the structure. The experimental results obtained the modal test and the results of the theory of FE simulation have been used to identify the damage. In the first step, after creating the prototype and preparing the test setup, the specimen was subjected to a modal test, so the modal data were extracted, and the Coherence curve test were plotted to confirm the accuracy. Similarly, the FE model is also simulated after validation, so the modal data of the theory were also extracted. In the second step, based on the obtained data, the comparison of frequencies, MAC and COMAC criteria, mode shape and damping of an undamaged and damaged specimens were performed, and the identification of the damage was dealt with. In the third step, the Continuous Wavelet Transform(CWT) tool was used in order to determine the location of the damage in both methods (FE and experimentally), to identify the damage location on the mode shape (CWT input signal). The results show that in the both the methods, the existence of damage in the CFT column is well identified and its location is also determined with high precision, which indicates the ability of damage detection method by CWT techniques.

1. Introduction

CFT columns are very important because of their widespread use in high-rise buildings. On the other hand, due to the combination of two materials with a distinct mechanical behavior, the possibility of the occurrence of malfunction and damage under load is high. Identifying damage in this highly applied structural element is very important. Accordingly, the number of researches done on the identification and localization of the estimation of the health status of CFT columns is increasing, which is due to: 1. Executive weakness, 2. Thinness of plates and their buckling probability, 3. Extensive application, 4. High age of structure, and 5. Lack of proper connection between concrete and steel. In the present study, the detection of damage to the CFT column under the plate local buckling damage (shrinkage of the plate under pressure) has been carried out, where to simulate a part of the column is cut in parallel grooves to indicate the buckling damage. In addition, laboratory modal data and extracted theory and modal analysis have been carried out on them to identify the presence of damage and its exact location.

Most damage detection methods are based on data obtained from the Fourier transform spectra. Damage to structures is usually local, which can usually be identified by identifying Mode shapes. [1–3].

The study of A. Lyapina and Y. Shatilov Investigates the identification of the position of damage in concrete columns using vibration analysis techniques. The method for detecting and locating damage is based on the analysis of the dynamic characteristics of a structure, such as Eigen-frequencies, mode shapes and modal damping. The results of the FE analysis show that increasing the number of sensors increases the accuracy of the location of the damage [4]. A theoretical and experimental study of the frequency-based

Younesi, A., Rezaifar, O., Gholhaki, M., Esfandiari, A. Structural health monitoring of a concrete-filled tube column. Magazine of Civil Engineering. 2019. 85(1). Pp. 136–145. DOI: 10.18720/MCE.85.11.

damage detection method has been presented in Chen Yang and S. Olutunde Oyadiji. Based on the eigenvalue problem and perturbation assumption of defect in modal response, the theoretical basis of the modal frequency curve method is established. The numerical and experimental results show that the damage indicator is more accurately detected than the wavelet coefficients. Additionally, the damage estimator shows the size of damages with high precision [5]. A number of researchers have examined the effects of frequency changes on damaged structures compared to healthy structures. [6–9]. In addition, Gadelrab studied the frequency change due to damage on a two-layer beam. The results showed that frequency changes depend on boundary conditions [10]. Results of studies Kessler et al. [11] showed that the reduction of frequency in low modes is proportional to the reduction of general stiffness. Della and Shu investigated several numerical modeling techniques of damage detection. The results indicate that natural frequency changes detect the position and size of the damage [12]. Alnefaie [13] showed that the defect-induced variation of mode shape is more distinct for higher flexural vibration modes. Salawu has reviewed various agencies. This study shows the possibility of using modal frequency data in identifying damage and structural health monitoring [14]. Comprehensive studies of structural health monitoring methods based on vibrational methods have been reported [15]. Although the natural frequencies of the structure can be accurately measured with a number of sensors, but modal frequency changes cannot be detected the location of the damage [16, 17]. In recent years, the CWT method has been considered for further damage identification. Hong et al. investigated damage detection based on Mexican hat wavelet coefficients using CWT and Discrete Wavelet Transform (DWT). They suggested that the number of vanishing moments of wavelets in crack detection should be at least two [18, 19]. Chang and Chen used the DWT to obtain Gabor wavelet transform coefficients for crack detection and localization in the beam [20].

The damage is estimated based on the specified parameters of the criterion and the damage summation procedure by employing the FE method. With a reasonably fine mesh of the FE model of the “critical location” structure, the condition of the identity of damage in the material of the test specimen and the structure is provided and, respectively, the effect of uncertainty on the fatigue life assessment of the structure is reduced. The implementation of this version of the method is using the example of the fatigue life evaluation of a ship hull and superstructure detail at expansion joint. For comparison, the fatigue life of the detail is estimated using the standard S-N approach. The results are in approximate agreement; however, reducing the computational uncertainties with the help of the deformation criterion shows more physically reasonable fatigue properties of the detail [21–23].

Due to the defects in the connections and the force transfer from the beam flanges to the column of the hollow section and concrete filled tube steel columns, different types of internal and external stiffeners have been suggested. By installing external stiffeners, the implementation problems of the construction of the columns and the internal hardening of the installation is minimized [23–28].

The paper reviews the recent applications of piezoelectric materials in structural health monitoring and repair conducted by the authors. First, commonly used piezoelectric materials in structural health monitoring and structure repair are introduced. The analysis of plain piezoelectric sensors and actuators and interdigital transducer and their applications in beam, plate and pipe structures for damage detection are reviewed in detail. Second, an overview is presented on the recent advances in the applications of piezoelectric materials in structural repair. In addition, the basic principle and the current development of the technique are examined [29]. The identification of the segregation of steel tube from the central core in the rectangular CFT column has been evaluated based on the energy spectrum of the CWT with the piezo ceramics [30–32]; the segregation of core enclosed from the steel tube reduces bearing capacity and structural shape ability. In the study of Xu, B. et al., with the installation of piezoelectric in predetermined locations on the external surfaces as a sensor, a new method is proposed to monitor the interior state. In this study, wavelet energy spectrum analysis was also performed and a weight-based damage index (WPES) was defined for the determination of artificial segregation regions. The results show that the proposed indices are sensitive to segregation defects and fully assess the internal surface of a CFT column. In addition, the results show that there can be no undetectable segregation defects in the monitoring of the health of CFT column in high-rise structures.

Since the damage of shrinkage of steel tube plate in CFT column, because of its thinness – due to its high ratio of strength to steel weight – is one of the most noticeable damages occurring to this structural element, it is evaluated in this study. In order to simulate damage, the damage location is cut in parallel grooves. Also, in order to reveal damage in steel columns filled with concrete, laboratory modal analysis was used. After the modal data were extracted, the process of the presence of damage was detected by comparing frequencies, mode shape and parameters of MAC and COMAC, and a one-dimensional CWT method has been used to determine the exact location of the damage.

2. Methods

2.1. Test Specimens

Two specimens of CFT columns with similar characteristics were used to perform the test that an intentional damage has been created in the wall of one of the specimens. The column section of the specimens is 120*120mm from the steel plate with a thickness of 3mm and a length of 800mm which is filled with fine aggregate concrete. In order to simulate damage a Parallel groove (thickness of grooves are 2.5mm) with the size of 114*45mm with similar thickness of the plate has been created in the middle of one of the column, which indicates the local buckling in the column plate. The specimen specification has been presented in Table 1 and Figure1.

Table 1. Introduction of Specimens.

Specimen	Damage dimension(mm)	Damage type	Damage location
UDS-P	-	Healthy	-
DLB-P	114 * 45	Column plate buckling	Middle of the column

It is worth noting that the damage was created by the high precision before filling the column and the site of damage is completely filled in order to prevent the release of the concrete. After the concrete has reached the strength required, the filler material has been removed from the site of damage (see Figure 1).

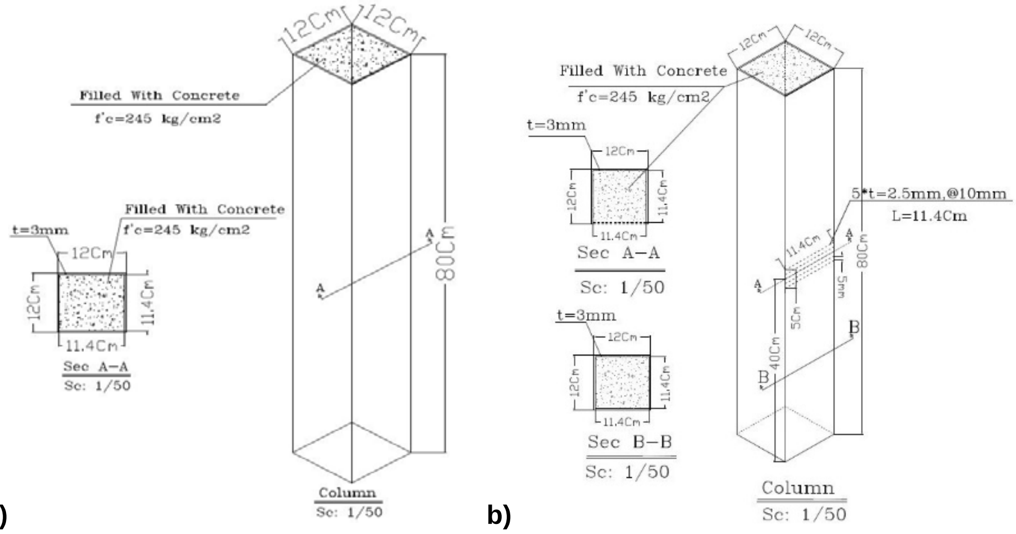

a) b)

Figure 1. Test specimens; (a) UDS-P, (b) DLB-P.

2.2. FE models

ABAQUS limited component software was used for modeling specimens. Solid and Sell elements were used for modeling concrete and steel plates. At the point of concrete contact with steel, the coefficient of friction is 0.7. The final models are shown in Figure 2.

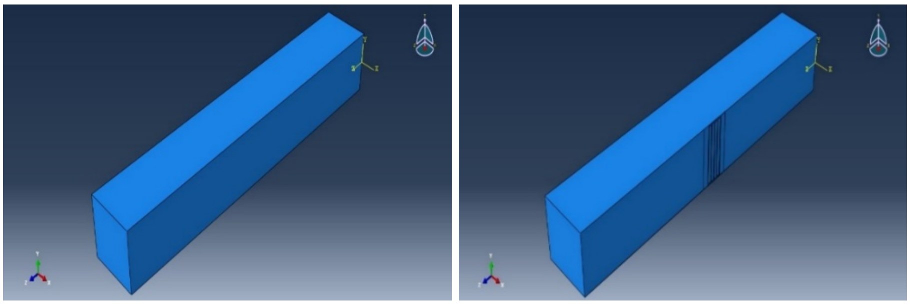

a) UDSP **b) DLBP**

Figure 2. FEmodels.

2.3. Material Properties

The main materials used in this study were steel and concrete. The steel used was of type st37, the characteristics of which after the tensile test are presented in Table 2. The concrete used was composed of the fine grain materials, the mechanical properties of which after the compressive test on cubic specimens are presented in Table 2.

Table 2. Material properties.

Materials	$f_y(MPa)$	$f_u(MPa)$	$f'_c(MPa)$	$E(MPa)$	ϑ	Specific gravity ($\frac{kN}{m^3}$)
Steel	327.26	391.12	-	2.00×10^5	0.29	78.50
Concrete	-	-	26.06	0.79×10^5	0.20	24.40

2.4. Test setup and instrumentation

Since the existence of any supporting conditions causes a high rigidity in the structure and a large force is required to stimulate it for modal analysis. This force may cause unforeseen damage and even damage of the structure and error in the results of the analysis. Therefore, the free-free support conditions have been used in the present study. To achieve this goal, the CFT column was suspended by an elastic ribbon with high elasticity (or on a low inflation tube) and the accelerometer was connected to it at a point in the column. (Figures.3 and 4). The location of connection of the accelerometer sensor has been selected between the midpoint and the edge of the beam so that firstly, not to be detached when an impact is applied, and secondly, to be placed at zero-moment point in order to be with the least error. In the next step, a force was applied to the stimulation points (the site of the mesh nodes) by a stimulus (stimulator hammer or shaker) and the frequency response function was extracted for each excitation. Finally, using the sum of the resulting frequency functions, the first to third modes of the frequency response function have been obtained in two different methods as follows.

The frequency response functions were obtained in two different ways: 1) Stimulation using a hammer: In this method, the specimen was placed on a tube. The sensor was then fixed at a specific location and stimulated by the impact hammer in different locations. It is important to note that the location of the sensor should not be placed on the node of the mode shape, which is why the point between the end and midpoint of the column was chosen as the location of the sensor installation. 2) Stimulation using a shaker: In this approach, the specimen was suspended using an elastic band. The shaker was fixed at a specific location on the specimen and the sensor was replaced in different places. Here it is also important that the shaker not to be located in the node. The random type of stimulus signal was selected to interpolate nonlinear effects of the specimen and provide the best linear model. Choosing the best type of stimulation depends on the geometry and structure of the specimen. For most of the specimens due to their non-linear nature, the hammer stimulation was not suitable and therefore, the shaker stimulation was applied. Finding the best method does not follow a general rule and is achieved with trial and error (Figures 3 and 4).

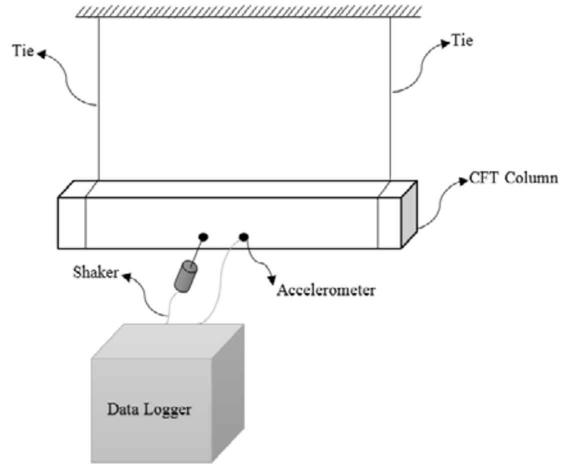

Figure 3. Test setup.

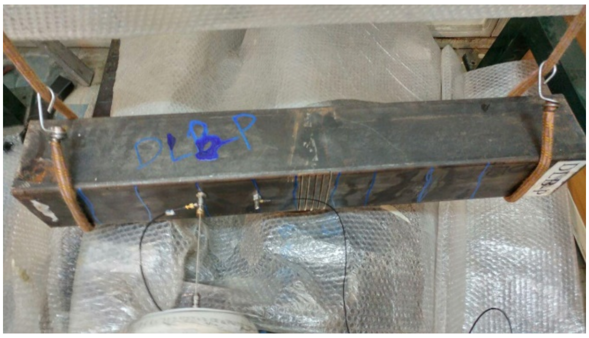

Figure 4. Tooling and testing method.

Table 3. The tools of tests.

No.	**Equipment**	**Model**	**Manufacturer**	**Country of origin**
1	PorTable Pulse 4/2 I/O Module	3560C	B&K	Denmark
2	Impulse Hammer	AU02	AP Tech	Netherland
3	Accelerometer	4397	B&K	Denmark
4	Charge Convertor	2646	B&K	Denmark
5	Force Transducer	9301B	Kistler	Switzerland
6	Power Amplifier	BAA120	Tira	Germany

3. Results and Discussion

3.1. General Observation of Experimental Tests

After the specimens are made and the structure is installed in the setup and the sensor is installed, the specimens are subjected to the shaker which shows how the specimens are tested in Figure4 then, the frequency, mode shape and damping patterns of the specimens have been extracted as modal data.

The specimen frequency in all modes is reduced compared to the healthy state which indicates the change in the mechanical characteristics and, consequently, the change in the dynamic behavior of the structure. In the monitoring of the health of the structures, frequency variation can be considered as an example of damage in the specimen. On the other hand, the damping coefficient in the DLB-P specimen has been increased in proportion to the healthy specimen (UDS-P). This is due to the hardening of the damaged specimen.

By observing the shape of the specimen mode, it is concluded that the amplitude of the mode in the damaged specimen is higher than the normal specimen and the structure has a softer behavior. It can also be concluded that the point-to-point slope of the mode shape in the specimen after damage is lower, which in general indicates a reduction in the stiffness of the structure. To determine the frequencies of each curve mode, FRF of the specimens have been extracted (Figure 5). On the other hand, COHERENCE curve has been plotted to monitor the accuracy of the tests. As the points in the COHERENCE curve are closer to one, it indicates the high accuracy of the experiments (Figure 6).

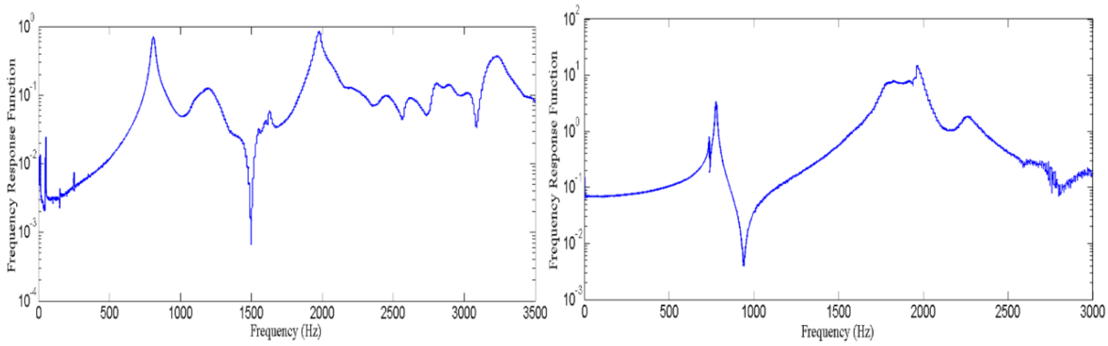

(a) UDS-P **(b) DLB-P**

Figure 5. Phase-Amplitude curve of the specimens.

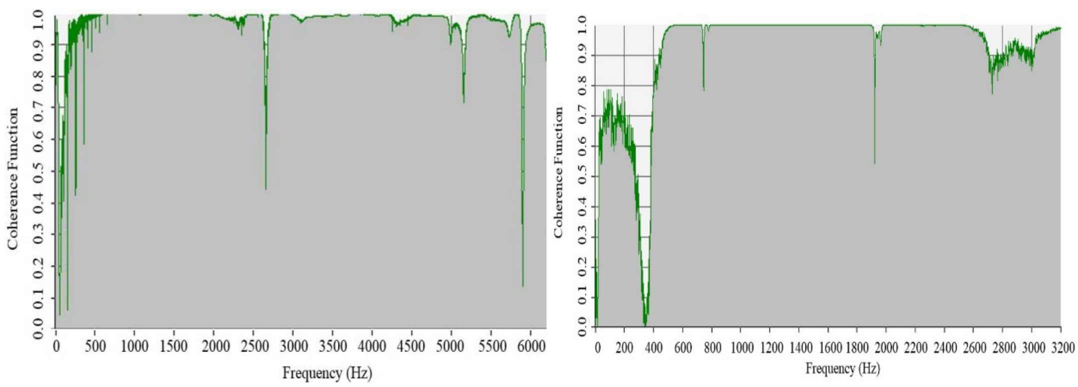

(a) UDS-P **(b) DLB-P**

Figure 6. COHERENCE curve of the specimens.

3.2. Mode Shape

Figures 7a to 7c shows the mode shape of both a normal and damaged specimen based on theoretical and laboratory data. As shown in Figure 7a, mode shape of the damaged specimens are further elongated in the damaged region (mid-column at 5 cm of length), indicating that changes are made in the mechanical properties. In addition, similar results have been achieved in models created in ABAQUS software. Similarly, in the second and third modes, both theoretical and experimental modes of simulated damage in the DLBP specimen have caused the shape of the mode to change from its normal mode (UDSP), which generally indicates the presence of damage in the structure.

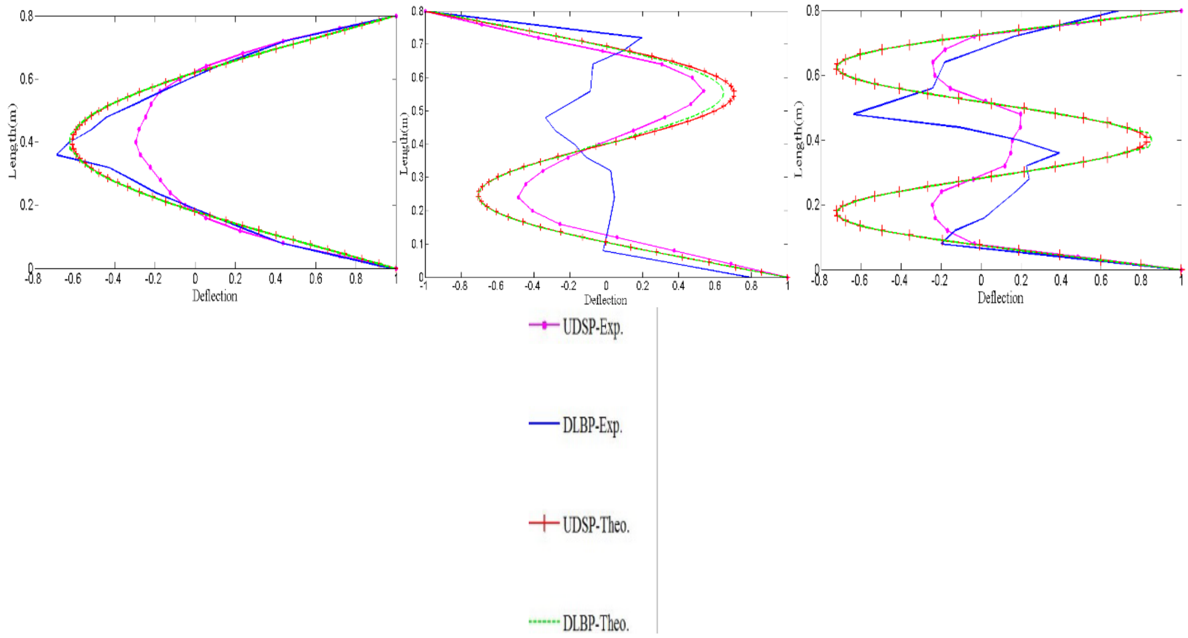

a) Mode I b) Mode II c) Mode III

Figure 7. Mode shapes of experimental specimens and Theoretical models.

3.3. Frequency

Another parameter for damage detection in structures is to compare the frequencies of damaged and normal specimens. In real structures, having a database of structures, you can continually monitor the health of the structure. In the present study, a normal specimen was first made and based on the mechanical properties obtained, the damaged specimen was made completely similar and only with a predetermined damage.

Table 4. Frequency of experimental specimens and theoretical models.

Type of test	Mode No.	Health	Damaged	Difference(%)
Experimental	Mode I	808.40	777.09	-3.87
	Mode II	1971.50	1962.40	-0.46
	Mode III	3218.90	2257.30	-29.87
Theoretical	Mode I	874.29	872.21	-0.24
	Mode II	2138.10	2135.80	-0.11
	Mode III	3686.80	3663.40	-0.63

According to Table 4, the frequency in the damaged specimen decreases in both theoretical and laboratory conditions, which indicates a change in the mechanical properties of the specimen, followed by a change in the modal parameters (frequency and model shape). The results show that the frequency change in the third mode is higher than other modes, so identifying damage at higher modes is easier and since achieving higher modes is difficult and requires more spending and may even cause serious damage to the specimen, frequency change in theoretical mode is less than that of laboratory whose reason is the more even simulation of materials and the connection between concrete and steel.

3.4. MAC and COMAC Parameters

One of the valid criteria for examining the damage in structures is the Modal Assurance Criteria (MAC) and Coordinate Modal Assurance Criterion (COMAC) [33].

$$MAC_{(j,k)} = \frac{\left(\sum_{i=1}^{n} \Phi_{Aj}^{i} \times \Phi_{Bk}^{i}\right)^2}{\sum_{i=1}^{n} (\Phi_{Aj}^{i})^2 \times \sum_{i=1}^{n} (\Phi_{Bk}^{i})^2} \qquad With: \quad j = 1,...,m_A \quad and \quad k = 1,...,m_B \tag{1}$$

where: Φ_A and Φ_B are two series of mode shape expressed in matrix from, respectively of $n \times m_A$ and $n \times m_B$ class, with m_A and m_B equal to the number of investigated modes and n equal to the number of considered coordinates; Φ_{Aj}^{i} is the ith coordinate of the jth column of Φ_A, while Φ_{Bk}^{i} is ith coordinate of the kth column of Φ_B.

As MAC index does not take into account local deviations of displacement, it has been introduced another index, the COMAC, expressed the following [34]:

$$COMAC_{(i)} = \frac{\left(\sum_{k=j=1}^{L} \Phi_{Aj}^{i} \times \Phi_{Bk}^{i} \right)^2}{\sum_{j=1}^{L} (\Phi_{Aj}^{i})^2 \times \sum_{k=1}^{L} (\Phi_{Bk}^{i})^2} \qquad (2)$$

Where L is the total number of investigated modes and i = 1…n is the generic point of measure. This index can be used to identify the positions in which the two series Φ_A and Φ_B of mode shape are discordant, because it measures the correlation between all the displacements at i`th point corresponding to the different modes. The value of one indicates the integrity of the structure and values less than one representing the probability of damage in the structure [34].

These criteria, by examining and comparing the modes of healthy and damaged specimens according to Eq. 1 and 2, investigate the presence of damage in these structures; the closer this value to one, the more the overlap of the modes under investigation, such that the number 1 represents the complete coincidence of the mode shapes (vectors) and the zero number represents the perpendicularity of these vectors (Table 5).

Table 5. Parameters of MAC and COMAC.

Theoretical		Experimental		Specimen	
DDB-P	UDS-P	DLB-P	UDS-P		
0.99993	1	0.92150	1	MAC	Mode1
0.99990	1	0.92150	1	COMAC	
0.99819	1	0.30390	1	MAC	Mode2
0.9982	1	0.71640	1	COMAC	
0.99972	1	0.46050	1	MAC	Mode3
0.99970	1	0.76350	1	COMAC	

One of the ways of detecting the presence of damage in structures is examining MAC and COMAC criteria. The more these values are less than one, indicates a greater change of the interested mode in the normal structure than damaged structure (the value of 1 indicates the complete conformation of the mode shape of the normal and damaged structure). Based on Table 5 and Figure 8, the values of MAC and COMAC in both laboratory and theory modes are reduced. In theory, the reduction of values is less than the experimental one. So that in the second mode, the MAC value is about 30 %, which indicates a very low conformation of the normal and damaged structures. In addition, the COMAC of this mode is also smaller than other modes. Generally, given the change of MAC values, it could be concluded that a damaged is occurred to the structure whose severity is greater in higher modes.

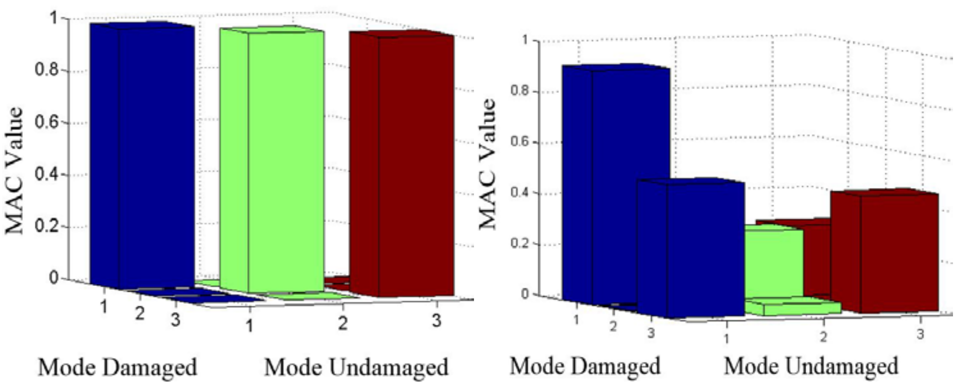

a) Theoretical **b) Experimental**

Figure 8. MAC graphs of experimental specimen and theoretical model.

3.5. Damage detection by wavelet

One of the most widely used and suitable methods for detecting damage in structures is the WT method. In the present paper, the CWT was used to detect the location of the damage in the specimens. The wavelet and specially, the CWT will be discussed in the following.

3.5.1. Wavelet transform

A wavelet transform is a mathematical tool that transforms the original signal into another form to indicate the characteristic of the original signal [35, 36].

3.1.1.1. Continuous Wavelet Transform(CWT)

The wavelet transform of a signal x(t) is calculated using Eq. (4), in which, the signal is compared with a set of template functions $(\psi_{s,\tau}(t))$obtained from the scaling (i.e., dilation and contraction) and shifting (i.e., translation along the time axis) of a base wavelet $\psi(t)$ and looking for their similarities.

The base wavelet is a small wave that has an oscillating wavelike characteristic and has its energy concentrated in time [35, 36].

$$\psi_{s,\tau}(t)=\frac{1}{\sqrt{s}}\psi\left(\frac{t-\tau}{s}\right) \tag{3}$$

$$wt(s,\tau)=\langle x(t),\psi_{s,\tau}\rangle=\frac{1}{\sqrt{s}}\int_{-\infty}^{+\infty}x(t)\psi^{*}\left(\frac{t-\tau}{s}\right)dt \tag{2}$$

Where the symbol $s>0$ represents the scaling parameter, which determines the time and frequency resolutions of the scaled base wavelet $\psi(t-(\tau/s))$. The specific values of s are inversely proportional to the frequency. The symbol τ is the shifting parameter, which translates the scaled wavelet along the time axis. The symbol * denotes the complex conjugation of the base wavelet $\psi(t)$ [35-37].

As the wavelet contains two parameters, transforming a signal with the wavelet basis means that such a signal will be projected into a 2D, time-scale plane. Because of the localization feature of the violin, the wavelet transform is obtained from its time characteristics.

Wavelet deubechies (db) was used for damage localization in this study. According to Figure 9, the damage location is carefully and accurately determined. As shown in Figure 9, in all the three modes of theoretical (Figures 9a-c) and laboratory (Figures 9d-9f), in the damage location which is in the center of the column, a jump is made; where the starting point and the ending point of the jump, shows the first and end of the damage which is highlighted in the Figure 9.

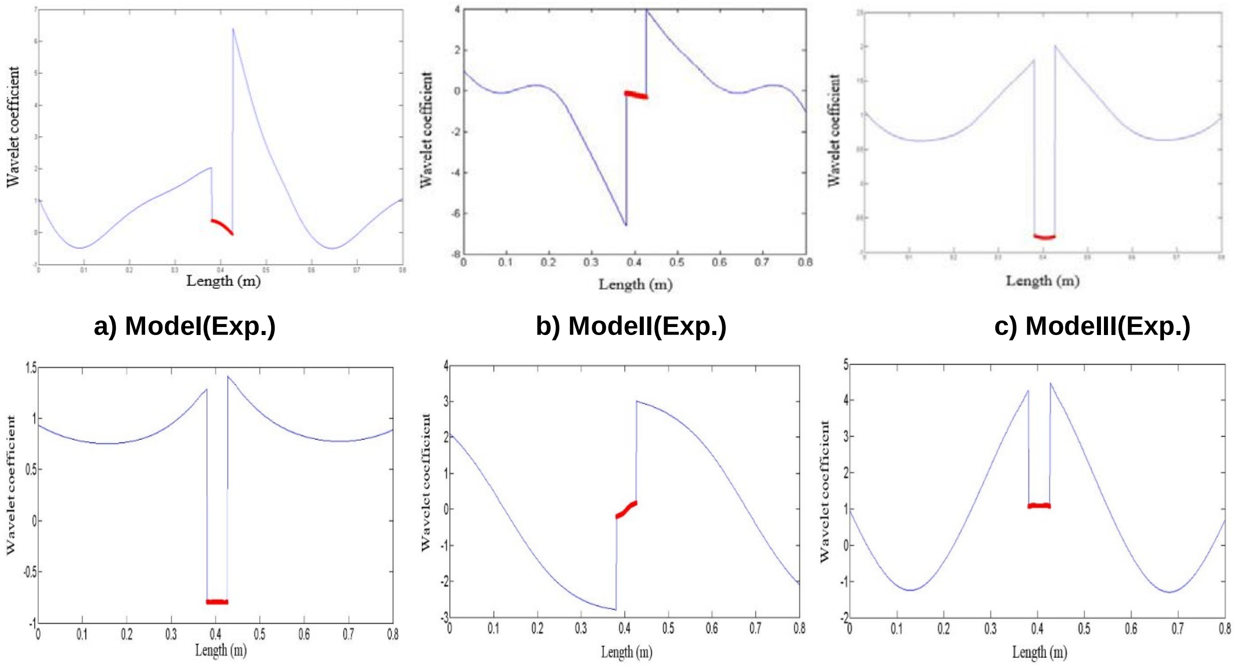

a) Model(Exp.) **b) ModelI(Exp.)** **c) ModelII(Exp.)**

d) Model(Theo.) **e) ModelI(Theo.)** **f) ModelII(Theo.)**

Figure 9. Wavelet transform of specimens and models.

4. Conclusion

Frequency analysis, mode shape, and MAC and COMAC criteria were used in the present study to detect the presence of damage. The results of the analysis indicate that the above parameters have changed and confirm the presence of damage in the structure. Additionally, a CWT method was used to determine damage location, and a db wavelet was used to investigate it which could well detect the location of damage. The above studies have been performed in both theoretical and laboratory conditions. In laboratory mode, a

Coherence parameter has been determined to confirm the accuracy of the test, which indicates the high accuracy of the tests performed and the accuracy of the data.

5. Acknowledgements

The tests of the present study were carried out in the Vibration Laboratory of the ITRAC Company. Hereby, Mr. K. B. Abadi and Mr. Khatami who have worked hard and helped researchers in performing the tests, are sincerely appreciated.

References

1. Salawu, O.S. Williams, C. Bridge assessment using forced-vibration testing. Journal of structural engineering. 1995. Vol. 121. No. 2. Pp. 161–173.
2. Salawn, O.S. Damage location using vibration mode shapes. Proceedings of 12th IMAC. 1994. Pp. 933–938.
3. Salawu, O.S. Detection of structural damage through changes in frequency: a review. Engineering structures. 1997. Vol. 19. No. 9. Pp. 718–723.
4. Lyapin, A., Shatilov, Y. Vibration-based Damage Detection of the Reinforced Concrete Column. Procedia Engineering. 2016. Vol. 150. Pp. 1867–1871.
5. Yang, C., Oyadiji, S.O. Damage detection using modal frequency curve and squared residual wavelet coefficients-based damage indicator. Mechanical Systems and Signal Processing. 2017. Vol. 83. Pp. 385–405.
6. Wang, J.T.S., Liu, Y.Y., Gibby, J.A. Vibrations of split beams. Journal of Sound Vibration. 1982. Vol. 84. Pp. 491–502.
7. Narkis, Y. Identification of crack location in vibrating simply supported beams. Journal of sound and vibration. 1994. Vol. 172. No. 4. Pp. 549–558.
8. Messina, A., Jones, I.A., Williams, E.J. Damage detection and localization using natural frequency changes. Proceedings of conference on Identification in Engineering Systems. 1996. Pp. 67–76.
9. Messina, A., Williams, E.J., Contursi, T. Structural damage detection by a sensitivity and statistical-based method. Journal of sound and vibration. 1998. Vol. 216. No. 5. Pp. 791–808.
10. Gadelrab, R.M. The effect of delamination on the natural frequencies of a laminated composite beam. Journal of Sound and Vibration. 1996. Vol. 197. No. 3. Pp. 283–292.
11. Kessler, S.S., et al. Damage detection in composite materials using frequency response methods. Composites Part B: Engineering. 2002. Vol. 33. No. 1. Pp. 87–95.
12. Della, C.N., Shu, D. Vibration of delaminated composite laminates: A review. Applied Mechanics Reviews. 2007. Vol. 60. No. 1. Pp. 1–20.
13. Alnefaie, K. Finite element modeling of composite plates with internal delamination. Composite Structures. 2009. Vol. 90. No. 1. Pp. 21–27.
14. Salawu, O.S. Detection of structural damage through changes in frequency: a review. Engineering structures. 1997. Vol. 19. No. 9. Pp. 718–723.
15. Fan, W., Qiao, P. Vibration–based damage identification methods: a review and comparative study. Structural health monitoring. 2011. Vol. 10. No. 1. Pp. 83–111.
16. Kim, J.T., Ryu, Y.S., Cho, H.M., Stubbs, N. Damage identification in beam–type structures: frequency–based method vs mode-shape-based method. Engineering structures. 2003. Vol. 25. No. 1. Pp. 57–67.
17. Wei, Z. Yam, L.H. Cheng, L. Detection of internal delamination in multi–layer composites using wavelet packets combined with modal parameter analysis. Composite Structures. 2004. Vol. 64. No. 3–4. Pp. 377–387.
18. Hong, J.-C., et al. Damage detection using the Lipschitz exponent estimated by the wavelet transform: applications to vibration modes of a beam. International journal of solids and structures. 2002. Vol. 39. No. 7. Pp. 1803–1816.
19. Katunin, A. Damage identification in composite plates using two–dimensional B–spline wavelets. Mechanical Systems and Signal Processing. 2011. Vol. 25. No. 8. Pp. 3153–3167.
20. Chang, C.-C., Chen, L.-W. Detection of the location and size of cracks in the multiple cracked beam by spatial wavelet based approach. Mechanical Systems and Signal Processing. 2005. Vol. 19. No. 1. Pp. 139–155.
21. Petinov, S.V., Guchinsky, R.V., Sidorenko, V.G. Damage identity in fatigue assessment of structures. Magazine of Civil Engineering. 2016. 61(1). Pp. 82–88. DOI: 10.5862/MCE.61.8
22. Benin A.V., Semenov A.S., Semenov S.G., Beliaev M.O., Modestov V.S. Methods of identification of concrete elastic–plastic–damage models. Magazine of Civil Engineering. 2017. 77(8). Pp. 279–297. DOI: 10.18720/MCE.76.24
23. Wang, Q.-T., Chang, X. Analysis of concrete–filled steel tubular columns with. Steel and Composite Structures. 2013. Vol. 15. No. 1. Pp. 41–55.
24. Rezaifar, O., Yoonesi, A., Yousefi, S. H., Gholhaki, M. Analytical study of concrete–filled effect on the seismic behavior of restrained beam–column steel joints. Scientia Iranica. Transaction A, Civil Engineering. 2016. Vol. 23. No. 2. Pp. 475.
25. Rezaifar, O. Younesi, A. Finite element study the seismic behavior of connection to replace the continuity plates in (NFT/CFT) steel columns. Steel and Composite Structures. 2016. Vol. 21. No. 1. Pp. 73–91.
26. Rezaifar, O., Nazari, M. Experimental Study the Seismic Behavior of Types of Continuity Plates in Beam–to–HSS Column Connections, 2016. MSc. Thesis, Semnan university, Semnan, Iran.
27. Rezaifar, O., Monavari, M. Experimental Study the Seismic Behavior of Types of Continuity Plates in Beam–to–CFT Column Connections, 2016. MSc. Thesis, Semnan university, Semnan, Iran.
28. Rezaifar, O, Younesi, A. Experimental study discussion of the seismic behavior on new types of internal/external stiffeners in rigid beam–to–CFST/HSS column connections. Construction and Building Materials. 2017. Vol. 136. Pp. 574–589.
29. XU, B., Li, B., Song, G. Active debonding detection for large rectangular CFSTs based on wavelet packet energy spectrum with piezoceramics. Journal of Structural Engineering. 2012. Vol. 139. No. 9. Pp. 1435–1443.
30. Xu, B., Zhang, T., Song, G., Gu, H. Active interface debonding detection of a concrete–filled steel tube with piezoelectric technologies using wavelet packet analysis. Mechanical Systems and Signal Processing. 2013. Vol. 36(1). Pp. 7–17.

31. Ri, H., Ni, B. Embedded Interface Debonding Detection for an Irregular Complex Multi–chamber Steel Reinforced Concrete Column with PZT Impedance. Structural Health Monitoring. 2015.
32. Pandey, A.K., Biswas, M., Samman, M.M. Damage detection from changes in curvature mode shapes. Journal of sound and vibration. 1991. Vol. 145. No. 2. Pp. 321–332.
33. Duan, W.H., Wang, Q., Quek, S.T. Applications of piezoelectric materials in structural health monitoring and repair. Selected research examples. Materials. 2010. Vol. 3. No. 12. Pp. 5169–5194.
34. Frswell, M., Mottershead, J.E. Finite element model updating in structural dynamics. Springer Science & Business Media. 2013.
35. Gao, R.X., Yan, R. Wavelets: Theory and applications for manufacturing. Springer Science & Business Media. 2010.
36. Debnath, L., Shah, F.A. Wavelet transforms and their applications. Boston: Birkhäuser, 2002.
37. Stephane, M. A wavelet tour of signal processing: the sparse way. Academic press. 2008.

Contacts:

Adel Younesi: +989113242951; a.younesi@semnan.ac.ir
Omid Rezaifar: +982333383761; orezayfar@semnan.ac.ir*
Majid Gholhaki: +982333654121; mghlhaki@semnan.ac.ir
Akbar Esfandiari: +982164545041; a_Esfandiari@aut.ac.ir

Федеральное государственное автономное образовательное учреждение высшего образования
Санкт-Петербургский политехнический университет Петра Великого

ПОЛИТЕХ
Санкт-Петербургский политехнический университет Петра Великого

Инженерно-строительный институт
Центр дополнительных профессиональных программ

195251, г. Санкт-Петербург, Политехническая ул., 29,
тел/факс: 552-94-60, www.stroikursi.spbstu.ru,
stroikursi@mail.ru

Приглашает специалистов проектных и строительных организаций,
не имеющих базового профильного высшего образования
на курсы профессиональной переподготовки (от 500 часов)
по направлению «Строительство» по программам:

П-01 «Промышленное и гражданское строительство»

Программа включает учебные разделы:

- ***Основы строительного дела***
- ***Инженерное оборудование зданий и сооружений***
- ***Технология и контроль качества строительства***
- ***Основы проектирования зданий и сооружений***
- ***Автоматизация проектных работ с использованием AutoCAD***
- ***Автоматизация сметного дела в строительстве***
- ***Управление строительной организацией***
- ***Управление инвестиционно-строительными проектами. Выполнение функций технического заказчика***

П-02 «Экономика и управление в строительстве»

Программа включает учебные разделы:

- ***Основы строительного дела***
- ***Инженерное оборудование зданий и сооружений***
- ***Технология и контроль качества строительства***
- ***Управление инвестиционно-строительными проектами. Выполнение функций технического заказчика и генерального подрядчика***
- ***Управление строительной организацией***
- ***Экономика и ценообразование в строительстве***
- ***Управление строительной организацией***
- ***Организация, управление и планирование в строительстве***
- ***Автоматизация сметного дела в строительстве***

П-03 «Инженерные системы зданий и сооружений»

Программа включает учебные разделы:

- ***Основы механики жидкости и газа***
- ***Инженерное оборудование зданий и сооружений***
- ***Проектирование, монтаж и эксплуатация систем вентиляции и кондиционирования***
- ***Проектирование, монтаж и эксплуатация систем отопления и теплоснабжения***
- ***Проектирование, монтаж и эксплуатация систем водоснабжения и водоотведения***
- ***Автоматизация проектных работ с использованием AutoCAD***
- ***Электроснабжение и электрооборудование объектов***

П-04 «Проектирование и конструирование зданий и сооружений»

Программа включает учебные разделы:

- ***Основы сопротивления материалов и механики стержневых систем***
- ***Проектирование и расчет оснований и фундаментов зданий и сооружений***
- ***Проектирование и расчет железобетонных конструкций***
- ***Проектирование и расчет металлических конструкций***
- ***Проектирование зданий и сооружений с использованием AutoCAD***
- ***Расчет строительных конструкций с использованием SCAD Office***

П-05 «Контроль качества строительства»

Программа включает учебные разделы:

- ***Основы строительного дела***
- ***Инженерное оборудование зданий и сооружений***
- ***Технология и контроль качества строительства***
- ***Проектирование и расчет железобетонных конструкций***
- ***Проектирование и расчет металлических конструкций***
- ***Обследование строительных конструкций зданий и сооружений***
- ***Выполнение функций технического заказчика и генерального подрядчика***

По окончании курса слушателю выдается диплом о профессиональной переподготовке установленного образца, дающий право на ведение профессиональной деятельности